

Fernando Almazán Román

# Development of $\mu$ -sensors and $\mu$ -preconcentrators for explosives and chemical threats detection

Director/es

María Pilar Pina Iritia  
Miguel Ángel Urbiztondo Castro

<http://zaguan.unizar.es/collection/Tesis>

© Universidad de Zaragoza  
Servicio de Publicaciones

ISSN 2254-7606

Tesis Doctoral

DEVELOPMENT OF M-SENSORS AND M-  
PRECONCENTRATORS FOR EXPLOSIVES AND  
CHEMICAL THREATS DETECTION

Autor

Fernando Almazán Román

Director/es

María Pilar Pina Iritia  
Miguel Ángel Urbiztondo Castro

**UNIVERSIDAD DE ZARAGOZA**  
**Escuela de Doctorado**

Programa de Doctorado en Ingeniería Química y del Medio Ambiente

2020





**DEVELOPMENT OF  
 $\mu$ -SENSORS AND  $\mu$ -PRECONCENTRATORS  
FOR EXPLOSIVES AND CHEMICAL THREATS  
DETECTION**

**Fernando Almazán Román**

Ph.D. dissertation submitted to the Chemical and Environmental Engineering  
Department at the University of Zaragoza (Spain) in partial fulfilment of the  
requirements for the degree of Doctor.

Zaragoza, February 2020



## Summary and Thesis outline

The present work has been performed in the Chemical and Environmental Engineering Department at the University of Zaragoza, within the Nanostructured Films and Particles (NFP) research group, linked to the Nanoscience Institute of Aragon (INA). This research, carried out in INA over a 5-year period (2014-2019), was aligned with the research project NanoTRAPTOR (CTQ2013-49068-C2-1-R) funded by the MICINN (Spain) and defined in the research plan for doctoral scholarship founded by the same ministry as Training of Researcher Personnel (FPI, BES-2014-068036). Also, during the course of this Thesis a scholarship for an Academic Stay (August – December 2016) to the University of Michigan (USA) has been granted by MICINN (EEBB-I-16-10740).

This work is focused on studying new solutions to prevent and rapid actuate against CBRNe (chemical, biological, radiological, nuclear and explosive) threats. Thus, it is proposed herein the integration of micro- and mesoporous sorbents (zeolites, metal-organic frameworks and mesoporous silica materials) as well as imidazolium-based polymeric ionic liquid films with intrinsic affinity properties towards nitro- and organophosphorous compounds into functional electronic nose for preconcentration and detection of explosive and nerve agents (NA) vapours. The proposed electronic nose is composed of a micropreconcentration unit and a gas sensor based on an array of  $\mu$ -cantilevers modified with nanostructured materials.

The potential of the devices in this work has been assessed by their exposition to explosive related compounds and nerve agents (NA) surrogates; all of them in gas phase at relevant conditions (trace level concentration). Thus, the functionalized array of  $\mu$ -cantilevers has been applied to the detection of nitroaromatic compounds (orto-mononitrotoluene, o-MNT), as well as explosive taggants (dimethyl methyl dinitrobutane, DMDNB) and commercial explosives (detonant cord and C-4) vapors in ambient conditions. The modified micropreconcentrators have been extensively tested for the adsorption and preconcentration of a common NA surrogate dimethyl methylphosphonate DMMP at ppb and ppm level. Finally, as proof of concept, the micropreconcentration unit has been coupled with the functionalized array of  $\mu$ -cantilever to enhance the sensing performance of the sensing unit for volatile organic compounds (VOC) detection at ppm level.

This thesis is structured in seven chapters for the sake of easy understanding:

- Chapter I introduces one of the main concerns in Homeland Security: defence against CBRNe threats derive from terrorist attacks and particularly those derived from explosive and chemical warfare agent threats (particularly with NA). It is presented a brief review of commercial solutions that nowadays is being used by local law enforcement agencies to prevent and rapid actuate against one of such threats. Then, the main scientific progress in the area of explosive and NA detection in gas phase is given as well as selective sorbent materials towards nitro- and phosphoryl-groups, characteristics in nitro-related explosives and organophosphorus NA, respectively.
- Chapter II presents the micro- and mesoporous materials as well as polymeric ionic liquid films that are proposed as sorbents to be integrated into the  $\mu$ -devices (micropreconcentrator unit and gas sensor). The synthesis protocols for powder or films are given as well as the integration approaches in the microdevices for each material. Finally, the morphological, textural, crystallographic and thermal stability characterization of the materials is discussed.
- Chapter III is dedicated to the detection of explosive compounds using a gas sensor based on  $\mu$ -cantilevers modified with nanoporous solids. The functionalized  $\mu$ -cantilevers are exposed to vapours of explosive related compounds as well as commercial explosives (detonant cord and explosive plastic C-4). The different coatings are tested in order to compile a database of responsive materials whose combination could potentially derive into a distinctive fingerprint of each explosive, that allow its detection and identification.
- Chapter IV describes the fabrication of the microfluidic chip on Si substrate, including the ancillary elements needed to obtain a functional micropreconcentrator. The design of the microfluidic devices is assisted by 3-D finite element modelling. This numerical model accounts for fluid dynamics inside the microfluidic path as well as heat distribution from the integrated heating coil. The equation of the numerical model has been solved in the COMSOL Multiphysics simulation environment.
- Chapter V presents the evaluation of the micropreconcentrators modified with micro- and mesoporous materials, as well as polymeric ionic films, for



organophosphorus compounds preconcentration, using as target molecule a common nerve agent surrogate (DMMP) at ppm level. Different analytic expressions to evaluate the sorption process on the modified microdevices are presented. Additionally, a 3D mathematical model, implemented in COMSOL Multiphysics, has been also developed to simulate the fluid and sorbent phase evolution during the sorption process.

- Chapter VI is devoted to the evaluation of the preconcentration coefficient of some selected functional micropreconcentrators after exposure of ppb-traces of the organophosphorus compound DMMP. Finally, the performance of a miniaturized gas detection system comprising a micropreconcentrator unit placed upstream of the functionalized microcantilever array is illustrated with n-hexane vapors at ppm level.
- Chapter VII compiles the main conclusion of this Thesis and introduces some of the research lines of investigation that emerge as result of the work presented.



## Resumen y esquema de la Tesis

El presente trabajo ha sido realizado en el Departamento de Ingeniería Química y Tecnologías del Medio Ambiente de la Universidad de Zaragoza, dentro del grupo de Partículas y Películas Nanoestructuradas (NFP) perteneciente al Instituto de Nanociencia de Aragón (INA). Esta investigación, sido llevada a cabo en el INA en un periodo de 5 años (2014-2019), estaba alineada con el proyecto de investigación NanoTRAPTOR (CTQ2013-49068-C2-1-R) financiado por el MICINN (España) y enmarcada dentro del plan de ayuda para la formación de doctores financiado por el mismo organismo como plan de Formación de Personal Investigador (FPI, BES-2014-068036). Además, durante el transcurso de esta Tesis se realizó una Estancia Académica (agosto – diciembre 2016) a la Universidad de Michigan (EE. UU.) financiada por el MICINN (EEBB-I-16-10740).

Esta Tesis se enfoca en el estudio de nuevas soluciones en prevención y actuación rápida contra amenazas NRBQe (nuclear, radiológica, biológica, química y explosiva). Este trabajo propone la integración de sorbentes micro- y mesoporosos (zeolitas, polímeros de coordinación porosa y materiales mesoporosos basados en sílice) así como de películas poliméricas de líquidos iónicos basados en imizadol con afinidades intrínsecas hacia compuestos nitro y organofosforados en una nariz electrónica funcional para la preconcentración y detección de vapores de explosivos y agentes nerviosos. La nariz electrónica propuesta se compone de una unidad de micropreconcentración y de un detector de gases basados en micropalanca funcionalizadas con materiales nanoestructurados.

El potencial de los dispositivos desarrollados en este trabajo se ha evaluado mediante su exposición a materiales relacionados con explosivos y simulantes de agentes nerviosos (AN), todos ellos en fase gas a concentraciones relevantes (concentraciones a nivel traza). Así, el sensor de gas basado en micropalanca funcionalizadas ha sido evaluado en la detección de vapores de compuestos nitroaromáticos (orto-mononitrotolueno, o-MNT) así como de marcadores de explosivos (dimetil dinitrobutano, DMDNB) y explosivos comerciales (cordón detonante y C-4) en condiciones ambientales. Los preconcentradores funcionalizados han sido ensayados para la adsorción y preconcentración del simulante de AN dimetil metilfosfonato DMMP en concentraciones de parte por billón y parte por millón. Finalmente, como prueba de concepto, la unidad de micropreconcentración fue conectada con el chip de micropalanca funcionalizadas para mejorar la sensibilidad de este último para compuestos orgánicos volátiles a concentraciones de partes por millón.

Esta tesis se estructura en siete capítulos en aras de una fácil comprensión:

- En el Capítulo I se introduce una de las mayores preocupaciones de muchas Agencias de Seguridad: la defensa contra amenazas NRBQe derivadas de ataques terroristas, particularmente, de aquellas relacionadas con el uso de explosivos y agentes de guerra química (particularmente agentes nerviosos). Se presenta un breve resumen de las soluciones comerciales que actualmente están siendo usadas por los Cuerpos de Seguridad del Estado para prevenir y actuar en caso de amenaza. A continuación, se repasan los principales progresos científicos en el área de detección de explosivos y agentes nerviosos en fase gas, así como de materiales para la adsorción preferencial de compuestos que contengan grupos nitro y fosforil, característicos de compuestos explosivos y organofosforados, respectivamente.
- El Capítulo II presenta los materiales micro- y mesoporosos, así como las películas poliméricas de líquido iónico propuestos en este trabajo para su integración en los microdispositivos (micropreconcentrador y sensor de gas). Los protocolos de síntesis de cristales discretos y películas policristalinas son presentados, así como de las técnicas de integración de capas dentro del dispositivo atendiendo a las características de cada material. Finalmente, se discute la morfología, propiedades texturales, cristalografía y estabilidad térmica de los sorbente.
- El Capítulo III está dedicado a la detección de compuestos explosivos usando sensores de gases basados en micropalancas modificadas con sólidos nanoporosos. Las micropalancas funcionalizadas son expuestas a vapores de compuestos relacionados con explosivos, así como de explosivos reales (cordón detonante y C-4). Los distintos recubrimientos nanoestructurados son ensayados con la finalidad de elaborar una base de datos con su respuesta ante cada explosivo, que potencialmente pueda derivar en una biblioteca de huellas olfativas que permita su detección e identificación de estos.
- El Capítulo IV describe el proceso de fabricación en sustrato silíceo de los chips microfluídicos, incluyendo la fabricación de los elementos auxiliares necesarios para su funcionamiento. El diseño del microdispositivo ha sido asistido por un modelo tridimensional basado en elementos finitos. Este modelo se ha usado para calcular la distribución del fluido en el interior del dispositivo, así como la

distribución del calor proveniente de la espira de calefacción integrada en la parte inferior del mismo. Las ecuaciones numéricas han sido resueltas usando el entorno de simulación COMSOL Multiphysics.

- El Capítulo V presenta los resultados de la evaluación de los micropreconcentradores modificados con sorbentes micro- y mesoporosos, así como con películas poliméricas de líquido iónico, usando como molécula diana el simulante de agente nervioso DMMP a concentraciones de parte por millón. Se presentan también las distintas expresiones analíticas empleadas para evaluar el proceso de sorción. Igualmente, se ha desarrollado un modelo matemático tridimensional para modelar la evolución en la fase fluida y sólida del proceso de sorción. Nuevamente, las ecuaciones matemáticas del modelo han sido resueltas en el entorno COMSOL Multiphysics.
- El Capítulo VI recoge la evaluación del coeficiente de preconcentración de una selección de micropreconcentradores funcionales después de haber sido expuestos a trazas de DMMP (concentraciones de parte por billón). Finalmente, el funcionamiento del sistema miniaturizado de detección de gases compuesto por la unidad de micropreconcentración aguas arriba del chip de micropalancas funcionalizadas se demuestra con vapores de n-hexano a concentraciones de parte por millón.
- El Capítulo VII recoge las principales conclusiones de esta Tesis y presenta algunas de las diferentes líneas de investigación que han emergido a partir de los resultados obtenidos.



# INDEX

<b>1. Introduction.....</b>	<b>1</b>
<b>1. 1. Challenges in Homeland Security .....</b>	<b>1</b>
<b>1. 2. Commercial explosives and Improvised explosive devices .....</b>	<b>2</b>
<b>1. 3. Chemical weapons.....</b>	<b>3</b>
1. 3. 1. Nerve Agents.....	4
<b>1. 4. Defining characteristics of sensors .....</b>	<b>8</b>
<b>1. 5. Explosive and CWA commercial gas detection systems.....</b>	<b>10</b>
<b>1. 6. Novel trends in explosives and CWA vapor detection: state of the art .....</b>	<b>13</b>
<b>1. 7. Selective materials towards nitro- and phosphoryl- groups .....</b>	<b>16</b>
<b>1. 8. Proposed sorbents in this work.....</b>	<b>20</b>
1. 8. 1. Microporous materials.....	20
1. 8. 2. Silica-based mesoporous materials .....	25
1. 8. 3. Ionic liquids.....	26
<b>1. 9. Objectives .....</b>	<b>27</b>
<b>2. Materials for sorption of nitro- and organophosphorus vapors .....</b>	<b>31</b>
<b>2. 1. Introduction.....</b>	<b>31</b>
<b>2. 2. Synthesis of microporous sorbents.....</b>	<b>31</b>
2. 2. 1. Zeolitic materials.....	31
2. 2. 2. ETS-10 and post-synthesis treatments .....	33
2. 2. 3. Metal-Organic Frameworks .....	35
<b>2. 3. Synthesis of mesoporous silica MCM-48 .....</b>	<b>47</b>
<b>2. 4. In situ polymerization of ionic liquids.....</b>	<b>49</b>
2. 4. 1. Modified graphitized-carbon adsorbents with IL.....	49
2. 4. 2. Deposition on Si microdevices.....	50
<b>2. 5. Characterization of sorbent materials .....</b>	<b>54</b>
<b>2. 6. Conclusions.....</b>	<b>56</b>

<b>3. Explosive related compounds detection using <math>\mu</math>-cantilevers modified with nanoporous solids .....</b>	<b>61</b>
<b>3. 1. Introduction.....</b>	<b>61</b>
<b>3. 2. <math>\mu</math>-cantilevers as chemical sensors .....</b>	<b>61</b>
3. 2. 1. Actuation methods.....	62
3. 2. 2. Detection methods .....	63
3. 2. 3. Mechanics of the rigid solid .....	65
<b>3. 3. Experimental set-up.....</b>	<b>68</b>
3. 3. 1. Microfabrication of Si $\mu$ -Cantilevers .....	68
3. 3. 2. Material deposition.....	69
3. 3. 3. Experimental set-up for gas sensing measurements.....	71
<b>3. 4. Detection of o-MNT in synthetic gas mixtures.....</b>	<b>76</b>
3. 4. 1. o-MNT detection on titanosilicates modified $\mu$ -cantilevers.....	77
3. 4. 2. o-MNT detection on mesoporous silica modified $\mu$ -cantilevers .....	79
3. 4. 3. o-MNT detection on metal-organic frameworks modified $\mu$ -cantilevers .....	81
<b>3. 5. Explosive adsorption in simulated environment.....</b>	<b>83</b>
<b>3. 6. Conclusions.....</b>	<b>88</b>
<b>4. Fabrication of Si-based <math>\mu</math>Devices.....</b>	<b>91</b>
<b>4. 1. Introduction.....</b>	<b>91</b>
<b>4. 2. Design of the microfluidic device.....</b>	<b>95</b>
4. 2. 1. 3-D Finite Element Model of the Microfluidic device.....	96
4. 2. 2. Standard microcavity designs.....	102
4. 2. 3. Heating coil design .....	107
4. 2. 4. Particular designs for in-situ growth .....	109
<b>4. 3. Microdevices Fabrication Process.....</b>	<b>109</b>
4. 3. 1. Cavity etching process.....	110
4. 3. 2. Substrate preconditioning and fabrication for adsorbent deposition.....	115
4. 3. 3. Cavity Sealing and Bonding.....	118
4. 3. 4. Heating Element .....	121
4. 3. 5. Final mechanization .....	122
<b>4. 4. Summary of the Microdevices .....</b>	<b>123</b>
<b>5. Adsorption of organophosphorus compounds on functional <math>\mu</math>-preconcentrators.....</b>	<b>129</b>
<b>5. 1. Introduction.....</b>	<b>129</b>
<b>5. 2. Adsorption process on fixed sorbents .....</b>	<b>129</b>



5. 2. 1. Wheeler model .....	131
5. 2. 2. Yoon-Nelson Model .....	132
<b>5. 3. Computational simulation of sorption process on <math>\mu</math>-preconcentrators .....</b>	<b>133</b>
5. 3. 1. Mathematical model .....	133
5. 3. 2. Evaluation of adsorption parameters $k_{ads}$ and $\Gamma_s$ .....	139
<b>5. 4. Experimental set-up used for the evaluation of performance of modified <math>\mu</math>-devices .....</b>	<b>142</b>
5. 4. 1. Trace-level analyte atmospheres generation .....	142
5. 4. 2. Experimental Set-Up .....	145
<b>5. 5. Initial assessment on <math>\mu</math>-preconcentrator performance with <math>C_6H_{14}</math> vapours.....</b>	<b>148</b>
<b>5. 6. Evaluation of DMMP sorption on functional <math>\mu</math>-preconcentrator .....</b>	<b>151</b>
5. 6. 1. $\mu$ -preconcentrators modified with microporous materials .....	151
5. 6. 2. $\mu$ -preconcentrators modified with mesoporous silica .....	162
5. 6. 3. $\mu$ -preconcentrators modified with poly-ionic liquids.....	166
<b>5. 7. Conclusions.....</b>	<b>173</b>
<b>6. Preconcentration of organophosphorus compounds.....</b>	<b>179</b>
<b>6. 1. Introduction.....</b>	<b>179</b>
<b>6. 2. Evaluation of the preconcentration coefficient .....</b>	<b>180</b>
<b>6. 3. Proof of concept: preconcentration of VOCs.....</b>	<b>181</b>
6. 3. 1. Desorption temperature analysis on silicalite-modified $\mu$ -preconcentrators.....	182
6. 3. 2. Performance of the combined $\mu$ -preconcentrator – $\mu$ -cantilever system for n-hexane detection....	183
<b>6. 4. Experimental set-up for evaluating preconcentration coefficient.....</b>	<b>185</b>
<b>6. 5. Evaluation of the <math>\mu</math>-preconcentrator coefficient.....</b>	<b>188</b>
6. 5. 1. Determination of experimental conditions .....	189
6. 5. 2. DMMP preconcentration coefficient on $\mu$ -devices modified with siliceous based sorbents .....	192
6. 5. 3. DMMP preconcentration coefficient on Cu-BTC modified $\mu$ -devices .....	196
6. 5. 4. DMMP preconcentration coefficient on PILs modified $\mu$ -devices .....	197
<b>6. 6. Conclusions.....</b>	<b>200</b>
<b>7. Main conclusions and future work .....</b>	<b>205</b>
<b>7. Conclusiones y trabajo futuro .....</b>	<b>211</b>
<b>8. Bibliography.....</b>	<b>219</b>



# **CHAPTER I:**

## **INTRODUCTION**



# 1. INTRODUCTION

## 1. 1. CHALLENGES IN HOMELAND SECURITY

Defence against CBRNe (chemical, biological, radiological, nuclear and explosive) threats derive from possible terrorist attacks constitutes one of the mayor concerns of many Homeland Security administrations, local law enforcement agencies and overall citizenship. In fact, 2019 Eurobarometer report positioned ‘combating terrorism and organised crime as third top priority (along unemployment) of the European citizens consulted [1], only behind climate change and social poverty (Figure 1.1).

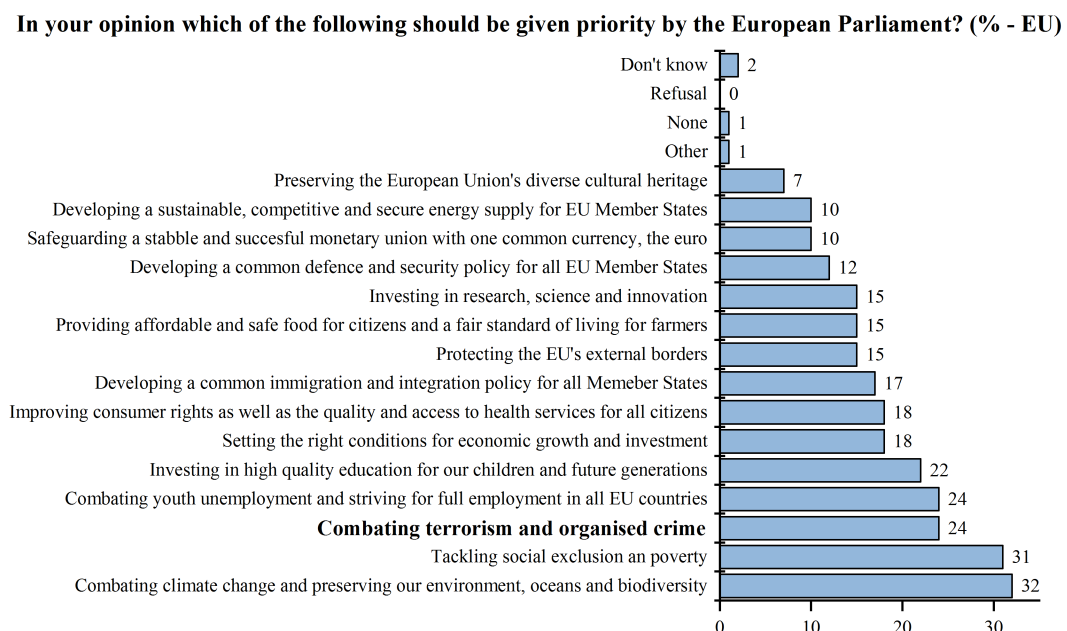


*Figure 1.1. Results of 2019 Eurobarometer concerning top priorities of European citizens. Data from [1].*

Although the methodology of latest terrorist actions has evolved to the direct assault with improvised weapons, it should be notice the latest, deadliest terrorist attack in European territory were performed by coordinated terrorists cells using CBRNe warfare in highly populated areas, as in the Madrid train bombings in March 2004 (191 people were killed and 1841 injured) [2] or the London bombings in July 2005 (56 people were killed and 784 injured) [3]. Fortunately, inside EU there has not been so far any terrorist attack involving mass destruction weapons since WWII, as it had happened previously in Tokyo subway sarin attack by the members

of the cult movement Aum Shinrikyo in 1995 [4] or the sarin poisoning of civilians in Syria in 2013 [5], the treat of an incident of such characteristics in European soil is still present.

CBRNE defence is considered as the protective measures taken in situations in which chemical, biological, radiological, nuclear or explosive warfare hazards may be present. Its goal is the passive protection, contamination avoidance and mitigation. Particularly, in this work we have focused on developing novel tools for explosive and chemical warfare rapid detection and identification in gas phase at trace level (ppb, ppm).

## **1. 2. COMMERCIAL EXPLOSIVES AND IMPROVISED EXPLOSIVE DEVICES**

Explosives are chemical compounds capable of liberate rapidly large amounts of energy, after being subjected to an impact, heat, detonation or friction. The rapid energy release results in a fast rising of pressure of temperature, sublimating or evaporating the compounds into a hot compressed gas. Due to its high pressure and temperature, they expand fast resulting in a high-pressure shock wave to the surrounding environment [6].

Based on structure and performance, explosives are commonly divided according their velocity of detonation (VoD) into 1) low explosives (VoD = cm/s) and 2) high explosives (VoD = km/s) [7]. Low explosives include propellants, smokeless powder, black powder, pyrotechnics, etc. On the other hand, high explosives can be further divided into three groups according its applications: 1) commercial, 2) military and 3) improvised explosive devices (IEDs). Whereas commercial and military explosives can be purchased from legit distributors by legitimate buyers under control, IEDs are home-made devices that can be easily manufactured from non-military chemicals, components or compounds [6].

The detection of explosive and related compounds in gas phase is extremely challenging since most of the solid explosives exhibit low vapor pressure and their vaporization kinetics are usually very slow to the gas phase [8]. The vapor pressure of explosive compounds ranged from highly volatile, e.g. 28 Pa @ 298 K for the taggant DMDNB, to nearly involatile, e.g.  $1.07 \cdot 10^{-6}$  Pa @ 298 K for the commercial explosive PETN, which difficult their detection greatly. Direct vapor detection is even more challenging due additional intrinsic difficulties of gas detection

approaches: environmental interferents (humidity, other VOCs) or ambient diffusion among other.

## 1. 3. CHEMICAL WEAPONS

Chemical Weapons (CW) are, according to the Organisation for the Prohibition of Chemical Weapons (OPCW) [9], chemicals used to cause intentional death or harm through its toxic properties. Unlike conventional weapons, such as nuclear or explosive weapons, CW cause no destruction and are meant to harm or incapacitate the target.

Thousands of toxic substances are toxic enough to be considered CW, or may be considered as precursors, though not all of them are considered a threat. CWC defines three different categories under which these chemicals can be classified according to their purpose:

- Schedule 1 – Chemicals that have few legitimate uses and can only be produce or use for research, medical, pharmaceutical or protective purpose. Most known CW are included in this category, such as, sarin, soman or mustard gas.
- Schedule 2 – Chemicals that have no large-scale industrial uses, but may have legitimate small-scale use, such as, dimethyl methylphosphonate (a precursor of sarin gas, but also use as flame retardant or additive in some fuels [10]) or thiodiglycol (a precursor of mustard gas, but also use as solvent in some inks [11]).
- Schedule 3 – Chemicals that have legitimate large-scale industrial use, such as, phosgene (use in the plastic industry as precursor of polyurethanes [12]) or chloropicrin (use as a broad-spectrum antimicrobial, fungicide, herbicide, insectice and nematicide [13]).

Furthermore, CW can also be classified into several categories according to how they interact with the human body (Table 1.1) [14]:

TABLE I.1. CLASSIFICATION OF CWA

Type of Agent	Agents	Dispersal	Mode of action	Effects
<i>Choking Agents</i>	Chlorine (Cl) Chloropicrin (CG) Diphosgene (DP) Phosgene (Ps)	Gas	Adsorption through lungs	Inflict injury mainly on the respiratory tract.
<i>Blister Agents</i>	Sulphur mustard (H, HD) Nitrogen mustard (HN) Lewisite (L) Phosgene oxine (CX)	Liquid, aerosol, vapour, dust	Adsorption through skin and lungs	Cause large and often life-threatening skin blisters, and may result in blindness and permanent damage to the respiratory system
<i>Blood Agents</i>	Hydrogen cyanide (AC) Cyanogen chloride (CK) Arsine (SA)	Gas	Adsorption through lungs	Inhibit the oxygen transfer of blood cells, causing the body suffocation
<i>Nerve Agents</i>	G-Series agents V-Series agents Novichok agents Insecticides	Liquid, aerosol, vapor, dust	Adsorption through lungs or contact with skin	Block impulses between nerve cells or across synapses.
<i>Riot control agents</i>	Tear gas (CS) Pepper spray (OC)	Liquid, aerosol	Adsorption through lungs, skin and eyes	Temporarily incapacitate by causing eye, mouth, throat, lungs and/or skin irritation

### 1.3.1. NERVE AGENTS

Nerve agents (NAs) are one of the most toxic CWA, in fact, the symptoms appear within seconds and death within minutes depending on concentration and exposure time. Although, all nerve agents are presented in liquid form, some of them exhibit relatively high vapor pressure (~100 Pa) and are easily vaporized or aerosolized. They can be classified as follows:

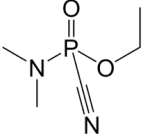
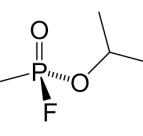
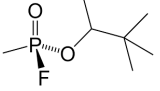
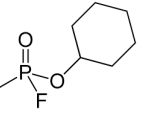


- G-Series – G-series agents are named after being first synthesized by German scientists during World War II and is the oldest family of nerve agents. In this family are included: Tabun (GA), Sarin (GB), Soman (GD) and Cyclosarin (GF).
- V-Series – They were developed after World War II in the United Kingdom. They are persistent gases, i.e., they do not degrade or wash away easily, with high boiling point and low vapor pressure. In this family are included: VE, VG, VM, VR and VX.
- Novichok agents – They were developed by the Soviet Union during the Cold War (from mid-1960s to 1990). They were designed to be undetectable by NATO chemical detection equipment during 1970s and 1980s, to be safer to handle and to circumvent the CWO list of controlled precursors. Some of these agents are binary weapons, which means that the precursors are mixed on site, making them safer to handle and transportation, although a careless preparation may produce a non-optimal agent.
- Insecticides – Some insecticides, including carbamates and other organophosphonates may be potentially used as a CW, although the metabolic path of insects is different enough from mammals that they are not considered a direct threat.

#### 1.3.1.1. G-Series nerve agents

G-Series nerve agents is a family of organophosphorus CW that characterize by being easily vaporized due to their high vapour pressure, though less persistent than their V-agent counterparts. G-Series comprise tabun (GA), sarin (GB), soman (GD) and cyclosarin (GF). In pure state are colourless, but impure agents range from yellow to brown liquids depending on the level of impurities. Also, in pure state they are odourless, though it has been mainly reported a somewhat fruity smell – which most likely be due to impurities. Table 1.2 compiles the main characteristic of the G-series NA compounds.

TABLE 1.2. CHARACTERISTIC PROPERTIES OF G-SERIES NERVE AGENTS

	Tabun	Sarin	Soman	Cyclosarin
<i>NATO designation</i>	GA	GB	GD	GF
<i>Discover</i>	1936	1938	1944	1949
<i>Appearance</i>	Colourless to brown	Colourless	Colourless	Colourless
<i>Odour</i>	None	None	Fruity	None
<i>Vapor density (relative to air)</i>	5.6	4.8	6.3	6.2
<i>Vapor pressure</i>	8 Pa	331 Pa	53 Pa	12 Pa
<i>Structure</i>				

Sarin gas shines out among the G-series nerve agents to be the most lethal and easy to disperse due to its high volatility and has been used not only in war conflicts but also in terrorist attacks against civil population, as in the Tokyo subway sarin attack in 1995 [4] or the sarin poisoning of civilians in Syria in 2013 [5]. Some few studies are available for sarin vapour exposures on human volunteers in order to directly derive acute exposure guideline levels (AEGl). According the symptoms after exposition, exposure time at certain concentration are classified into [15]:

- Level 1: notable discomfort, irritation or certain asymptomatic non-sensory effects. These effects are not disabling and are transient and reversible upon cessation of exposure.
- Level 2: irreversible or other serious, long-lasting adverse health effects or an impaired ability to escape.
- Level 3: life-threatening health effects or death.

As published by the U.S. Environmental Protection Agency [16], in Table 1.3 are compile AEGL for sarin gas exposures. Results indicate that the threshold for miosis and other minimal toxic effects falls in the range of 0.05 – 0.50 mg/m<sup>3</sup> for 30 – 10 min exposures, respectively.

TABLE 1.3. AEGL FOR SARIN GAS EXPOSURES

Effect	Sarin exposure time				
	10 min	30 min	60 min	240 min	480 min
AEGL-1 (Nondisabling)	1.2 ppb (6.9 µg/m <sup>3</sup> )	0.7 ppb (4.0 µg/m <sup>3</sup> )	0.5 ppb (2.8 µg/m <sup>3</sup> )	0.2 ppb (1.4 µg/m <sup>3</sup> )	0.1 ppb (1.0 µg/m <sup>3</sup> )
AEGL-2 (Disabling)	15 ppb (87 µg/m <sup>3</sup> )	8.5 ppb (50 µg/m <sup>3</sup> )	6.0 ppb (35 µg/m <sup>3</sup> )	2.9 ppb (17 µg/m <sup>3</sup> )	2.2 ppb (13 µg/m <sup>3</sup> )
AEGL-3 (Lethal)	64 ppb (380 µg/m <sup>3</sup> )	32 ppb (190 µg/m <sup>3</sup> )	22 ppb (130 µg/m <sup>3</sup> )	12 ppb (70 µg/m <sup>3</sup> )	8.7 ppb (51 µg/m <sup>3</sup> )

### 1.3.1.2. CWA surrogates

After the Chemical Weapons Convention (CWC) was enacted by the OPCH in 1997, the production, stockpiling, transport and use of chemical warfare agents was severely restricted. Not only CWCs does control CWA in their native form but also places control on the precursors used in the productions of CWAs. Since these precursors are far less toxic and easier to handle, and yet they can mimic the physical and chemical properties of CWA, they are often used in researching and personnel training [17]. The Table 1.4 presents some of the typical surrogate compounds as well as their CWA counterparts.

TABLE 1.4. TYPICAL CWA SURROGATES AND CWA COUNTERPARTS

Surrogate*	Surrogate chemical structure	CWA chemical structure	CWA
CEES			Mustard gas
DMMP			Sarin
PMP			Soman
DEPA			Tabun
BAET			VX

\*List of acronyms. CEES: 2-chloroethyl ethyl sulphide. DMMP: dimethyl methylphosphonate. PMP: pinacolyl methyl phosphonate. DEPA: diethyl phosphoramidate. BAET: 2-(butylamino) ethanethiol.

## 1. 4. DEFINING CHARACTERISTICS OF SENSORS

A sensor is a device meant to detect an event or change in its environment (temperature, pressure, chemical concentration) and converts it into a measurable signal. Basically, a sensor is divided into a sensitive material that interacts with the external force (e.g., a change of the properties of the sensitive material due to temperature or due to the binding with a protein), a transducer that converts the interaction between the sensitive material and the environment into a measurable signal (e.g., transforming the mass increasing of the sensitive material due to adsorption of a molecule into an electric signal) and a processor that converts that measurable signal into quantitative or qualitative value (e.g., converting the electric signal into a number or a yes/no response) (Figure 1.2).

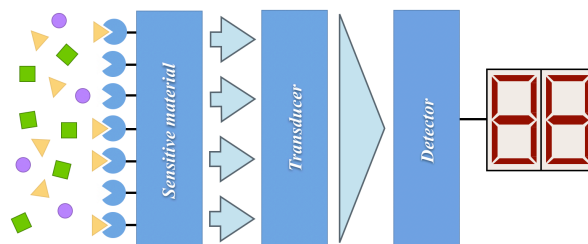


Figure 1.2. Representative schematic of the different parts of a sensor. In this case, a gas sensor where the sensitive material only interacts with one specie (triangles). The interaction between the sensitive material and the analyte is converted into a measurable signal that is understandable for the user (a number).

s

Main characteristics that define the performance of a sensor are:

- *sensitivity*: defined as the degree of signal variation per unit of stimuli that causes it. In the case of gas sensors, it can be given by the shift of the measured signal per mass unit (per unit of mass that adsorbs or interacts with the sensitive materials) but also in terms of the shift of the signal per analyte concentration. This sensitivity must not necessarily give a linear response with concentration; in fact, for gas sensor, it increases as the target concentration decreases. In order to establish a unique sensitivity value, we must calculate the sensitivity at each concentration and fit the resulting data as a function of concentration.
- *limit of detection*: defined as the minimum amount of analyte that can be measured. Commonly, minimum response must be three times higher than noise signal in order to assure that the measured signal is due to the stimulus and not to a perturbation or interference.
- *selectivity*: referred as the ability of the sensor to distinguish the target analyte from interferences at the background. For gas sensors, this characteristic plays an important role and defines the capability of the sensor to correctly identify the target molecule from complex gas mixtures, where some interferences are found in greater concentration than others or may share the similar functional groups. Sometimes, a gas sensor is not defined for a specific target but for a family of

molecules who share functional groups or chemical properties, e.g., alcohols, aromatics, acids, aldehydes...

- *response time*: the time needed by the sensor to overpass certain signal threshold when it is exposed to a constant stimulus. For CBRN (chemical, biological, radiological, nuclear threats) application, it may be a limiting parameter due to the rapid response that must be taken when a threat is detected.
- *signal stability*: referred to the signal response under a constant stimulus and conditioned to transduction characteristics, sort of response signal and equipment used to acquire it. The quality of the signal is conditioned by the drift and the noise. The drift of the signal is defined as a deviation from predicted values of the response under a constant stimulus. It may be derived from unconsidered stimuli of which the transducer is also sensitive, such as temperature. It may be avoided by subtracting the measured signal with a reference value. On the other hand, the noise is defined as the spurious fluctuation of the signal due to external perturbations (electronic parasitic interferences...). In this case, it has to be considered the signal to noise ratio (S/N), which limits the limit of detection of the sensor. However, new electronic read-out systems are able to amplify the level of the measuring signal, thus minimizing S/N values and increasing sensitivity.
- *lifespan*: defined as the working time of a sensor. This parameter is of importance for long-lasting application or harsh working conditions (corrosive media, high temperature, humidity or pressure).

## 1. 5. EXPLOSIVE AND CWA COMMERCIAL GAS DETECTION SYSTEMS

Regarding explosive detection, the most efficient tool used to effectively identify hidden explosive related compounds has been the use of police dogs [18]. Although the sensitivity of some emerging instrumental technologies is on par, or even higher, their ability to individualize the scent picture, ignoring any background interferent, to focus on single odours. Along with their selectivity, their combined mobility and independent thinking rank police dogs as the current best method for real-time explosive detection, with detection limits down to tens of part

per billion to five hundred part per trillion [19]. Although widely used, police dogs can easily get distracted and tired, can only be used effectively for a few hours a day and they may be affected by local diseases and climate effects. Furthermore, they might easily become confused in case of scenarios with several sources of explosive smell [6]. Finally, the use of trained dogs is only well-established for explosive detection, and although some studies about the feasibility of using animals as sentinels of bioterrorism agents, the results are yet inconclusive [20].

Typically commercial solution for CBRNE rapid in-field detection (which besides explosives and CWA detection, also include biological and nuclear threats) are based on smaller, lighter version of standard laboratory-based analytical instruments, such as IR instruments, ion mobility spectrometers (IMS), capillary electrophoresis instruments and gas chromatography-mass spectrometers. In Table 1.5 are presented some of the actual commercial technologies available on the market. It can be seen that the offer in the market ranges from affordable solutions (hundreds of dollars, e.g. QRAE Plus) to overly expensive equipment (millions of dollars, e.g. Hardened MobilTrace) which is unaffordable for many agencies. Furthermore, these solutions are highly specific to certain CBRNE agents so, if one law enforcement agency wants to cover the full range of possible threats, must acquire several of this equipment. Finally, although these solutions are available in the market, the proper use of them required skilled and trained professionals and are not designed for the causal user.

TABLE I.5. COMMERCIAL CBRNE DETECTOR SYSTEMS

Product	Detection method	Technical specifications	Price
BioCapture 650	None described. Collects typical agents released in a bio-threat attack.	Dimensions: 13.3x15.2x37.0 cm Weight: 3.4 kg Sampling times: 5, 15, 30 and 60 min Libraries: spores, bacteria, viruses and toxins	\$ 13 641
C-Scout	Molecular Property (DTA, TG and DSC) and Gamma Spectrometer	Dimensions: 12.7x25.4x43.2 cm Weight: non-available Libraries: Explosives (including TNT, PETN, RDX, HMTD, AN, ANFO), isotopes (137Cs, 241Am), nuclear weapon materials (103Pd, 238Pu, 239Pu, 234U, 235U, 238U).	-
MAB	Selective sampling (particle from 2 to 10 µm), flame spectrometry.	Dimensions: 30.0x16.0x89.5 cm Weight: 14 kg Libraries: bacteria, viruses, toxins	\$ 140 600 (detector, software, cables, laptop)
QRAE Plus	Protected dual-mode catalytic bead (combustible gas detection), electrochemical fuel-cell (oxygen detection) and interchangeable electrochemical for CO, H <sub>2</sub> S, SO <sub>2</sub> , NO, NO <sub>2</sub> , CL <sub>2</sub> , HCN, NH <sub>3</sub> and PH <sub>3</sub> .	Dimensions: 11.5x7.6x4.6 cm Weight: 0.425 kg Libraries: O <sub>2</sub> , Combustible, CO, H <sub>2</sub> S, SO <sub>2</sub> , NO, NO <sub>2</sub> , CL <sub>2</sub> , HCN, NH <sub>3</sub> and PH <sub>3</sub> .	\$ 500 – \$ 2 000 (basic model to top notch model)
ChemPro 100i	Open-loop Ion Mobility Spectroscopy sensor, Temperature, Humidity, Mass Flow, 6 Semiconductor Sensors	Dimensions: 23.0x10.1x5.7 cm Weight: 0.8 kg Libraries: CWAs, TICs, VOCs, CAPs	\$ 9 500
FIDO C3	Patented enzyme polymer technology	Dimensions: 33.7x20.3x18.4 cm Weight: 6.8 kg Libraries: CWAs (G- and V- nerve agents)	-
FIDO X3	FLIR Sensing Element Technology (Fluorescence based, no radioactive source)	Dimensions: 37.0x11.5x7.0 cm Weight: 1.36 kg Libraries: Explosives (including AN, TATP, H <sub>2</sub> O <sub>2</sub> , CH <sub>3</sub> NO <sub>2</sub> )	-
Hardened MobilTrace	Ion Trap Mobility Spectrometer (Nickel 63, 370 MBq strength)	Dimensions: 43.8x15.9x32.4 cm Weight: 5.44 kg Libraries: CWAs, TICs, explosives, precursors, narcotics and taggants	\$ 2 414 803
Itemiser 4DX	Ion Trap Mobility Spectrometer (non-radioactive ion source)	Dimensions: 41.0x48.0x50.0 cm Weight: 12.02 kg Libraries: Explosives and Narcotics	-
Quantum Sniffer QS-H150	Ion Mobility Spectrometry (non-radioactive ion source)	Dimensions: 49.3x12.7x18.8 cm Weight: 5.44 kg Libraries: Explosives (including Semtex, C4, RDX, NG, PETN, EGDN, TNT, Dynamite, HMX, ANFO, Smokeless powder, Black powder, AN)	\$ 39 000
µRAID	Ion Mobility Spectrometer	Dimensions: 6.5x13.0x21.5 cm Weight: 1.2 kg Libraries: CWAs, TICs	-

\*List of acronyms. CWA: chemical warfare agents. TIC: toxic industrial chemicals. VOC: volatile organic compounds. CAP: chemical agent precursors. TNT: trinitrotoluene. RDX: cyclonite. NG: nitro-glycerine. PETN: pentaerythritol tetranitrate. EGDN: nitroglycerol. HMX: octogen. ANFO: ammonium nitrate/fuel oil. AN: ammonium nitrate. TATP: peroxyacetone.



## 1. 6. NOVEL TRENDS IN EXPLOSIVES AND CWA VAPOR DETECTION: STATE OF THE ART

Whilst the use of analytical equipment is widely extended on forensic application, novel researching trends are focused on developing small, portable devices based on MEMS technologies, such as interdigitated resistive or capacity sensors, QCMs (quartz crystal microbalance) or tiny cantilever working as micro-balance. Although the detection methodology is somewhat restricted to certain sensors, what actually characterized the solutions published is the sensing material and its interaction with the target molecules.

For explosive detection, we can observe in Table 1.6 the diversity of approaches taken in order to detect from ppt to ppm traces of explosive-related compounds, including surrogates (oMNT, DNT) to real explosives (TNT, PETN, RDX...) in gas and liquids phase using sensor techniques ranging from optical detection using fiber optic sensors [21] to disposable screen-printed electrochemical sensors [22]. The sensing materials used in this sensor covers from novel single wall carbon nanotubes (SWCNTs) [23] to mesoporous materials (SBA-15) [24] or polymer nanocomposites [25]. Reported limit of detection range from sub ppt values (for PETN and TNT using microcantilevers coated with TiO<sub>2</sub> nanotubes) [25] to ppm level in complex gas mixtures [26].

Regarding, CWA detection, sensor methodologies and sensing materials follow the same trends as with explosive detection, as can be seen on Table 1.7. The main approach difference lies on the lack of actual research with actual CWAs due to the elevate restrictions impose by the OPCH regarding manufacturing and stockpiling CWA even for research application. Furthermore, the highly expensive measures that must be taken care of to safely work with such compounds force the research to be done with surrogate compounds such as DMMP or CEES (surrogate of sarin gas and mustard gas respectively). The few works reporting sensing of actual CWA offer detection limits of ppm (for tabun detection using SERS substrates) [27] or  $\mu\text{M}$  concentration levels in liquid phase (for VX [28], sarin and soman [29] using colorimetric and fluorometric sensors).

TABLE I.6. RECENT ADVANCES IN EXPLOSIVE DETECTION

Sensor methodology	Sensing material	Detection limit	Ref.
Resistive sensor	SWCNTs functionalized with peptides	12 ppb TNT	[23]
Electrochemical sensor	Ordered mesoporous carbon	0.2 ppb TNT	[30]
Optical sensor (fluorescence)	SBA-15 functionalize with AIE luminogen	0.35 ppm NB (in water) 0.64 ppm 4-NT (in water) 1.01 ppm PA (in water)	[24]
Mass sensor	QCM coated with Calix(n)arenes	0.4 ppm DNT	[31]
Mass sensor	Microcantilevers coated with vertically aligned TiO <sub>2</sub> nanotubes	0.8 ppt PETN, TNT	[32]
Mass sensor	Polymer nanocomposite microcantilever coated with self-assembled monolayers of 4-mercaptobenzoic acid, 6-mercaptonicotonic acid and 2-mercaptonicotonic acid	31 ppb TNT 2.1 ppb RDX 5 ppt PETN	[25]
Optical sensor	Portable UV (190-400nm) spectrophotometric based reflected fiber optic sensor	Tested for these concentrations: 149 ppm PETN 47 ppm CE 49 ppm TNT 37 ppm DNT 101 ppm RDX 45 ppm HMX 49 ppm PA	[21]
Field effect	Organic field effect transistors (OFET) with regioregular poly 3-hexylthiophene (rr-P3HT) and hexafluoro-2-propanol-substituted polysiloxane (SXFA) as an organic layer.	100 ppt TNT 70 ppt RDX	[33]
Optical sensor	Gold nanoparticle coated u-bend fibre optic probe	10 ppb DNT, TNT	[34]
Resistive sensor	TiO <sub>2</sub> nanotubes	112 ppt PETN	[35]
Optical sensor	Fluorescence proteins isoforms (GFP <sub>UV</sub> , mTFP0.7, ECFP, eCGP123, ZsYellow, AsRed2)	Tested for: 240 ppm oMNT In solution: DNT, RDX, TNT	[36]
Electrochemical sensor	Disposable screen-printed electrodes (gold working electrode, platinum counter electrode and a silver pseudo-reference electrode)	0.7 ppm NM	[22]
Mass sensor	QCM coated with PP (poly(pentipentycene), PcZn (Ooct) <sub>8</sub> (Phthalocyanine) and PCN (polycyanopropylmethylsiloxane)	120 ppb DNT 8 ppb TNT 18 ppt PETN	[37]
Mass sensor	Polymer (PDMS-AN-NT y PDMS-AN-CA) coated QCM sensors	Analytes recognized and discriminated thanks to Principle Component Analysis: 28737 ppm Toluene 33198 ppm n-octane 687 ppm Nitrobenzene 198 ppm 2-MNT 1315 ppm 2,4-DNT	[26]
Resistive sensor	ZnO-doped nanoparticles	Tested for: 3.34 µg/L 2,6-DNT, picric acid, mineral explosives, NH <sub>4</sub> NO <sub>3</sub>	[38]
(cTD-CRDS) Spectrometer	Heated platinum (IV) oxide catalyst	0.3 ppb TNT	[39]

TABLE 1.7. RECENT ADVANCES IN CWA DETECTION

<i>Sensor methodology</i>	<i>Sensing material</i>	<i>Detection limit</i>	<i>Ref.</i>
SAWs sensor (Love-wave)	Polymers	40 ppb of DMMP	[40]
Electrochemical biosensor (cyclic voltammetry)	Peptide nanotubes on gold electrodes	12 ppb of malathion, but only the activity is up to 45 days	[41]
Electrochemical (cyclic voltammetry)	Sodium tetraborate	1.33 ppm for DCNP (diethyl chlorophosphate)	[42]
Resistive sensors	Polymer doped with copper	Tested at 5 ppm of DMMP	[43]
Resistive sensors	SWCNTs	1.57 ppm of DMMP	[44]
Resistive sensors	SWCNTs functionalized with –OH groups	50 ppb of DMMP	[45]
Resistive sensors	SWCNTs – aniline composite	1 ppm of DMMP is 10% of resistance change	[46]
Resistive sensors	SWCNTs	1 ppm of DMMP is 3.6% of resistance change	[47]
Resistive sensors	SnO <sub>2</sub> thin films	100 ppb of DMMP	[48]
Resistive sensors	Conducting Polymer Nanotubes	10 ppt of DMMP	[49]
Optical sensor	LC – Liquid crystals doped with copper	3 ppb of DMMP	[50]
Optical sensor (Fluorescence)	Functionalized polymer paper	25 ppb of DCNP	[51]
Optical sensor (Fluorescence)	Sensing film coated with a colorimetric and fluorescence probe (4-(6-(tertbutyl)pyridine-2-yl)-N,N-diphenylaniline)	2.6 ppb of DCP	[52]
SAW sensor	Love-wave devices coated with graphene oxide	9 ppm of DMMP, 40 ppmv of DPGME (dipropylene glycol monomethyl ether, simulant of nitrogen mustard)	[53]
SERS	Flexible gold-covered Si nanopillars substrate	ppm of Tabun	[27]
SAW sensor	Molecular imprinting monolayer for sarin acid	0.10 mg/m <sup>3</sup> of sarin	[54]
Optical sensor (colorimetric and fluorometric)	Heptamethine cyanine	7.5 mM of Sarin 2.5 mM of Soman	[29]
Optical sensor (colorimetric and fluorometric)	Squaraine	8 μM of Tabun 8 μM of VX	[28]
Optical sensor	Self-propelled micromotor-based fluorescent “On-Off” detection	10 <sup>-6</sup> M of DCP	[55]
Optical sensor	Spiro benzopyran system	10 <sup>-8</sup> M of DCP	[56]

Finally, the latest researching trend is the integration of CBRNE detectors into UAVs (unmanned aerial vehicles) with the final goal of avoid personal contact with possible hazardous threats in order to minimize collateral casualties and cover big susceptible areas. Some of the recent projects are presented in Table 1.8.

TABLE I.8. UAVS FOR CBRNE DETECTION

<i>Company</i>	<i>Project type</i>	<i>Description</i>	<i>Ref.</i>
ESG/Bruker	R&D collaborative project	UMAT helicopter (Unmanned Mission Avionics Test Helicopter) from German company ESG, equipped with the chemical sensor “ $\mu$ RAID” (Rapid Alarm and Identification Device), from Bruker, company with headquarters in Germany and USA.	[57], [58]
Research International	American company devoted to CBRN systems	Various solutions:  1) Flying Laboratory: fixed wing UAV, up to 15 hours flight, with full CBRN monitoring capabilities, equipped with several sensors for toxic gases, radiation and biological aerosols detection.  2) UAV-Based Aerosol Collectors and Detectors, many possible combinations, between sensors and different flying platforms, for more specific missions (detailed in the web site).	[59], [60]
German Air Force / EMT	German Air Force defence project based on a UAV from EMT	Fixed wing UAV (LUNA model) for reconnaissance and surveillance, up to 8-hour flight, from the company EMT, used by German Air Force for multiple missions since 2000, with CBRN detection missions among them.	[61], [62]

## 1. 7. SELECTIVE MATERIALS TOWARDS NITRO- AND PHOSPHORYL- GROUPS

Adsorption is the adhesion of atoms, ions or molecules from a gas, liquid or dissolve solid into a surface. This process creates a film of the adsorbate – target analyte – on the surface of the adsorbent – substrate. The reverse process is called desorption. Adsorption is a surface phenomenon which is consequence of surface energy. Depending on the bonding of adsorbate – adsorbent, it can be classified as physisorption and chemisorption. In physisorption processes the nature of both species are not being electronically altered, and bonding is mainly a weak force interaction – van der Waals, hydrogen bonds, London forces, etc. On the contrary,

chemisorption involves a chemical reaction between the surface and the adsorbate, thus new chemical bonds are generated at the interface.

Surface area and pore structure of adsorbents as well as surface chemical functional groups are key factors that determine the performance of guest molecules adsorptions [63]. Although, we should not only consider adsorbent properties but also adsorbate characteristics such as: molecular structure and size (compatibility between adsorbent's pore size and guest molecule kinetic diameter) [64], molecular polarity (polar compounds prefer to be adsorbed onto adsorbents with polar groups, while nonpolar compounds prefer adsorbents without polar groups) [65] or boiling point (high boiling point adsorbates would be preferentially adsorbed due to stronger intermolecular forces) [66]. Finally, adsorption conditions may impact greatly the performance of the adsorbent. Experimental temperature and humidity may play an important role, along with analyte concentration, gas velocity and co-existing adsorbates (competitive adsorption of two or more species).

Explosive nitro compounds exhibit the functional nitro group ( $-\text{NO}_2$ ); whereas organophosphorus agents present a phosphoryl group ( $-\text{P}=\text{O}$ ) in their composition. As we have seen earlier, one of the strategies to identify these compounds among other volatile compounds with similar chemical properties (partial pressure, polarity, kinetic diameter) is by promoting the interaction of the adsorbent with that particular functional group. This strategy, along with pore size and polarity of the adsorbent, will allow us to have selective adsorbent.

This approach has been applied previously, for example in the work of Patolsky et al, where they reported a multiplexed high-throughput detection and identification of explosives by a single SiNW-FETs (Silicon NanoWire attached to a Field Effect Transistor) multiarray chip [67]. Herein, each unit consisted on eight subarrays of eighteen FET nanodevices, each individually modified by a unique surface binding agent. Results after exposure to solutions of explosives in liquid phase (0.1 % DMSO in  $\text{H}_2\text{O}$ ) revealed the need for electron-donating functional groups, such as amine or thiol groups, required for the binding interaction of the electron-deficient explosive species. In fact, most of the functional groups, that they reported to have used, consisted on aminosilanes derivatives.

Also, the incorporation of certain transition metals inside the microporous frameworks of zeolitic materials has been also explored to promote sorption of nitro compounds. Particularly, this approach has applied to nitroaromatic adsorption with modified zeolites whose

compensation cation has been exchange by a transition metal, e.g. Co, Fe or Cu [68]. The modification of zeolites with  $\text{Co}^{2+}$  ions have been previously used to promote the nitration of toluene [69], as well as,  $\text{Cu}^{2+}$  and  $\text{Fe}^{3+}$  have been used to improve the catalytic reduction of nitrogen oxides using modified zeolites as catalyst [70], [71]. On the other hand, nitro group present a distinctive electrophilic character, thus the use of acidic zeolites would favour the formation of charge-transfer complex and acid-base interactions [72].

Phosphoryl interaction with silica surfaces have been both theoretically [73] and experimentally [74] conducted. Adsorption is governed by strong hydrogen bond established between surface silanol groups, which act as hydrogen-bond donors. Particularly, the  $\text{sp}^2$  O atom linked to the central P atom via a double bond establishes the strongest hydrogen-bond acceptor with silanol groups.

Phosphoryl interaction is also being favoured by the presence of certain transition metals. In this case, metal-organic framework (MOF) compounds exhibit high potential for organophosphorus adsorbents, due to the metal cluster that form their framework. Remarkable sorption capacities have been reported for Zn based MOFs such as, IRMOF-1 or  $\text{Zn}_4\text{O}(\text{dmcapz})_3$ , up to  $950 \text{ mg}_{\text{DMMP}}/\text{g}_{\text{IRMOF-1}}$  for  $27.45 \text{ mg}/\text{m}^3$  ( $5413 \text{ ppmV}$ ) of dimethyl methylphosphonate (DMMP) at  $50 \text{ }^\circ\text{C}$  [75] as well as milder sorption heat values ( $-\Delta H_{\text{ads}} = 44.8 \text{ kJ}/\text{mol}$  for  $92 \text{ g}/\text{m}^3$  diisopropylfluorophosphate (DIFP) at temperatures ranging from 313 to 513K [76]. Newly developed Zr based MOFs such as NU-1000, UiO-66 or MOF-808 have attracted interest in NAs decontamination, not only due to their sorption properties ( $713 \text{ mg}_{\text{DMMP}}/\text{g}_{\text{NU-1000}}$  and  $152 \text{ mg}_{\text{DMMP}}/\text{g}_{\text{UiO-66}}$  for  $507 \text{ mg}/\text{m}^3$  DMMP at 298K [77]), but also due to their catalytic properties towards organophosphorus degradation by hydrolysis [78]. NU-1000 have been reported to exhibit in dehydrated form up to 50% conversion of  $0.025 \text{ mmol}$  ( $6.2 \text{ mg}/\text{mL}$ ) dimethyl 4-nitrophenyl phosphate (DMNP) in just 90 s at room temperature in aqueous buffered solution containing N-ethylmorpholine (1 mL, 0.45 M) [79]. Cu based MOFs, such as HKUST-1 (also named MOF-199) have also been widely reported as adequate sorbents for organophosphorus vapors due the high affinity that those compounds exhibit towards Cu clusters and the stability of the resulting metal complexes. Fourier-transformation infrared (FTIR) spectroscopy analysis on surface acoustic wave type sensors functionalized via self-assembled monolayer with  $-(\text{CO}_2^-)_2\text{Cu}^{2+}$  as terminal group and exposed to diisopropyl methylphosphonate (DIMP) in gas phase reveal the formation of  $\text{Cu}^{2+}$ -DIMP complexes ( $\text{P}=\text{O}-(\text{Cu}^{2+})$ ) [80]. The affinity of organophosphorus compounds to copper ions still prevails in KHUST-1, Cu-BTC, as demonstrated

by the experimentally measured sorption heat values for diisopropylfluorophosphate (DIFP), i.e. ( $-\Delta H_{\text{ads}} = 48.4$  kJ/mol); higher in comparison to commercial Carboxen material, i.e. ( $-\Delta H_{\text{ads}} = 38.3$  kJ/mol) [81]. Finally, theoretical computational models using density functional theory (DFT) point out that the most favorable MOFs for Sarin gas adsorption are those with pore sizes in the range of 6-8 Å, since smaller pores cannot accommodate Sarin molecules; and, on larger pores the molecular interactions with the framework become weaker [82].

Somewhat different is the case of IL used as adsorbents. In this case, it is not considered so much an adsorption process but a solvation of a solute – target analyte – into a solvent – active layer. Overall, ionic liquids are said to have similar polarities; however, their solvent properties can differ considerably from one another. Given their structure and diversity of functionality, they are capable of most types of interactions: dispersive,  $\pi$ - $\pi$ , n- $\pi$ , hydrogen bonding, dipolar, ionic/charge–charge. For this purpose, the Abraham solvation model is commonly assumed [83]. This model is based on a linear free energy relationship (40) that describes the solvation process according the following solute descriptors:  $R_2$  is an excess molar refraction calculated from the solute's refractive index;  $\pi_2^H$  is the solute dipolarity/polarizability;  $\alpha_2^H$  and  $\beta_2^H$  are the solute hydrogen bond acidity and hydrogen bond basicity, respectively; and  $L^{16}$  is the solute gas-hexadecane partition coefficient at 298K.

$$\log k = c + rR_2 + s\pi_2^H + a\alpha_2^H + b\beta_2^H + l \log L^{16} \quad (1)$$

Lower case coefficients represent the descriptors of the ionic liquid – both cation and anion contribution –:  $r$  is the ability of the IL to interact with  $\pi$ - and n- electrons of the solute;  $s$  is a measure of dipolarity/polarizability of the IL;  $a$  defines the hydrogen bond basicity;  $b$  defines the hydrogen bond acidity; and  $l$  describes the dispersion forces and indicates the goodness of the separation of homologues in any homologous series. Finally,  $c$  coefficient encompasses uncharacterized information by other solvent-solute terms.

As expected, nitroaromatic explosives and organophosphorus materials exhibit relatively high polarizability and basicity ( $S=1.110$ ,  $B=0.280$  for nitro-compounds [84] and  $S=1.62$ ,  $B=1.01$  for organophosphorus related compounds [85]), thus ideal ionic liquid used as solvent should exhibit also high polarizability and acidity, meaning high  $s$  and  $b$  coefficients. Calculation of  $k$  factor may orient the IL selection, nevertheless, other factor such as thermal or water stability must also be taken care of.

Overall, we can conclude that, for our nitro-based explosive compounds as well as organophosphorus agents, we should focus on materials whose porosity (micro- or meso-) should be close to the target molecule size, exhibit high superficial area so they can accommodate the largest amount of guest molecules, its surface chemistry favors the interaction of target molecules (forming hydrogen-bonds, interacting through non-dispersive low-energy forces) and exhibit preferential sorption affinity towards nitro- and organophosphorus compounds in the presence of common co-adsorbents, such water.

## 1. 8. PROPOSED SORBENTS IN THIS WORK

### 1. 8. 1. MICROPOROUS MATERIALS

---

Microporous materials are those, which contain pores with diameters less than 2 nm [86]. On the basis of framework composition, there are three types of crystalline porous solids: inorganic framework materials (e.g. aluminosilicate zeolites), inorganic-organic hybrid framework solids (e.g. metal-organic frameworks), and organic framework materials (e.g. covalent organic frameworks). In this work, we are going to focus on the first two families; particularly, we have worked with zeolitic materials (silicalite and modified BEA zeolites), titanosilicate materials (ETS-10 and modified ETS-10) and MOFs (Cu-BTC, Zn-DMCAPZ and Zn-MIM)

#### 1. 8. 1. 1. Zeolitic materials

Zeolite are three dimensional, microporous, crystalline materials with well-defined structures compose of silicon and aluminium atom tetrahedrally interconnected through shared oxygen atoms. They are thermally stable and can withstand a wide range of pH media. Electrically,  $\text{SiO}_4$  tetrahedrons are neutrally charged, however  $\text{AlO}_4$  units present a charge of -1, so that the overall zeolite framework is negatively charged. These charges can be compensated by additional cations or protons, however they are not an inherent part of the framework, and move freely inside the framework [87].

The ratio Si/Al allow the ionicity of material modulation and range from high hydrophile materials such as Zeolite X (Si/Al = 1:1) to high hydrophobic, as silicalite (Si/Al =  $\infty$ :1). On the other hand, the zeolite compensating cation can be exchanged with other ions to favour the preferential interaction of concrete compounds over others. These strategies allow giving the



zeolite materials a enhance selectivity and customize properties according target molecule and application.

In this work, we proposed the use as adsorbents for organophosphorus compounds thin films of hydrophobic zeolites with pore size in the order of target molecule as well as the post-synthesis modification of commercial zeolites by ionic exchange with Cu, Fe or Co ions to promote the preferential sorption of nitro derivative compounds.

MFI-type zeolite structure consists on a three-dimensional porous system with two different channels configurations: straight channels (0.56 x 0.53 nm) along  $\langle 010 \rangle$  crystal plane ('b' orientation) and sinusoidal elliptic channels (0.55 x 0.51 nm) along  $\langle 100 \rangle$  crystal plane ('c' orientation), which both are connected. Particularly, we have focused on the dealuminated form of MFI-type zeolite: silicate (SIL-1). This zeolite characterizes for its  $\text{SiO}_4$ -only framework ( $\text{Si}/\text{Al} = \infty:1$ ), high thermal stability and selectively adsorbs organic molecules over water [88] (Figure 1.3).

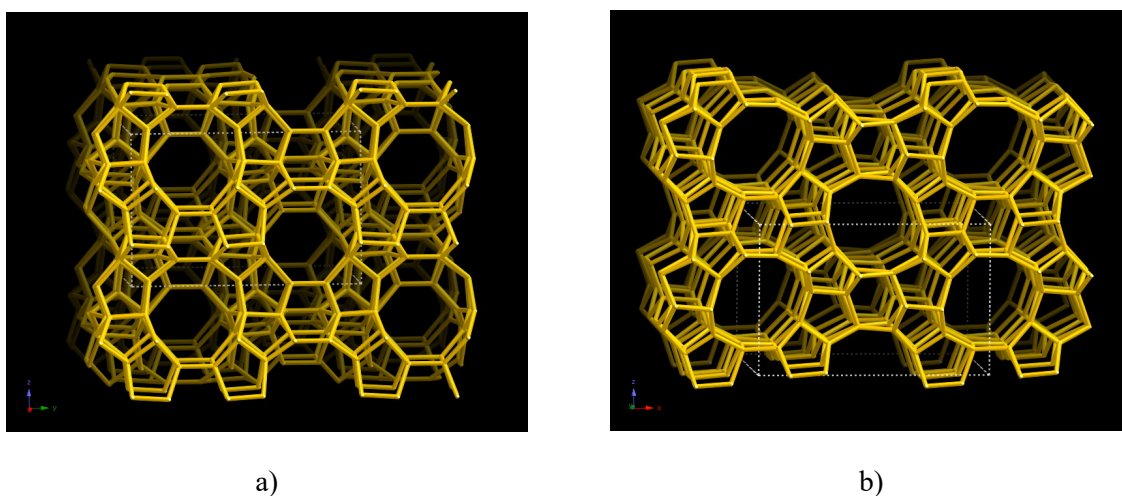


Figure 1.3. MFI framework view along a)  $[100]$  and b)  $[010]$ . Along  $[100]$  can be seen the characteristics sinusoidal elliptic channels whereas along  $[010]$  present straight channels. Images have been obtained from the International Zeolite Association (IZA) on-line database (available at: [www.iza-structure.org](http://www.iza-structure.org)).

#### 1. 8. 1. 2. Titanosilicate materials: ETS-10

Titanosilicates are a family of materials whose microporous structure is comprised of octahedral-pentahedral-tetrahedral framework (OPT) containing different transition metals

[89]. Since their discover in 1983 by Taramasso et al [90], they have been scarcely explored for selective chemical adsorption [91] [92] [93]. Owing to its wide-pore nature, ETS-10 – ETS stands for Engelhard Corporation Titanosilicate – is arguably the most important OPT microporous titanosilicate.

Unlike zeolites, the basic properties of ETS-10 type nanoporous titanosilicates enlarge the variety of interactions between the target molecules and the chemical receptors. Owing to the framework-centred two-minus charge at the  $\text{Ti}^{4+}$  site, the ETS-10 presents interesting opportunities to exploit on the basis on its ion-exchange capability and low acidity. The porous structure of ETS-10 is defined by 12-membered ring units along three dimensions and it is the result of the combination of octahedral  $\text{TiO}_6$  and tetrahedral  $\text{SiO}_4$  (Figure 1.4). These are straight along [100] and [010] with a pore opening of 0.49 nm X 0.76 nm and crooked along the direction of disorder. In this respect, ETS-10 exhibits excellent diffusion characteristics for guest species.

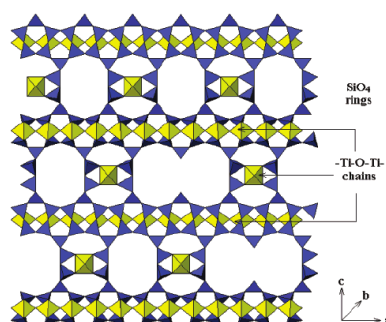


Figure 1.4. Graphical representation of ETS-10 framework structure. Adapted from [94].

### 1. 8. 1. 3. Metal-Organic Frameworks

Metal-Organic Frameworks (MOFs), also called porous coordination polymers, are a family of materials characterized by being built by metal ions and multitopic organic ligand that are linked in Werner-type complexes to yield extended structures. Metal ions (often transition metals or lanthanides) act as connectors, and multitopic organic ligands (often rigid aromatic molecules) act as linkers. The organic molecules bind to the metal via two or more Lewis-basic groups. Typical examples of appropriate functional groups are carboxylic acids, nitrogen donor groups (pyridyl, azoles) or phosphoric acid. Compared to microporous zeolites or mesoporous silica, MOFs exhibit higher chemical versatility due to the tailorability of the organic linker and functional moieties (e.g.  $-\text{NH}_2$  or  $-\text{OH}$ ) [95].

Commonly, MOF synthesis strategies involves the reaction of metal ions from first or second transition metal serie – or even lanthanides – with organic linkers. There are many synthesis processes, some of them are: direct combination of metal salts and organic linkers in solvents, solvothermal synthesis, microwave assisted synthesis or solid-state reactions induced by temperature or pressure. MOF synthesis is influenced by solvents concentration, pH, polarity, temperature or even molecule size of reactants. These parameters influence not only the crystallinity of resulting material but also reaction yield or even the synthesis of certain phase.

### **Cu-BTC**

Cu-BTC (also named HKUST-1 after Hong Kong University of Science and Technology) was firstly reported by the group of Chui et al in 1999 [96]. Cu-BTC consists on copper nodes and organic ligands (benzene-1,3,5-tricarboxylate, BTC), with each copper coordinated with four oxygen atoms and water molecules. It forms face-centered-cubic crystal that contain an intersecting three-dimensional system of square-shaped pores (Figure 1.5).

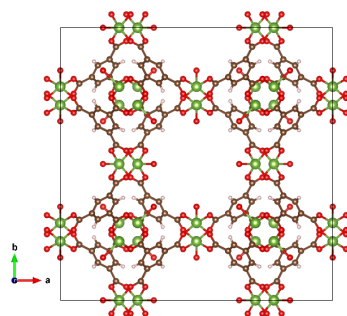


*Figure 1.5. Graphical representation of Cu–BTC unit cell. It can be seen a big cage in the center of the cubic crystal surrounded by four smaller cages. Color legend: Cu (green), H (white), C (brown) and O (red).*

### **Hydrophobic MOF-5**

Montoro et al focused their research in the pursue of a robust, hydrophobic, analogous MOF-5-alike (clusters of metal carboxylates linked together with dicarboxylates) material, which they reported in 2011 [76]. Zn-DMCAPZ ( $Zn_4O(dmcapz)_3$ , dmcapz: 4-carboxy-3,5-dimethylpyrazolate) was structurally similar to MOF-5, though this new material substituted the Zn–O (carboxylate) coordination bonds – highly hydrolysable – with more robust Zn–N (pyrazolate) bonds. Furthermore, methyl groups present at the organic spacers did play an important role since they protected  $Zn_4O$  cluster form hydrolysis (Figure 1.6)

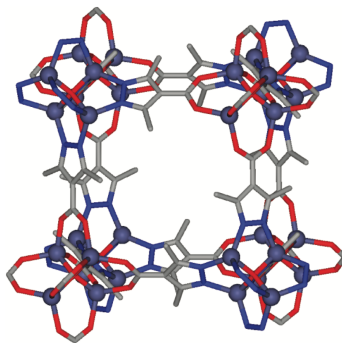


Figure 1.6. Idealized graphical representation of Zn-DMCAPZ. Color legend: Zn (blue), O (red), N (light blue) and C (grey). From [76].

Structurally, Zn-DMCAPZ crystallizes in a cubic  $fm-3m$  framework where the tetranuclear  $Zn_4O$  cluster are connected to other six in a symmetrical fashion through organic 3,5-dimethyl-4,5-carboxypyrazolate linkers.

### **Zn-MIM**

Zn-MIM belongs to the ZIF (zeolitic imidazole framework) MOFs family was described by Yaghi et al in 2006 when they reported a general synthesis of structures based on zeolite framework topologies in which all tetrahedral atoms were transition metals and all bridging ones are imidazolate units, which resembles of traditional zeolite structures [97] (Figure 1.7).

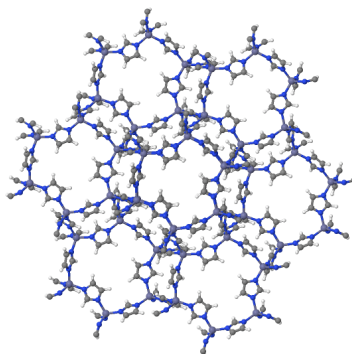


Figure 1.7. Graphical representation of ZIF-8 framework. Color legend: Zn (dark blue), O (light blue), C (grey), H (white).

ZIF-8 exhibits a sodalite topology – a typical zeolite framework –, in which each bivalent Zn cation joins four 2-methylimidazole, generating a resistant structure with large cages (diameter of  $\sim 11.6$  Å) interconnected via narrow 6-ring windows ( $\sim 3.4$  Å) [98].

## 1. 8. 2. SILICA-BASED MESOPOROUS MATERIALS

Mesoporous materials are those material with a pore size from 2 nm to 50 nm [86]. Firstly attempts to synthesize low-density silica materials were reported by Chiola et al in a patent published in 1971 which led to what can be considered as the first mesoporous silica type materials [99]. However, it was not until 1992 that the group of Beck reported the synthesis of a new family of ordered mesoporous silica materials through the use of liquid crystal template at the Mobile Research and Development Corporation [100]. Collectively, they were named as M41S, though they were classified according the order of their pores. MCM-41 (MCM stands for Mobile Composition of Matter) presented a hexagonal phase, whereas MCM-48 presented a cubic mesostructure and MCM-50 a meso-lamellar phase.

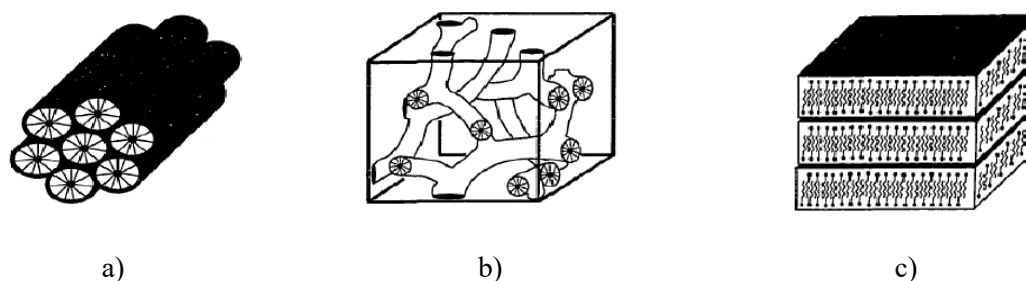


Figure 1.8. Graphical representation of the mesoporous silica: a) MCM-41, b) MCM-48 and c) MCM-50. From [101].

Whereas MCM 41 and MCM-50 share 2D structure – in the sense of an in-plane feature that repeats along the other dimension –, the MCM-48 presents a 3D cubic mesostructure, which consists of two interpenetrating continuous networks of chiral channels [102]. These pairs of porous channels are separated by a  $\text{SiO}_2$  wall that follows the gyroid (G-surface) infinite periodic minimal surface (IPMS). This channel network offers a highly opened porous host that provides easy and direct access for guest species, thus facilitating inclusion or diffusion throughout the pore channels without pore blocking.

This work we have focused on the application of MCM-48 mesoporous silica nanoparticles for chemical warfare agents preconcentration as well as explosive markers sensing. Although most of the work has been performed with MCM-48 nanoparticles, other silica mesoporous materials that have been synthesized within the NFP group or in collaboration with other scientific groups have been employed as well as post-synthesis functionalization on MCM-48 nanoparticles performed within NFP group as well. In collaboration with the Universitat

Politécnica de Valencia (UPV), MCM-41 nanoparticles were applied in the detection and recognition of explosive related compounds. Outside the M41S mesoporous materials family, other mesoporous materials were also applied to explosive compound detection, such as SBA-15 ordered mesoporous silica nanoparticles.

### 1. 8. 3. IONIC LIQUIDS

Ionic liquids constitute a group of organic salts composed of discrete cations and anions with melting points below 100 °C. They have emerged as an extensive class of soft materials due to their highly interesting physicochemical properties: negligible vapor pressure, excellent thermal and chemical stability, wide electrochemical potential window and outstanding solubility for organic, inorganic and organometallic substances [103]. Polymerized ionic liquids (PIL) are a subclass of polyelectrolytes that feature an IL specie (mostly cations) in each monomer repeating unit, connected through a polymeric backbone to construct a macromolecular architecture. PIL conjugates some of the physical and viscoelastic properties of ionic liquids with those of polymers, such as, processability, mechanical stability, or facile functionalization. Furthermore, they proved to be of interest also as a stationary phase in conventional gas chromatography columns [104], [105] due to their ability to separate polar from non-polar analytes as well as undergo multiple solvent-solute interactions, such as non-bonding and  $\pi$ -electron, dipole, hydrogen bonding and cohesion and dispersion interactions [83].

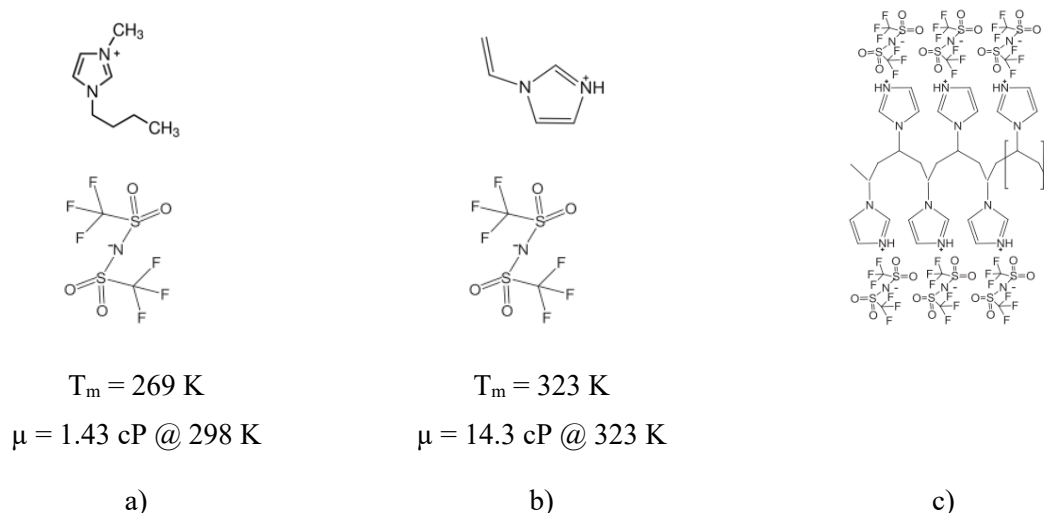


Figure 1.9. Chemical structure of the imidazolium-based ionic liquids: a) BIL, b) VIL and c) PIL.  $T_m$ : melting point,  $\mu$ : viscosity. Physicochemical properties from [106].

In this work we have focused on imidazolium-based ionic liquids: 1) the protic ionic liquid 1-H-3-vinylimidazolium bis(trifluoromethanesulfonyl)imide (VIL, 98 %, Solvionic) and 2) and the non-protic ionic liquid 1-butyl-3-mehtylimidazolium bis(trifluoromethanesulfonyl)imide (BIL, 98%, Sigma Aldrich) (Figure 1.9.a). VIL is a polymerizable ionic liquid (Figure 1.9.b), i.e., after the addition of a photo-initiator can be polymerized by irradiating with an ultraviolet (UV) source into continuous films of poly[1-(H-3-imidazolium)ethylene] bis(trifluoromethanesulfonyl)imide (PIL) (Figure 1.9.c). PIL films are hydrophobic and present high chemical and thermal stability ( $T_{\text{decomposition}} = 648 \text{ K}$ ) [107]. On the other hand, BIL is a room-temperature ionic liquid, i.e., it exhibits a melting point below room temperature ( $T_{\text{m}} = 269 \text{ K}$ ), low viscosity ( $\mu = 1.43 \text{ cP @ } 298\text{K}$ ) and high thermal stability ( $T_{\text{decomposition}} = 712 \text{ K}$ ) [106].

## 1. 9. OBJECTIVES

As we have pointed out above, defence against CBRNE threats derive from possible terrorist attacks constitutes one of the mayor concerns of many Homeland Security administrations, local law enforcement agencies and overall citizenship. In fact, 2019 Eurobarometer report positioned ‘combating terrorism and organised crime’ as third top priority of the European citizens consulted [1]. In this context, this PhD dissertation is focused on researching and developing new solutions to prevent, and rapid actuate if so, against CBRNE attacks. Thus, we herein proposed the integration of novel materials with distinctive properties towards nitro- and organophosphorus compounds in preconcentration and detection units, with the final goal of developing a smart electronic nose for early detection and identification of explosive and CWA related materials. In order to do so, this work will cover the following objectives:

- identify and characterize novel materials with enhanced properties towards the sorption of nitro and organophosphorus material that can be integrated into functional gas detection platforms and *ad hoc* preconcentration  $\mu$ -fluidic systems. The study will be focused on nano- and mesoporous materials (including zeolites, metal-organic frameworks and mesoporous silica materials) as well as polymerizable ionic liquids. Characterization will be performed both with surrogate compounds (orto-mononitrotoluene as nitro-related explosives surrogate and dimethyl methylphosphonate as G-series nerve agents surrogate) as well as real compounds (plastic explosive RDX, commercial explosive PETN and the habitual explosive taggant DMDNB) in dry and humid conditions.

- integration of the most promising nanostructured, nitro-related compounds adsorbents into an *ad hoc* developed gas sensor platform based on functionalized  $\mu$ -cantilever array. Testing of the resulting gas sensor with challenging gas mixtures comprised of real explosives and common interferents in simulated field conditions.
- design and fabrication of silicon  $\mu$ -fluidic devices for preconcentration of analytes in gas phase at trace level. The design will be optimized using the computer fluidic dynamics (CFD) and microelectromechanical systems (MEMS) analysis software: COMSOL Multiphysics. The  $\mu$ -fluidic devices will be fabricated by standard clean-room techniques: dry and wet etching, anodic bonding sealing, metal lift-off patterning, etc.
- integration of the most promising, organophosphorus adsorbents into the proposed  $\mu$ -fluidic devices. According each material characteristic properties, different synthesis and deposition approaches will be proposed: *in situ* hydrothermal synthesis, electrosynthesis, spin-coating of synthesized material, UV *in situ* polymerization.
- characterization of preconcentration coefficient as well as sorption process properties the functionalized  $\mu$ -fluidic devices for challenging dimethyl methyl phosphonate (a sarin surrogate) at trace-level concentrations (ppb and ppm). Computational modelling of the sorption process in the functionalized  $\mu$ -fluidic devices using computer fluidic dynamics (CFD) and microelectromechanical systems (MEMS) analysis tools (COMSOL Multiphysics).



**CHAPTER II:**  
**MATERIALS FOR SORPTION OF NITRO- AND**  
**ORGANOPHOSPHORUS VAPOURS**



## 2. MATERIALS FOR SORPTION OF NITRO- AND ORGANOPHOSPHORUS VAPORS

### 2. 1. INTRODUCTION

This Chapter presents the synthesis protocols of the materials introduced in Chapter I. As mentioned previously, the sorbent selection was based on their distinctive properties for nitro-related and organophosphorus compounds sorption, such as pore size, surface area or surface chemistry. The sorbents synthesized have been classified according its porosity, and are divided into microporous (zeolites, titanosilicates and metal-organic frameworks) and mesoporous materials (MCM-48). Furthermore, it has been explored the in-situ polymerization of imidazole-based ionic liquids into sealed  $\mu$ -devices by irradiating through the Borofloat cover.

Synthesis protocol includes the preparation of discrete crystals as well as the synthesis of polycrystalline layer on rigid substrates. Depending on their nature and their application (explosive sensing or chemical warfare agents preconcentration), the incorporation routes of those materials range from the use of commercial compounds to the batch synthesis of discrete crystals or the in-situ growth of thick layers by electrochemically aided synthesis. Also, it has explored different post-synthesis treatments to promote the interaction of toward nitro-compounds. Particularly, it has been prepared zeolitic materials with inter-exchanged  $\text{Cu}^{2+}$  and  $\text{Fe}^{2+}$  cations and titanosilicates materials grafted with imidazole- and amino-based organosilanes.

### 2. 2. SYNTHESIS OF MICROPOROUS SORBENTS

#### 2. 2. 1. ZEOLITIC MATERIALS

---

##### 2. 2. 1. 1. *In-situ silicalite polycrystalline coating synthesis*

The incorporation of SIL-1 on our microdevice have been performed in form of continuous, polycrystalline films that have been in situ synthesized by hydrothermal synthesis. The synthesis procedure can be divided in two main steps: 1) seeding of the substrate with silicalite nanocrystals, and 2) growth of those crystals along the desired direction.

The synthesis of silicalite nanocrystals was according the work reported by Mintova, Sterte, Schöman et al [108] [109] [110]. It was prepared a synthesis gel with molar composition 9 TPAOH : 25 SiO<sub>2</sub> : 480 H<sub>2</sub>O : 100 EtOH. To obtain 50 g of synthesis gel, 29.08 g of 1M TPAOH (Sigma Aldrich) is mixed with 4.01 g H<sub>2</sub>O. Keeping the mixing under stirring, it is added 16.95 g of the silicon source TEOS (Sigma Aldrich). The solution is aged for 24 h, to allow the hydrolyzation of the mixture. After which, the gelk is put in an oven at 373 K for 20h. The nanocrystals are recovered by centrifugation at 10000 rpm for 45 min and washed with water. This procedure is repeated until the supernatant present a neutral pH. The seeds are finally redispersed in ethanol and kept stored under cooling.

The nanocrystals are seeded over the substrate by spin-coating. Two different revolution steps were used: 1) the first one at low revolution (500 rpm for 10s) allow the correct homogeneity of the seed all over the surface, and 2) the second at high revolution (1000 rpm for 50s) to evaporate the solvent. Also, the substrate was preheated (at 150 °C) before deposition, in order to dehydrate the surface and improve the homogeneity.

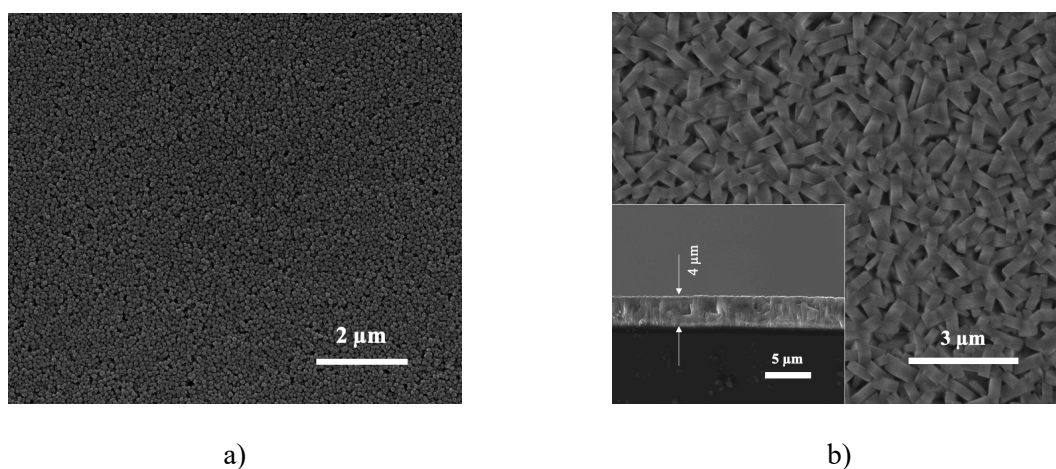


Figure 2.1. Scanning electron microscopies: a) silicate seeds deposited by spin coating over Si substrate, b) top view of the silicalite polycrystalline coating (insert: cross-section of Si wafer after silicalite synthesis).

The growth gel is prepared after the protocol reported by Chau et al [111]. A synthesis with molar composition 2 TPAOH : 40 SiO<sub>2</sub> : 20000 H<sub>2</sub>O was prepared. 800 g of growth gel were prepared by mixing 21.86 g of 1M TPAOH with 759.77 g of water. After dissolved, it is

added 18.37 g of TEOS and the solution is aged overnight. Then, the seeded wafer is introduced in a 1 L autoclave with the synthesis gel. The synthesis takes place at 403 K for 72 h, after which, the autoclave is cooled down and the wafer is washed with distilled water and dried.

The proposed seeding conditions, effectively, lead to a packed coating of well-ordered silicate nanoparticles as seen by SEM (Figure 2.1.a). Eventually, seeds grow into a continuous layer of 4  $\mu\text{m}$  of c-oriented silicalite crystals attached to the surface of the Si substrate. An intertwined topology of crystals can be seen all along the surface with no mayor defects, though some precipitates from synthesis gel are observed sparsely (Figure 2.1.b).

### 2. 2. 1. 2. Fe and Cu based zeolites.

$\text{Fe}^{2+}$  and  $\text{Cu}^{2+}$  cations were introduced into commercial BEA type zeolite CP814E (Zeolyst, Si/Al=12.5,  $\text{NH}_4^+$  as compensation cation) and FAU type zeolite CBV780 (Zeolyst, Si/Al=40,  $\text{H}^+$  as compensation cation) respectively following procedures already published in the literature. For the preparation of CP814E/Fe, firstly, the zeolite was calcined at 500°C under inert condition to render the easier-functionalized, acid form ( $\text{H}^+$ ). After which, the acid CP814E was mixed with the Fe source  $\text{Fe}(\text{NH}_4)_2(\text{SO}_4)_2 \cdot 6\text{H}_2\text{O}$  (Sigma Aldrich) at 353 K in aqueous solution [112]. CBV780/Cu was prepared by mixing together CBV780 zeolite with the Cu source  $\text{Cu}(\text{NO}_3)_2 \cdot 2.5\text{H}_2\text{O}$  (Sigma Aldrich) in aqueous solution at room temperature [113]. Both materials were recovering by filtering and rinsed with water. The functionalized zeolites were calcined at 753 K to eliminate the precursors.

### 2. 2. 2. ETS-10 AND POST-SYNTHESIS TREATMENTS

---

The synthesis of ETS-10 crystals and post-synthesis functionalization has been performed by Dr. Adela Eguizabal [114]. ETS-10 discrete crystals were prepared from a gel with molar composition 4.4  $\text{Na}_2\text{O}$  : 1.4  $\text{K}_2\text{O}$  : 1.0  $\text{TiO}_2$  : 5.5  $\text{SiO}_2$  : 125  $\text{H}_2\text{O}$ . Firstly, an aqueous solution of 0.86g of KCl (Sigma Aldrich) and 3.5 g of NaCl (Sigma Aldrich) in 16.5 g of water was prepared. While stirring, 12.3 g of  $\text{Na}_2\text{O}(\text{SiO}_2)_x$  (Sigma Aldrich) was added, after which 1.11 g of KF (Sigma Aldrich) was added. Finally, 0.8 g of  $\text{TiO}_2$  (Sigma Aldrich) is incorporated under continuous stirring until obtaining a homogeneous, white gel. The gel is poured into Teflon lined autoclave and crystallization takes place under hydrothermal conditions at 503 K during 24 h. The material is recovered by centrifugation at 8500 rpm for 15 min and washed until the solution pH is less than 10.

Two different post-synthesis treatments have been also performed: Ti enrichment and surface functionalization. Ti enrichment have been performed following already known Al enrichment protocols for zeolites [115]. A 0.05 M solution of  $\text{Na}_2\text{Ti}_3\text{O}_7$  (Sigma Aldrich) was prepared and stirred for 10 min with 1.20 %<sub>w</sub>t of ETS-10. Then, NaOH (Sigma Aldrich) was added until the solution reached pH 13 and kept stirred for 2 h at room temperature. Afterwards, the solution was put in a Teflon autoclave for recrystallization at 443 K for 12 h. The functionalized material presented a Si/Ti atomic ratio of 4.5 assessed by EDX analysis.

TABLE 2.1. SURFACE FUNCTIONALIZATION CONDITION FOR THE AS SYNTHESIZED ETS-10 TYPE TITANOSILICATES

Organosilane	Functionalization procedure			mmol/g <sub>ETS-10</sub>
	ETS-10 (g) / organosilane (cm3) / solvent (cm3)	Reaction conditions	Extraction process	
<i>Imidazolin-1-glycidylpropyltriethoxysilane</i>	1 / 9.5 / 47 (cumene)	T = 152 °C t = 24 h	2-Propanol (centrifugation and Soxhlet)	8.4
<i>3-Aminopropyltriethoxysilane</i>	1 / 10 / 150 (toluene)	T = 110°C t = 24 h	Ethanol (centrifugation)	0.2

The surface functionalization was carried out over as synthesized ETS-10 by covalent linkage using organosilanes as coupling agents. In particular, imidazolin-1-glycidylpropyltriethoxysilane and 3-aminopropyltriethoxysilane groups are grafted on the external nanoporous surface. The functionalization takes place in a three-neck round bottom flask, filled with Ar to avoid hydration. Anhydrous solvent is injected along with the ETS-10 powder and the dispersion is sonicated for 15 min. Once the solvent reflux temperature is achieved, the organosilane is added under mechanical stirring and kept overnight. The specific conditions for each functionalization are shown in Table 2.1.

### 2. 2. 3. METAL-ORGANIC FRAMEWORKS

#### 2. 2. 3. 1. *Electrochemical synthesis of Cu-BTC polycrystalline coatings*

Electrochemical synthesis involves the oxidation of a metal electrode to provide the metal ions to a solution where the organic ligand is dissolved, where they react rendering in MOF crystals [116] (Figure 2.2). To oxidize the metal electrode an electric field is applied between the former, which act as an anode (or working electrode) and a cathode (or counter-electrode), either in amperometric or potentiometric mode. In amperometric mode, the voltage is fixed, and the reaction can be monitored through changes on the current applied, which can be inferred as a measure of the reaction rate expressed at the speed at which the metal ions are dissolved. On the other hand, the potentiometric mode relies on applying a constant current and therefore, variations on the voltage applied are due to the energy needed to dissolve the electrode. Both methods can be applied using direct current power sources or with wave or square function power supply [117]. In general, electrochemical synthesis allows the MOF synthesis under milder conditions than typical solvothermal (393 – 453K for 12 – 24 h) or microwave assisted procedures, furthermore, the synthesis time is also greatly reduced to few minutes.

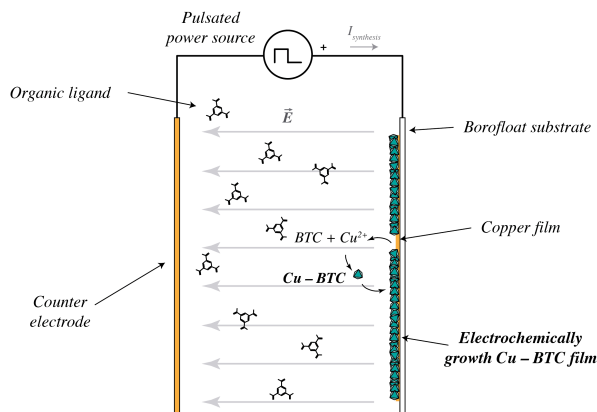


Figure 2.2. Schematic of the electrochemical synthesis of Cu-BTC on Cu substrate.

The electrochemical synthesis of the Cu-BTC was performed on the Cu electrodes micropatterned on a Borofloat substrate (Sigert Wafer,  $500 \pm 20 \mu\text{m}$  thickness, surface roughness  $< 1.2 \text{ nm}$ ). In particular, two different Cu modified glass substrates have been investigated (to analyse the influence of the metal adhesion layer: i) 200 nm of Cu over an adhesion layer of 10

nm Cr and 50 nm Au denoted as Cu-Cr/Au substrate (0.52 cm<sup>2</sup> surface area) and ii) 500 nm Cu over an adhesion layer of 40 nm Ti denoted as Cu-Ti substrate (0.69 cm<sup>2</sup> surface area).

The electrosynthesis of Cu-BTC was carried out as previously reported [118], using an Autolab potentiostat PGSTAT302N, cyclic pulses of current (ranging from 1 to 15 mA) have been applied between the Cu modified glass substrate and the counter-electrode.

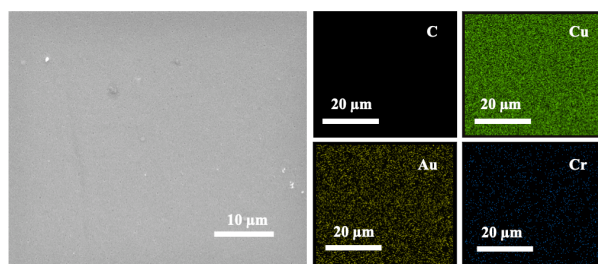
Different electrosynthesis parameters were tested in order to maximize Cu-BTC crystallization, surface coverage and homogeneity on the electrode (Table 2.2). Former experiments carried out in the group with the same electrochemical cell revealed the existence of a minimum current density value, i.e. 1.5 mA/cm<sup>2</sup> for heterogeneous synthesis on Cu-Cr/Au substrates. Above this current density, an adequate concentration of Cu<sup>2+</sup> ions remain in the electrolyte solution as net mass balance resulting from the generation term by Cu electrode oxidation and the consumption term by Cu-BTC formation. Current duty cycle, i.e. on/off switching time of applied current, was kept constant through all of the experiments ( $t_{\text{cycle}} = 20$  s, duty cycle = 0.75, i.e.  $t_{\text{on}} = 15$  s,  $t_{\text{off}} = 5$  s).

TABLE 2.2. ELECTROSYNTHESIS PARAMETERS TESTED

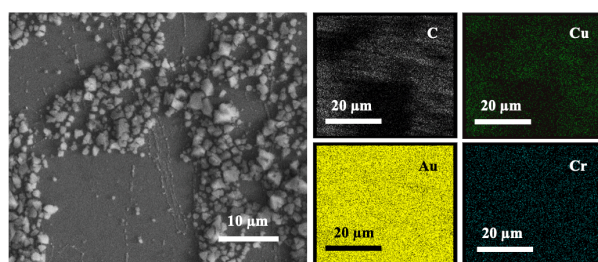
Substrate	Test	$I_{\text{synthesis}}$ (mA)	$J_{\text{synthesis}}^*$ (mA/cm <sup>2</sup> )	$N_{\text{cycles}}$
Cu-Cr/Au	#1	1.0	1.6	12
	#2	9.0	17.3	12, 15, 20
	#3	15.0	28.8	12
Cu-Ti	#4	6.0	8.7	15
	#5	12.0	17.4	7, 15

\*calculated assuming 0.52 cm<sup>2</sup> as electroactive surface area on assays #1 to #3 and 0.69 cm<sup>2</sup> on #4 and #5.

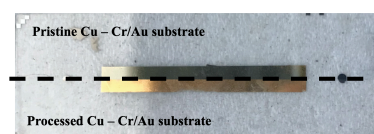




a)



b)



c)

Figure 2.3. SEM-EDS results and visual inspection on Cu–Cr/Au substrates. a) pristine Cu–Cr/Au substrate: on the left side a SEM micrograph of the analyzed area; on the right, from top to bottom and left to right, the registered signals of C (white), Cu (green), Au (yellow) and Cr (blue) on the centered area of the SEM micrograph. b) sample #2\_20 ( $J_{\text{synthesis}}=17.3 \text{ mA/cm}^2$ , 20 cycles): the images are displayed as previously. c) Composed image of the back side of Cu–Cr/Au substrates before and after electrosynthesis conditions.

Current density  $J$  plays a crucial role in electrosynthesis as it governs the Cu electrode oxidation rate; and consequently, the concentration of  $\text{Cu}^{2+}$  ions in the electrolyte solution available for Cu-BTC crystallization. A pristine Cu–Cr/Au substrate as well as a processed one were analysed by energy-dispersive X-ray spectroscopy (EDX) to illustrate the reactive Cu processes. As shown on Figure 2.3.a, the atomic analysis reveals an homogenous distribution of Cu, Au and Cr layers, with a signal intensity proportional to layer thickness and beam penetration (theoretical electron penetration of incident beam is 427 nm for an accelerating voltage of 10 kV on the Cu–Au/Cr substrate calculated according [119]). After electrochemical

synthesis, the mapping of C signal (mainly attributed to the organic linker) correlates well with the distribution of Cu-BTC crystals over the substrate where the most intense Cu signals are also recorded (Figure 2.3.b). In contrast, the Cu signal is clearly attenuated on the naked surface in accordance to the lesser Cu thickness; whereas the Au and Cr signals are proportionally increased.

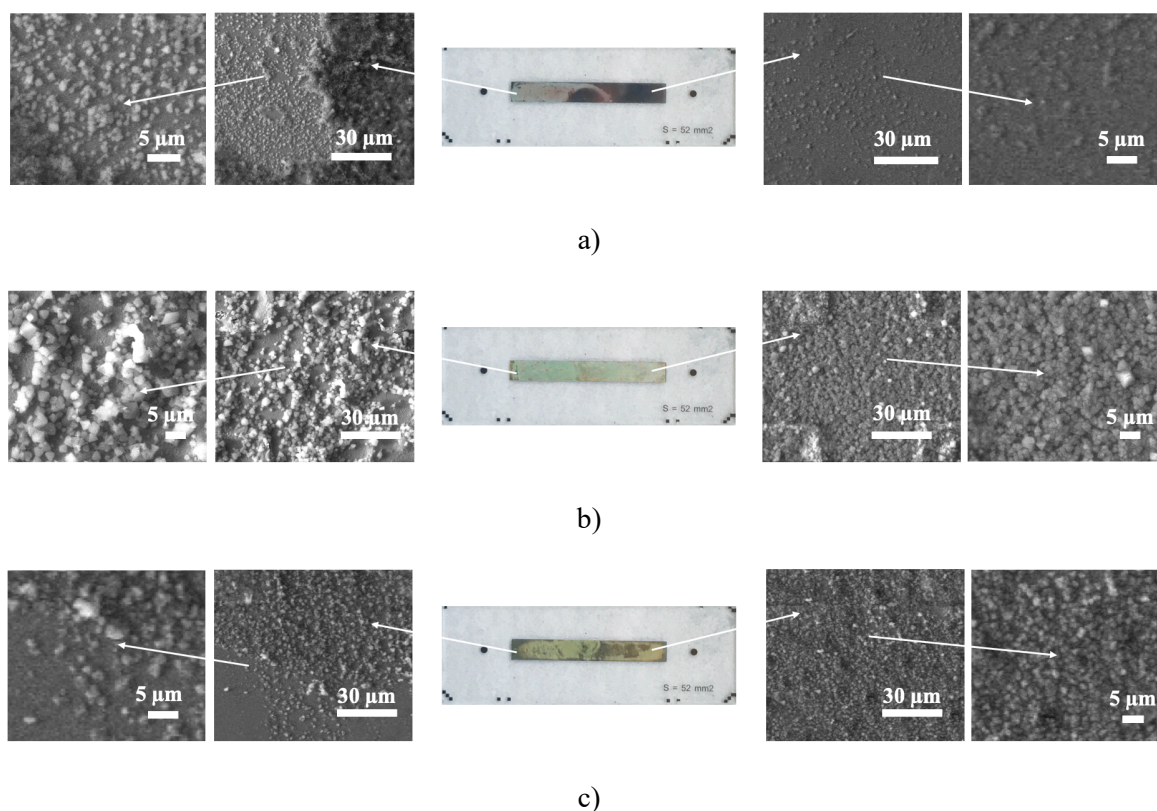


Figure 2.4. Electrochemical synthesis of Cu-BTC on Cu-Cr/Au substrates: a) sample #1\_12:  $J_{\text{synthesis}} = 1.6 \text{ mA/cm}^2$ . b) #2\_15:  $J_{\text{synthesis}} = 17.3 \text{ mA/cm}^2$ . c) #3\_12:  $J_{\text{synthesis}} = 28.8 \text{ mA/cm}^2$ .

At current densities above  $1.6 \text{ mA/cm}^2$ , Cu-BTC crystallization begins to occur preferentially at the borders of the metal electrode where the Gibbs free energy of the nucleation process is decreased due to a more existence of grain boundary defects. By increasing the number of cycles, the population of discrete Cu-BTC crystals grows rapidly all along the metal substrate but without forming a continuous and homogenous layer (Figure 2.4.a). At the highest current density tested ( $J_{\text{synthesis}} = 28.8 \text{ mA/cm}^2$ ), Cu-BTC layer formation is equally unsuccessful (Figure 2.4.c). This observation is attributed to the instability of the glass Cr/Au-Cu interface, more pronounced at higher overpotential (up to 8.9 V) due to the electro-migration of Cr atoms into the Au films [120]. In addition, the inter-diffusion of Cr into Au layers is temperature

dependent, i.e. solubility of Cr in Au at 323 K increases up to 5 atom % [121]. This mechanism would provoke an unsteady current density distribution profile over the working Cu electrode immersed in the electrolyte solution at 313 K resulting in a heterogeneous coverage of the substrate. Among the tested conditions, the most homogeneous Cu-BTC coatings are attained at  $J_{\text{synthesis}} = 17.3 \text{ mA/cm}^2$  in a range of synthesis cycles from 10 to 20 (Figure 2.4.b). The characteristic green shade of Cu-BTC is clearly noticed over the whole electrode surface. This observation correlates well with the SEM analysis performed at random spots of the surface.

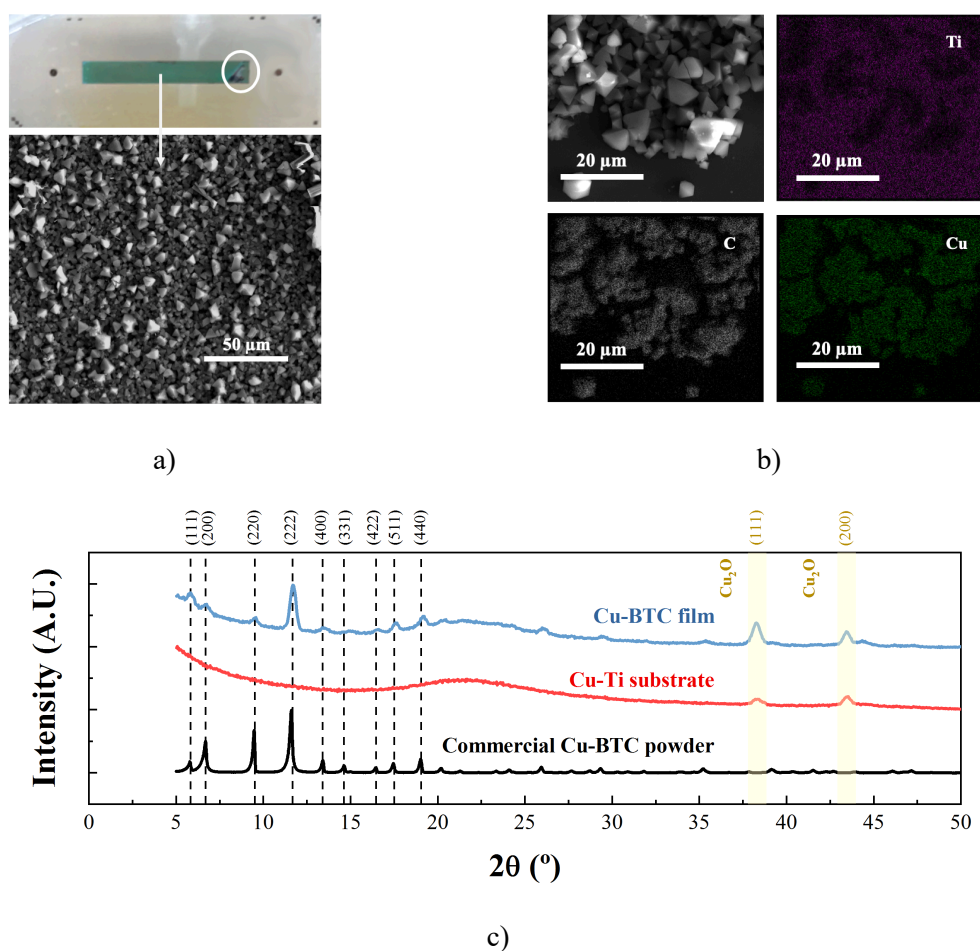


Figure 2.5. Electrochemical synthesis of Cu-BTC on Cu-Ti substrates: sample #4 ( $J_{\text{synthesis}} = 8.6 \text{ mA/cm}^2$ ,  $N_{\text{cycles}} = 15$ ). a) Optical image, below SEM micrograph of a representative area of the coating. b) SEM-EDS results on the clamping region highlighted in a), showing the overlapping of Cu (green) and C (white) signals. c) XRDs of the Cu-BTC film (blue), pristine Cu-Ti substrate (red) and commercial Cu-BTC powder (black). Crystallographic patterns from [96].

To overcome the instability issues of the glass-Cu interface due to chromium electro migration (Figure 2.3.c), Cu-BTC electrosynthesis on Cu-Ti substrates were also investigated. As

reported on [122], titanium atoms do not tend to diffuse into Cu films and a well-defined Ti layer with an stable Ti-Cu interface is commonly obtained. Unlike Cu-Cr/Au substrates, the Cu thickness in Cu-Ti substrates was increased up to 500 nm to ensure that Cu-BTC crystal growth is not eventually hindered by the concentration of Cu ions in the electrolyte solution. Likewise, the electrosynthesis parameters were slightly modified in accordance to the variations in the energy required to overcome the electric resistance of the equivalent circuit, i.e. metal substrate – reaction media – counter-electrode. Figure 2.5 summarizes the characterization of #4 substrate, i.e.  $J_{\text{synthesis}} = 8.6 \text{ mA/cm}^2$ ,  $N_{\text{cycles}} = 15$ . The visual inspection (Figure 2.5.a) clearly confirms the homogeneity of the continuous Cu-BTC film  $4.7 \pm 1.1 \mu\text{m}$  thick, as measured by profilometry. The spatial EDX mapping of Cu and C atoms (Figure 2.5.b) is clearly overlapped each other, whereas the Ti signal remains nearly constant, only slightly shielded where agglomerated octahedral Cu-BTC crystals are encountered on the electrode surface. The crystallinity of the supported Cu-BTC film was evaluated by XRD analysis. In Figure 4.c the main characteristic Bragg reflections at small  $2\theta$  angles for KHUST-1 ( $2\theta = 5.8^\circ, 6.7^\circ, 9.5^\circ, 11.6^\circ$ ; corresponding to (111), (200), (220) and (222) crystallographic planes), are observed [96]. Unlike the XRD of commercial Cu-BTC, a preferential crystallographic orientation along the [111] direction is observed for the electrosynthesized Cu-BTC film. In addition, the coexistence of  $\text{Cu}_2\text{O}$  impurities, already present in the pristine Cu-Ti substrate (diffract ion peaks at  $38.3^\circ$  and  $43.5^\circ$  [123]), is clearly noticed as pointed out in previous works [124].

Figure 2.6 shows the chronopotentiometric measurements with time on stream. This analysis is revealed as a reliable characterization tool for the assessment on the heterogeneous Cu-BTC crystallization process. A smooth increase of the electric potential difference across the working and counter electrodes would be expected with electro synthesis time and number of cycles. Assuming constant the electrolyte's and the counter-electrode's resistivity, this slight effect would be explained by the evolving working electrode which becomes more insulator with synthesis time due to the lesser conductivity of Cu-BTC films ( $\sigma_{\text{Cu-BTC}} < 3 \times 10^{-9} \text{ S/m}$  vs.  $\sigma_{\text{Cu}} = 5.96 \times 10^7 \text{ S/m}$  [125]). Overlapped voltage signals are registered for #4\_15 (1) and #4\_15 (2) substrates, respectively; both prepared under identical conditions ( $J_{\text{synthesis}} = 8.6 \text{ mA/cm}^2$ ,  $N_{\text{cycles}} = 15$ ). More specifically, the applied overpotential slightly increases from 4.1 V of the 1<sup>st</sup> cycle to 4.7 V in the 15<sup>th</sup> cycle in agreement with the controlled formation of homogeneous Cu-BTC films. Accordingly, these conditions have been those selected for the fabrication of the functional microdevices for sampling and preconcentration of neurotoxic agents (NAs) diluted in gaseous streams.

On the contrary, on substrates #5\_7 and #5\_15, both at  $J_{\text{synthesis}} = 17.4 \text{ mA/cm}^2$ ; the overpotential evolution rate with time on stream is substantially higher from the 4<sup>th</sup> cycle and particularly noticeable on 9<sup>th</sup> cycle. This observation is attributed to the detachment of the Cu-BTC layer from the working electrode due to the exhaust of the Cu layer and the reduction of the electroactive surface area.

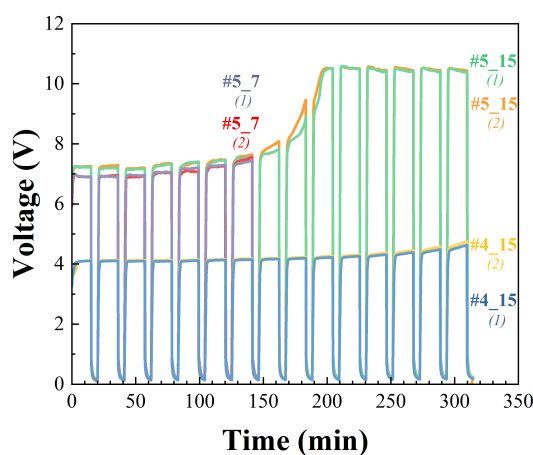


Figure 2.6. Chronopotentiometric analyses along the Cu-BTC electrosynthesis over Cu-Ti substrates: #4\_15 (1) in blue, #4\_15 (2) in yellow, #5\_7 (1) in purple, #5\_7 (2) in red, #5\_15(1) in green and #5\_15(2) in orange.

### 2. 2. 3. 2. Batch and layer-by-layer synthesis of Zn-DMCAPZ

#### **Discrete crystals synthesis**

Following the work of Montoro et al [76] and the modifications made by Fisher et al [126], for the synthesis of Zn-DMCAPZ zinc acetate ( $\text{Zn}_4\text{O}(\text{OAc})_6$ ) was used as metal-cluster and 3,5-dimethyl-4-carboxylate ( $\text{H}_2\text{dmcapz}$ , Sigma Aldrich) as organic linker.  $\text{Zn}_4\text{O}(\text{OAc})_6$  was obtained by sublimation of the hydrated zinc  $\text{Zn}_4\text{O}(\text{AcO})_2 \cdot 2\text{H}_2\text{O}$  (Sigma Aldrich) at 553 K under vacuum. Then, two solutions were prepared: 1) 729 mg of  $\text{Zn}_4\text{O}(\text{OAc})_6$  in 23 cm<sup>3</sup> of ethanol and 23 cm<sup>3</sup> of dimethyl formamide (1:1 v/v) and 2) a solution of 500 mg of  $\text{H}_2\text{dmcapz}$  in 27 cm<sup>3</sup> ethanol and 9 cm<sup>3</sup> water (3:1 v/v). As both solutions are mixed together at room temperature in a proportion 3 : 1 (organic linker : metal cluster), Zn-DMCAPZ crystallization takes place. The solution is put in an oven at 323 K for 1 h to allow fully crystallization and is stored overnight at room temperature. The material is recovered by centrifugation and washed with

water, ethanol and diethyl ether. The material is activated, i.e. the removal of the remaining solvent inside the porous structure, at 383 K under vacuum for 3 days.

### Layer-by-layer films synthesis

The synthesis of coatings of Zn-DMCAPZ is based on the work reported by Fisher et al [126], [127]. It is newly used as metal precursor basic zinc acetate  $Zn_4O(OAc)_6$ , obtained by sublimation of its hydrated form as seen previously, and  $H_2dmcapz$  as organic linker. The layer-by-layer (LbL) synthesis consists on separating both precursors (metal source and organic linker) in different solutions and immersing the substrate subsequently on both of them with a cleaning step in between. With this approach, thin films of controllable size are achieved by increasing the number of cycles of immersion in each reactant (Figure 2.7).

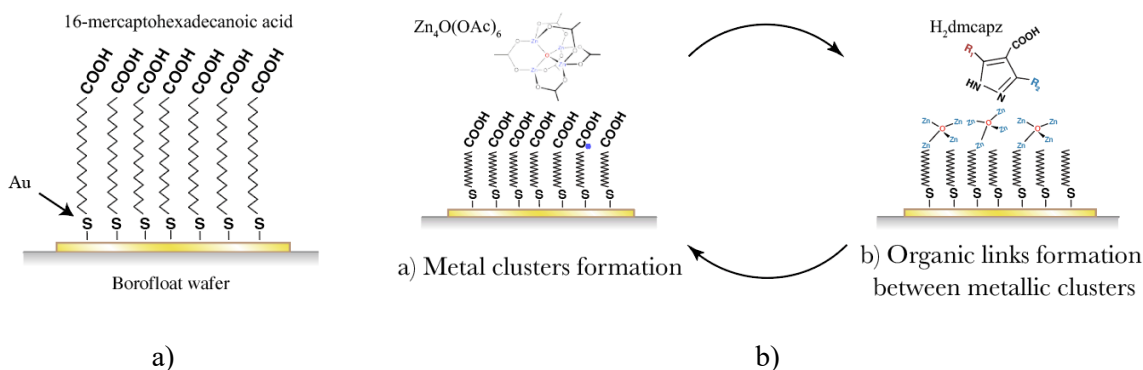


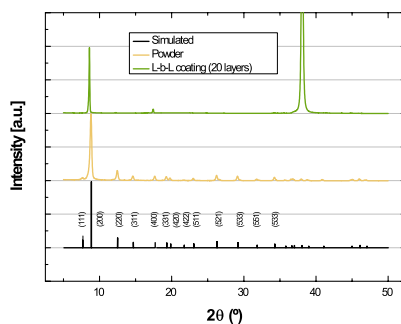
Figure 2.7. Schematic of layer by layer synthesis of thin Zn-DMCAPZ films. a) Functionalization of the the Au patterned substrate on Borofloat wafer with 16-mercaptohexadecanoic acid. b) Layer by layer synthesis of Zn-DMCAPZ.

The layer was growth on a modified Au-evaporated Pyrex substrate – the substrate fabrication is discussed in Chapter IV. The Au surface was activated by the formation of a carboxylic acid self-assembled monolayer (SAM), i.e. carboxylic groups are used as nucleation centers for the MOF by anchoring them to the Au substrate through a thiol group. On the other hand, the exposed Pyrex surface is preferentially bond with the carboxylic group of the MHDA, having on top of it a thiol group that difficult the formation of the MOF. In order to improve the homogeneity of the SAM, the substrate was previously cleaned with acetone, isopropanol and water and then treated with  $O_2$  plasma. Plasma treatment eliminated the remaining organic residue and exposed the hydrophilic reactive groups on the surface. The SAM formation was

performed by immersing the substrates in a 20  $\mu\text{M}$  16-mercaptohexadecanoic acid (MHDA, Sigma Aldrich) solution with ethanol and acetic acid (95 : 5 v/v), and incubate for 24 h. The substrates were washed afterwards with a solution of ethanol and acetic acid (9 : 1 v/v, respectively) and dried with air.

The LbL process begins by immersing the functionalized substrate in 80  $\text{cm}^3$  of 1 mM of  $\text{Zn}_4\text{O}(\text{OAc})_6$  in ethanol : dimethyl formamide (DMF) (1:1 v/v) for 5 min, after which the substrate is cleaned with anhydrous ethanol for 5 min. Then immersed in 80  $\text{cm}^3$  of 0.5 mM of  $\text{H}_2\text{dmcapz}$  in ethanol : water (3:1, v/v) for 5 min, after which the substrate is cleaned again with anhydrous ethanol for 5 min. Each solution is placed in 100  $\text{cm}^3$  glass beaker and maintained in an oil bath at 323 K. The solution is stirred only at the begin of the process until the reactant powders are fully diluted. This whole process – immersion in the metal solution, cleaning with EtOH, immersion in the organic solution, cleaning with EtOH – is considered to be a cycle and form a layer, in order to increase the number of them, it is repeated as will. When the whole process is over, the substrate is eventually dried with air.

Figure 2.8.a depicts the resulting diffractograms of 30 synthesized layers, the MOF powder and a simulation according its theoretical structure obtained by XRD. It can be clearly seen a big diffraction line at  $2\theta = 38.3^\circ$  that belongs to the gold substrate. Also, characteristic diffraction lines of the Zn-DMCAPZ are present in all the samples:  $2\theta = 8.9^\circ$  (200),  $12.6^\circ$  (220) and  $18.0^\circ$  (400). Although, it is hard to identify all of the diffractogram lines clearly, probably due to the low density of crystals distributions along the substrate, diffractograms prove the growth of Zn-DMCAPZ in all the samples. In fact, it can be correlated the number of LbL cycles with the ratios of intensities between the characteristic MOF diffractogram line at  $8.9^\circ$  and the substrate at  $38.3^\circ$  (Figure 2.8.b), resulting in a linear correlation with a coefficient of determination of 0.9885 (Figure 2.8.c).



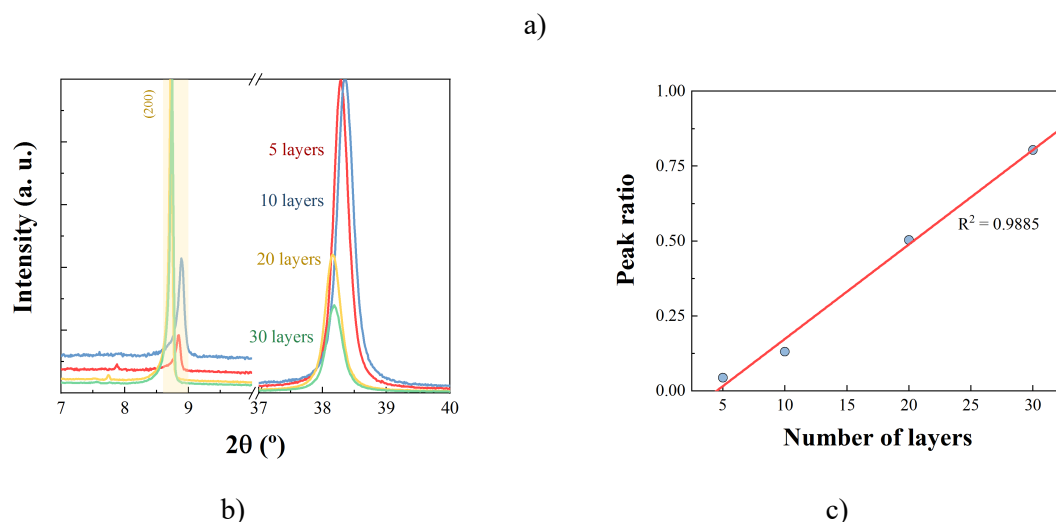


Figure 2.8. a) XRDs of the Zn-DMCAPZ film after 30 LbL cycles (blue), pristine Cu-Ti substrate (red) and commercial Cu-BTC powder (black). b) Comparison of characteristic Zn-DMCAPZ diffractogram peak at  $\sim 8.9^\circ$  vs substrate characteristic peak at  $\sim 38.3^\circ$  after 5 (red), 10 (blue), 20 (yellow) and 30 (green) LbL cycles. c) Ratio of characteristic MOF peak at  $\sim 8.9^\circ$ , which corresponds to (200) crystal plane, to substrate peak at  $\sim 38.3^\circ$  vs number of LbL cycles (blue dots) which are linearly dependent (red line).

DLS results reveal a broad particle distribution centred on  $103 \pm 34$  nm that is assessed by SEM inspection (Figure 2.9.a). Figure 2.9.b compiles the gold substrate over which 5, 10, 20 and 30 layers have been assembled and single crystals synthesized in batch. As expected, the higher the number of layers performed, the denser is the crystal distribution. Crystal growth appears not to depend on the number of layers, instead with increasing the number of LbL-cycles, new material is assembled in the space in between fully growth crystals. At the interface of the Pyrex and gold substrate (Figure 2.9.c) can be seen the preferential growth of Zn-DMCAPZ over the carboxylic group of the SAM deployed on it. However, the growth of MOF crystal on Pyrex side is still not desired and cannot be removed even mechanically. The cross-section examination by SEM of Zn-DMCAPZ films after 30 LbL cycles reveals a homogeneous, polycrystalline thin film of 0.8 nm in thickness.



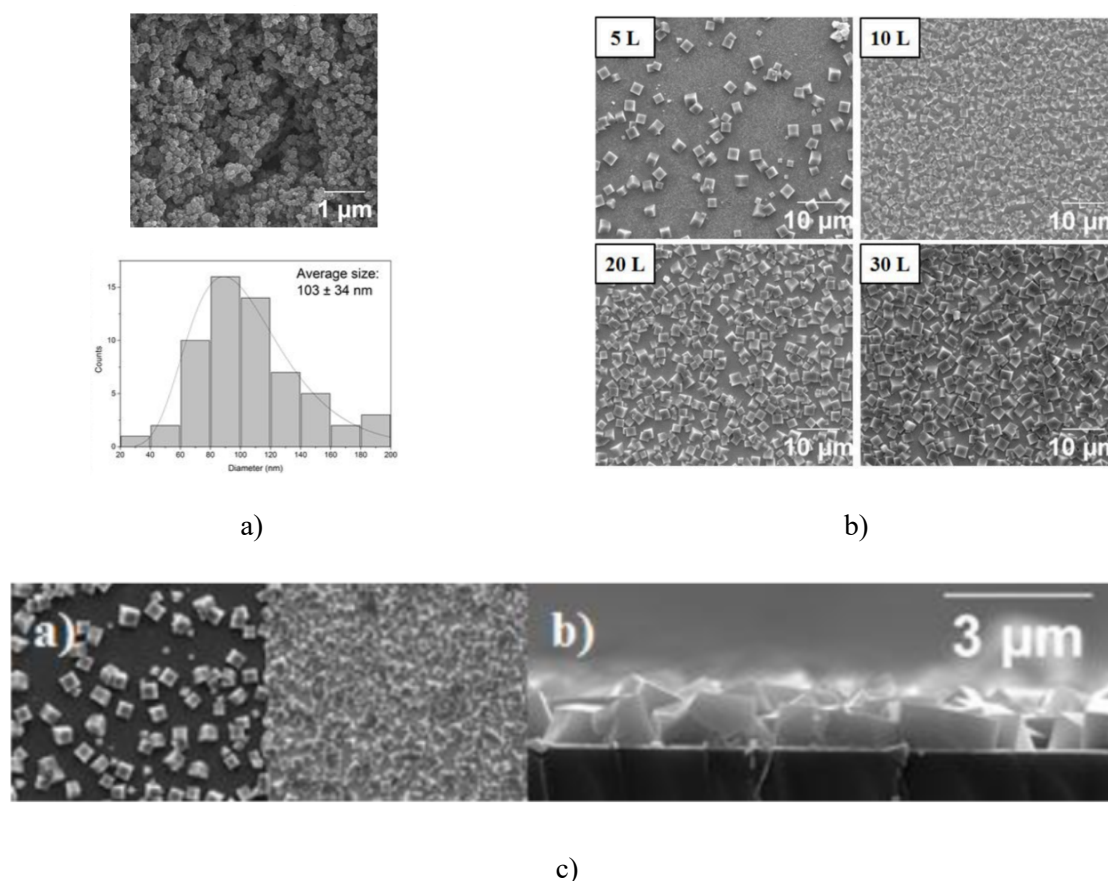


Figure 2.9. a) Upper: SEM microscopy of discrete Zn-DMCAPZ crystals. Down: particles distribution measured by DLS. b) SEM microscopies of Zn-DMCAPZ crystal distribution over Au substrates after 5, 10, 20 and 30 LbL cycles. c) Left: SEM microscopy depicting preferential growth of Zn-DMCAPZ crystals over the Au substrates. Right: cross-section of Borofloat wafer pattern with Au substrate and Zn-DMCAPZ film after 30 LbL cycles.

### 2. 2. 3. 3. Batch and layer-by-layer synthesis of Zn-MIM

#### **Discrete Zn-MIM crystals synthesis**

Zn-MIM was synthesized following the hydrothermal method described by Lai et al [128] using  $\text{Zn}(\text{NO}_3)_2 \cdot 6\text{H}_2\text{O}$  (Sigma Aldrich) as metal source and 2-methylimidazole (Sigma Aldrich) as organic linker. Firstly, 1.17 g  $\text{Zn}(\text{NO}_3)_2 \cdot 6\text{H}_2\text{O}$  was dissolved in 8 g of water and whereas 22.70 g of 2-methylimidazole was dissolved separately in 80 g of water. The two solutions were stirred together at room temperature. Zn-MIM crystal formation occurs instantly, and after stirring for 5 min, the product was collected by centrifugation and washed with water. The material was activated at 65 °C in air overnight.

### **Hydrothermal synthesis of Zn-MIM using ZnO deposited by ALD as metal source**

The metal source ZnO was deposited by atomic layer deposition (ALD). ALD is a chemical vapor deposition process, where different chemicals react with the surface of the substrate sequentially, forming almost atomic monolayers. By repeating the exposition to the different precursors, thin films are formed over the substrate [129] (Figure 2.10). In this work, sequential exposures of diethyl zinc (DEZ,  $\text{Zn}(\text{CH}_2\text{CH}_3)_2$ , Sigma Aldrich) and water at 373 K, separated by a purge with 100 STP  $\text{cm}^3/\text{min}$  of dry Argon. The deposition protocol was: 1) 4 s pulse of DEZ, 30 s exposure and 50 s of purge with dry Ar, after 2) 3 s pulse of  $\text{H}_2\text{O}$ , 40 s exposure and 60 s purge with dry Ar. Pulse, exposure and purge times were chosen to ensure completion of the ALD surface reaction. And to prevent mixing of the reactive species. The growth rate was about 0.2 nm/cycle. Final thickness was about 100 nm.

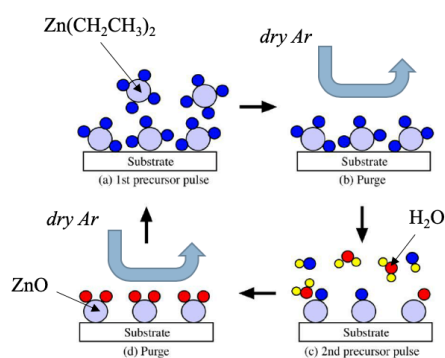
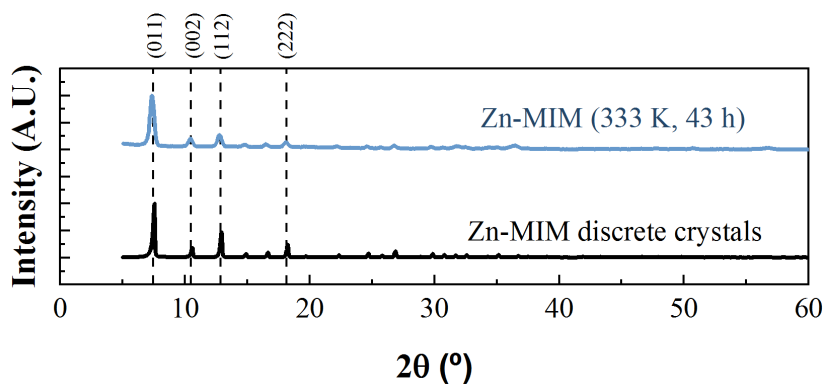


Figure 2.10. Schematic of deposition of ZnO coatings on the substrate by ALD.

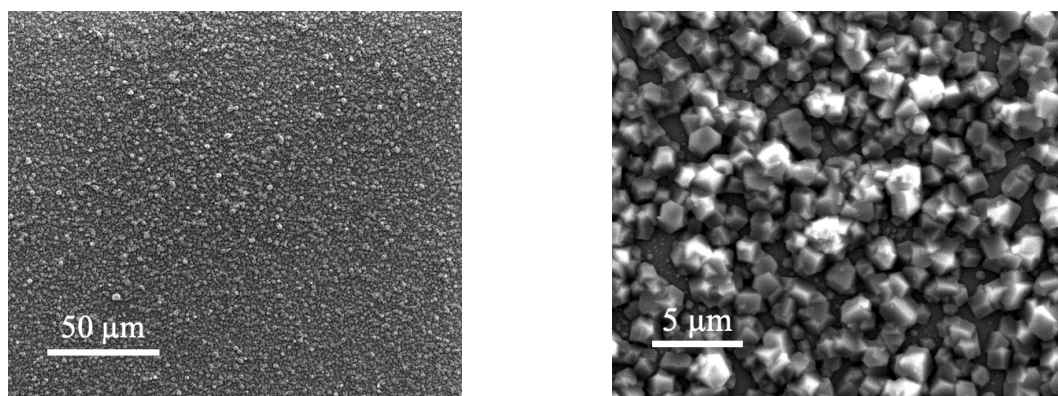
The conversion of ZnO thin layer to ZIF-8 was done by solvothermal synthesis. The seeded substrate was placed in a 45  $\text{cm}^3$  autoclave, containing a solution of 1 %<sub>w/v</sub> of 2-methyl imidazole (2-mim) in methanol. The synthesis takes place at 333 K for 43 h, after which, the substrate was washed with ethanol and activated at 343 K for 2 h.

XRD analysis reveals that Zn-MIM films at 333 K for 43 h present the correct crystallography as the Zn-MIM discrete crystals and characteristics peaks at  $2\theta = 7.6^\circ$ ,  $10.6^\circ$ ,  $12.0^\circ$  and  $18.3^\circ$ , which corresponds to crystallographic planes (011), (002), (112) and (222) respectively [129], appears on both samples (Figure 2.11.a). SEM micrographs assess the growth of polycrystalline Zn-MIM film over the substrate after synthesis at 333 K for 43 h. Figure 2.11.b reveals an homogeneous layer over the substrate of a dense polycrystalline Zn-MIM films with

a crystal size of about 1  $\mu\text{m}$ . As can be seen on the higher magnification micrograph (left picture), the resulting layer appears to be a monolayer of Zn-MIM crystals without preferential crystal orientation.



a)



b)

Figure 2.11. a) XRD of Zn-MIM films (blue). XRD pattern of Zn-MIM discrete crystals has been added to assess the correct crystallography of thin films (black). Crystallographic planes from [129]. b) SEM micrography of the Zn-MIM thin.

## 2. 3. SYNTHESIS OF MESOPOROUS SILICA MCM-48

The MCM-48 nanoparticles were synthesis using cetyltrimethylammonium bromide (CTAB, Sigma Aldrich) and ethanol as structure-directing agents, whereas the silica source was provided by tetraethyl ortosilicate (TEOS, Sigma Aldrich) and a tri-block copolymer Pluronic F127 (Sigma Aldrich) was used as particle dispersion agent. The molar composition of the reaction mixture was 2.5 TEOS : 50  $\text{NH}_3$  : 216 EtOH : 0.4 CTAB : 1668  $\text{H}_2\text{O}$  : 0.047 F127. 0.50 g of CTAB was dissolved together with 2.05 g of F127 in 96  $\text{cm}^3$  of water, 34.00 g of

EtOH and 10.05 g of ammonium hydroxide at room temperature. After complete dissolution, 1.80 g of TEOS was added and the mixture was stirred at 650 rpm for 4 h. After a final stir at 1000 rpm for 1 min, the solution was kept at static condition for 24 h at room temperature to allow the silica condensation. The solid product was recovered by centrifugation at 10000 rpm for 15 min, then washed with distilled water and dried overnight at 343 K. The organic template is removed by a final calcination at 823 K in air with a heating rate of 1 K/min for 6 h.

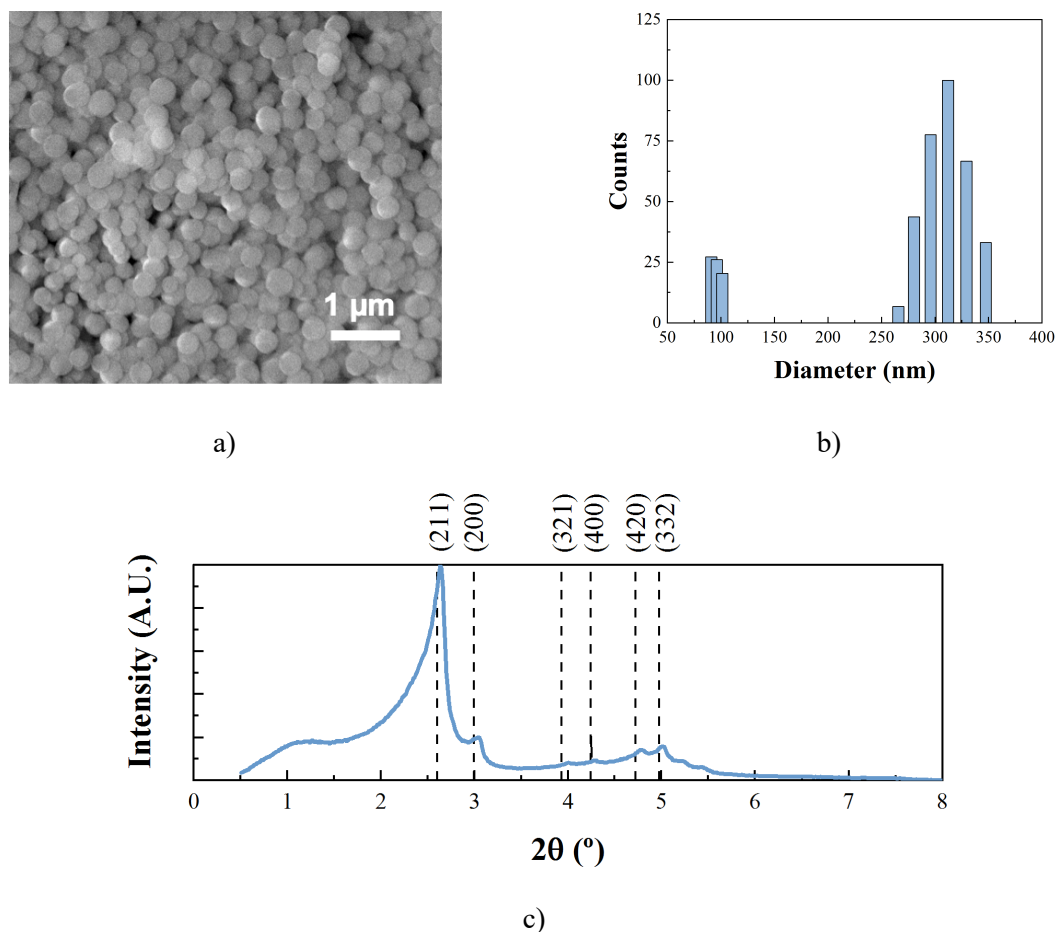


Figure 2.12. a) SEM micrograph of synthesized spherical MCM-48 nanoparticles. b) Particle size distribution measured by DLS. c) XRD of synthesized MCM-48.

As can be observed on the SEM micrographs (Figure 2.12.a), the resulting particles exhibit the expected sphericity and homogeneity, with an apparent uniform diameter of  $308 \pm 31$  nm. Dynamic light scattering (DLS) result reveal two population of particles sizes, being the most relevant the one centred on 312 μm, which, on the other hand confirms the size observed by SEM. The correct crystallography of the synthesized particles was assessed by low-angle X-ray diffractometry. As we can observed in Figure 2.12.c, the characteristic (211)

crystallographic plane at  $2.6^\circ$  can be found on both samples as well as other prominent crystallographic planes such as (200) @  $3.0^\circ$ , (420) @  $4.8^\circ$  or (332) @  $4.9^\circ$  which corroborate that spherical MCM-48 share the same crystal structure that conventional synthesized MCM-48.

Additionally, MCM-48 was functionalized by grafting to the surface of the material mono-, di- and tri-amine silane agents by Dr. Hakan Nigar. The amine-functionalization is reported in [130]. The synthesis of MCM-41 was performed at the Universitat Politècnica de Valencia (UPV) as part of a collaboration with the University of Zaragoza, following the protocol published in [131]. The synthesis of SBA-15 was performed within the NFP group following the synthesis protocol reported in [132].

## 2. 4. IN SITU POLYMERIZATION OF IONIC LIQUIDS

Films of polymeric ionic liquids (PIL) have been prepared on two substrates: 1) over modified graphitized-carbon adsorbents and 2) on Si substrates. Additionally, it has been prepared over graphitized-carbon adsorbent coating of room temperature ionic liquid.

### 2. 4. 1. MODIFIED GRAPHITIZED-CARBON ADSORBENTS WITH IL

---

BIL and PIL coatings were performed over the commercial graphitized-carbon Carbo-pack-X (C-X, Supleco). As with the majority of graphitized-carbon adsorbents, C-X is highly hydrophobic, presents high affinity towards polar compounds and exhibits a surface area of  $250 \text{ m}^2/\text{g}$  and pore size of  $100 \text{ \AA}$  [133]. In order to guarantee a good bed packing without preferential flow paths, the C-X beads were manually sieve in the size range of  $212 - 250 \text{ }\mu\text{m}$ .

BIL coating were performed by dissolving 4 mg of IL ( $0.20 \text{ g}_{\text{BIL}}/\text{g}_{\text{C-X}}$ ) in acetone (5 mL) and adding to this solution 20 mg of C-X. The solution was slowly stirred together for 2 h and the solvent was evaporated in a vacuum oven at  $100 \text{ }^\circ\text{C}$  overnight.

On the other hand, the PIL coating was performed by covering the carbon beads (20 mg) with 8 mg of VIL ( $0.41 \text{ g}_{\text{VIL}}/\text{g}_{\text{C-X}}$ ) dissolved in 5 mL acetone mixed with 0.1 mg the photo-initiator 2-hidroxy-2-methylpropiophenone (97%, Sigma Aldrich). As previously, the solution was stirred for 2 h and the evaporated overnight in a vacuum oven, after which is irradiated for 72 h with UV light (Vilber Lourmat lamp,  $\lambda=365 \text{ nm}$ , incident power = 1.1 mW), resulting in the *in-situ* polymerization of the monomer over the surface of the carbon beads. Ionic liquid

mass loadings were calculated to be slightly above theoretical mono-layer coatings in order to guarantee full coverage of carbon beads. Theoretical monolayer coatings were  $0.2 \text{ g}_{\text{BIL}}/\text{g}_{\text{C-X}}$  for BIL,  $0.2 \text{ g}_{\text{HIL}}/\text{g}_{\text{C-X}}$  for HIL and  $0.3 \text{ g}_{\text{VIL}}/\text{g}_{\text{C-X}}$  for PIL, calculated according [134].

Ionic liquid loading and thermal stability of the coated graphitized carbons were assessed by thermogravimetric analysis (Pyris 1 TGA, Perkin Elmer) from room temperature to 873 K with a heating rate of 10 K/min under air. Figure 2.13 shows TGA results of the three coated carbons as well as a reference sample of uncoated C-X. It can be observed that, whereas C-X is stable up to 873 K, the coated carbon beads present a weight loss in the range of 573 to 773 °C that correlates to the decomposition temperature of the corresponding ionic liquids ( $T_{\text{d, BIL}} = 439 \text{ °C}$  [135] and  $T_{\text{d, PIL}} = 375 \text{ °C}$  [107]). Assuming the fully decomposition of ionic liquids coating at 873 K, it can be estimated a coating loading of  $0.29 \text{ g}_{\text{RTIL}}/\text{g}_{\text{C-X}}$  and  $0.53 \text{ g}_{\text{PIL}}/\text{g}_{\text{C-X}}$  (Figure 2.13.b). Such values are higher than those theoretically calculated assuming a 100% yield and a homogenous distribution of the IL on the CX surface.

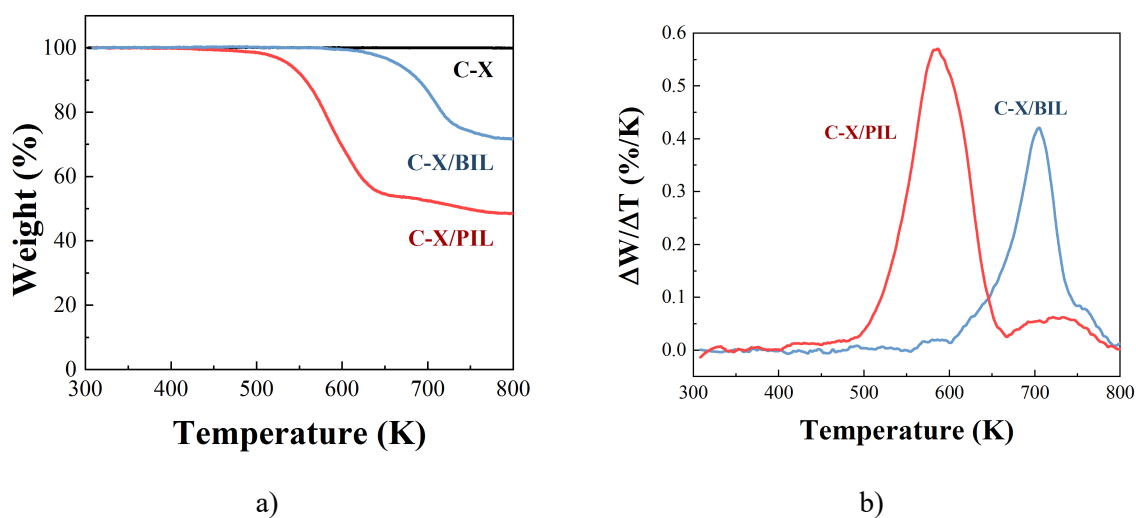


Figure 2.13. TGA a DTA from room temperature to 873 K of pristine C-X (black) and coated with BIL (blue) and PIL (red): a) weight loss per mass unit and b) first derivative of weight loss per mass unit.

#### 2. 4. 2. DEPOSITION ON SI MICRODEVICES

The polymerization of the PIL films took place on the inner walls of the microfluidic device upon UV exposure (Vilber Lourmat lamp,  $\lambda=365 \text{ nm}$ , incident power = 1.1 mW) of a VIL solution in acetone with the photo-initiator: 2-hydroxy-2-methylpropiophenone (97%,

Sigma Aldrich). Two different coating techniques have been used: 1) static deposition or 2) dynamic deposition.

#### 2. 4. 2. 1. *Static deposition*

Static deposition consists on casting a solution of MIL and photoinitiator in acetone inside the microcavity. The acetone is evaporated, and MIL film is polymerized. The microdevice is eventually sealed with a Borofloat cover (Figure 2.14).

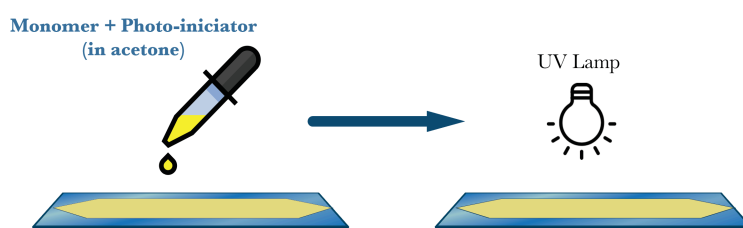


Figure 2.14. Schematic of static deposition method over an empty microchannel. After solvent evaporation, the MIL is exposed to UV light.

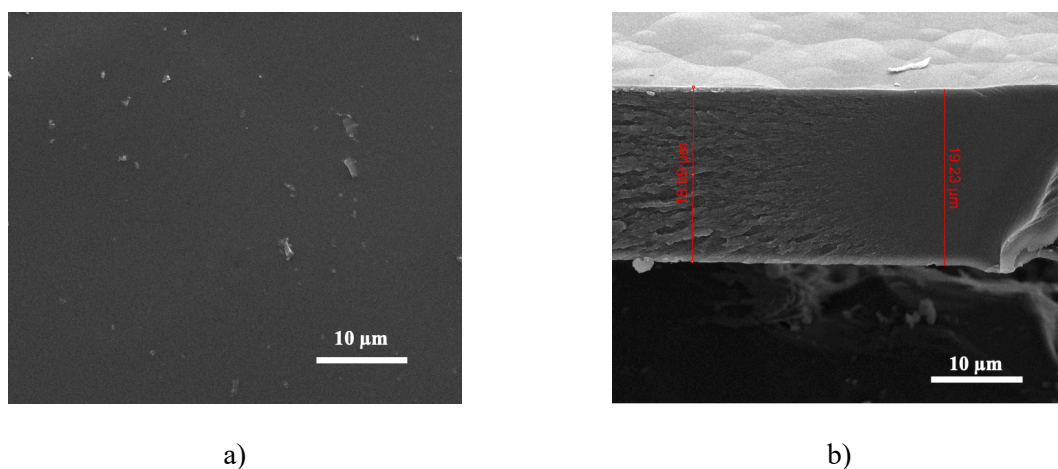


Figure 2.15. SEM micrograph of the top view (a) and cross-section (b) of a PIL film over a Si substrate.

The solution to cast was optimized in order to increase the amount of MIL polymerization and the concentration was increased from 1:0.2 to 1:10 v:v (MIL:acetone). Solutions below 1:1 concentration were discarded due to its high viscosity and complicate manipulation. Rapid acetone evaporation on such solution led to clogging due to formation of deposits inside

dispensing element and heterogeneous, thick layer. A proper concentration was found with 1:5 solution, leading to a film of  $19.50 \pm 1.8 \mu\text{m}$  as observed by SEM (Figure 2.15).

#### 2. 4. 2. 2. *Dynamic deposition*

Dynamic deposition consists on the co-injection of a solution of MIL and photo-initiator in acetone using the inlet port of a sealed microdevice and simultaneous irradiation through the Borofloat wafer. Parameters to be considered in this approach are solution concentration, solution inlet mass flow, co-injected inert gas mass flow and residence time.

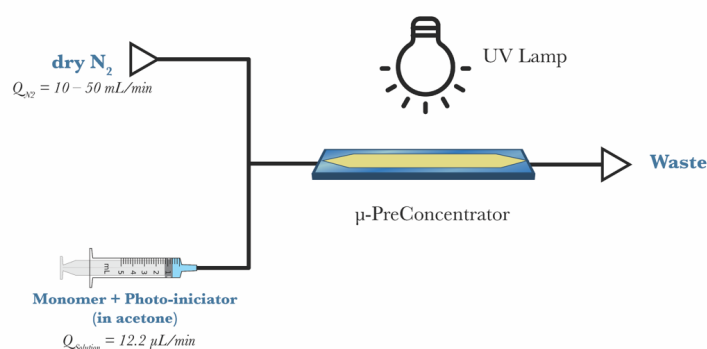


Figure 2.16. Schematic of dynamic deposition method through a closed, empty microdevice. While the monomer-photoinitiator-solvent and N<sub>2</sub> gas are being co-injected, they are being polymerized by UV irradiation.

The protocol carried out to perform the PIL coatings consisted on flushing the MIL solution (1 : 60, MIL : acetone) with 2 %<sub>w</sub> (per mass of MIL) of photo-initiator at 12  $\mu\text{L/min}$  from 5 to 15 min while irradiating through the Borofloat cover. After which, N<sub>2</sub> was used to sweep out the unpolymerized solution as well as evacuate the acetone during the polymerization. The polymerization of the MIL was assessed after 4 h by FTIR (Figure 2.17). It was observed an intensity damping in bending ( $955 \text{ cm}^{-1}$ ) and stretching ( $1649 \text{ cm}^{-1}$ ) modes of vinyl group ( $-\text{CH}=\text{CH}_2$ ) along the UV exposure time.



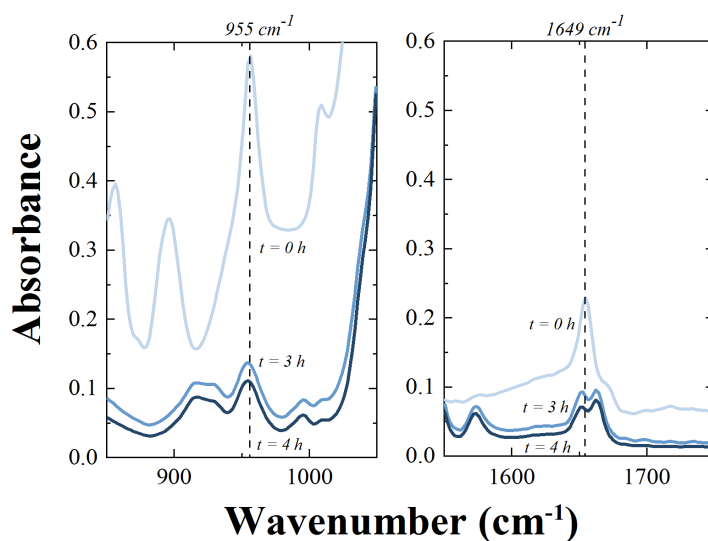


Figure 2.17: Polymerization assessment of MIL irradiating through the Borofloat cover by FTIR analysis.

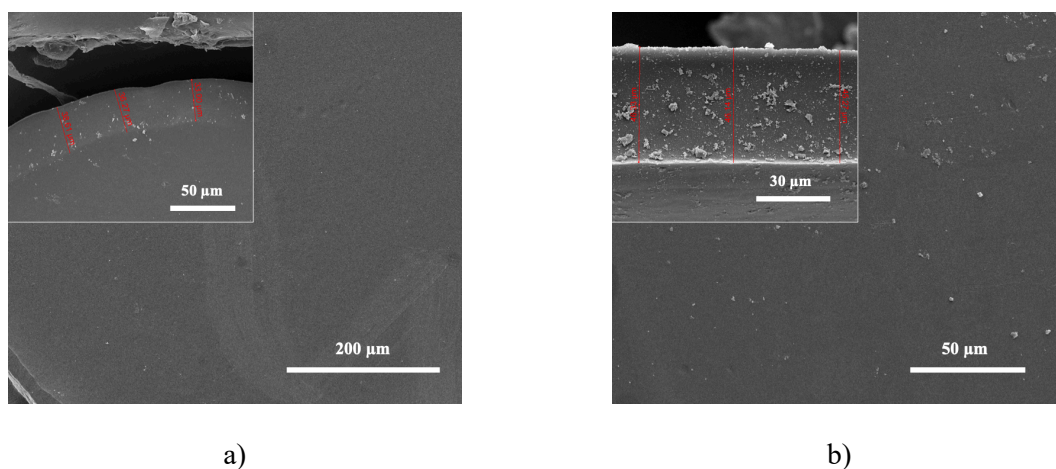


Figure 2.18. SEM micrographs of the top view and cross-section (insert) of PIL films in situ polymerized after flushing the MIL solution for 5 min (a) and 15 min (b).

PIL films were prepared after flushing the MIL solution for 5 min and 15 min. Both cases resulted in non-continuous coatings, preferentially deposited in the Borofloat surface. These films are as result of the polymerization of the MIL close to the irradiation source, i.e. the Borofloat cover, that hindered the photoreaction of the monomer below. Additionally, the hydrophobic character of Si substrate with the MIL solvent, i.e. acetone, resulted in a poor

wettability of the fluidic path a thus in a non-homogeneous coating. For 5 min flushing, the PIL coating resulted in a 24 % of the total coverage surface, whereas for 15 min, resulted in 37 %. As observed by SEM (Figure 2.18), both PIL films exhibit a smooth surface with a thickness of  $34.6 \pm 3.3 \mu\text{m}$  for the coating prepared after flushing 5 min and  $46.6 \pm 1.2 \mu\text{m}$  for the one prepared after flushing 15 min.

## 2. 5. CHARACTERIZATION OF SORBENT MATERIALS

Textural properties of the sorbents use in this work were either measured by Ar physisorption at 87.3 K (occasionally by N<sub>2</sub> physisorption at 77.4 K) as well as obtained by bibliography or giving by the supplier. In the case of silicalite, Zn-DMCAPZ and Zn-MIM measurements were performed on discrete crystals. For Cu-BTC, measurements were performed on commercial MOF Basolite C-300 (Sigma Aldrich).

As can be observed in Table 2.3, the selected sorbent present high surface area and pore volume as it is characteristic of micro- and mesoporous materials. In comparison with other popular commercial sorbents, the graphitized carbon Carbopack-X presents a surface area ( $250 \text{ m}^2/\text{g}$ ) [133] or polymeric sorbents, such as Tenax TA exhibits even lower surface area ( $35 \text{ m}^2/\text{g}$ ) [133]. Particularly, MOFs material stand out due to their high surface area, with values up to  $1900 \text{ m}^2/\text{g}$ . On the other hand, the functionalization of both ETS-10 and MCM-48 led to a decrease of the surface area, pore volume and pore size. For the highly functionalized ETS-10/IGPTS (up to 8.4 mmol of grafted organosilane per g of ETS-10), the surface area diminishes from  $316 \text{ m}^2/\text{g}$  of the pristine ETS-10 to  $95 \text{ m}^2/\text{g}$  as well as pore volume from  $0.13 \text{ cm}^3/\text{g}$  to  $0.09 \text{ cm}^3/\text{g}$  due to a possible micropore clogging by the grafted organosilane on the structure. The same explanation can be attributed to the decrease of surface area on the MCM-48, which is more noticeable in the tri-amine functionalized material, with a decrease of surface area from  $1225 \text{ m}^2/\text{g}$  of the pristine material to  $463 \text{ m}^2/\text{g}$ .

TABLE 2.3. TEXTURAL CHARACTERISTIC OF THE SORBENTS USED IN THIS WORK

	Sorbent	BET surface (m <sup>2</sup> /g)	Pore Volume (cm <sup>3</sup> /g)	Pore Size (nm)	Ref
Zeolites	Silicalite	334	0.19	0.5	*
	CP814/Fe	680	-	-	[136]
	CBV780/Cu	780	-	-	[136]
Titanosilicates	ETS-10	316	0.13	0.5 x 0.8	[137]
	ETS-10/IGPTS	95	0.09	-	[137]
	ETS-10/NH <sub>2</sub>	216	0.10	-	[137]
MOFs	Cu-BTC	1812	0.81	0.5, 0.9	*
	Zn-DMCAPZ	1200	0.71	0.6	*
	Zn-MIM	1960	0.85	0.9	**
Mesoporous silica materials	MCM-48	1225	0.92	3.5	*
	MCM-48/NH <sub>2</sub>	1072	0.52	2.9	[138]
	MCM-48/2NH <sub>2</sub>	698	0.39	2.6	[138]
	MCM-48/3NH <sub>2</sub>	463	0.23	2.5	[138]
	MCM-41	1000	0.50	1.0 – 10	[139]
	SBA-15	956	1.40	12	[132]

\*Measured by Ar physisorption at 87.3 K. \*\* Measured by N<sub>2</sub> physisorption at 77.4 K.

Thermal properties of the proposed sorbents have been also evaluated by thermogravimetric analysis in inert atmosphere. Whereas zeolite, titanosilicate and mesoporous materials present enough thermal stability, MOF materials and polymeric ionic liquids present lower decomposition temperatures that can compromise the correct functioning of the  $\mu$ -device. Since some procedures in the fabrication of the  $\mu$ -device (temperatures over 500 K) as well as during the working of the sensor (temperatures from 373 K to 473 K) are carried out at temperatures close to decomposition, a characterization of the working temperature of the sorbents must be performed.

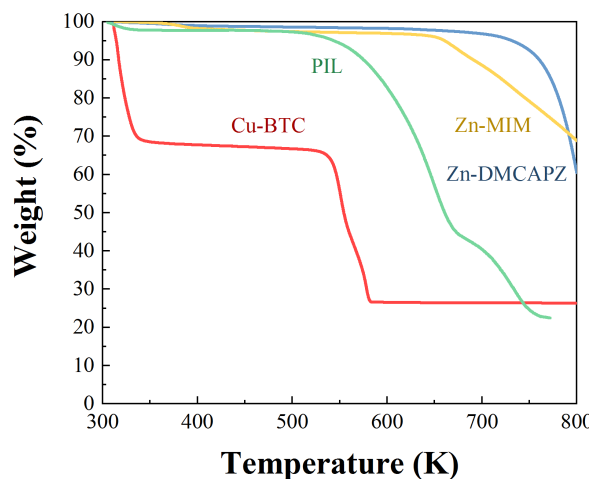


Figure 2.19. TGA result of the MOF and PIL sorbents.

TGA results shows that the four tested sorbents are stable in ranges from 300 to 500 K, so are within the range of the operational work of the sensor. On the other hand, fabrication protocols at 500 K are suitable for the four sorbents, although degradation temperature of Cu-BTC (circa 550 K) was only slightly above that value. Thermal stability of Cu-BTC was assessed in isothermal conditions at 550 K for 36 h. Results reveal no significant mass loss after 5 h; however, after 36 h a mass loss of 13 %<sub>wt</sub> was registered. Additionally, TGA analysis highlighted the high hydrophilic character of Cu-BTC, with a weight loss up to 30 %<sub>wt</sub> at  $T < 373\text{K}$ , which can be associated with water uptake. The hydrophobic character of Zn-DMCAPZ, Zn-MIM and PIL was as well observed, with no significant weight loss at temperatures below 373 K.

## 2. 6. CONCLUSIONS

This Chapter has presented the different approaches that have been carried out order to incorporate the nanoporous sorbent in the  $\mu$ -devices. These procedures include the synthesis ex-situ of discrete crystals as well as the in-situ synthesis of polycrystalline layer on a Si substrate or on a metal layer deposited on a Borofloat substrate.

Particularly outstanding have been in-situ synthesis and polycrystalline film growth of silicalite, Cu-BTC, Zn-DMCAPZ and Zn-MIM coatings. Hydrothermal growth of silicalite ex-situ synthesized seed deposited on Si substrates yield to homogenous and reproducible coatings of 4  $\mu\text{m}$  thickness. Polycrystalline Cu-BTC films have been performed by electrochemical synthesis on Cu-Ti electrodes micropatterned on a Borofloat substrate, achieving coatings of 4.7

$\mu\text{m}$ . Zn-DMCAPZ coatings have been synthesis over an Au substrate on a Borofloat substrate as well following a layer-by-layer approach. After 20 cycles, the maximum thickness of Zn-DMCAPZ however is less than  $1 \mu\text{m}$ . Finally, Zn-MIM coatings have been performed by solvothermal synthesis on the Si substrate after being coated with a thin layer (100 nm) of ZnO that is used as metal source for the MOF synthesis. Newly, the polycrystalline film thickness is less than  $1 \mu\text{m}$ .

Finally, in situ UV polymerization of imidazole-based ionic liquid (PIL) has been achieved in already sealed microdevices, in flat or patterned cavity configurations. Final PIL coatings result in flat cavities non-continuous films of  $30 \mu\text{m}$  to  $45 \mu\text{m}$ . On patterned configurations the deposition is preferentially performed at the inlet of the microdevices and scarce on the inner patterned pillars, thus a proper quantification of the layer thickness as well as the mass loading has not been feasible. Additionally, it has been satisfactorily performed the functionalization of graphitized carbon sorbents with PIL films in situ polymerized with theoretical coating loadings of  $0.53 \text{ g/g}$ .

The selected sorbents have been classified their potential application in Table 2.4. Classification of the adsorbents proposed according its application: explosive detection or organophosphorus vapor preconcentration. Additionally, it has also included the commercial adsorbent TENAX-TA (Sigma Aldrich) as sorbent for nitro-compounds for comparison purposes.

TABLE 2.4. CLASSIFICATION OF THE ADSORBENTS PROPOSED ACCORDING ITS APPLICATION

		Explosive detection	CWA preconcentration
Microporous materials	Zeolitic materials	CBV780 CBV780/Cu CP814E/Fe CP814/Co	Silicalite
	Titanosilicates	ETS-10 ETS-10/NH <sub>2</sub> ETS-10/IGPTS	-
	MOFs	Cu-BTC	Cu-BTC Zn-DMCAPZ Zn-MIM
Mesoporous materials	Mesoporous silica materials	MCM-41 MCM-48 MCM-48/mono-NH <sub>2</sub> MCM-48/di-NH <sub>2</sub> MCM-48/tri-NH <sub>2</sub> SBA-15	MCM-48
Others	Ionic liquids	-	BIL PIL C-X/BIL C-X/PIL
	Commercial adsorbents	TENAX-TA	C-X

**CHAPTER III:**  
**EXPLOSIVE RELATED**  
**COMPOUNDS DETECTION USING  $\mu$ -CANTILEVERS**  
**MODIFIED WITH NANOPOROUS SOLIDS**





### **3. EXPLOSIVE RELATED COMPOUNDS DETECTION USING $\mu$ -CANTILEVERS MODIFIED WITH NANOPOROUS SOLIDS**

#### **3. 1. INTRODUCTION**

Chapter I introduces electronic noses as biomimetic systems design for gas monitoring and sensing both for laboratory and field purposes. In analogy with human olfactory system, the electronic nose were comprises of a sampling unit (the nasal cavity), a sensory unit (the olfactory receptors), the data acquisition unit (the olfactory bulb) and the pattern recognition unit (the olfactory cortex) [140]. Herein, in this Chapter, we are going to focus on the sensor unit of our electronic nose and in a lesser extent we are going to introduce the data acquisition unit and the identification and discrimination of the target analyte.

In our case, it has been proposed as sensing unit an array of functionalized  $\mu$ -cantilevers fabricated in collaboration with Prof. E. Figeras from the Institute of Microelectronics of Barcelona (IMB-CNM). The functionalization has been performed using the micro- and mesoporous materials presented on Chapter II. The electronic interface, developed for both acquiring data and drive the  $\mu$ -cantilever unit, has been developed by Prof. Medrano from the Institute of Engineering Research of Aragon (I3A).

The functionalized  $\mu$ -cantilever array has been exposed to vapours of explosive related compounds as well as commercial explosives. Different coatings have been tested in order to compile a database of materials response to proposed analytes, so all the combined responses could derive into a characteristic and unique fingerprint of each explosive, thus allowing the satisfactory detection and identification.

#### **3. 2. $\mu$ -CANTILEVERS AS CHEMICAL SENSORS**

$\mu$ -cantilever based sensor is based in the monitoring of changes in the surface stress, bulk stress or mass. The first mode of operation is based on the measurement of the static deflection of the beam, which is related to differences in surface stresses of both faces of the cantilever.

Commonly, one of the sides of the cantilever beam is functionalized and the interaction of the sensing layer with the analyte is what produce a stress on one of the surfaces and thus the bending – upwards or downwards – of the cantilevers. This approach is widely used in biosensing applications, such as peptide-functionalized array of  $\mu$ -cantilevers used for antibiotics detection [141], DNA-functionalized  $\mu$ -cantilevers for the detection of pathogenic bacteria in food samples [142] or  $\mu$ -cantilevers functionalized with gold nanoparticles combined with DNA strands for determination of dopamine level for neurodegenerative diseases monitoring [143].

In a second mode of operation, alike the first one, it is newly measured the static deflection of the beam but of a bilayer  $\mu$ -cantilever. Top and bottom surfaces are fabricated with different materials that performs differently under an external stimulus such as temperature or humidity. Since the behaviour of top and bottom layer are not equal, this led to an induced stress in the structure that yields in a bending of the beam. This approach has been used for fabricated thermal sensor, such as, for hydraulic application using bilayer cantilevers of thin-film NiTi shape memory alloy [144] or sensitive thermometers based on Au/SiN  $\mu$ -cantilevers with limits of detections down to  $10^{-5}$  K [145]

Finally, the third mode of operation is based on changes of natural resonant frequency of the cantilever due to variations of its mass. Commonly, this change in mass is due to the interaction of the sensing layer with the analyte, which led to an increase of the beam mass and thus a decrease of the natural resonant frequency. This technique allow the fabrication of tiny microbalances with theoretical mass limit of detection in the range of atto- ( $10^{-18}$ ) to zepto- ( $10^{-21}$ ) grams, characterized in vacuum and low temperature ( $T = 25$  K) [146]. This approach has been used to the fabrication of gas sensor for VOCs sensing, such as, for detection organophosphorus compounds using resonant  $\mu$ -cantilever coated with MOF layers as sensitive material reaching limit of detection down to 5 ppb [147] or mesoporous silica nanoparticles functionalized  $\mu$ -cantilever for VOC (acetic acid and aniline) monitoring in humid conditions [148]. The functionalized  $\mu$ -cantilevers are based on this mode of operation, and their performance to nitro-related compounds has already been assessed satisfactorily with zeolite-modified  $\mu$ -cantilevers in previous works within the group [149], [150].

### 3. 2. 1. ACTUATION METHODS

---

Dynamic operation mode is based on measuring shift on resonant frequency, in order to provoke the resonance of the cantilever, an external force must be applied. A variety of

techniques have been explored to actuate cantilevers, although the choice of the method has to be coordinated with the read-out approach. Common actuation methods are:

- *electro-static actuation*: an alternating current is applied over an external electrode, which results in a periodic electrostatic force on the cantilever that provokes its vibration. This technique is often used in conjunction with capacitance read-out since its ease to fabrication [151].
- *thermal actuation*: the cantilever is subject to heating cycles that, due to its intrinsic design or material configuration (the use of two materials with different thermal coefficients), results in the oscillation of the beam. Actuation can be due to an integrated heating element [152], an external laser [153] or even the natural thermal vibration due fluctuations on the temperature of the structure itself [154].
- *electromagnetic actuation*: the oscillation of the beam is due to Lorentz forces as result of the interaction between an external magnetic field and an alternative current that circulates over the beam. Our array of  $\mu$ -cantilevers is based on this actuation method and piezoresistive detection.

### 3. 2. 2. DETECTION METHODS

---

In order to quantify the deflection of the beam, either in static or dynamic conditions, different read-out approaches have been investigated. Most common approaches are optical, capacitive, piezo-electric and piezo-resistive read-out systems [155], [156]:

- *optical read-out*: this method is commonly used for measuring the deflection of the beam in static operation modes. Alike in AFM systems, a laser is focused on the back of the cantilevers, which acts as a mirror. The reflection of the laser is detected by a position sensitive photodetector. In the case of resonating  $\mu$ -cantilever, the read-out process is based on the interference produce by the reflection of the laser on the back of an active  $\mu$ -cantilever and a reference one [157]. The main advantage of this approach is its simplicity and versatility, since it can be applied to any cantilever with a good optical quality. On the other hand, it is difficult to scale-up for large arrays of  $\mu$ -cantilevers; it is sensitive to refractive media

changes, which may lead to optical artefacts; and due to the focused laser spot size, maximum miniaturization is about 1 – 2  $\mu\text{m}$ .

- *capacitive read-out*: this approach is based on the change of the capacitance of a capacitor due to variation of the distance between the two electrodes. Commonly, a planar electrode is placed on the fixed substrate and the other electrode is situated on one of the cantilever's surfaces. This approach outstands by 1) a high degree of miniaturization, which allows the fabrication of cantilevers in the nanoscale, and 2) its implementation into the beam does not alter its mechanical properties. However, the measured capacitance changes may be hindered by parasitic capacitances, which required of pre-amplification stages which, along the fabrication under complementary metal-oxide-silicon (CMOS) conditions, may over-complicate the manufacturing for certain applications.
- *piezo-electric read-out*: this method is based on the electric potential that is generated across a material when a stress is induced on it and vice versa. Piezoelectric materials that have been used are zinc oxide [158], lead zirconate titanate (PZT) [159] or aluminium nitride [160]. The highlight of this technique is the possibility of being used both for actuation of the cantilever (in dynamic operation mode) as well as for read-out. It also stands out for its scalability and low power consumption. On the other hand, many piezoelectric materials are difficult to deposited or growth and some may be even incompatible with clean room conditions.
- *piezo-resistive read out*: in this case, each cantilever has an integrated piezoresistive resistor. Piezoresistive materials are those whose resistance is dependant of its deformation, so when the cantilever bends, the integrated piezoresistive resistor also bends and its resistance is proportional to the degree of deformation. This approach allows the system integration and facilitates large arrays of cantilevers. It is adequate for both static and dynamic operation modes and works satisfactorily for gas and liquid applications. On the contrary, a piezoresistive layer must be integrated inside the beam, so it may affect its mechanical performance. This approach has been selected for our functionalized  $\mu$ -cantilever gas sensor, where we have integrated a piezoresistive resistor on the beam as well as on the substrate in a half Wheatstone bridge configuration.

### 3. 2. 3. MECHANICS OF THE RIGID SOLID

In order to be able to explain how cantilever-based sensors can be used as sensitive micro-balance, we must first model the motion of a beam. Considering a cantilever as a thin beam where one dimension is larger than the other two (in this case, length  $L$  is greater than width  $w$  or thickness  $h$ ), we can assume that rotational inertia and shear deformation can be neglected. Assuming as well a linear elastic material and small deflection, the equation of the motion of the beam is described by the Euler-Bernoulli equation:

$$\frac{\partial^2 U(z,t)}{\partial t^2} \rho \Gamma + \frac{\partial^4 U(z,t)}{\partial z^4} \hat{E} I_z = 0 \quad (2)$$

where  $U(z,t)$  is the displacement in the x-direction,  $\rho$  is the density,  $\Gamma = w \cdot h$  is the cross-section area,  $\hat{E}$  is Young's modulus and  $I_z$  is the geometric moment inertia. (40) yields in a harmonic solution that can be expressed into a position dependent and time dependent term, where  $\omega_n$  is the frequency of motion and  $n$  is the modal number:

$$U(z,t) = U_n(z) e^{-i\omega_n t} \quad (3)$$

substituting (40) into (2), we can rewrite the initial equation into:

$$\frac{\partial^4 U(z,t)}{\partial z^4} = K^4 U(z,t) \quad (4)$$

$$K^4 = \frac{\omega^2 \rho \Gamma}{\hat{E} I_z} \quad (5)$$

The solutions (eigenfunctions) to (4) can be written as:

$$U_z(z) = A_n (\cos k_n z - \cosh k_n z) + B_n (\sin k_n z - \sinh k_n z) \quad (6)$$

Considering the boundary conditions in our case – single-clamped beam – the frequency equation is:

$$1 + \cos k_n L \cdot \cosh k_n L = 0 \quad (7)$$

and the solutions for  $n = 1, 2, 3, n > 3$  are  $\lambda_n = k_n L = 1.8751, 4.6941, 7.8548, (2n-1)\pi/2$  [161]. We can interpret this solution as the beam does vibrate distinctively in each mode. This oscillation characterizes to have high (peaks) and low (valleys) amplitude points, which increase with the mode number.

The frequency of oscillation of each mode-shape is called eigenfrequency and can be obtained from (5) and the corresponding solution for the eigenfunction (6). Assuming a beam with rectangular cross-section, thus  $I_z = h^3w/12$  and  $\omega_i = 2\pi f_i$  the resulting equation is:

$$\omega_i = \frac{\lambda_n^2}{L^2} \sqrt{\frac{\hat{E}I_z}{\rho\Gamma}} \rightarrow f_i = \frac{\lambda_n^2}{4\pi\sqrt{3}} \frac{h}{L^2} \sqrt{\frac{\hat{E}}{\rho}} = r_n \cdot \frac{h}{L^2} \cdot \sqrt{\frac{\hat{E}}{\rho}} \quad (8)$$

where  $r_n = \lambda_n^2/(4\pi\sqrt{3})$ . For the fundamental mode –  $n = 1$ ,  $\lambda_1 = 1.875$  –, (40) is written as:

$$f_0 = \frac{1}{2\pi} \sqrt{\frac{k_{eff}}{m_{eff}}} \quad (9)$$

where  $k_{eff}$  and  $m_{eff}$  are the effective spring constant and effective mass at the beam. For the first bending mode of the cantilever, these are expressed as:

$$m_{eff} = 0.24 \cdot m_0 \quad (10)$$

$$m_0 = \rho\Gamma L \quad (11)$$

$$k_{eff} = \frac{\hat{E}h^3w}{4L^3} \quad (12)$$

From (9) we can deduce that a change in the mass of the cantilever (in our case, related to the interaction of the sensitive material with the target molecules) will result in a decrease of the resonant frequency, which is the sensing principle of our transducer. We can relate a shift in the mass  $\Delta m$  with the shift of the natural resonant frequency  $\Delta f$  through:

$$\frac{\Delta f}{f_0} = \sqrt{\frac{1}{\Delta m/m + 1}} - 1 \quad (13)$$

If we assume that  $\Delta m$  is small enough in comparison to  $m$ , we can simplify (40) into:

$$\frac{\Delta f}{f_0} = -\frac{1}{2} \frac{\Delta m}{m} \quad (14)$$

This expression allows us to determine the sensitivity  $S$  of our sensor as well as the mass resolution  $\Delta m_{min}$  as the results of the minimum measurable frequency  $\Delta f_{min}$  divided by the sensitivity:

$$S = \frac{\Delta f}{\Delta m} = -\frac{1}{2} \frac{f_0}{m} \quad (15)$$

$$\Delta m_{min} = S^{-1} \cdot \Delta f_{min} \quad (16)$$

From (40) and (16) as well as the dimensions and properties of the cantilever, we can rewrite mass shifts as:

$$\Delta m = S^{-1} \cdot \Delta f = \left( -r_n^{-1} \cdot L^3 w \sqrt{\frac{\rho^3}{\hat{E}}} \right) \cdot \Delta f \quad (17)$$

By analysing (40) we can deduce that in order to achieve high mass sensitivities, the cantilever must exhibit high natural resonant frequency, for which is given by its geometry and material properties ( $\rho$ , thickness). In order to increase natural resonant frequency, the beam has to present small dimension, high Young's modulus and low density. On the other hand, system's resolution is not only given by the characteristic of the cantilever but also on the read-out method characteristics, i.e.  $\Delta f_{min}$  above the electrical noise of the read-out system.

As most oscillating systems, our resonating beam will also suffer from damping and therefore dissipating energies that will cause a loss on its kinetic energy. We can relate this loss of energy as the ratio of energy lost per cycle to the stored energy, although commonly is used its inverse: the quality factor  $Q$ .

$$Q = 2\pi \frac{E_0}{E_{lost \text{ per cycle}}} = \frac{f_0}{\Delta f'} \quad (18)$$

being  $\Delta f'$  the resonant peak width at  $1/\sqrt{2}$  of the maximum resonant amplitude. This factor is related to the accurate determination of the resonant peak, i.e., as  $Q$  is decreased, the resonant peak becomes wider and thus is harder to precisely detect it. On the contrary, higher  $Q$  values lead to sharp, well-defined peaks that are easier to detect.

Energy dissipation is due to through several mechanisms either intrinsic to the resonant beam or to external processes. Intrinsic process are considered those that are related to the material of the beam itself, such as, interactions inside the crystalline network (phonon-phonon interactions, phonon-electron interactions and thermo-elastic interactions) [162], [163] as well as design factors such as anchor losses [162], [164]. Extrinsic dissipation occurs due to interaction with the surrounding media, pressure and viscosity of the fluid as well as adsorption-desorption mechanisms and interaction with the molecules of the systems.

### 3. 3. EXPERIMENTAL SET-UP

#### 3. 3. 1. MICROFABRICATION OF SI $\mu$ -CANTILEVERS

The micromechanical systems used for evaluating sorption capacities of the materials were designed by NFP in collaboration with Prof. J. Sesé from the Institute of Nanoscience of Aragon (INA).

The fabrication run uses a standard n-type Si on insulator (SOI) wafer, where the  $\mu$ -cantilevers are defined using standard optical lithography and bulk micromachining technologies with five-level of masks [150] (Figure 3.1).

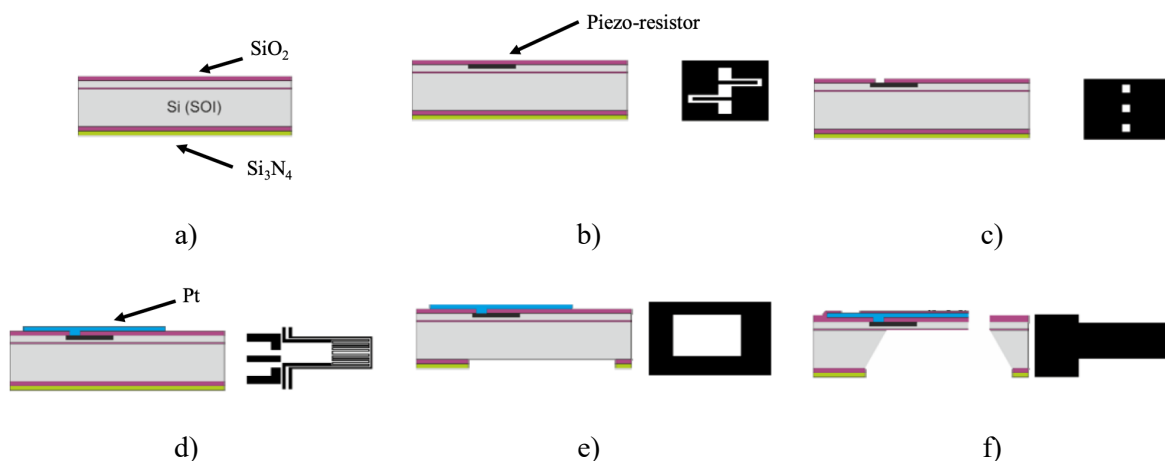


Figure 3.1. Simplified schematic of the  $\mu$ -cantilever fabrication run and corresponding mask: a) wafer oxidation on both faces, b) patterning and fabrication of the piezo-resistors, c) piezo-resistor contact definition, d) Pt metallization, e) openings on the backside definition and f) definition of the cantilever and freeing.

In this thesis,  $\mu$ -cantilevers 200  $\mu\text{m}$  wide, 15  $\mu\text{m}$  thick and from 500 to 535  $\mu\text{m}$  in length have been used (Figure 3.2.a). Theoretical mass sensitivity ( $S$ ) values ranging from 16 to 20 Hz/ng, which had been estimated from (17). With the aim of miniaturization and integration, individual heating wires, actuation of the cantilever and mechanical resonance are integrated on each cantilever. The actuation is based on the induced Laplace electromagnetic force due to the coupling between the perpendicular magnetic field created by the magnet allocated on the



chip basis and the electrical current passing through the coil patterned on the top surface of the  $\mu$ -cantilever. In order to detect the cantilever oscillation, semiconductor strain gauges are implanted at the surface of the microstructures which are arranged in half Wheatstone bridge configuration. A first gauge is located where the stresses are maximum (the clamped end of the beam) whereas the other is used as reference on the rigid substrate (Figure 3.2.b).

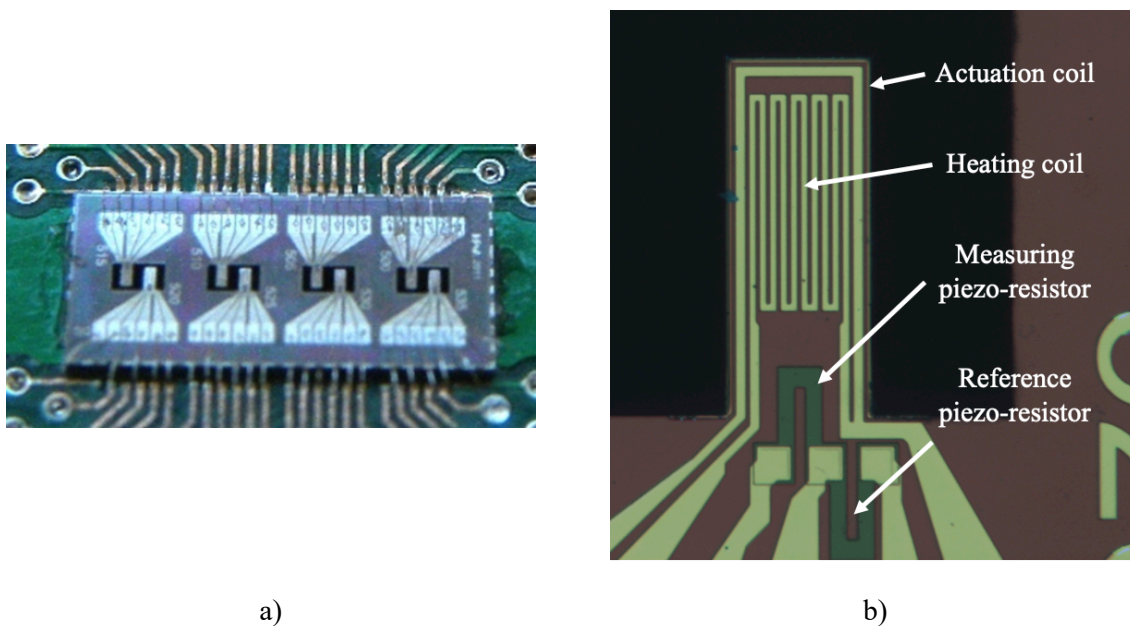


Figure 3.2: a) Chip containing 8 unfunctionalized microcantilever. b) Detail of one of the unfunctionalized microcantilevers.

### 3. 3. 2. MATERIAL DEPOSITION

---

The Si  $\mu$ -cantilevers have been coated with the tested materials by evaporative microdropping technique [149]. An ethanolic dispersion of each material (4 %<sub>w/v</sub>) is spread on the  $\mu$ -cantilever top surface using piezodriven inkjet printing technology (MD-E-201H, Microdrop Technologies). For a proper control of the sensing material location over the Si transducer, the instantaneous solvent evaporation is induced during the dispersing process by means of the meander-type heating resistor. This integrated heater is also used at the end of the programmed measurement sequences for a proper degassing of the sensitive material to ensure the full recovery of the sorption capabilities. Thus, the regeneration cycles, leading to average temperature values on the beam circa 160 °C and kept for 15 min have been systematically applied for a reliable and reproducible operation. Consequently, the sensor's response has been normalized

per mass of sensing material for a proper comparison. The Table 3.1 compiles the main characteristics of the coated  $\mu$ -cantilevers: natural resonant frequency after coating ( $f_0$ ), mass sensitivity ( $S$ ) and mass loading. Figure 3.3 shows a representative compilation of some of the functionalized  $\mu$ -cantilevers. It can be seen that the sensitive materials have been preferentially deposited on the tip of the cantilever, where the displacement of the beam is maximum. Mass loading ranges from 72 to 534 ng due to the differences in bulk density, polarity, hydrophobicity of the sensing materials. In order to perform a proper comparison, the response of the sensor is commonly normalized.

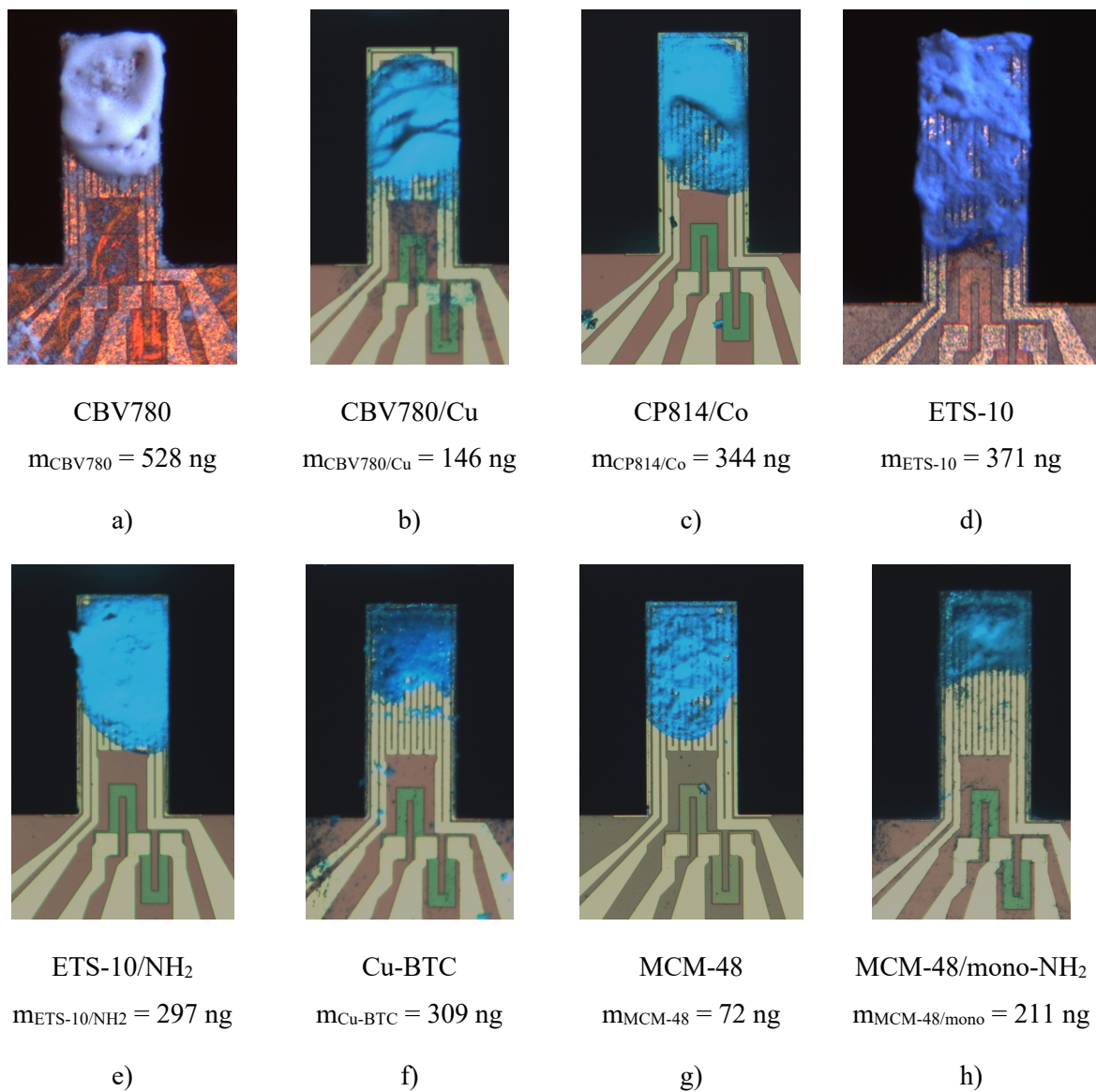


Figure 3.3. Optical image of the functionalized  $\mu$ -cantilevers used in this work: a) CBV780, b) CBV780/Cu, c) CP814/Co, d) ETS-10, e) ETS-10/ $\text{NH}_2$ , f) Cu-BTC, g) MCM-48 and h) MCM-48/mono- $\text{NH}_2$ .

TABLE 3.1. MAIN CHARACTERISTICS OF THE COATED  $\mu$ -CANTILEVERS

Coating		$f_0$ (Hz)	S (Hz/ng)	Coating loading (ng)
Zeolitic materials	CBV780/Cu	71 340	17.69	146
	CP814E/Fe	78 170	19.31	168
Titanosilicates	ETS-10	62 000	16.24	371
	ETS-10*	60 300	16.71	534
	ETS-10/NH <sub>2</sub>	65 170	17.19	297
	ETS-10/IGPTS	69 520	18.21	332
MOF	Cu-BTC (Basolite C-300)	69 700	16.71	309
Mesoporous silica materials	MCM-41	75 510	19.90	243
	MCM-48	73 800	18.21	72
	MCM-48/1·NH <sub>2</sub>	67 060	17.69	211
	MCM-48/2·NH <sub>2</sub>	64 500	17.19	290
	MCM-48/3·NH <sub>2</sub>	73 110	18.75	179
	SBA-15	63 100	16.71	313
Polymeric films	TENAX	75 440	18.21	123

### 3.3.3. EXPERIMENTAL SET-UP FOR GAS SENSING MEASUREMENTS

#### 3.3.3.1. Gas chamber

The Si array comprising 4  $\mu$ -cantilever pairs is firstly assembled on a PCB. Afterwards, it is placed in a custom sensor chamber made of Teflon or aluminium with circa 1 mL of free volume (**¡Error! No se encuentra el origen de la referencia..a**). The main gas inlet is distributed to four individual microchannels that deliver the gas stream to each  $\mu$ -cantilever pair. Thus,

a crossflow through the cantilever is ensured to maximize the interaction of the sample with the sensing elements. This gas-solid contact-mode configuration aims to reduce mass transfer limitations in the sorption process of target molecules present at trace level (Figure 3.4.b).8

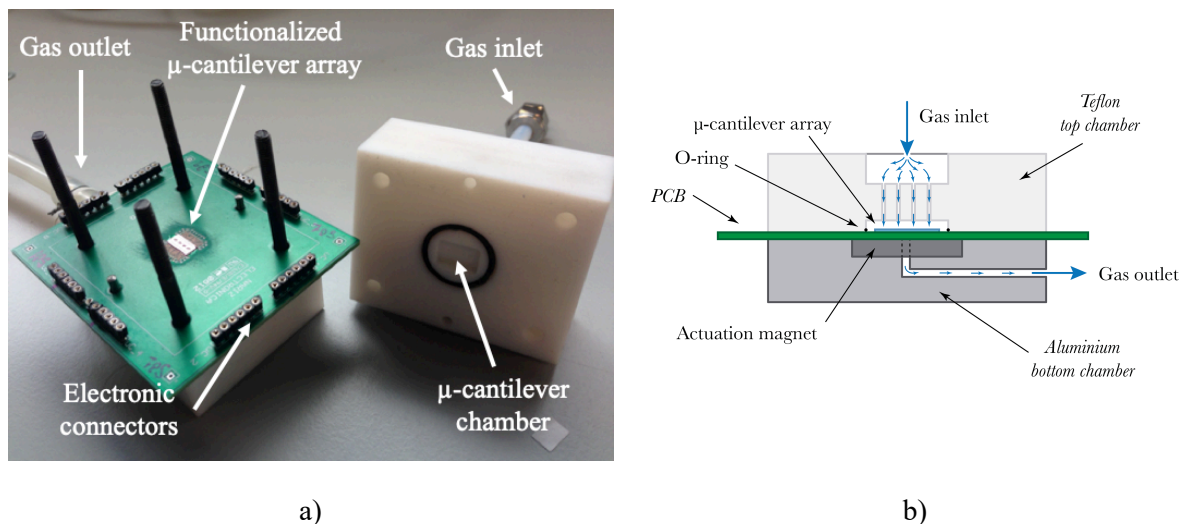


Figure 3.4. a)  $\mu$ -cantileveres gas chamber fabricated in Teflon. Below the  $\mu$ -cantilever array is place the magnets for actuate the beams. b) cross-section of the gas chamber.

### 3. 3. 3. 2. Electronic read-out system

A low-power electronic read-out interface capable to actuate and measure in parallel 4 functionalized  $\mu$ -cantilever output signals with a precision up to 20 mHz has been developed *ad hoc* for the cantilevers herein presented (Figure 3.5). The proposed platform is power through universal serial bus (USB) connected to a host computer and comprised three main blocks: 1) a power supply that generates the DC levels required by both the gas sensor and the electronic interface, 2) a read-out system based on a compact lock-in amplifier (LIA) and 3) a microcontroller that manages the system operation: DC excitation for the piezo-resistors, AC current bias for the actuating coil, system temperature control, frequency selection for the lock-in signals, LIA output reading and host computer communications [165]. Specific software has been also developed as a Matlab (MathWorks) implementation to characterize the natural resonant frequency of each  $\mu$ -cantilever as well as continuously monitoring the shifts of frequency's oscillation with four simultaneous  $\mu$ -cantilevers.

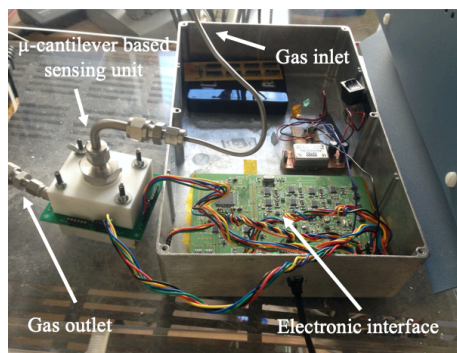


Figure 3.5.  $\mu$ -cantilever gas sensor connected with the electronic interface, which is used for both actuating and reading-out the functionalized  $\mu$ -cantilevers.

### 3. 3. 3. 3. Generation of explosives traces in vapor phase

The materials were evaluated for 1-mehtyl-2-nitrobenzene (o-MNT) adsorption to verify the promoted sorption properties, since this compound is recognized by the International Civil Aviation Organization as taggant for plastic bonded explosives. To generate, atmospheres containing trace-levels of the taggant, dry  $N_2$  (99.999%) was bubbled at set flow rates through saturation trains kept at controlled temperature and further  $N_2$  dilution. Considering that the liquids and gas phase of the analyte is in equilibrium and saturated inside the bubbler, the partial pressure of the liquid analyte was calculated by the Antoine equation:

$$p_v = e^{A - \frac{B}{T+C}} \quad (19)$$

where  $p_v$  is the partial pressure (mm Hg),  $T$  is the temperature of the analyte (K) and A, B, C are empirical parameters for each compound. For o-MNT:  $A = 19.0$ ,  $B = 6124.8$ ,  $C = 0$ ; whereas for water:  $A = 18.3$ ,  $B = 3816.4$ ,  $C = -46.1$ . Maximum concentration levels were  $140 \text{ mg/m}^3$  (25 ppmV) for o-MNT and  $7362 \text{ mg/m}^3$  (10000 ppmV) for water ( $\sim 30\%$  RH at 298 K) in 80 STP  $\text{cm}^3/\text{min}$  of  $N_2$  are obtained. For experiments at lower concentration, an additional dilution stream with dry  $N_2$  was added downstream the bubbler (Figure 3.6). The functionalized  $\mu$ -cantilevers were exposed to two consecutive o-MNT exposition at 80 mL/min from 5 min to 10 min with a sweeping of dry  $N_2$  at 80 mL/min from 5 to 10 min in between to provoke the analyte desorption from the sensitive layer. Before each sensing cycle, the sensitive materials were regenerated for 15 min under dry  $N_2$  using the integrated heating coil.

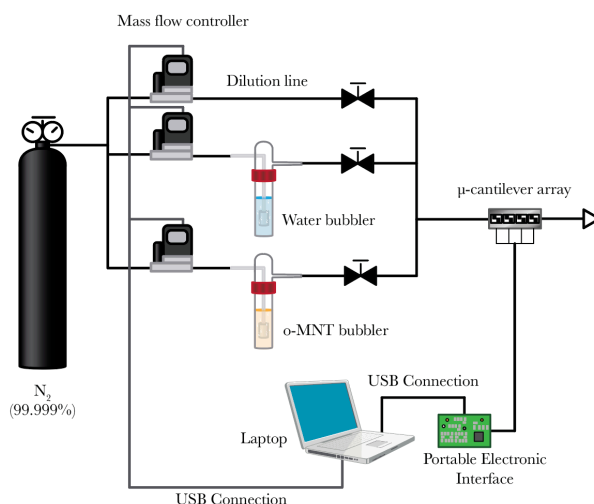
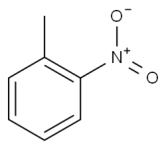
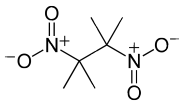
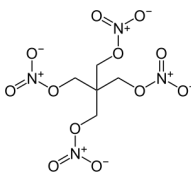
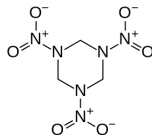


Figure 3.6. Experimental set-up for  $o$ -MNT/ $N_2$ ,  $H_2O$ / $N_2$  and  $o$ -MNT/ $H_2O$ / $N_2$  mixtures.

To validate the viability of explosive detection using the proposed material, experiments have been performed with two explosives widely used in both military and civil applications: detonation cord and C-4. Detonation cord are thin, flexible plastic tubes filled with pentaerythritol tetranitrate PETN (>98 %), with a relative effectiveness RE factor referred to TNT of 1.66. The C-4 is a common plastic explosive composed of 91% of cyclonite (or hexogen, RDX), 5.3% plasticiser (commonly diethylhexyl or dioctyl sebacate), 2.1% binder (polyisobutylene) and 1.6% SAE 10 non-detergent motor oil. Along with the actual explosives, two additional compounds have been tested: the explosive taggant 2,3-dimethyl-2,3-dinitrobutane (DMDNB) and a paraffin wax. These materials are also present in most common explosives' formulations. Particularly, DMDNB is an explosive marker, which is commonly found at 0.5 to 1.0% level in plastic bonded explosives. Incorporation of DMDNB is compulsory for ordnance factories in many countries, thus, it is an indicative of explosive material. The main properties of the analytes tested are summarized on Table 3.2. There are compiled the chemical name and formula, the molecular structure, molecular weight, vapor pressure at room temperature (298 K), melting point and decomposition temperature.

TABLE 3.2. PROPERTIES OF THE EXPLOSIVE RELATED COMPOUNDS TESTED

	o-MNT	DMDNB	PETN	RDX
Chemical name	1-methyl-2-nitrobenzene	2,3-dimethyl-2,3-dinitrobutane	pentaerythritol tetranitrate	1,3,5-trinitroperhydro-1,3,5-triazine
Formula	C <sub>7</sub> H <sub>7</sub> NO <sub>2</sub>	C <sub>6</sub> H <sub>12</sub> N <sub>2</sub> O <sub>4</sub>	C <sub>5</sub> H <sub>8</sub> N <sub>4</sub> O <sub>12</sub>	C <sub>3</sub> H <sub>6</sub> N <sub>6</sub> O <sub>6</sub>
Molecular structure				
Molecular weight	137.14 g/mol	167.17 g/mol	316.14 g/mol	222.12 g/mol
Vapor pressure @ 298 K	1 517 Pa	0.28 Pa	$1.9 \times 10^{-6}$ Pa	$6.3 \times 10^{-7}$ Pa
Melting point	264 K	483 K	414 K	479 K
Decomposition temperature	543 K	490 K	423 K	490 K

Solid explosives detection was performed in the lab simulating real field conditions. A small amount of explosive (~500 mg) was placed in a hermetic glass container of 2.5 L. In order to avoid high humidity conditions, the bottom of the recipient was filled with a desiccant material (silica gel) (Figure 3.7.a). The challenging detection of explosives is further exacerbated by their inherently low vapor pressure:  $1.2 \times 10^{-8}$  Pa in the case of PETN and  $4.1 \times 10^{-9}$  Pa for RDX at room conditions. For the sensing experiments with real explosives, the solid samples were placed on a heating mat (RS Components) and heated up to 343 K to increase the generation of vapours emanating from the solids. Like currently available trace detection systems, the inlet sample contains the air from the vicinity of the soil. Sample collection is performed on the glass container with the aid of a micro air pump (Xavitech® AB), which pulls the sample into the sensor chamber. Using a  $\mu$ -pump (D200, RS Pro), the vapours were drag into the functionalized  $\mu$ -cantilevers chamber for 5 min at  $\sim 500$  STP cm<sup>3</sup>/min (Figure 3.7.b). Before and after each vapor injection, the chamber was flushed for 5 min with air, after being flushed through a humidity trap (containing zeolite 3A, Sigma Aldrich) to evacuate interferences and desorb the sensitive material. Before each experiment, the adsorbent material on each  $\mu$ -

cantilever was thermally regenerated under dry air for 15 min. As reference, it has also sampled the ambient air from the lab, whose humidity content is rather similar to the study in previous experiments. Naturally, working with complex environment, such as ambient air from a room, involves a great number of unknown factors difficult to identify, i.e., temperature, convection, CO<sub>2</sub>, VOCs... This blank assay allows us to have a baseline reference for each individual microsensor and correct the baseline.

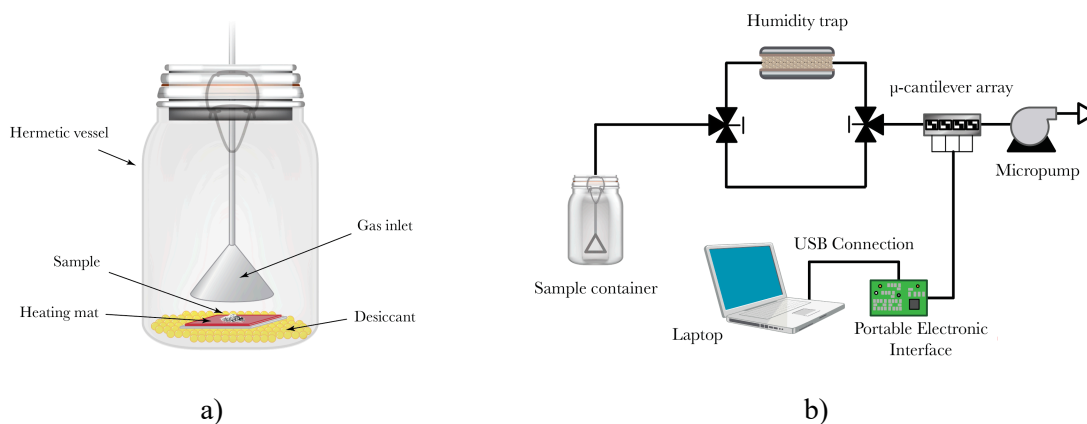


Figure 3.7. a) Sample hermetic container detail. b) Explosive sensing set-up.

### 3. 4. DETECTION OF O-MNT IN SYNTHETIC GAS MIXTURES

Our approach to detect and identify a possible threat is through the characteristic fingerprint that each analyte exhibits. A fingerprint is the combination of the distinctive responses that certain molecule provokes in an array of sensors. In our case, each of the eight  $\mu$ -cantilevers that comprises a chip is functionalized with a different material, which each of them interacts differently under the same stimulus. The combination of those signals is what we catalogue as fingerprint. This strategy acquires its true potential when it is not used only a chip of eight sensors, but when use tens of them coupled to artificial intelligence (AI) for data analysis, and thus having a precise fingerprint based on tens or hundreds of distinctive signals.

So far, the NanoFilms and Particles groups (NFP) has focused on the detection of VOCs and explosive-related compound using Si cantilevers coated with zeolitic materials. For VOCs compounds, detection limits below 3 mg/m<sup>3</sup> for both ethanol and toluene at room temperature have been achieved with 3000 x 200  $\mu$ m Si cantilevers coated with 9.96  $\mu$ g of protonated zeolite



Y (Zeolyst CBV400) [150]. Co-exchanges BEA zeolites have been used as sensitive adsorbents for explosive related compounds at room temperature and have been deposited on  $500 \times 350 \mu\text{m}$  Si cantilever reaching limits of detection for o-MNT down to  $6 \text{ mg/m}^3$  at room temperature [149]. Based on these results, we have continue exploring new families of materials for explosive related compound detection in order to stablish a wide and detailed materials. In this section, the characterization of the response towards the common explosive surrogate o-MNT of three materials families (titanosilicates, mesoporous silica materials and Cu-based metal-organic frameworks) is shown.

### 3. 4. 1. O-MNT DETECTION ON TITANOSILICATES MODIFIED $\mu$ -CANTILEVERS

---

The normalized frequency shift per unit of mass of the titanosilicate-functionalized  $\mu$ -cantilever array when they are exposed to two consecutive steps of gas mixtures of  $140 \text{ mg/m}^3$  o-MNT in dry  $\text{N}_2$  and  $7362 \text{ mg/m}^3$  water in dry  $\text{N}_2$  both at 298 K are shown in Figure 3.8. As it was expected, post-synthesis treatment alters the interaction of analyte and sorbent, thus it can be used to finely tune sorption capabilities of the material. Among the functionalization procedures, the amino grafting (ETS-10/ $\text{NH}_2$ ) and the Ti enrichment (ETS-10\*) lead to affinity enhancement towards o-MNT compared to pristine ETS-10 (0.20 and 0.19 Hz/ng for ETS-10/ $\text{NH}_2$  and ETS-10\* respectively vs 0.08 Hz/ng for ETS10 at first o-MNT step). The sorption capability of amino grafted sample is 2.6-fold higher than the exhibit by bare titanosilicate ( $13 \text{ mg/g}$  vs  $5 \text{ mg/g}$ , ETS-10/ $\text{NH}_2$  vs ETS-10). This behaviour is explained on the basis of the electron deficient character of the nitroaromatic explosive, and the electron donor properties of grafted amine groups [166], [167]. A similar effect, although less notorious, is observed for the Ti enriched coating (ETS-10\*). The basic properties promotion leads to charge transfer from  $\text{Ti}^{4+}$  to the aromatic ring and electron-withdrawing nitro roup. In this case, the mass gain of ETS-10\* is  $9 \text{ mg/g}$ , whereas pristine ETS-10 is  $5 \text{ \%}_{\text{wt}}$ .

On the other hand, the imidazole grafted sample, ETS-10/IGPTS, is less-sensitive towards o-MNT ( $0.06 \text{ Hz/ng}$  for ETS-10/IGPTS vs  $0.08 \text{ Hz/ng}$  for ETS-10). This fact is attributed to its extremely high functionalization degree (up to  $8.4 \text{ mmol}$  of grafted organosilane per unit mass of ETS-10). As we presented on Chapter II, the volume of micropores in pristine ETS-10 sample (which is about 78% of total pore volume) becomes negligible after imidazole grafting ( $V_{\text{pore}} = 0.08 \text{ cm}^3/\text{g}$  for ETS-10/IGPTS vs  $V_{\text{pore}} = 0.17 \text{ cm}^3/\text{g}$  for ETS-10). We can assume that much of the micropores volume has been clogged by the hydrated organosilane molecules

grafted on the external surface of the crystals. This bulky network hinders the diffusion of target analytes through the ETS-10. Among the tested, EST-10/NH<sub>2</sub> represents the optimal trade-off between external surface modification and exposed volume of micropores. Furthermore, the response recovery of ETS-10/NH<sub>2</sub> after flushing with N<sub>2</sub> is the less pronounced. In regard of response time ( $t_{response}$ ), clearly pristine ETS-10 exhibits faster response, mainly due to its higher surface area (316 m<sup>2</sup>/g) which involves an easy access of o-MNT molecules inside de structure. However, all material but ETS-10/IGPTS present response times under 80 s.

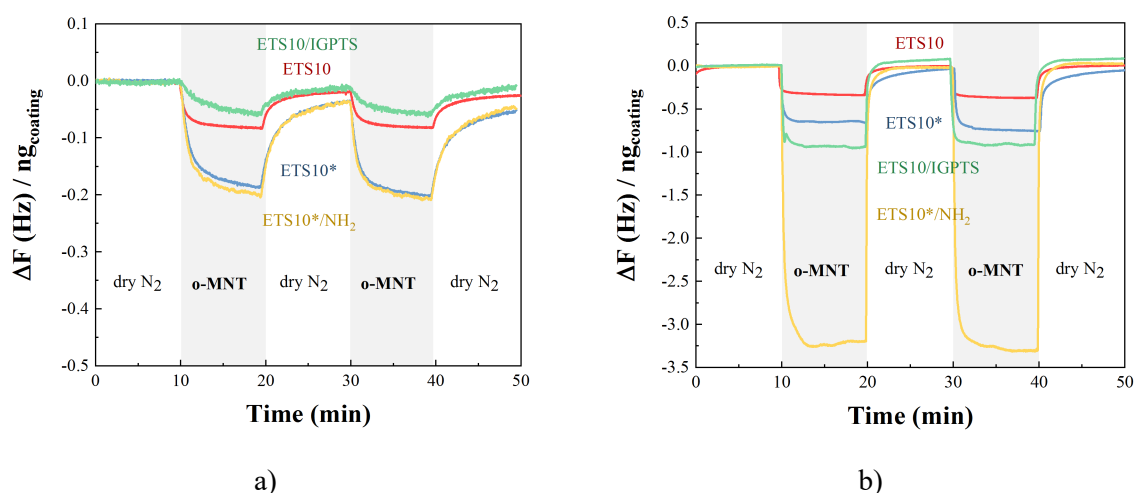


Figure 3.8. Evolution of the resonance frequency shift of the ETS-10 (red), ETS-10\* (blue), ETS-10/NH<sub>2</sub> (yellow) and ETS-10/IGPTS (green) functionalized  $\mu$ -cantilevers in presence of a) 140 mg/m<sup>3</sup> o-MNT and b) 7362 mg/m<sup>2</sup> water.

The water sorption on ETS-10 nanoporous coatings has also been analysed, due to the unavoidable presence of humidity as interference (Figure 3.8.b). We have considered around 30 % relative humidity at 298 K, which corresponds to 7632 mg/m<sup>3</sup> of water in dry N<sub>2</sub>. It is found that all the post-synthesis treatments increase the water uptake (3.20, 0.90 and 0.65 Hz/ng for ETS-10/IGPTS, ETS-10/NH<sub>2</sub> and ETS-10\* respectively vs 0.33 Hz/ng for ETS-10). However, this effect is quite remarkable for amino-grafted and imidazole-grafted samples in agreement with the intrinsic properties of the coupled organosilanes. Especially noticeable is the behaviour of ETS-10/IGPTS. Water uptake in that case increases from 18 mg/g in pristine material to 173 mg/g in the functionalized. Such hydrophilicity is explained by the hydrogen bonding network provided by the organosilane molecules anchored to the crystal surface.

3. 4. 2. o-MNT DETECTION ON MESOPOROUS SILICA MODIFIED  $\mu$ -CANTILEVERS

Pseudo equilibrium nitroaromatic adsorption has been evaluated for three mesoporous materials families: MCM-41, MCM-48 and SBA-15. Additionally, it has been also evaluated the sorption properties after modification by grafting amino groups through organic ligands. Three different o-MNT concentrations have been tested: 3, 6 and 140  $\text{mg}/\text{m}^3$ .

The pristine MCM-48 clearly outstands among mesoporous materials, with a o-MNT mass adsorbed at 140  $\text{mg}/\text{m}^3$  7-fold higher than SBA-15 and 20-fold than MCM-41 ( $m_{\text{oMNT, MCM48}} = 485 \text{ mg/g}$ ,  $m_{\text{oMNT, SBA15}} = 68 \text{ mg/g}$  and  $m_{\text{oMNT, MCM41}} = 24 \text{ mg/g}$ ) (Figure 3.9.a). As feeding o-MNT concentration lowers, the difference among mass adsorbed between MCM-48 and SBA-15 diminishes, though the first one is still outperforming the last ( $m_{\text{oMNT, MCM48}} = 89 \text{ mg/g}$  vs  $m_{\text{oMNT, SBA15}} = 33 \text{ mg/g}$  @ 6  $\text{mg}/\text{m}^3$  o-MNT and  $m_{\text{oMNT, MCM48}} = 54 \text{ mg/g}$  vs  $m_{\text{oMNT, SBA15}} = 22 \text{ mg/g}$  @ 3  $\text{mg}/\text{m}^3$  o-MNT).

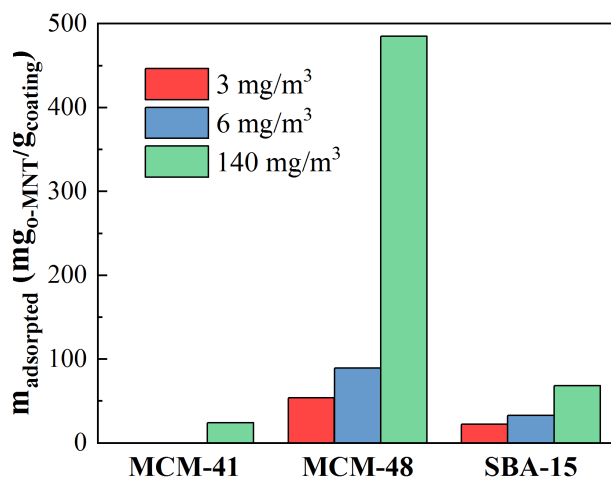


Figure 3.9. a) Pseudo equilibrium o-MNT adsorption results of the three mesoporous families tested at 3 (red bars), 6 (blue bars) and 140  $\text{mg}/\text{m}^3$  o-MNT (green bars).

Three different amino grafting functionalization were tested: with one (MCM-48/ $\text{NH}_2$ ), two (MCM-48/2 $\cdot\text{NH}_2$ ) and three (MCM-48/3 $\cdot\text{NH}_2$ ) amino groups per organosilane molecules respectively. As can be seen on Figure 3.10.a, contrary to our expectations, amino functionalization did not improve o-MNT adsorption, in fact, the sensor's response decrease on functionalized MCM-48. After first o-MNT step, MCM-48 exhibits a normalized frequency shift of

8.04 Hz/ng that decreased to 1.29 Hz/ng for MCM-48/2·NH<sub>2</sub> and MCM-48/3·NH<sub>2</sub> and 0.29 Hz/ng for MCM-48/NH<sub>2</sub>. That is, functionalized materials with two and three amino groups trapped 7-fold less than pristine MCM-48 at 140 mg/m<sup>3</sup> o-MNT at 298 K ( $m_{\text{oMNT, MCM48/2NH}_2} = 79$  mg/g and  $m_{\text{oMNT, MCM48/3NH}_2} = 68$  mg/g @ 140 mg/m<sup>3</sup> o-MNT). Also, it is noticeable the different sorption properties between functionalization with one or two amino groups, increasing o-MNT sorption even with smaller pore size and surface area of the latest one ( $m_{\text{oMNT, MCM/NH}_2} = 17$  mg/g vs  $m_{\text{oMNT, MCM/2NH}_2} = 79$  mg/g @ 140 mg/m<sup>3</sup>, while  $S_{\text{MCM/NH}_2} = 1072$  m<sup>2</sup>/g and  $S_{\text{MCM/2NH}_2} = 698$ ). On the contrary, not much difference can be seen on the one with two or three amino groups, mostly due to having both of the them, the same amount on amino terminals although coordinated differently ( $m_{\text{NH}_2, \text{MCM/2NH}_2} = 4.44$  mmol/g and  $m_{\text{NH}_2, \text{MCM/3NH}_2} = 4.45$  mmol/g). Normalizing the o-MNT mass adsorbed with the pore volume (Figure 3.10.b) we can observed that MCM-48/3·NH<sub>2</sub> surpasses MCM-48/2·NH<sub>3</sub> and its able to adsorb 1.5-fold more o-MNT molecules. On the other hand, MCM-48 even having the higher pore volume, after normalization, the differences between it and the MCM-48/3·NH<sub>2</sub> are not as accused as before, as a consequence of the adsorption of o-MNT on the walls of the mesoporous material and not occupying the whole pore volume.

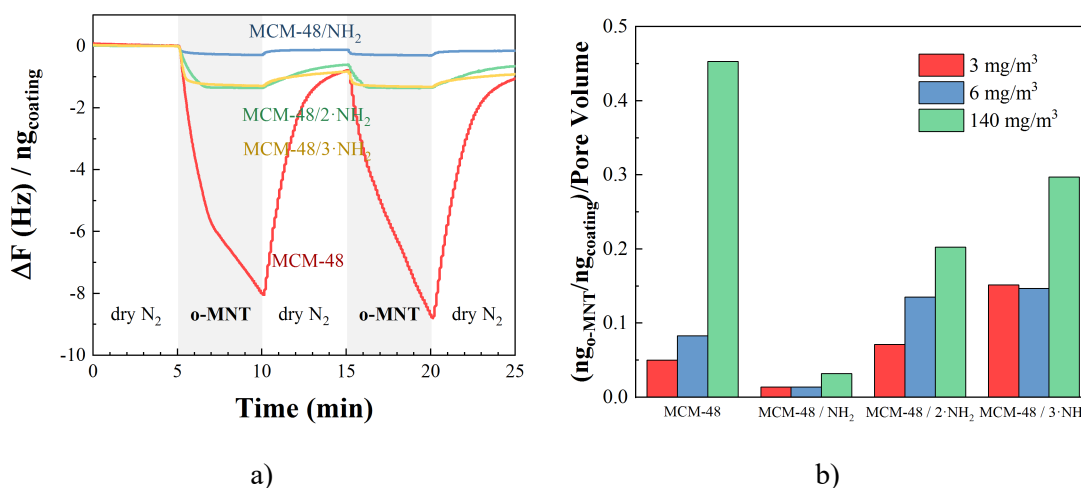


Figure 3.10. a) Evolution of resonance frequency of pristine and amino-functionalized MCM-48 after being expose to two consecutive 140 mg/m<sup>3</sup> o-MNT in dry N<sub>2</sub> steps at 298K: MCM-48 (red), MCM-48/NH<sub>2</sub> (blue), MCM-48/2·NH<sub>2</sub> (green) and MCM-48/3·NH<sub>2</sub> (yellow). b)

Finally, it has been analyzed the influence of ambient humidity (RH 30 % at 298 K) in o-MNT adsorption for MCM-48. The material has been exposed to 56 mg/m<sup>3</sup> o-MNT in dry N<sub>2</sub>, afterwards to 7362 mg/m<sup>3</sup> water in dry N<sub>2</sub> and finally to a mixture of both vapours (56 mg/m<sup>3</sup>

o-MNT and  $7362 \text{ mg/m}^3$  water in dry  $\text{N}_2$ ). The experiments have been performed at three temperatures to observe the strength of interaction: 298 K, 313 K and 333 K. Between each experiment the material has been regenerated for 15 min at 423 K in dry  $\text{N}_2$  using the integrated heater in the  $\mu$ -cantilever.

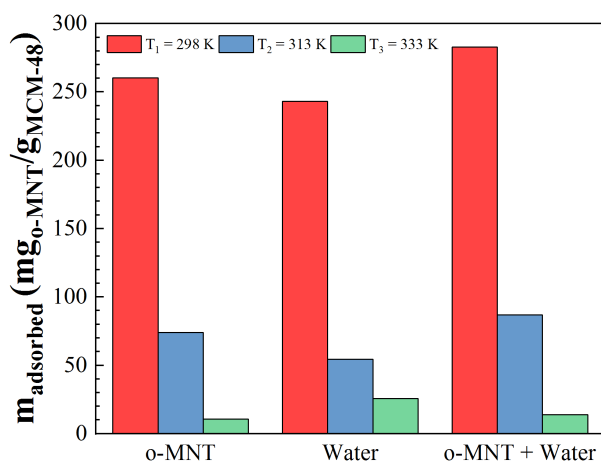


Figure 3.11. o-MNT, water and o-MNT + water adsorption on MCM-48 coated  $\mu$ -cantilevers at 298 K (red bar), 313 K (blue bar) and 333 K (green bar).

As we can see in Figure 3.11, with the increase of the temperature, the mass uptake of each analyte clearly diminishes. In the case of the o-MNT, falling from 260 mg/g at 298 K to 11 mg/g at 333 K, whereas for water is from 243 mg/g to 26 mg/g. We can see, thus, at low temperatures, MCM-48 presents more affinity towards o-MNT than water than at higher temperatures. Regarding the co-adsorption of o-MNT in the presence of humidity, we can see an increase in the mass adsorbed (from 260 mg/g for pure o-MNT to 283 mg/g) indicating that both species are competing for the same active sites, although we cannot assure which one is the most preferential adsorbed. At high temperatures, we observed that the mass uptake is also inferior than at low temperatures, falling down to 14 mg/g.

### 3. 4. 3. O-MNT DETECTION ON METAL-ORGANIC FRAMEWORKS MODIFIED $\mu$ -CANTILEVERS

Nitro-related compounds adsorption properties for metal organic frameworks has been explored by coating  $\mu$ -cantilevers with Basolite C-300 (Sigma Aldrich), the commercial counterpart of Cu-BTC. The MOF-functionalized  $\mu$ -cantilever was exposed to  $140 \text{ mg/m}^3$  o-MNT

in dry  $N_2$  at 298 K, previously degassed for 10 min in dry  $N_2$  using the integrated heating coil in the sensor. To assess reproducibility of the sensor, the same experiment was repeated three times with intermediate thermal regeneration step and cantilever characterization between after each measurement.

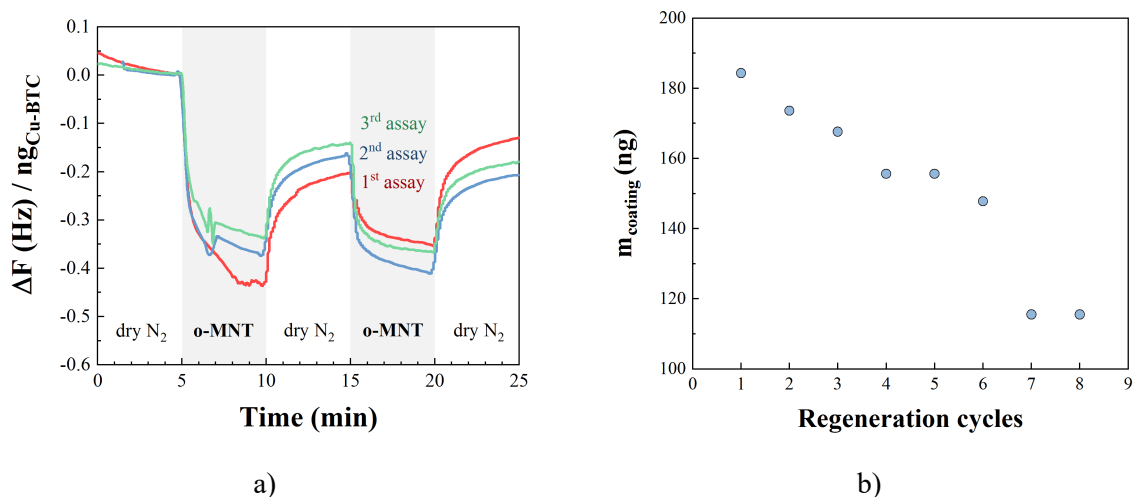


Figure 3.12. a) Evolution of resonance frequency of Cu-BTC-functionalized  $\mu$ -cantilevers when they are exposed to  $140 \text{ mg/m}^3$  o-MNT in dry  $N_2$  at 298 K. The material has been exposed for three consecutive cycles with a heating regeneration step of 10 min in dry  $N_2$  between each cycle. b) Evolution of Cu-BTC coating after 8 regeneration cycles. The experiments with o-MNT were performed during the first 3 cycles.

Figure 3.12.a shows the normalized resonant frequency shift per mass of Cu-BTC of the three consecutive cycles. From the first assay we can observe that o-MNT strongly interacts with Cu-BTC, after the first exposure step, the sorption capacity of the MOF is up to 25 mg/g. The strength of the interaction is such that the material cannot be regenerated just by sweeping dry  $N_2$  at room temperature. As we discussed in Chapter II, the presence of  $Cu^{2+}$  ions in the framework promote the preferential sorption of electrophilic nitro-compounds, due to the charge transfer from the ion to the aromatic ring and the nitro group. After regeneration the adsorbent, we can see a decreased in the normalized resonant frequency signal, which drops from 0.43 Hz/ng to 0.33 Hz/ng after the first exposure of the third assay. That is, sorption capacity of Cu-BTC has been diminished from 25 mg/g to 20 mg/g indicating the framework stability has been compromised, although still retaining some of its active sites accessible. Thus, it has been evaluated the thermal stability of Cu-BTC at regenerating conditions ( $T = 423 \text{ K}$ ,  $t = 10 \text{ min}$  under dry  $N_2$ ) (Figure 3.12.b). After each regeneration, it has been observed a decrease in the deposited mass, from 184 ng to 115 ng, which assesses the collapsing of the

material. Although the regeneration of the material is being performed at a temperature below decomposition temperature ( $T_d = 550$  K), the material still exhibits effects of thermal stress.

### 3. 5. EXPLOSIVE ADSORPTION IN SIMULATED ENVIRONMENT

Explosives detection in simulated environments was carried out as a proof of concept on how a real hand-held device would operate in the field, just like commercial detection systems. Since the  $\mu$ -cantilever array is comprised of eight beams, we selected eight materials that behave notably different when exposed to explosive vapours. In order to get a unique fingerprint of each explosive, the more diverse the response is, the better the recognition would be. For these experiments four titanosilicates (ETS-10, ETS-10\*, ETS-10/NH<sub>2</sub> and ETS-10/IGPTS), two functionalized zeolites (CBV780/Cu and CP814E/Fe), a commercial MOF (Basolite C300, Sigma Aldrich) and commercial resin type sorbent (TENAX TA, Sigma Aldrich) were studied.

The experiments were performed firstly by sweeping dry air (pump from the room and dried with water trap filled with zeolite 3A) for 5 min, in order to get a stable resonance frequency. Afterwards, air was sampling from the glass container where the explosive is placed for other 5 min. In this step, the water trap is bypassed and the whole air sample is circulated towards the  $\mu$ -cantilevers array. Finally, a flush of dried air allows the  $\mu$ -cantilevers to recover the baseline signal. Prior to the sensing, all the materials on the  $\mu$ -cantilevers are degassed for 15 min at  $\sim 150$  °C under dried air. As reference, it has also sampled the ambient air from the lab, whose humidity content is rather similar to the study in previous experiments. Naturally, working with complex environment, such as ambient air from a room, implies a great number of factors, such as temperature, convective streamlines, CO<sub>2</sub>, VOCs content, which are influencing the sensor response. This blank assay allows us to have a baseline reference for each individual microsensors.

Figure 3.13 shows the normalized response (frequency shift per adsorbent mass unit) of the 8 functionalized  $\mu$ -cantilevers array when exposed to ambient air from the lab, used as reference. A distinctive response of each cantilever to the same stimulus is observed, from cantilever with barely any frequency shift (TENAX) to noticeable response (Cu-BTC). This behaviour can be attributed to the level of humidity of the ambient air and thus the distinctive hydrophobic character of the sensing materials (RH 30 %). Thanks to this blank assay, the reference

for each individual microsensors is established and conveniently used to discard potential interferences from the background.

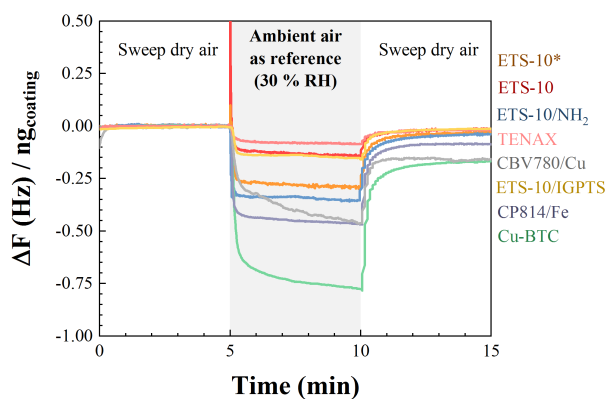


Figure 3.13. Sensor response to ambient air interferences, used as a baseline reference. Functionalized  $\mu$ -cantilevers: ETS-10 (red), ETS-10\* (orange), ETS-10/NH<sub>2</sub> (blue), ETS-10/IGPTS (yellow), Cu-BTC (green), CBV780/Cu (gray) and CP814/Fe (purple).

Similarly, Figure 3.14 shows the responses of the vapours emanating from the taggant (DMDNB), a common interferent (coating wax) and the two explosives (PETN and RDX) when they are heated at 343 K. It can be observed that the most predominant signal is the Cu-BTC, both for nitro-compounds (DMDNB, PETN and RDX) as for the interferent (coating wax). On the first case, that can be correlated to the presence interaction of the Cu cluster with the nitro group (particularly for the DMDNB, where the frequency shift is significant) whereas for the coating wax, that may be attributed to the inherent humidity of gas sample. It is noticeable, that ETS-10/NH<sub>2</sub> exhibit one of the most outstanding performance for solid explosives, but not for the taggant. In the case of the explosives, this behaviour matches with the presence of the 4 and 3 electron-withdrawing nitro groups (PETN and RDX) but is surprisingly that this does not correlate with the 2 nitro-groups that exhibit DMDNB. When comparing with the blank assay results (Figure 3.13), the response of ETS-10/IGPTS and CBV780/Cu towards PETN seems quite similar, although, the response to DMDNB or RDX are smaller than the baseline. This behaviour could be explained by the hygroscopic character of some explosives. Thus, RDX would behave as a desiccant during the sample collection step. Above all, it should be considered that the tested explosives are essentially a complex mixture where plastifiers and binders are commonly present. These additives, with substantial vapour pressure, may act as interferences in the recognition of the explosive materials.



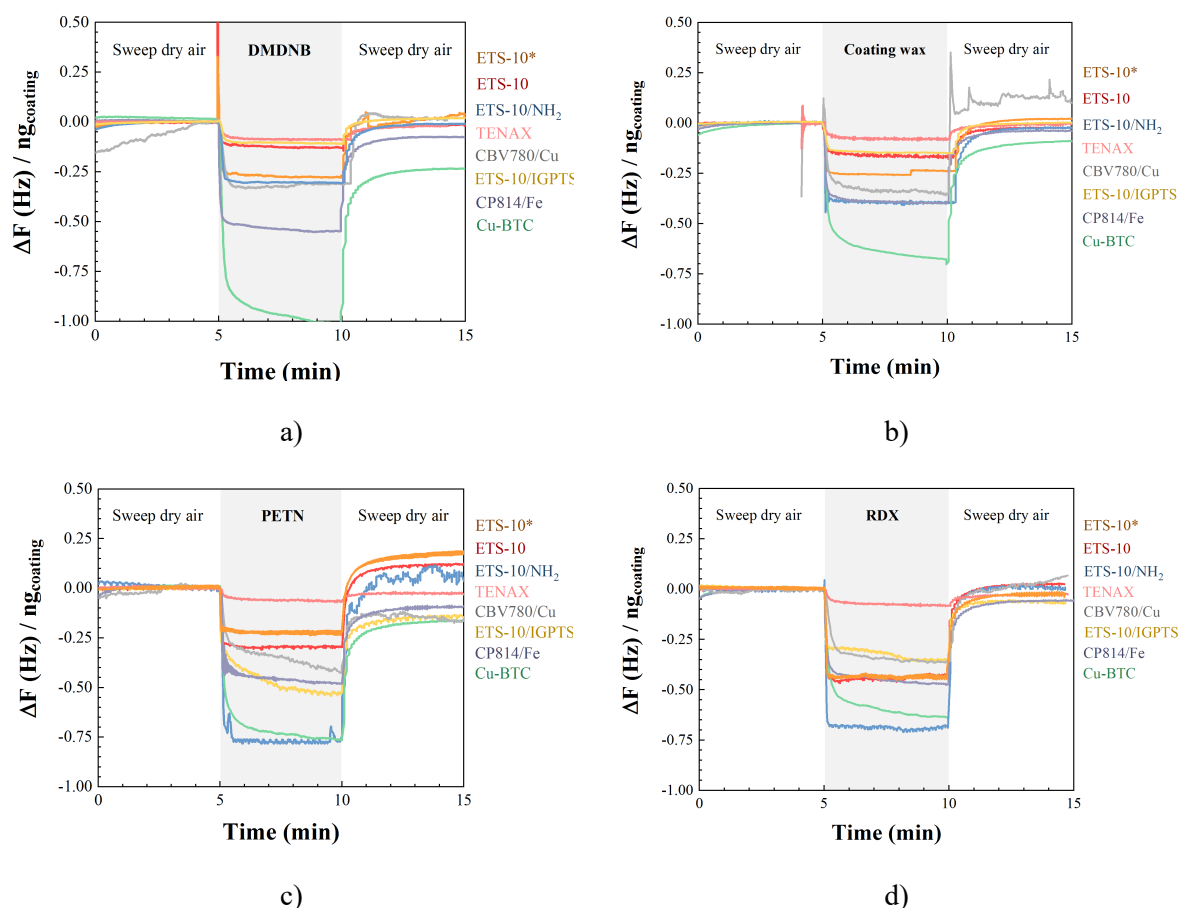


Figure 3.14. Fingerprints of a) DMDNB, b) coating wax, c) PETN and d) RDX. Functionalized  $\mu$ -cantilevers: ETS-10 (red), ETS-10\* (orange), ETS-10/NH<sub>2</sub> (blue), ETS-10/IGPTS (yellow), Cu-BTC (green), CBV780/Cu (gray) and CP814/Fe (purple).

Table 3.3 compiles the results obtained after analysing the vapours emanating from the taggant, the two explosives (PETN and C-4) and the wax with the functionalized  $\mu$ -cantilevers. As before, it has calculated the pseudo-equilibrium mass gained per unit of coating ( $Y_{eq} = ng_{adsorbed}/ng_{coating} \%$ ) (20) and the reaction time  $t_{response}$ , calculated as the time needed to reach 90 % of the stable signal value.

$$Y = Y_{eq} \left( 1 - e^{-\frac{t}{t_1}} \right) \quad (20)$$

The evaluated  $t_{response}$  for the taggant compound are below 1 min for all the evaluated cantilevers. In the case of explosive compounds, this value is even lower some of the cantilevers, reaching some of them values down to 10 s (ETS-10, ETS-10, ETS-10/NH<sub>2</sub>). This behaviour is due to the high flow rate (at  $\sim 500$  STP cm<sup>3</sup>/min) which increases the amount of analyte feed to the detector, as well as the solid heating at 343 K that increases the vapour pressure of

the molecules eluted from the tested materials. In spite of the huge differences in vapour pressure of DMDNB, PETN and RDX species (Table 3.2) the pseudo-equilibrium sorption values for real solid explosives are, in general, higher than for taggant (Cu-BTC exhibits the opposite behaviour). In fact, what it may be recognizing is not explosive related molecules, but concomitant additives (as observed on the coating wax pseudo-equilibrium values). From results herein obtained, it is difficult to establish a direct correlation among the concentration of the explosive compound and the  $Y_{eq}$  and  $t_{response}$  parameters. For such purposes, a comprehensive characterization of the multisensing platform as a function of the solid temperature during sample collection would be required.

TABLE 3.3. SENSING PERFORMANCE OF MODIFIED  $\mu$ -CANTILEVERS FOR DMDNB, PETN, RDX AND WAX

	DMDNB		PETN		C-4		Coating wax	
	$Y_{eq}$ %	$t_{response}$ s	$Y_{eq}$ %	$t_{response}$ s	$Y_{eq}$ %	$t_{response}$ s	$Y_{eq}$ %	$t_{response}$ s
ETS-10	0.7	47	1.8	4	2.6	6	1.0	30
ETS-10*	1.6	17	1.5	3	2.5	7	1.6	11
ETS-10/IGPTS	0.8	32	2.9	125	1.9	142	0.8	17
ETS-10/NH <sub>2</sub>	2.3	14	4.4	10	3.9	5	2.3	5
CBV780/Cu	1.8	20	2.4	203	2.0	56	2.0	71
CP814/Fe	2.8	16	2.5	37	2.5	27	2.1	23
Cu-BTC	6.0	62	4.5	58	3.8	70	4.0	74
TENAX	0.5	45	0.4	72	0.4	74	0.4	24

The previous experiments show the specific response of each  $\mu$ -cantilever upon the exposure to different species in gas phase. Although most of the results can be qualitatively explained on the bases of chemical interactions, some behaviours diverge from what it is expected due to the complexity of the explosive mixture. Since a detailed study of each single possible molecular interaction with certain species in the gas phase is unaffordable, our sensing approach deals with the analysis of the overall fingerprint.

For the purposes of this work, the  $\Delta F_{\text{adsorbed}}/\Delta F_{\text{background}}$  ratio is identified as the characteristic parameter of the sensor performance in complex mixtures. This value reflects the differential response due to the presence of additional extra species not present in the background (i.e. ambient air in the proximity of the solid compound). Figure 3.15 shows the calculated values for DMDNB, PETN, RDX and coating wax detection sequences. We can see that, ETS-10/ $\text{NH}_2$  reacts under the presence of real explosive, but not to the taggant; and the reverse behaviour is observed for the Cu-BTC. CP814/Fe on the other hand appears to react moderately to the presence of the nitro-related compounds but not to common interferences (coating wax). ETS-10, ETS-10\* and TENAX coatings present unexpected responses towards nitro-based compounds due to contribution of chemical interaction with the concomitant additives. In the case of hydrophilic ETS-10/IGPTS and CBV780/Cu coatings, the response seems to be highly conditioned by the hygroscopic character of the solids.

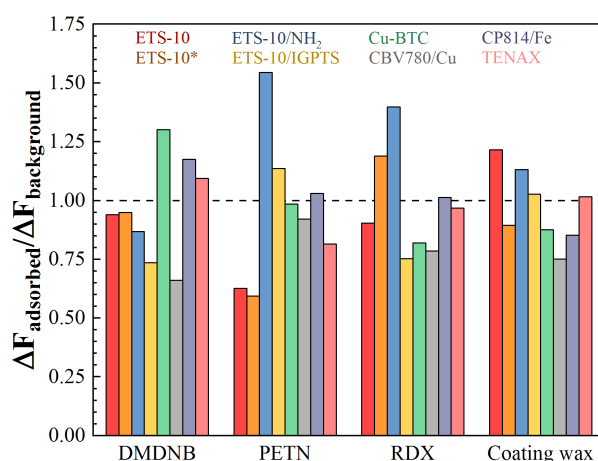


Figure 3.15. Differential responses of the functionalized  $\mu$ -cantilever array upon the exposure to vapours of DMDNB, PETN, C-4 and coating wax when they are heated at 343 K. Functionalized  $\mu$ -cantilevers: ETS-10 (red), ETS-10\* (orange), ETS-10/ $\text{NH}_2$  (blue), ETS-10/IGPTS (yellow), Cu-BTC (green), CBV780/Cu (gray) and CP814/Fe (purple).

Due to the fact that each sensing nanoporous material classifies the complex vapour phase according to sorbent-sorbate molecular interactions, it is not necessary to identify each one of the individual chemical species in the mixture. In our case, specific fingerprints have been obtained for three explosive related molecules with a multisensing platform comprising eight different  $\mu$ -cantilevers. Undoubtedly, this approach can be naturally extended to dozens of  $\mu$ -cantilevers for redundancy and reliability.

## 3. 6. CONCLUSIONS

In this Chapter we have presented a gas sensor array based on functionalized  $\mu$ -cantilevers that has been developed at the NFP in collaboration with the I3A and the IMB-CNM and tested its functionality to detect two nitro-related explosives compounds (PETN and C-4), an explosive taggant (DMDNB) and a common interferent found in plastic explosives (coating wax) in a simulated scenario.

The core of the detection and identification principle of our gas sensor is the use of a multiple array of functionalized cantilever. Each cantilever is coated with a micro- or mesoporous material that interacts uniquely with the target analyte. The combination of the different interactions under the same stimuli allow us to create a distinctive fingerprint of each compound that identifies it. In this work, we have incorporated three new families of micro- and mesoporous materials to the catalogue of sensitive adsorbents that has been building in the group: titanosilicates, mesoporous silica materials and metal-organic frameworks. Particularly, it has been incorporated adsorbents functionalized with amino-groups (ETS-10/NH<sub>2</sub> and MCM-48 with 1/2/3-amino-groups) as well as with imidazole-group (ETS-10/IGPTS) and with electron-donor metal ions (titanium enriched ETS-10 and the MOF Cu-BTC). These materials have been characterized for 140 mg/m<sup>3</sup> of nitro-related explosive surrogate o-MNT in dry conditions at room temperature (298 K) revealing uptakes up to 13 mg/g for titanosilicates (ETS-10/NH<sub>2</sub>), 25 mg/g for MOFs (Cu-BTC) and 485 mg/g for mesoporous silica materials (MCM-48).

Finally experiments with real compounds at ambient conditions reveals the true potential of our proposal. In despite of our efforts, the identification of explosives compounds has been found extremely difficult and misleading, particularly for plastic compounds, where the manufacturing process implies the use of unknown additives and binder that also interacts with our gas sensor and may masks the explosive compound. Furthermore, although for commercial explosives is mandatory to be marked with an established taggant which facilitates their identification, the main threat is non-commercial, improvised explosive devices (IED).

# **CHAPTER IV:**

## **FABRICATION OF SI-BASED $\mu$ -DEVICES**



## 4. FABRICATION OF SI-BASED $\mu$ DEVICES

### 4. 1. INTRODUCTION

In the previous chapter we have summarized the different materials that have arisen our interest in explosives and CWA adsorption and we have explored their potential as adsorbents by direct exposure with nitroaromatic and organophosphorus compounds. However, to fully exploit their particular characteristics in vapor preconcentration, we must integrate these materials in actual devices specifically designed for the purpose of this work. This Chapter is focused on the integration of the beforementioned materials into an *ad hoc* Si microdevice, as well as the fabrication of adjacent elements that are needed in order to obtain a functional  $\mu$ -preconcentrator.

Many authors have explored the benefits of materials such as active carbons, silica nanoparticles or polymer films for preconcentration of volatile organic compounds or explosive markers in gas phase [168] [169] [170]. There is not specific rule of thumb in the design of such microdevices and each group exhibit their own characteristic model.

The group of Zellers, for example, presented their first works [133] on VOC micropreconcentration VOC using as samplers thin-walled glass capillaries (inner diameter about 1.15 mm) of 7.5 cm in length, where 1 to 10 mg of material was introduced. The device was heated using a Pt wire connected to a PID controller that measures the outer temperature with a thermocouple wrapped around the tube. This system was improved by the incorporation of an additional preconcentration stage that sharpen the desorption peak, increasing greatly the concentration of the desorbed analyte. At first, this stage was held on a different Si substrate connected upstream the sampler that resembles the used in their earlier works [168] (Figure 4.1.a), although, later they improve the overall system by redesigning their devices into a preconcentrator/focuser (PCF) unit [171]. In order to promote the adsorption of the analyte into the adsorbent, the gas sample was dragged with a micropump into the sampler, where the gas contacted the adsorbent in a crossflow fashion. These “active” sampling devices were left behind in their later works, where the main focus lied on passive concentration, i.e., the analyte was not injected into the sampler, but transported by diffusion into the device.

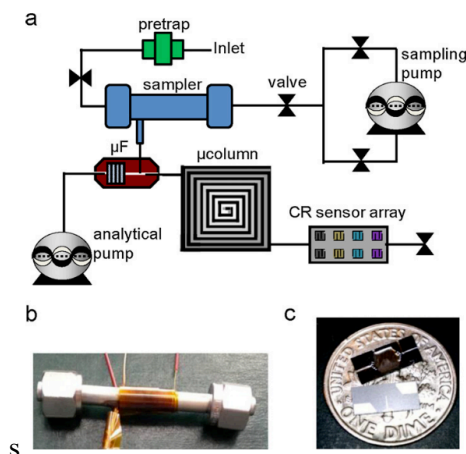


Figure 4.1. Layout of the key components of the preconcentrator/focuser (PCF) module and additional units of the  $\mu$ GC prototype presented by Zellers on [168].

The group of Prof. Pijolat developed 120 $\mu$ m-depth, planar Si microdevices with small features on the microcavity in the shape of what they called “scales” [172]. The adsorbents proposed in this work for pollution monitoring and VOC adsorption were activated carbons, single and multiple walled carbon nanotubes and Tenax polymer particles. The incorporation of the adsorbent has been realized either dispersed in a solution or in a paste form before sealing. They observed, the first deposition method was adequate for small particles such as activated carbon (<100 nm) or carbon nanotubes, while the second one was suitable for Tenax particles (250  $\mu$ m). Furthermore, the “zig-zag” geometry they included inside the cavity facilitated the homogenization of the solution, thus improving the distribution of the adsorbent inside the device (Figure 4.2.a). The desorption of the material was performed with a screen-printed Pt coil situated on the back of the substrate and claimed to reach up to 500 °C with very homogenous temperature distribution.



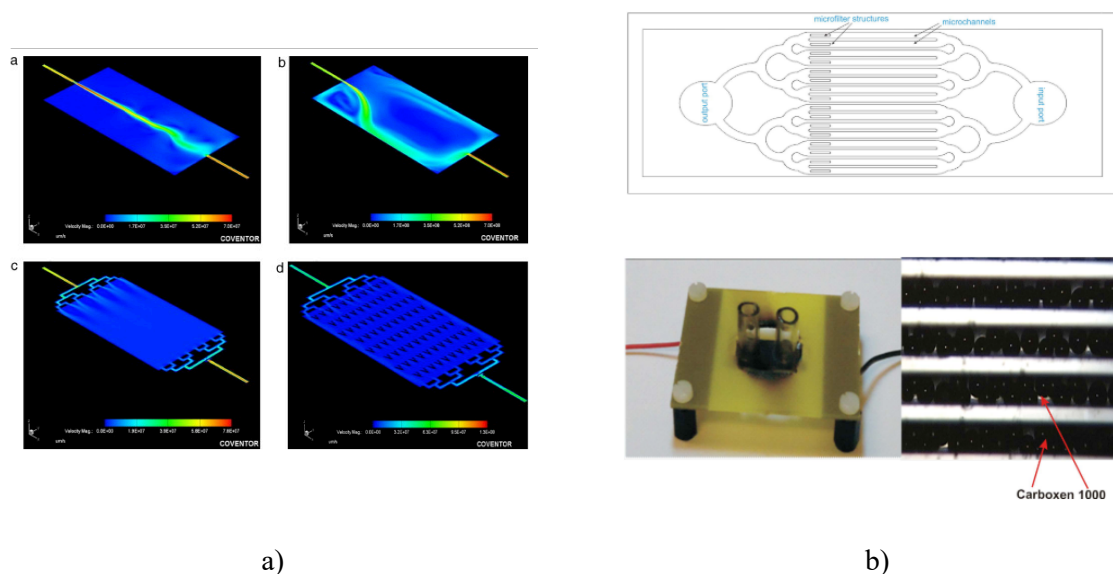


Figure 4.2. CFD simulations of the devices reported in [172]. b) Preconcentrator focuser presented on [173].

A more complex design is found in the work of Lang for micropreconcentration and focusing of chemical species (in the work, they mainly investigated on ethylene adsorption and concentration) [173] (Figure 4.2.b). The device consisted on 16 Si microchannels (cross-section of  $270 \times 550 \mu\text{m}$ ), fabricated by DRIE and sandwiched between two Pyrex wafers (top and bottom) by anodic bonding. The adsorbent, active carbon Carboxen 1000, was loaded in the finished device by pouring the particles thorough the inlet port and generating a depression inside the system that dragged the particles using a vacuum pump in the outlet. The main feature of the design is the heating concept, instead of integrating additional elements such as heating coils or external metal wires, the authors use the walls of the Si trenches as microheaters. This approach was able to reach up to  $300 \text{ }^\circ\text{C}$  inside the microdevice with a power consumption of  $1.9 \text{ W}$  and a heating rate of  $13.4 \text{ }^\circ\text{C}/\text{min}$ .

Finally, although not directly related to micropreconcentration, it is interesting to review the work from group of Prof. Agah on ionic liquid functionalized semi-packed columns for high-performance gas chromatographic separations [104]. The device was fabricated on Si substrate by DRIE resulting in  $1 \text{ m}$  long,  $240 \mu\text{m}$  depth and  $190 \mu\text{m}$  wide columns packed with  $20 \mu\text{m}$  circular pillars separated  $40 \mu\text{m}$ . The device was connected to a GC-FID equipment in substitution of the equipment separation column and heated using the GC oven. For our purposes, what is interesting is how the ionic liquid is integrated inside the semi-packed column.

They proposed two different approaches: static and dynamic deposition. As they reported, static coating did not produce high yields due to air bubbles trapped in the adsorbent during coating procedure, preventing the deposition of the ionic liquid in some of the columns. Therefore, the evaluation of the columns was performed mainly with the dynamic coated semi-packed columns.

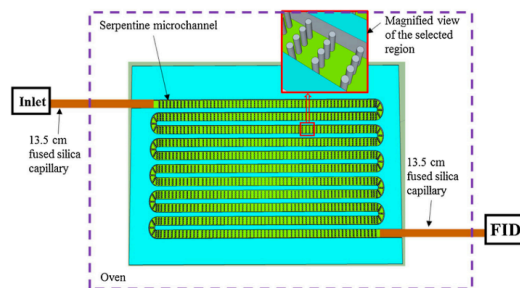


Figure 4.3. Schematic diagram of the ionic liquid functionalized semi-packed columns for high-performance gas chromatography presented on [104].

As we have seen, the possibilities of  $\mu$ -preconcentrator designs are numberless and each approach presents remarkably interesting innovations and potential. In our case, we have decided for narrow, planar Si structures where the gas and the adsorbent are contacted tangentially through the Borofloat cover. The desorption of the material is performed using a metal heating coil situated on the backside of the microdevice and controlled by an external PID unit. (Figure 4.4).

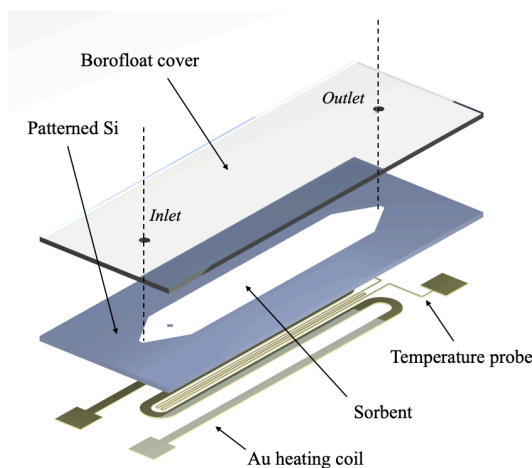


Figure 4.4. Schematic diagram of the proposed micro-device.

Throughout this Chapter, we first discuss the different design alternatives explored in this work using finite element analysis as a tool to predict the fluid dynamic behaviour inside the microdevice, as well as the heat transfer and temperature distribution. Then, we describe in detail the different fabrication techniques used in the fabrication of the microdevices, with particular emphasis on the strategies applied to each adsorbent. Finally, we summarize all of the  $\mu$ -devices herein developed and the fabrication procedure followed in each one.

## 4. 2. DESIGN OF THE MICROFLUIDIC DEVICE

The contact between the gas phase and solid is critical in terms of microdevice performance as sampler. Too wide cavities, i.e., big depth cavities, may suffer bypass issues – that is, the fraction of analyte further from the adsorbent is going to sweep the whole microfluidic path without interacting with the adsorbent. Having too narrow cavities, i.e., shallow depth cavities, may present huge pressure drops that may be difficult to overcome. Also, the incorporation of small features inside the cavity – such as pillars, columns, flow disruptors – may improve the mass transfer from the gas to the stationary phase, but again, that kind of geometries lead to high pressure issues. Overall, the main target is to maximize the mass transfer rate by improving the gas-solid contact. Attending this criteria, different cavities designs have been proposed and characterize by means of 3-D finite element analysis in Section 1.2.1.

Before sampling, the adsorbent must be preconditioned, that is the pores must be free of all impurities and residuals that it may be adsorbed during the fabrication, sealing or storage, such as humidity, organic volatiles or remaining analytes from previous experiments. The pre-treatment is often done by heating the microdevice up to a certain temperature – above evaporation temperature of most common interferences, e.g.,  $T_{\text{pretreatment}} > 100^{\circ}\text{C}$  which is above water evaporation and common organic solvents found at the lab such as ethanol ( $T_{\text{evap}} = 78^{\circ}\text{C}$ ), acetone ( $T_{\text{evap}} = 56^{\circ}\text{C}$ ), or chloroform ( $T_{\text{evap}} = 61^{\circ}\text{C}$ ) – and dragging under vacuum or sweeping with an inert gas the headspace of the microdevice. Also, once the analyte has been adsorbed on the stationary phase, in order to be able to desorb it in a sharp, concentrated peak, we must heat the adsorbent above certain desorption temperature – this temperature is determined by thermogravimetric analysis, as we have previously seen in Chapter II – with a heating ramp as high as possible while flushing with an inert carrier gas. A gold heating coil has been integrated on the backside of the Si wafer as heating source as well as a gold temperature probe to be used as part of a PID controller. Thermal conductivity of Si ( $k_{\text{Si}} = 148 \text{ W}/(\text{m}\cdot\text{K})$ ) and small wafer

thickness ( $\epsilon_{\text{Si wafer}} = 500 \mu\text{m}$ ) favour the fast heating of the whole microdevice as well as the adsorbent layer that is in contact with it. The heating of the microdevice has been numerically model in order to study different coils geometries as well as temperature profile distributions, particularly at the vicinity of the adsorbent.

Finally, different approaches have been considered to connect the microdevices to the rest of the set-up. First iterations used 1/8" straight connectors attached to the inlet and outlet through epoxy adhesive (Loctite Hysol 9492 A&B,  $T_{\text{max}} = 453 \text{ K}$ ). As the microdevice design evolve into a more compact solution, these connections were substitute by 320  $\mu\text{m}$ -diameter, fused silica capillaries through high temperature septa (Thermogreen LB-2 Septa) glued to the Pyrex substrate with thermoresistant silicone (Acc Silcoset 158,  $T_{\text{max}} = 573 \text{ K}$ ) with an intermediate layer of polyimide film (Kapton, RS Components). Last microdevices designs were mounted on a custom PEEK housing which includes both the fluidic connections through 1/16" Teflon pipes, O-ring sealings and the electric ports to connect the power source and the PID controller.

#### 4. 2. 1. 3-D FINITE ELEMENT MODEL OF THE MICROFLUIDIC DEVICE

---

The design of the microfluidic device was assisted by 3-D finite element modelling. This numerical model accounts for fluid dynamics inside the microfluidic path as well as heat distribution when certain voltage was applied to the heating coil on the bottom of the microdevice. This numerical model will allow us to predict flow lines distributions as well as pressure drops due to the geometry of the cavity. Also, since it is extraordinarily difficult to measure directly the temperature inside the microcavity on the sorbent surface, it helps us to estimate it by measuring surface temperature of the external surface of the microdevice.

##### 4. 2. 1. 1. Mathematical model

The numerical model was solved using FEM software Multiphysics, particularly, taking advantage of the *Thin-film flow* module to model fluid distribution and pressure drop inside the  $\mu$ -cavity and *Heat transfer* as well as *Electric current, shell* module to model Joule effect on the metallic resistor and the heat propagation. Our mathematical model was focused on the heat that was transferred to the gold heating coil to the adsorbent, which was located on the opposite side of the substrate and enclosed inside the cavity. Since the measurement of such temperature is not trivial, since it involves the introduction of a temperature probe somehow inside the

channel, we decided to infer the temperature inside by measuring the outside temperature. Outside temperature, however, not only depend on the heating transfer by conduction through solid but also it is highly dependable on the heating losses to the ambient.

### **Fluid dynamics**

Pressure drop and flow distribution inside de cavity has been modelled using Reynolds equation to the gas domain, which is a simplified version of Navier-Stokes equation valid when one of the dimensions is considerably smaller than the other two, thus considering the fluid volume as a thin film. We have only focused on the stationary state, since the mass flow value of the carrier gas component is going to be constant in each experiment. Assuming inertial forces negligible, the conservation of mass is described by the continuity equation:

$$\nabla \cdot (\rho \mathbf{u}) = 0 \quad (21)$$

where  $\rho$  is the density ( $\text{kg/m}^3$ ) and  $\mathbf{u}$  is the flow velocity ( $\text{m/s}$ ). Besides, in order to solve those equations, the following assumptions are made:

1. Gas flow rate is fixed at the inlet of the microdevice and constant during the over-all experiment.
2. No slip condition on the walls of the microcavity,  $\mathbf{u} = 0$ .
3. Outflow is at atmospheric pressure.

### **Heat transfer**

Heat transfer has been modelled using the heat equation:

$$\rho C_p \frac{\partial T}{\partial t} + \rho C_p \mathbf{u} \cdot \nabla T + \nabla \cdot (-k \nabla T) = Q_{heater} - Q_{loss} \quad (22)$$

where  $\rho$  is the density of the material ( $\text{kg/m}^3$ ),  $C_p$  is the specific heat capacity at constant pressure ( $\text{J}/(\text{kg}\cdot\text{K})$ ),  $\mathbf{u}$  is the velocity vector ( $\text{m/s}$ ),  $k$  is the thermal conductivity ( $\text{W}/(\text{m}\cdot\text{K})$ ),  $Q_{heater}$  is the heat source ( $\text{W/m}^3$ ), which in this case the source is the heating of the metallic coil caused by Joule effect, and  $Q_{loss}$  is the heating losses due to dissipation to its surroundings by convection – natural or forced convection. ( $\text{W/m}^3$ ).

Model heat loss by convection to the surroundings involves certain parameters such as room temperature at certain point, room humidity or even fluid velocity – if we want to consider forced convection phenomena instead, which is closer than natural convection to the actual heat transfer process. So, our approach has been measuring the temperature on the backside of the heater and use that measurement to match the temperature simulated by modifying the convection losses accordingly. To model losses to the environment we have proposed a natural convection phenomenon – where temperature and humidity are data taken from the airport of Zaragoza – and we have considered a 2 cm sphere of air in the surroundings of the microdevice whose outer temperature was imposed: at 5 and 10 V (was 20 °C), at 15 V was 25 °C and at 20 V was 30 °C. This assumption was validated by measurements taken with a thermocouple situation 2 cm far from the microdevice.

First term on the left side of (22) is the rate of heat accumulation, whereas second and third term are convective and conductive contributions to heat transfer. In our case, the only heating source is that coming from the resistor, which is coupled to the *Electric current, shell* module. Also, the following assumptions have been made:

1. Device is at room temperature at the beginning of the experiment ( $T_{RT} = 20^{\circ}\text{C}$ ) and atmospheric pressure ( $P_{\text{atm}} = 1 \text{ atm}$ ).
2. Heat is evacuated from the device by natural convective flux. It is defined as  $q_0 = h_{\text{air}} \cdot (T_{RT} - T)$ , where  $h$  is the heat transfer coefficient in air ( $\text{W}/(\text{m}^2 \cdot \text{K})$ ) and for natural convection is assumed to be  $h_{\text{air}} = 5 \text{ W}/(\text{m}^2 \cdot \text{K})$ .
3. Heat transfer in Si and Pyrex has only considered to be due to conduction, i.e,  $\mathbf{u} = 0$ . On the other side, heat transfer inside the cavity also considers heat losses due to convective heat transfer, where the velocity of the fluid circulating inside has been calculated by fluid dynamics previously.

### **Electric field and current distribution**

Electric field and current distribution have been calculated on the Au heating coil using the *Electric current, shell* module. This physics assumes that the geometry is thin enough to be considered as a 2-D entity. Since the thickness of the gold layer is 6 orders of magnitude smaller than the width or length of the coil, this approach leads to a more efficient and less resource

consuming meshing and calculation. The electric field and current distribution in the heating coil have been modelled based on:

$$\nabla_T \cdot (d_h \mathbf{J}) = d_h Q_{j,v} \quad (23)$$

$$\mathbf{J} = \sigma \mathbf{E} + \frac{\partial \mathbf{D}}{\partial t} \quad (24)$$

$$\mathbf{E} = -\nabla_T V \quad (25)$$

where  $\mathbf{J}$  is the current density ( $A/m^2$ ),  $Q_{j,v}$  is the power density ( $W/m^2$ ),  $d_h$  is the thickness of the heating coil,  $\mathbf{E}$  is the electric field ( $V/m$ ),  $\sigma$  is the electrical conductivity ( $S/m$ ),  $\mathbf{D} = \epsilon_0 \epsilon_r \mathbf{E}$  is electric flux density which depends also on electric permittivity of air ( $\epsilon_0$ ) and relative permittivity of the material ( $\epsilon_r$ ) and  $V$  is the electric potential ( $V$ ).

The power dissipated from the heating coil and transfer to the  $\mu$ -device is defined by (23) and it is the fundamental of Joule effect. The current density is defined by Ohm's law (24), whereas the electric field is due to the electric potential that is applied to the heating coil (25). Additionally, the following assumptions have been made:

1. Only the heating coil is made of conductive material, being considered Si and Pyrex perfect insulators, thus on the boundary of the heating coil and Si it is considered  $\mathbf{n} \cdot \mathbf{J} = 0$ .
2. Different voltages have been applied between the terminals, i.e.,  $V = 5 - 30 V$ . The oppose terminal have been grounded,  $V = 0$ .

#### 4. 2. 1. 2. Experimental validation of the numerical model

The numerical model has been validated through experimental analysis. To verify fluid dynamics, it has been measured the pressure drop under different mass flow rates in a functional microdevice prototype ( $40 \mu m$  cavity depth), that has been fabricated following the same lithographic techniques that will be used – which will be discussed in the next section. This experiment was performed using a mass flow controller (Alicat Scientific) set at known mass flows of dry  $N_2$  (5, 10, 15, 20 mL/min). The measurement of the pressure was taken directly from the mass flow controller. The connection of the mass flow controller to the microdevice was performed by placing the  $\mu$ -preconcentrator inside a custom PEEK housing connected to the controller through 1/16" Teflon tubing.

The heating due to Joule effect has been validated by applying a known voltage (5 to 30 V) to the heating coil and measuring the temperature both at the bottom of the device and at the top. The measurement of the temperature at the bottom of the microdevice was performed by registering the infrared radiation emitted by a black tape stick on top of the heating coil by a thermographic camera (Optris PI-400038T900). The top of the device is measured by a multimeter using a thermocouple as temperature sensor.

### **Fluid dynamics validation**

Experimental and numerical results have been obtained at the same conditions (Table 4.1). Numerical model is able to match the pressure drop trend, although a close value has not been obtained, the simulated results remain at the same order of magnitude. This overestimation is due of how the model has been implemented. Our numerical model assumes a planar geometry where the inlet and outlets are placed on both sides of the microdevice, on the smallest edge of the cavity and hence on the smallest cross-section, which gives the highest theoretical drop pressure (Figure 4.5).

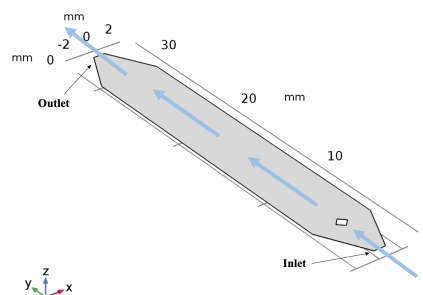


*Figure 4.5. Schematics of the planar geometry used to model flow distribution inside the  $\mu$ -cavity.*

On the experimental design, the placement of those ports is on the perpendicular plane and slightly closer together, on a bigger section of the cone-shaped sides. As result, the inlet and outlet cross-sections – and hence the drop pressure – are bigger. Nevertheless, assuming the limitations of the model, we can design on the basis of a maximum  $\Delta P$  value admissible to compare different designs under the same conditions.



TABLE 4.1. FLUID DYNAMICS VALIDATION

$Q$ (STP cm <sup>3</sup> /min)	$\bar{u}^*$ (m/s)	$\Delta P_{\text{modeled}}$ (mbar)	$\Delta P_{\text{experimental}}$ (mbar)
5	2.08	23.3	15.0
10	4.16	46.7	29.7
15	6.25	72.2	43.4
20	8.33	97.3	56.5
25	10.42	123.0	70.3

\*Calculated as  $u = Q/A$ , being A the free cross-section of the microcavity.

### **Heating transfer model validation**

Likewise, the heat transfer model has been validated by direct comparison to the results obtained by thermography. One of the problems of model any heat transport problem is the calculation of the heat dissipated by an object to its surroundings by convection – natural or forced convection.

Simulation results were able to match up to certain degree data taken from the thermographic camera (Figure 4.6). Mismatch from experimental and simulated data are due to the difficult to correctly model actual surrounding conditions. Nevertheless, this model allows us to estimate the temperature in the inside of the cavity by measuring the temperature at the outside of the microdevice.

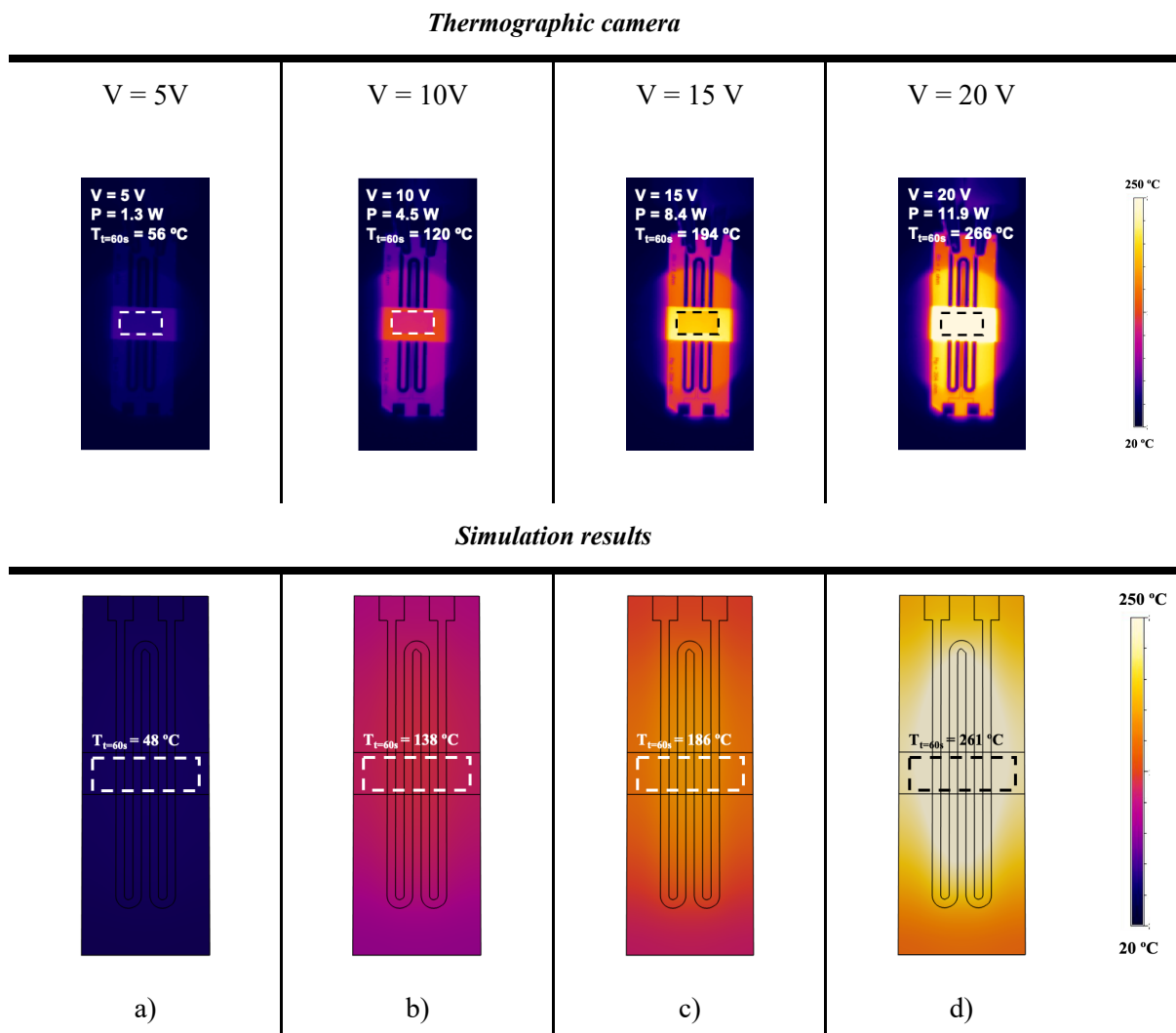


Figure 4.6. Thermographs of the gold heating coil when certain voltage is applied: a) 5V, b) 10 V, c) 15 V, d) 20 V. The temperature is measured on the top of the black tape (rectangular area marked on the images).

#### 4. 2. 2. STANDARD MICROCAVITY DESIGNS

Two sets of microdevices designs were proposed throughout this work: design 1 and design 2. Design 1 was our first attempt and was mainly based on straightforward fabrication process, whereas design 2, based on the previous best design, aimed for miniaturization and improve adsorbent/adsorbate contact.

The four designs proposed on design 1 are found on Figure 4.7. Design 1.A is oriented to maximize the coating loading (coating area of 535 mm<sup>2</sup>) of the microdevice and ease of fabrication. A flow disruptor has been integrated at the inlet to favour the correct gas distribution inside the cavity. Design 1.B (coating area of 517 mm<sup>2</sup>) features three arrays of flow disruptors

besides the inlet one, the first array of disruptors is located at the very begin of the cavity, whereas the second and third are found at the middle and close to the end of the flow path. Design 1.C (coating area of  $307 \text{ mm}^2$ ) features  $500 \mu\text{m}$  squared columns; whose separation depends on the wet etching conditions. Design 1.D (coating area of  $423 \text{ mm}^2$ ) is based on previous design, although it minimizes pressure drop by increasing the distance between each  $250 \mu\text{m}$  square column.

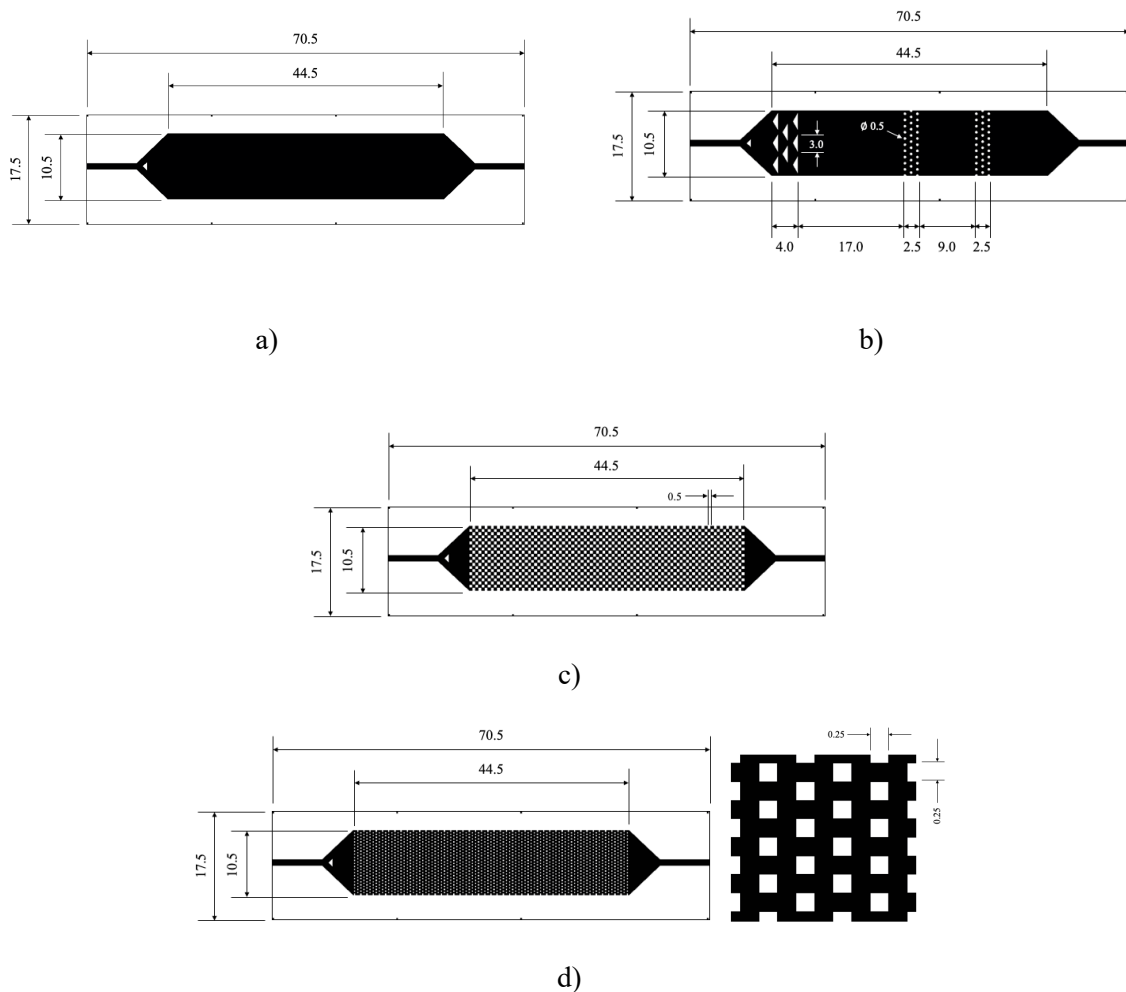


Figure 4.7. First set of microdevices design: a) design 1.A: empty cavity, b) design 1.B: flow disruptors along the microfluidic path, c) design 1.C:  $500 \mu\text{m}$  square columns, d) design 1.D:  $250 \mu\text{m}$  square columns, on the right side, a detail of the pillars pattern. Dimensions in mm.

Design 2 is roughly based on design 1.A but aimed to miniaturization. Another major improvement from previous design is the replacement of gas inlet and outlet: from lateral disposition to top position, thus minimizing dead volume of inlet/outlet channel from 8 mm to 0.5 – 1 mm (up to Pyrex wafer thickness) (Figure 4.8).

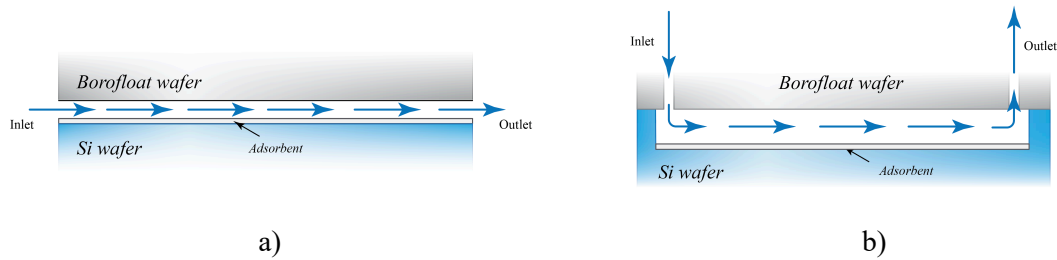


Figure 4.8.  $\mu$ -device longitudinal section. a) Inlet/outlet arrangement and flow distribution on design 1. b) Inlet/outlet arrangement and flow distribution on design 2.

In total, seven designs have been proposed in this set. Design 2.A shares the same cavity width as design 1.A but the length is 4-fold reduced (from 44.5 to 10 mm). Design 2.B.a preserves the width/length proportion, but the top view area is reduced down to the same as design 2.A (from 5.3 cm<sup>2</sup> to 1.48 cm<sup>2</sup>). Design 2.B.b came up as a solution to seal devices that were coated with materials not suitable for anodic bonding by using thermoresistant adhesive. The outer 1 mm trench is designed to be filled with a film of adhesive that provides air tightness to the cavity and avoid spreading the glue inside the microdevice. Design 2.B.c/d are based on design 1.D and features square shaped pillars along the cavity (20  $\mu$ m square pillars on design 2.B.c, and 50  $\mu$ m pillar on design 2.B.d). Design 2.B.e/f features rectangular pillars in a complex pattern of 10 x 50  $\mu$ m (design 2.B.e) and 20 x 50  $\mu$ m (design 2.B.f). Designs 2.B.c/d/e/f were proposed to serve as substrates for film deposition, where the pillars inside the cavity are used to increase the substrate – film contact area.

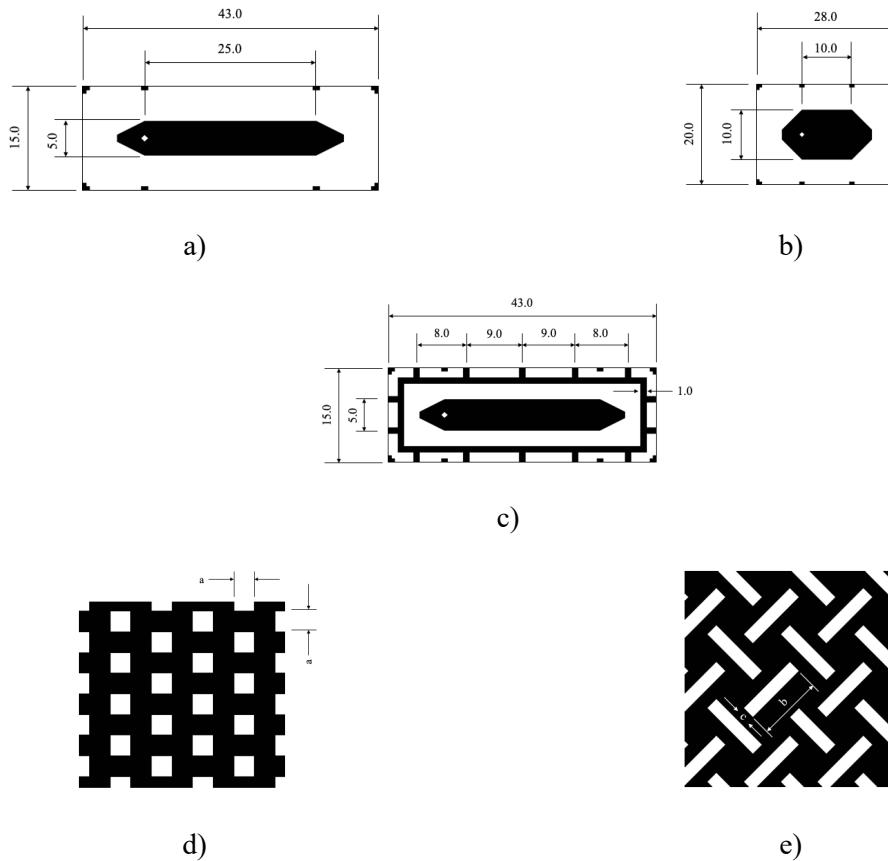


Figure 4.9. Second set of microdevices design: a) Design 2.A, b) Design 2.B.a, c) Design 2.B.b featuring a glue trench, d) detail of the square pillars pattern on the cavity of design 2.B.c/d ( $a = 20$  or  $50 \mu\text{m}$ ), e) detail of the pillars pattern inside the cavity of design 2.B.e/f ( $b = 50 - 100 \mu\text{m}$  and  $c = 20 - 50 \mu\text{m}$ , respectively). Dimensions in mm.

The main characteristics of the designs of both sets of designs are held on Table 4.2. Top surface refers to the top view area. Coating area refers to the whole area susceptible to be coating, which also includes the area of the cavity walls as well as disruptors or pillars that may be inside and it has been calculated assuming  $40 \mu\text{m}$  cavity depth. Free volume is the cavity volume assuming no coating and a  $40 \mu\text{m}$  cavity depth. Furthermore, using the mathematical model presented before, it has also calculated the pressure drop assuming a flow rate of  $10 \text{ mL/min}$ .

TABLE 4.2. MAIN FEATURES OF THE MICRODEVICES DESIGNS

Design	Top surface (mm <sup>2</sup> )	Coating area (mm <sup>2</sup> )	Free volume (μL)	$\Delta P_{\text{modelled}}^*$ (mbar)
Design 1.A: empty cavity	535	541	21.4	135
Design 1.B: flow disruptors	517	529	20.6	144
Design 1.C: 500 μm pillars	307	384	12.3	183
Design 1.D: 250 μm pillars	423	503	16.9	155
Design 2.A: empty cavity	148	151	5.9	17
Design 2.B.a: empty cavity	148	151	5.9	48
Design 2.B.b: empty cavity with outer glue trench	148	151	5.9	48
Design 2.B.c: 20 μm pillars	117	359	4.7	66
Design 2.B.d: 50 μm pillars	117	216	4.7	66
Design 2.B.e: 10 x 50 μm pillars	111	482	4.4	101
Design 2.B.f: 20 x 100 μm pillars	111	296	4.4	101

\*Assuming 40 μm channel depth.

As expected, shorter geometries present lower drop pressure than larger ones (48 mbar on design 2.B.a versus 135 mbar on design 1.A). Also, more complex cavities exhibit higher drop pressure than its simpler counterparts (183 mbar on design 1.C versus 133 on design 1.A and 66 mbar on design 2.B.d versus 48 mbar on design 2.B.a). However, flow simulations show

an even distribution of the gas along the microchannel in all the cases as result of the laminar flow regime. Even on complicated geometries such design 1.C, design 1.D or design 2.B.d, the flow surrounds nicely the pillars all over the cavity, the flow regime remains laminar and not turbulence is observed.

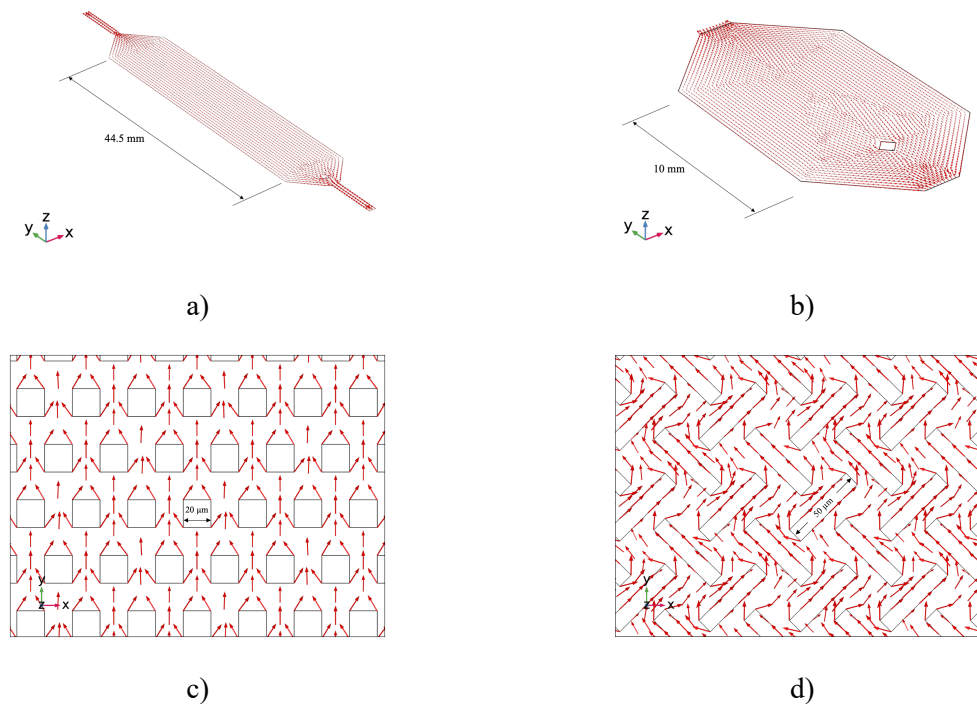
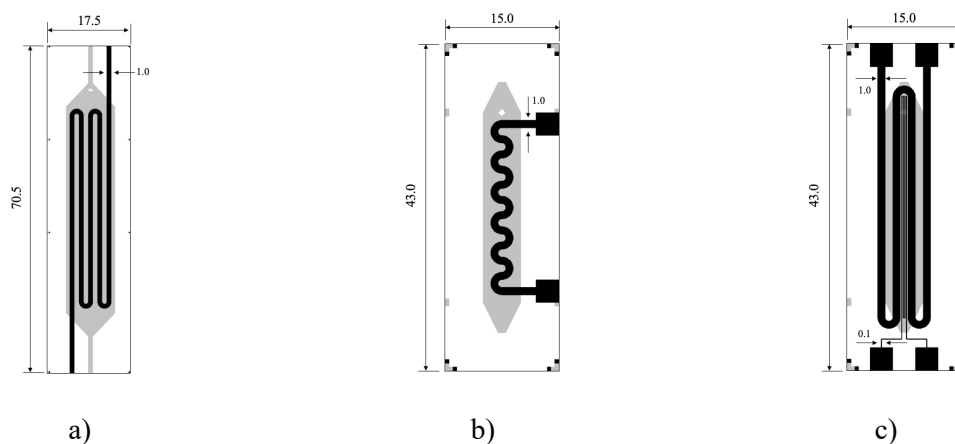


Figure 4.10. Flow distribution on some of the proposed design. The tip of the arrow points the direction of the flow. a) design 1.A, b) design 2.A, c) detail of flow distribution around  $20 \times 20 \mu\text{m}$  pillars on design 2.B.c, d) detail of the flow distribution around  $10 \times 50 \mu\text{m}$  pillars on design 2.B.e.

#### 4. 2. 3. HEATING COIL DESIGN

The heating coil was placed below the adsorbent material. On Figure 4.11 are depicted the different iterations of heating coils designed throughout this work. The first design was implemented on the first set of microdevices designs. It consisted on a meander-like metallic element with the electric ports situated at opposite edges of the substrate. Although the heating coil was slightly smaller than the cavity in length, it was not observed any significant temperature gradient among the central and the outer sections of the cavity, due to the good thermal conductivity of Si. The main drawback of this design – beside the oversized design of the microdevice – was the placement of the connection ports. Since fluidic ports design was rough and bulky and the electrical connection to the power source was performed using crocodile clips, having both ports at the same edge of the microdevice did not guarantee the correct electrical

connectivity. In order to guarantee the electrical continuity, silver paste was used at both ends to increase contact area.



*Figure 4.11. Heating coil designs proposed in this work. Heating coil and heating probe are depicted in black whereas the cavity is portrayed in grey as reference (inlet at top, outlet at down). a) first iteration used in the first sets of microdevices designs, b) second iteration used in the firsts batch of the second set of microdevices design; and c) third iteration used in the microdevices used for testing material adsorption properties, which includes a 100  $\mu\text{m}$  temperature probe that is used to control the power applied. Dimensions in mm.*

The second heating coil iteration was implemented on the second set of designs and it overpassed the flaws of its predecessor, featuring reduced size, bigger connection pads (3 x 3 mm in size) and lateral disposition. However, since some of the materials proposed could only work at a restricted temperature range that could not be overpassed, a temperature probe to act as sensor for a voltage controller was a must. On the other hand, in order to get a fast heating ramp for a fast desorption, the heating coil had to cover the whole cavity.

The third and final heating design was increased in size and an additional 100  $\mu\text{m}$  heating resistor was used as temperature probe. The temperature probe was based on the linear dependence of the conductivity of a metal with the temperature. Finally, the redesign of the gas ports and a new electrical connection ports allowed the placement of the heating coil pads at one edge of the substrate, whereas the temperature pads were placed at the opposite site. This heating coil design has been used in all of the DMMP adsorption experiments.



#### 4. 2. 4. PARTICULAR DESIGNS FOR IN-SITU GROWTH

*In situ* electrochemical synthesis of Cu-BTC as well as layer-by-layer synthesis of Zn-DCAMPZ were performed on a patterned metal substrate lithographed on the Borofloat wafer. Although the composition of the metal layers of each substrate was not identical, the design of the substrate was the same. Based on the same rectangular shape, two designs were proposed: a 50  $\mu\text{m}$  square pattern substrate of 52  $\text{mm}^2$  and flat, unpattern substrate of 69  $\text{mm}^2$  (Figure 4.12). The electro-synthesis and layer-by-layer synthesis substrates were design to fit the design 2.B with glue trench.

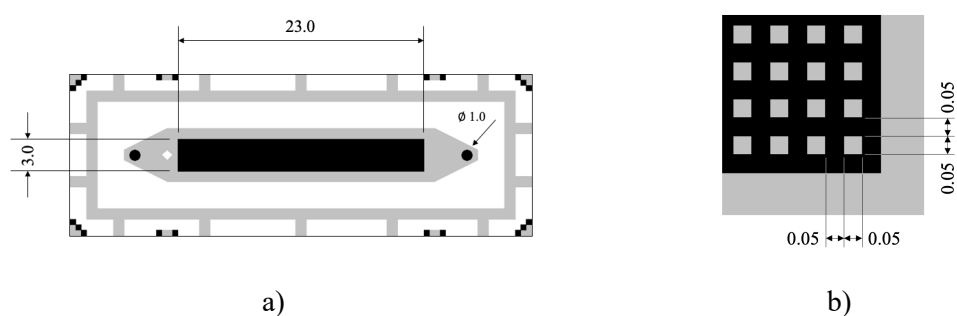


Figure 4.12. a) Electro-synthesis and layer-by-layer synthesis substrates (black) depicted along design 2.A microcavity (grey). b) Detail of the 50  $\mu\text{m}$  square pattern inside the rectangular 23 x 3 mm substrate. Dimensions in mm.

### 4. 3. MICRODEVICES FABRICATION PROCESS

Fabrication process is divided in five different steps: cavity etching, adsorbent incorporation, microdevice sealing, heater element integration and inlet/outlet ports mechanization (Figure 4.13). The microdevice is fabricated on a Si substrate and using standard photolithography processes at the clean room facilities in the Advance Microscopy Laboratory (LMA), at Zaragoza. The facilities are comprised of a 20  $\text{m}^2$ , class 100 clean room and a 100  $\text{m}^2$ , class 10 000 clean room. The first one holds the photoresist deposition station – SÜSS Microtec Delta spin-coater and hot-plate – and a mask aligner – SÜSS Microtec MA6 – as well as a chemical bench where the photoresist are developed. In the second one, among other equipment, are located the wet and dry etching stations, as well as the chemical vapor deposition equipment.

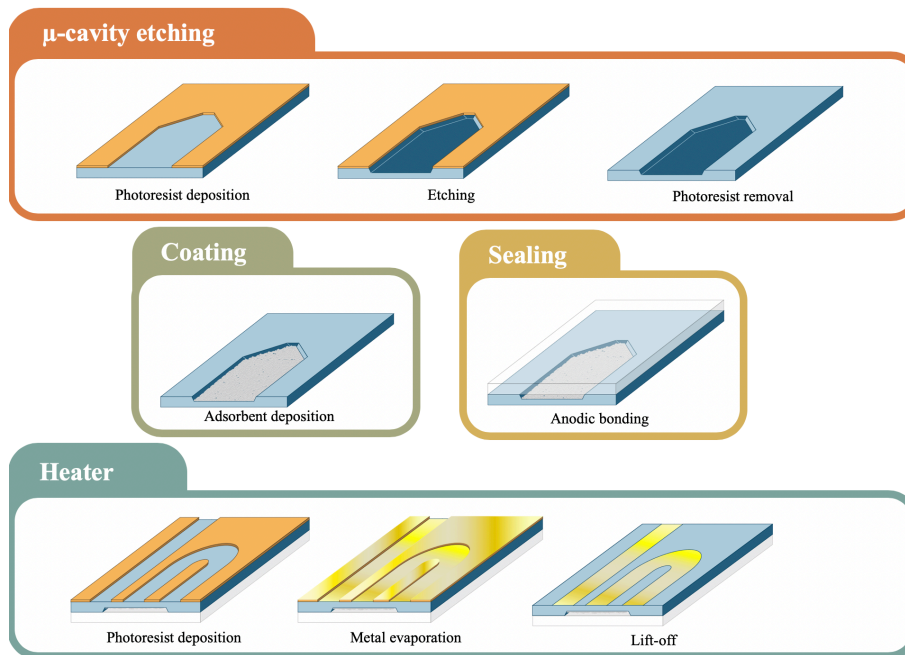


Figure 4.13. Schematic of microdevice fabrication run.

#### 4. 3. 1. CAVITY ETCHING PROCESS

Cavity etching is the first step performed to fabricate the microdevice. It is divided in to two steps: 1) photoresist deposition and 2) etching. The photoresist deposition is taken place in a class 100 clean room whereas the etching was done on a class 10 000 clean room. For simple geometries as well as large features ( $>100 \mu\text{m}$ ) and deep cavities ( $> 20 \mu\text{m}$ ), wet etching with KOH was used, whereas for more complex geometries and narrow cavities ( $< 15 \text{ nm}$ ), we chose dry etching procedures.

##### 4. 3. 1. 1. *Optical lithography*

4" diameter, P doped Si wafers ( $500 \pm 20 \mu\text{m}$  thickness,  $\langle 100 \rangle$  crystal orientation, 5 - 10  $\Omega \cdot \text{cm}$  resistivity) supplied by Sil'Tronix Silicon Technologies were used in all of our devices. For wet etching as well as for certain dry etch conditions, a specific negative-working photoresist ProTEK<sup>®</sup> (Brewer Science) was used. It features a non-degradable character under alkaline etching conditions – which is essential for wet etching and also for hydrothermal synthesis of silicalite 1 layers. The optical masks were designed using Clewin5<sup>®</sup> software and printed on high grade acetate film by Micro Lithography Services LTD. The standard optical lithography process is depicted in Figure 4.14.

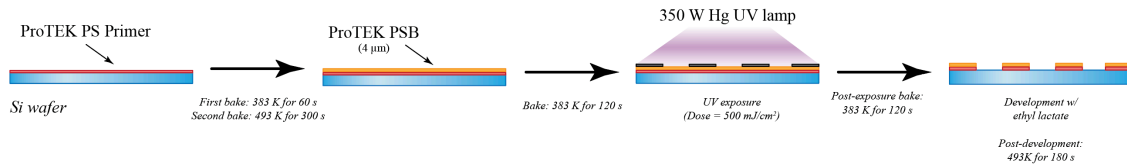


Figure 4.14. Standard optical lithography process.

On complex geometries such as cavities with pillars and small features inside the channel, an Al masks was used as protective coating. 50 – 200 nm Al masks was evaporated by Electron Bean Physical Vapor Deposition (EBPVD) (Edwards auto-500) using the photoresist TI35ESX as sacrificial layer. EBPVD is a deposition technique based on the boiling off (or sublimating) of a heated material (target) onto a substrate in a vacuum. In order to a high degree of evaporation of the target, it is used a high intensity electron beam gun (3 to 29 keV) that is magnetically oriented towards the metal, which evaporates only locally. This technique offers very low source-contamination, high quality films and high deposition rates (50 – 500 nm/min) [174]. To assure a good transferring of the geometry to the substrates, the designs were printed on chrome masks supported on quartz (Delta Mask BV). This process is depicted in Figure 4.15.

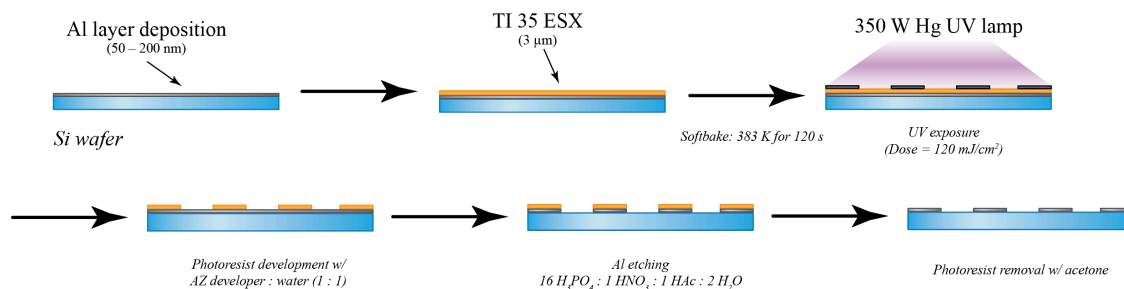
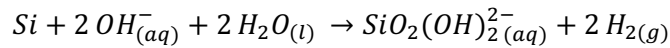


Figure 4.15. Patterning of Al masks on Si wafer by standard optical lithography.

#### 4. 3. 1. 2. Wet etching

Wet (or chemical) etching is based on the chemical reaction between a liquid reactant with the substrate or layer to be etched. The most important parameters in wet etching are etching rate, selectivity, anisotropy, feature size control, over-etch, tolerance and loading effects [174]. Etching value is adjusted by properly controlling temperature and concentration of the etchant agent. Substrates based on Si are selectively etched by alkaline media. It is commonly use potassium hydroxide (KOH) and tetramethylammonium hydroxide (TMAH). The etching reaction is described as [175]:



Due to the crystalline structure of Si, the wet etching is highly anisotropic, resulting in different etching rates depending on crystallographic plane. Main etching direction is following  $\langle 100 \rangle$  crystalline plane, whereas etching over  $\langle 111 \rangle$  is considerably slower (1100 and 17 nm/min following  $\langle 100 \rangle$  and  $\langle 111 \rangle$  respectively) [176]. Also, selectivity among crystalline planes is not only dependent on etching conditions (etchant concentration and temperature) but mainly on the reactant – TMAH presents lower selectivity than KOH. Commonly, wet etching requires the use of silicon dioxide ( $\text{SiO}_2$ ) or silicon nitride ( $\text{Si}_3\text{N}_4$ ) masks (7.7 and  $\sim 0$  nm/min for  $\text{SiO}_2$  and  $\text{Si}_3\text{N}_4$  respectively) [177], which add an additional fabrication step, since traditional photoresists cannot withstand alkaline media. On the contrary, our fabrication protocol involves the use of an alkaline-protective photoresist ProTEK<sup>®</sup> PSB-23. Once the photoresist is deposited, the Si wafer is placed in a custom PEEK holder and immersed vertically in a KOH (40%v) bath at 353 K for a set amount of time. It is reported Si etching times at 353 K of 1100 nm/min [177], although since this rate is highly dependent on etchant conditions – freshly or overused – a final analysis by profilometry was commonly practiced. Commonly, etching times ranged from 20 min to 90 min with etching depths of 20  $\mu\text{m}$  to 120  $\mu\text{m}$  (Figure 4.16.a). It was also observed certain over etching, particularly at the edges of the microchannel, due to an accumulation of bubbles of  $\text{H}_2$  on those spots (Figure 4.16.b). In general, these defects are associated with a poor verticality of the wafer inside the bath.

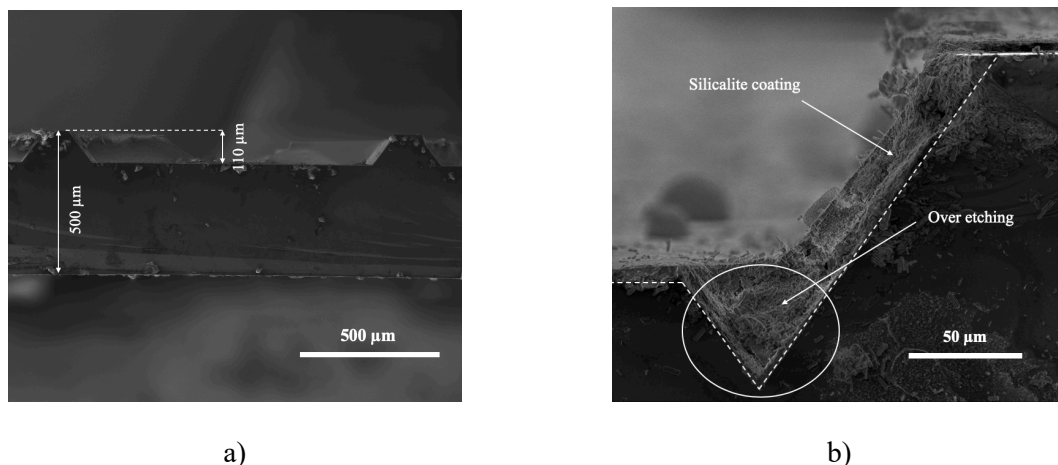
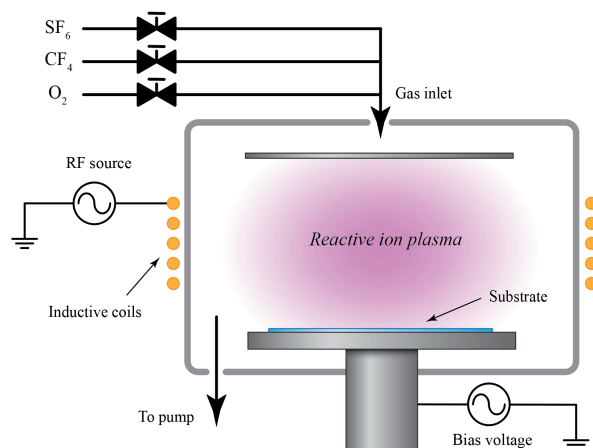


Figure 4.16. SEM of the profile of a 1 mm-width  $\mu$ -channel etched for 90 min resulting in a 110  $\mu\text{m}$  etching depth. b) Detail of the profile of a silicalite coated  $\mu$ -device where over etching on the walls of the cavity has been observed.

### 4.3.1.3. Dry Etching

Dry etching is a family of techniques, where the material is eroded by means of a gas or vapor reactant. It can be either by physical ion bombardment, chemical reaction through reactive species at the surface, or a combination of both. In our case, plasma reactive ion etching (RIE) has been used to define the cavity in the substrate only for some particular  $\mu$ -devices.

In RIE process, the plasma is generated by exciting ions from the reactant gas as a consequence of radio frequency (RF) electromagnetic waves (*Figure 4.17*). The reactant gas is flowed inside the reaction chamber through an array of diffusers and the plasma is generated between those and the sample to be etched. Since the holder where the sample is placed is connected to the RF source, an electric potential ( $V_{\text{bias}}$ ) between the sample and the holder is produced, which accelerates gas ions towards the sample's surface. RIE process not only etches the sample by chemical diffusion of highly reactive ions and radicals formed at the plasma, but also there is physical erosion due to the accelerated ions that impact against the exposed surface. The overall process is controlled by reaction chamber pressure, reactant gas mass flow, RF power and  $V_{\text{bias}}$ . For Si etching is commonly used as reactant gases  $\text{SF}_6$  and  $\text{CF}_4$  – sometimes in combination with  $\text{O}_2$ . Etching ratios range from 500 – 1500 nm/min ( $\text{SF}_6$ ) down to 100 nm/min ( $\text{CF}_4$ ), although those values are indicative, since the process is highly dependent on the before-mentioned parameters.



*Figure 4.17. Schematic of RIE chamber.*

TABLE 4.3. RIE CONDITIONS PROPOSED ON THIS WORK USING 200 W RF POWER SOURCE

	Mask	Reactant gases	Vacuum pressure (mbar)	Etch rate (nm/min)
Wet etching	ProTEK	-	-	1100
RIE_1	ProTEK	20 mL/min SF <sub>6</sub>	0.19	830
RIE_2	200 nm Al	20 mL/min SF <sub>6</sub>	0.19	1300
RIE_3	200 nm Al	20 mL/min CF <sub>4</sub>	0.19	100
RIE_4	200 nm Al	10 mL/min SF <sub>6</sub> 10 mL/min CF <sub>4</sub>	0.19	1000
RIE_5	200 nm Al	5 mL/min SF <sub>6</sub> 5 mL/min CF <sub>4</sub>	0.15	700

RIE process has been used to etch very narrow and complex geometries using either protective ProTEK mask for open, simpler microchannels of 50 to 200 nm thick Al masks for complex geometries. Since RIE is highly dependent on the gas use to generate the plasma, different gas mixtures were proposed in order to tune etching rates. On Table 4.3 are compiled the conditions proposed in this work at 200 W.

Simpler geometries, such as 2.B.a, were correctly etched using RIE\_1 (20 mL/min SF<sub>6</sub>,  $p_{\text{vacuum}} = 0.19$  mbar,  $RF_{\text{power}} = 200$  W) and 8  $\mu\text{m}$  narrow cavities on Si were performed after 10 min of plasma exposure. On the other hand, due to the highly isotropic nature of dry etching, small features presented on designs 2.B.c, 2.B.d, 2.B.e and 2.B.f were challenging to obtain for 20  $\mu\text{m}$  cavities. 50 x 50  $\mu\text{m}$  pillars on design 2.B.d were achievable using RIE\_2, 4 and 5 at exposure times from 15 min to 30 min although severely distorted due (Figure 4.18). Smaller 20 x 20  $\mu\text{m}$  pillars not feasible, resulting in a pyramid-shape due to over-etching. Designs 2.B.e and 2.B.f were not possible to define correctly in any circumstance, due to severe under-etching after long plasma exposure times. The fabrication of these designs was discarded with the equipment available at LMA. As result of this experiments, it was decided to use Al masks and 20 mL/min SF<sub>6</sub>, 200 W, 0.19 mbar (RIE\_2) with etchings performed in 10 min intervals, with visual inspection at the end of every step to verify the etching.

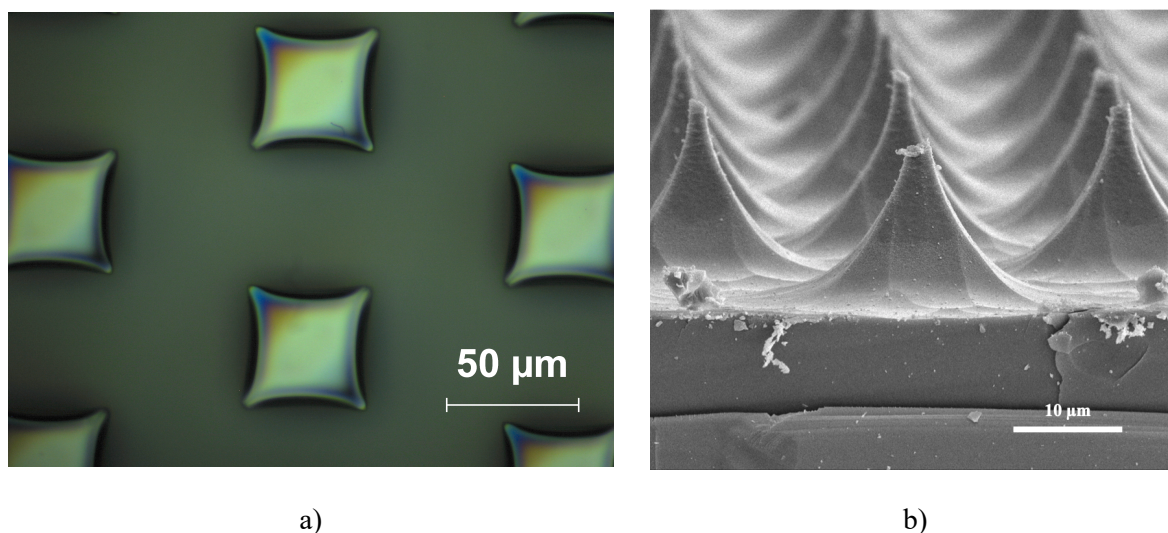


Figure 4.18.  $50 \times 50 \mu\text{m}$  pillars after 20 min at 20 mL/min  $\text{SF}_6$ , 200 W, 0.19 mbar using 200 nm Al mask (RIE\_2). a) Optical image of the top surface of the pattern cavity with the inner pillar still protected with the Al mask. b) SEM micrograph of the profile of the pattern cavity after removal of the Al mask.

#### 4. 3. 2. SUBSTRATE PRECONDITIONING AND FABRICATION FOR ADSORBENT DEPOSITION

The three explored techniques are: spin coating of powder materials, in situ growth of thick layers of porous materials and in situ polymerization of monomeric ionic liquids.

##### 4. 3. 2. 1. Spin coating of powder materials

Spin coating does not carry any pre-treatment of the wafer and is performed over an etched substrate (Figure 4.19). In order to avoid spillage of material all over the substrate, the wafer is protected with a custom, pre-cut adhesive tape that is resistant to the ethanolic solution where the adsorbent particles are dispersed (Figure 4.19.a). After exposure to UV, the adhesive film is easily peeled off (Figure 4.19.b). Using a solution of 1.7 %<sub>w</sub>t of adsorbent in ethanolic solution, the spin coating protocol is: 1) dispersion of the material over the substrate at low angular speed ( $\Omega = 300 \text{ rpm}$ ) for 15 s, 2) evaporation of the solvent at high angular speed ( $\Omega = 1000 \text{ rpm}$ ) for 60 s, 3) drying of the remanent solvent at 80 °C for 2 min. In order to increase the sorbent loading, step 1) and 2) are repeated consecutively as discussed on Chapter 2.

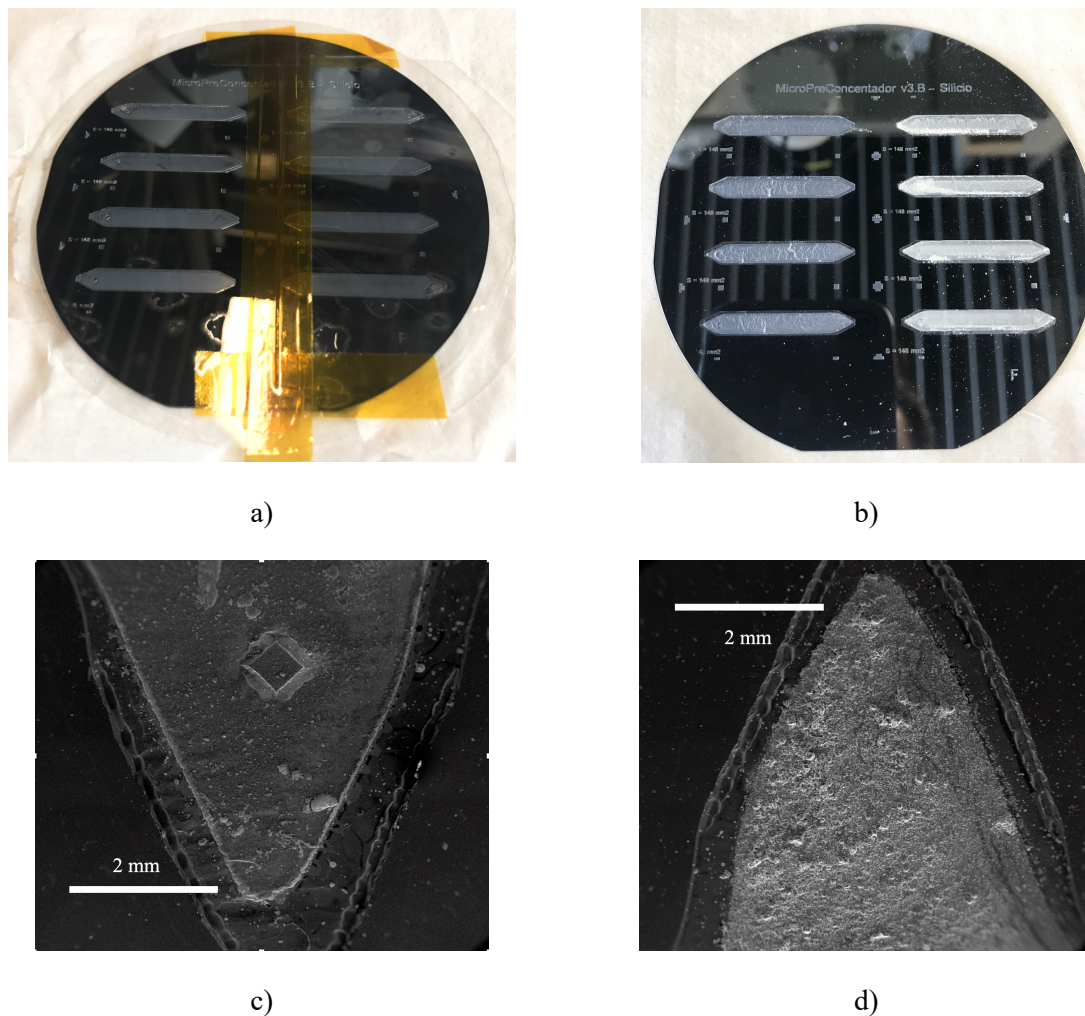


Figure 4.19. Preparation of Si substrates for spin coating of adsorbent materials. a) Si wafer protected with pre-cut adhesive tape. b) Si wafer with modified  $\mu$ -devices after peeling of the adhesive film. c) Detail of one of the left-side devices coated with Zn-DMCAPZ crystals after 10 spin-coating cycles. d) Detail of one of the right-side devices coated with MCM-48 particles after 10 spin-coating cycles. c) and d) images has been obtained by SEM.

One of the advantages of this technique is its high versatility: 1) batch fabrication (coating all of the devices in the wafer with the same adsorbent and same spinning conditions), 2) optimization of spinning conditions (using one material, it can be studied different spinning profiles by protecting the unused microdevices with additional adhesive tape) or 3) prepare up to 8 devices with different coatings per wafer (one material per devices by protecting the other cavities with the adhesive film).



#### 4. 3. 2. 2. *Substrate fabrication for in-situ growth of MOF layers*

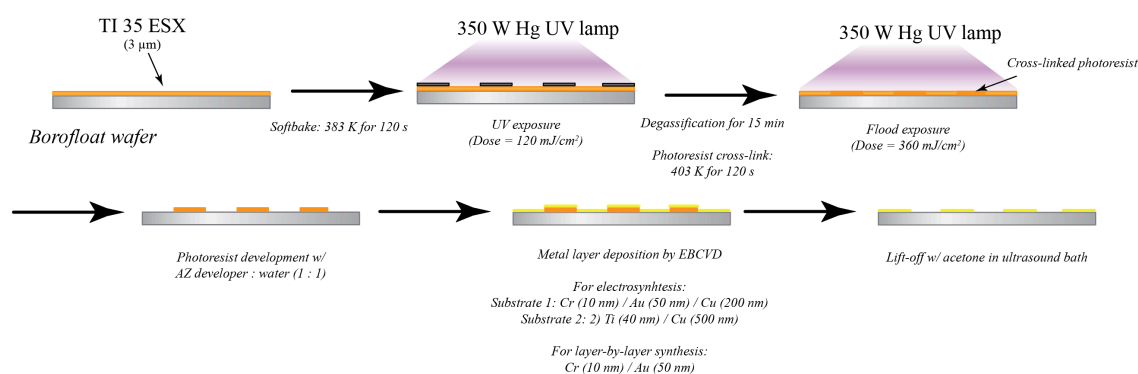


Figure 4.20. Patterning of metal substrate for electro-synthesis and layer-by-layer synthesis on a Borofloat substrate by standard lift-off process using the photoresist TI35ESX as sacrificial layer.

Among in situ growth of polycrystalline films of porous materials, we have investigated the following: hydrothermal synthesis of MFI type zeolite, electrochemical synthesis of Cu-BTC MOF, layer by layer synthesis of Zn-DMCAPZ and solvothermal synthesis of Zn-MIM using as precursor ZnO deposited by ALD. Hydrothermal and solvothermal synthesis of MFI and Zn-MIM layer respectively did not require any reactive thin film on the Si substrate but electrochemical synthesis of Cu-BTC and layer by layer synthesis of Zn-DMCAPZ required the presence of a metallic thin film. This metallic thin film was not performed on the Si cavity but on the top Borofloat cover by standard lift-off process as depicted in Figure 4.20.

#### 4. 3. 2. 3. *In situ polymerization of ionic liquids*

Finally, the in situ polymerization of ionic liquids has been performed on two different substrates as described on Chapter 2: on bare Si microchannels and on alumina ( $\text{Al}_2\text{O}_3$ ) coated Si microchannels. 500 nm alumina coating is performed by Electron Beam Physical Vapor Deposition (EBPVD) (Edwards auto-500) using 200 nm Al as protecting mask. The Al mask was chosen to simplify the fabrication process after RIE etching (previously described), since some of the cavity's designs incorporated complex features, it was unfeasible the deposition of a new photoresist over the etched Si substrate. On the other hand, the Al etchant use to remove the Al mask also etched the alumina coating, although 10-fold slower rate (Al etching = 50 nm/min vs  $\text{Al}_2\text{O}_3$  etching = 5.7 nm/min, both at 50  $^\circ\text{C}$  [177]). By carefully adjusting Al etching time and alumina thickness, it is possible to fabricate complex geometries on alumina coated Si microchannels. In our work, we use Al etchant type A (16  $\text{H}_3\text{PO}_4$  : 1  $\text{HNO}_3$  : 1  $\text{HAc}$  : 2  $\text{H}_2\text{O}$ ),

where the wafer was immersed for 4 min, until fully dissolution of Al mask. After, the wafer was rinsed thoroughly with water and dry with N<sub>2</sub>. Theoretically, alumina coated ranged roughly 475 nm. Figure 4.21 depicts the RIE process on a Si wafer with Al mask, as well as the Al<sub>2</sub>O<sub>3</sub> deposition by EBPVD and removal of Al mask.

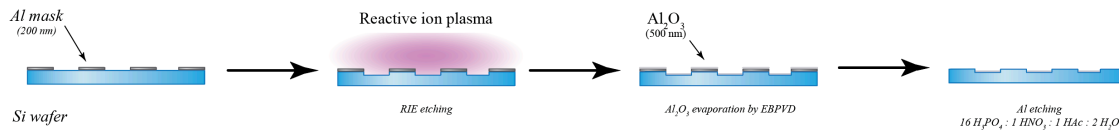


Figure 4.21. Alumina coating process on Si microchannels etched by RIE using Al protective mask.

### 4. 3. 3. CAVITY SEALING AND BONDING

There are a wide range of different techniques that can be applied to producing hermetic cavities with enough mechanical resistance to withstand high gas mass flow, thus high pressure, without leakages. Commonly used techniques include direct bonding, field-assisted thermal bonding (anodic bonding), solder bonding, eutectic bonding, thermocompression bonding, direct metal-to-metal bonding, ultrasonic bonding, low-temperature melting glass bonding and adhesive bonding [178].

#### 4. 3. 3. 1. *Field-Assisted Thermal Bonding*

Field-assisted thermal bonding – also known as anodic bonding, electrostatic bonding or the Mallory process – is a sealing technique commonly used to bond glass – or ceramics – with Si wafers.

This technique provides high-quality hermetic seals. It involves bonding the two wafers at elevated temperature (180 °C to 500 °C), using the assistance of a high electric field [179]. Among the advantages of the anodic bonding over other wafer bonding techniques – direct bonding, eutectic bonding... – is the fact that it can tolerate rougher surfaces and it is not so sensible to cleanliness of the bonding environment. On the other hand, it implies the use of alkali containing materials and it requires high electric fields. Furthermore, using relatively high temperature leads to thermal residue stress in the bonded structures which can induce their

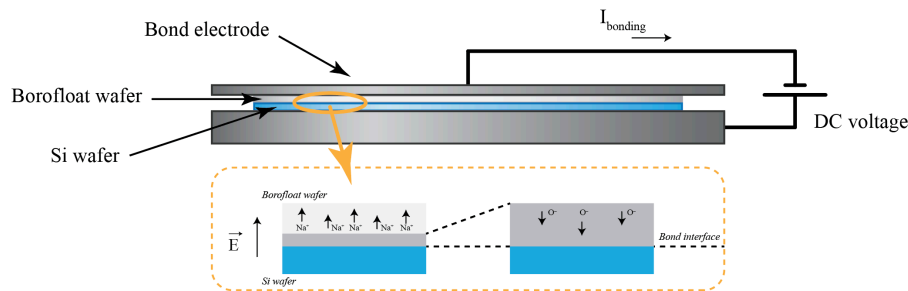
fracture, even though the thermal expansion curves of silicon and glasses that are used in this process are fairly close to each other [179].

Field-assisted thermal bonding is an electrochemical process that relies on the polarization of the alkali-containing glasses (Figure 4.22.a). It can be achieved by setting the two wafers together on a hot plate (180 – 500 °C) and applying a high DC voltage to the pair (400 – 1000 V), such that the glass is negative with respect to the Si. When a DC voltage is applied to a glass at elevated temperatures, the alkali cations are depleted from the vicinity of the anode and transported toward the cathode. The conduction is primarily realized by  $\text{Na}^+$  ions – in a small extent by  $\text{K}^+$  ions. At the bonding temperature, elastic and viscous flow of the glass make it come into intimate contact with the Si, even though the surface presents some roughness. The anodic bonding could be explained by the formation of Si–O–Si bonds originating from the silicon oxidation at the interface by thermodehydration of the silicon-glass ensemble or by the reaction of Si with O present on the surface of the two materials before bonding special in the form of  $\text{OH}^-$  groups [180] [181]. The formation of a  $\text{SiO}_2$  layer between silicon and glass during bonding has been proved by backscattering spectroscopy [182]. It has been observed that the bonding speed and quality increase when more hydroxyl groups are present on the Si surface before bonding [179], or when O in other forms is available during bonding.

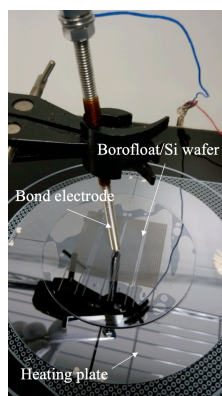
The most used glass materials for anodic bonding are Corning 7740 (commonly known as ‘Pyrex’) and Schott Borofloat. They were found to be suitable for anodic bonding due to their sodium content and the close match between their coefficient of thermal expansion and that of Si [183].

The anodic bonding process in our devices were performed in the clean room facilities at LMA using a home-made equipment. It was used double side polish Pyrex wafers (Siegert Wafer) from  $500 \pm 20$  to  $1000 \pm 20$   $\mu\text{m}$  thickness and a surface roughness below 1.2 nm. The Pyrex wafer was cleaned before use by immersing consecutively for 2 min on an ultrasonic bath with acetone, ethanol and water and dried with  $\text{N}_2$ . Si wafer was cleaned with the same procedure when possible, i.e., when the coating was not sensible to cleansing conditions (*in situ* growth of silicalite films), otherwise the Si surface was carefully cleaned using a cloth wetted in ethanol. Anodic bonding was carried out at 1000 V and a temperature from 250 to 450 °C (depending on the thermal properties of the adsorbent, i.e., on Cu-BTC devices was carried out at 250 °C whereas on silicalite and MCM-48 nanoparticles was performed at 450 °C). The duration of the procedure was controlled by visual inspection, a characteristic darkish, blue hue

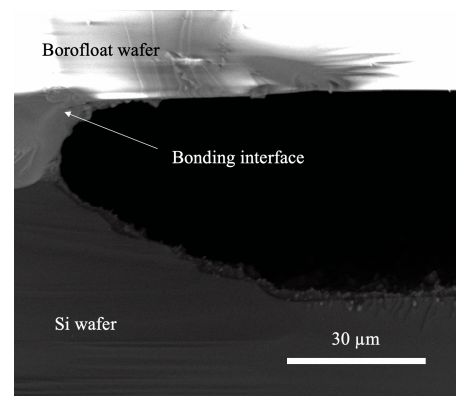
can be seen on the Si wafer when the bonding is performed, as can be seen on certain spots on the wafer on Figure 4.22.b. A SEM micrograph of the cross-section of a sealed wafer can be seen on Figure 4.22.c, where the Si-Pyrex interface can be perfectly recognized by the different contrast of each substrate: Pyrex appears highly bright due to its non-conductive nature, whereas Si presents a darker colour.



a)



b)



c)

Figure 4.22. a) Schematic of field-assisted thermal bonding or anodic bonding. b) Custom anodic bonding equipment at LMA. c) SEM microscopy of the Si and Pyrex wafer junction after bonded anodically.

#### 4. 3. 3. 2. Adhesive wafer bonding

Since anodic bonding requires the use of high temperature, this process is incompatible with some adsorbents that degrades at lower temperatures such as MOFs. Some synthesis methods, such as, layer-by-layer synthesis, result in the formation of small crystals on the glass surfaces that difficult or inhibit the contact between the interface, thus, the formation of the bonding.

Adhesive bonding is a low-temperature bonding process, whose main advantage is its applicability to different topologies of surfaces and the ability to join practically most common

materials. Adhesive wafer bonding does not require special wafer surface treatments and structures and/or particles on the wafer surfaces can be tolerated to some extent by the polymer adhesive. The adhesive used for this purpose has been the thermoresistant silicone Silcoset 158 (ACC Silicones), whose maximum working temperature is 300 °C and it can be cured at room temperature.

Adhesive wafer bonding has been used in this work to seal the devices coated with MOF-type materials that have been deposited either in the Pyrex wafer (Cu-BTC and Zn-DMCAPZ) or in the Si substrate (Zn-MIM). In the case of MOF growth on Pyrex wafer (such as electrochemically synthesized Cu-BTC and layer-by-layer growth Zn-DMCAPZ), it has been used as Si substrate those microfabricated according design 2.B.c, whose main feature is the outer trench that is used to canalize the adhesive and assess good sealing. Furthermore, to avoid any adhesive on the inner Si surface or over the adsorbent, an adhesive custom tape has been used as protecting masks. On the other hand, to seal the devices coated with Zn-mIM growth from ZnO deposited by ALD on the Si substrate, it has used a diced Pyrex wafer (whose size matches the substrate) and the glue has dispersed contouring both substrates.

#### 4. 3. 4. HEATING ELEMENT

The last step in the microdevice fabrication is the incorporation of a heating resistor and a sensing probe on the back side. This was carried out by a standard lift-off process with 150 nm of Au layer (with an adhesion layer of 50 nm Cr) deposited by Electron Beam Physical Vapor Deposition (EBPVD) (Edwards auto-500) and a photolithography resist used as a sacrificial layer (TI35ESX, Micromechanics). To guarantee electric isolation all over the back side of the wafer, it has been deposited a first layer of  $\text{Al}_2\text{O}_3$  over the Si also by EBPVD. The whole process run is depicted in Figure 4.23.

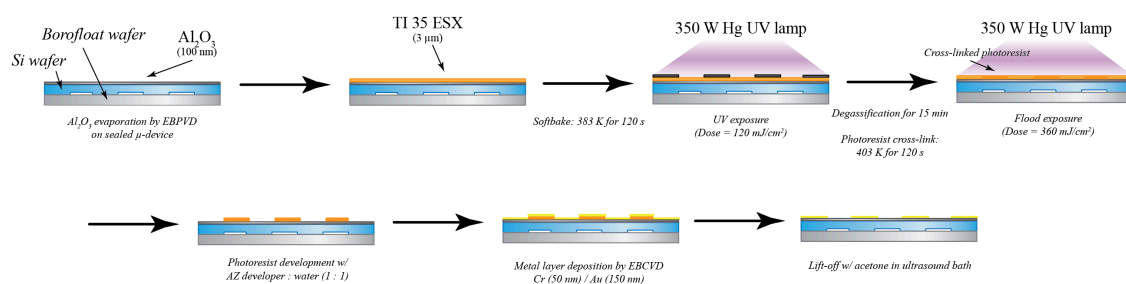


Figure 4.23. Incorporation of Au heating coil and sensing probe by standard lift-off process.

The sensing probe was calibrated by heating the Si substrate on a hotplate and measuring with a multimeter the increase in resistance value. The assay was performed in four different substrates. In Figure 4.24.a is shown the sensing probe calibration result from 313 to 523 K. As expected, the variation of the resistance value in the four tested substrates is linearly proportional to the temperature of the substrate, with a coefficient of determination of 0.9986. The temperature coefficient  $\alpha$  of the Au/Cr sensing probe was calculated solving:

$$R = R_{ref}(1 + \alpha(T - T_{ref})) \quad (26)$$

which yields  $\alpha = 2.18 \cdot 10^{-3} \text{ K}^{-1}$ , a value below Au ( $3.4 \cdot 10^{-3} \text{ K}^{-1}$ ) and Ch ( $3.0 \cdot 10^{-3} \text{ K}^{-1}$ ).

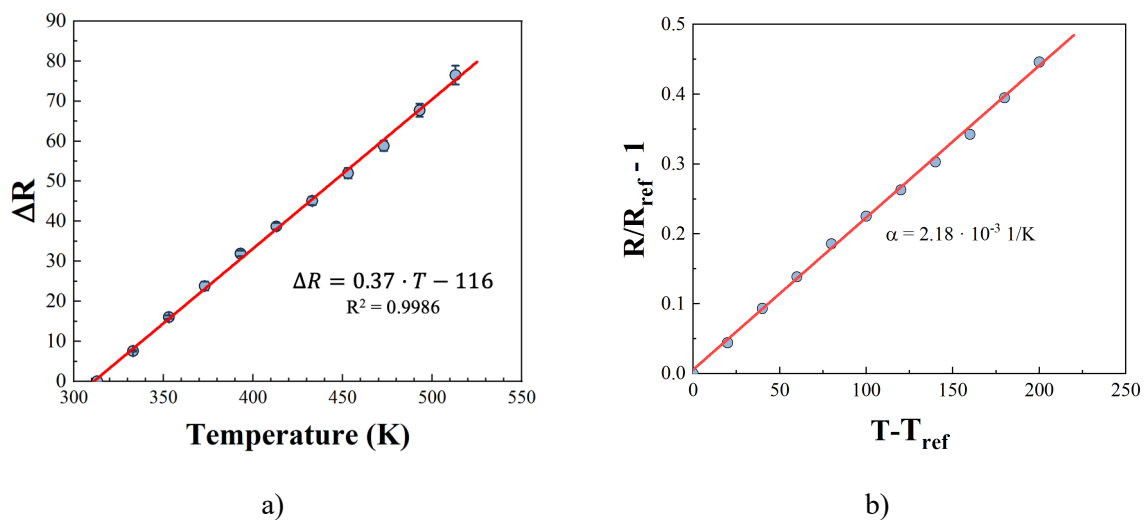


Figure 4.24. Sensing probe calibration results: a) resistance variation as a function of temperature, b) calculation of temperature coefficient of the Au film with intermediate adhesion layer of Cr (Cr/Au).

#### 4. 3. 5. FINAL MECHANIZATION

The sealed devices were diced using a computer aided diamond-saw and fluidic ports (1 mm in diameter) were drilled on the Borofloat side by sand blasting process (alumina dust 170 mesh). Three approaches were taken for microfluidic connections: 1) gluing 1/8" Swagelok stainless steel connections using an epoxy adhesive (Loctite Hysol 9492 A&B), 2) connecting 320  $\mu\text{m}$  fused-silica capillaries (Supelco) through a glued thermoresistive septa over the

Borofloat and 3) using a home-made PEEK housing with both fluidic (via 1/16" Teflon tubing) and electric connections built in.

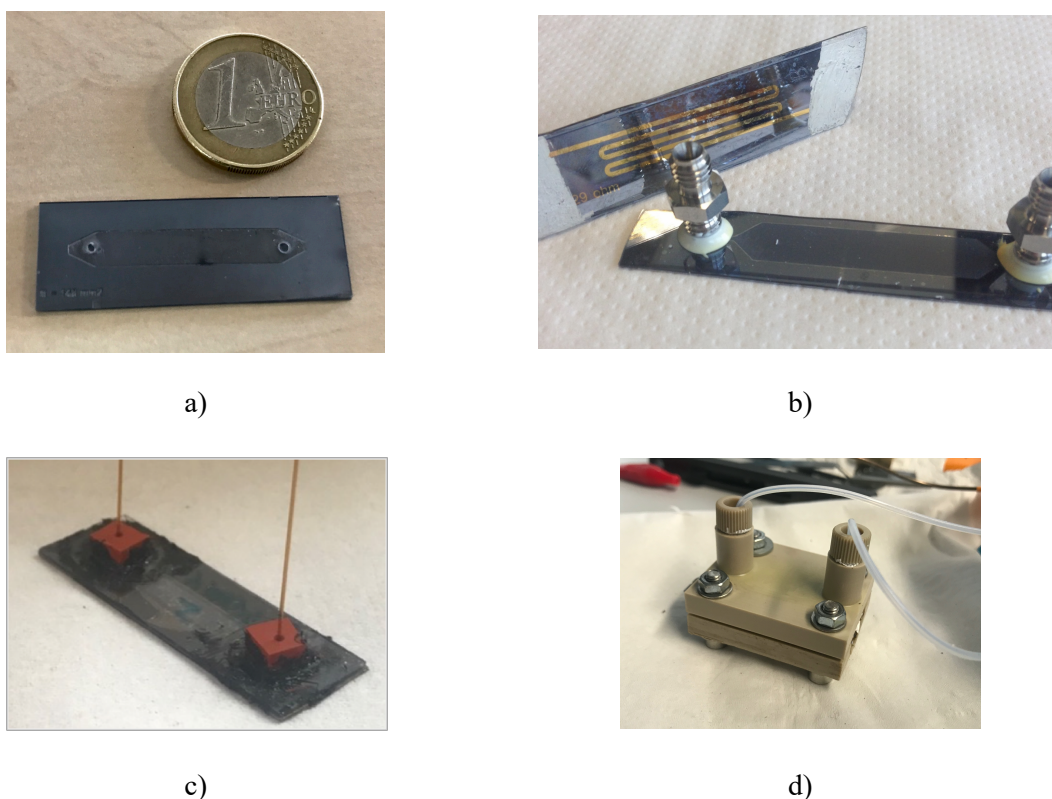


Figure 4.25. a) Fabricated microdevice with drilled inlet and outlet ports. b) Microdevice with 1/8" Swagelok fluidic ports glued with epoxy adhesive. c) Microdevice with 320  $\mu$ m fused silica capillary connection through high temperature septa glued with thermoresistant silicone. d) Custom PEEK housing with 1/16" Teflon tubing.

## 4. 4. SUMMARY OF THE MICRODEVICES

Throughout this work, several tens of microdevices have been fabricated. On Table 4.4 are compiled the main devices that have been characterized in this work. Among the designation that is going to be employ to refer to them in the next chapters, it is described the microdevice design, the depth of the microchannel (measured by profilometry), the adsorbent incorporated, as well as the coating procedure (HS: in situ hydrothermal synthesis, SC\_#: spin coating cycles, ES: electrochemically assisted synthesis on Cu layer over Pyrex substrate, LbL: layer-by-layer synthesis on Au layer over Pyrex substrate, HS-ALD: in situ hydrothermal synthesis using as a metal source a metal oxide deposited by atomic layer deposition, SD: static

deposition of the monomeric ionic liquid on Si substrate and subsequent photopolymerization, DD\_Si: dynamic deposition of the monomeric ionic liquids on an already sealed microdevices and photopolymerization on a Si substrate, DD\_Al<sub>2</sub>O<sub>3</sub>: dynamic deposition of the monomeric ionic liquids on an already sealed microdevices and photopolymerization on a Si substrate coated with an Al<sub>2</sub>O<sub>3</sub> layer).



TABLE 4.4. FABRICATION CHARACTERISTICS OF THE MICRODEVICES PRESENTED IN THIS WORK

Designation	Design	Cavity	Adsorbent	Coating method	Sealing
1.A-SIL-100um	1.A	W_100 $\mu$ m	Silicalite	HS	AB
1.B-SIL-100um	1.B	W_100 $\mu$ m	Silicalite	HS	AB
1.C-SIL-100um	1.C	W_100 $\mu$ m	Silicalite	HS	AB
1.D-SIL-100um	1.D	W_100 $\mu$ m	Silicalite	HS	AB
2.A-SIL-100um	2.A	W_100 $\mu$ m	Silicalite	HS	AB
2.B.a-SIL-100um	2.B.a	W_100 $\mu$ m	Silicalite	HS	AB
2.B.a-SIL-20um	2.B.a	W_20 $\mu$ m	Silicalite	HS	AB
2.B.a-MCM48-40um	2.B.a	W_40 $\mu$ m	MCM – 48	SC_10	AB
2.B.a-MCM48-8um-SC_1	2.B.a	D_8 $\mu$ m	MCM – 48	SC_1	AB
2.B.a-MCM48-8um-SC_20	2.B.a	D_8 $\mu$ m	MCM_48	SC_20	AB
2.B.b-CuBTC-20um-ES	2.B.b	W_20 $\mu$ m	Cu – BTC	ES	G
2.B.a-ZnDMCAPZ-20um-SC	2.B.a	W_20 $\mu$ m	Zn –DMCAPZ	SC	AB
2.B.b-ZnDMCAPZ-20um-LbL	2.B.b	W_20 $\mu$ m	Zn – DMCAPZ	LbL	G
2.B.b-ZnMIM-20um-SC	2.B.b	W_20 $\mu$ m	Zn – mIM	SC	G
2.B.b-ZnMIM-20um-ALD	2.B.b	W_20 $\mu$ m	Zn – mIM	HS – ALD	G
2.B.b-PIL-40um-SDSi	2.B.b	W_40 $\mu$ m	PIL	SD	G
2.B.a-PIL-40um-DDSi	2.B.a	W_40 $\mu$ m	PIL	DD_Si	AB
2.B.a-PIL-20um-DDSi	2.B.a	W_20 $\mu$ m	PIL	DD_Si	AB
2.B.c-PIL-20um-DDSi	2.B.c	D_20 $\mu$ m	PIL	DD_Si	AB
2.B.d-PIL-20um-DDSi	2.B.d	D_20 $\mu$ m	PIL	DD_Si	AB
2.B.c-PIL-20um-DDAl <sub>2</sub> O <sub>3</sub>	2.B.c	D_20 $\mu$ m	PIL	DD_Al <sub>2</sub> O <sub>3</sub>	AB
2.B.d-PIL-20um-DDAl <sub>2</sub> O <sub>3</sub>	2.B.d	D_20 $\mu$ m	PIL	DD_Al <sub>2</sub> O <sub>3</sub>	AB



**CHAPTER V:**  
**ADSORPTION OF**  
**ORGANOPHOSPHORUS COMPOUNDS ON**  
**FUNCTIONAL  $\mu$ -PRECONCENTRATORS**



## **5. ADSORPTION OF ORGANOPHOSPHORUS COMPOUNDS ON FUNCTIONAL $\mu$ -PRECONCENTRATORS**

### **5. 1. INTRODUCTION**

This Chapter is dedicated to the evaluation of the microporous and mesoporous materials, as well as poly-ionic liquid films (presented in Chapter II) which have been integrated into  $\mu$ -fluidic devices fabricated as described in Chapter IV, for nerve agents (NAs) preconcentration using as target the sarin gas surrogate: dimethyl methyl phosphonate (DMMP). As stated on Chapter III, the preconcentration of explosive related compounds was not a feasible as they are masked by the rest of the compounds used to stabilize and mask/hide the energetic compound (wax, paraffins, taggants). Some of these compounds may present higher volatility, so the preconcentration stage has to be selective and quantitative enough to avoid false negative alarms. On the other hand, chemical warfare agents are relatively easier to identify since they are used without further additives. Additionally, since they present acute toxicity at extremely low concentrations [16], the usage of a preconcentration stage upstream of a gas detector is a common solution to enhance the analytical performance of the whole systems.

Firstly, different analytic expression to evaluate the DMMP sorption process on modified  $\mu$ -preconcentrators are described. In addition, a 3D mathematical model, implemented in COMSOL Multiphysics, has been developed to simulate the fluid and sorbent phase evolution during the sorption process. Thus, the most suitable operational conditions (flow rate, sorption time) for the fabricated  $\mu$ -preconcentrators could be determined. Finally, the results in this chapter would allow us to propose improved designs (dimensions of the sorption layer, depth of the  $\mu$ -fluidic cavity) with outperforming preconcentration performance for ‘on-field’ application.

### **5. 2. ADSORPTION PROCESS ON FIXED SORBENTS**

Sorption dynamics of the modified  $\mu$ -preconcentrators were evaluated by analysis of the monitored breakthrough curve. A typical breakthrough curve, as depicted on Figure 5.1, follows the evolution in time or volume (of circulated gas) of the eluted analyte concentration

downstream of the sorption unit. Mostly, the eluted concentration  $C_x$  is normalized by the feeding concentration  $C_0$ , so it ranges from 0 to 1.

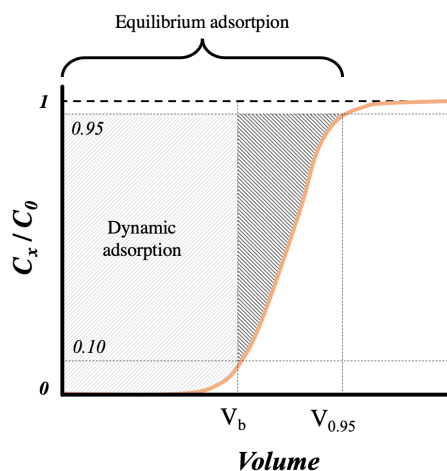


Figure 5.1. Typical breakthrough curve where the normalized concentration is plotted as a function of the volume that has been circulated inside the sorption unit.

For this work, we have considered breakthrough point as the moment where  $C_x/C_0 = 0.1$ , which implies that the adsorbent is becoming saturated and begins to be unable to trap all the analyte molecules carried by the feeding gas. The moment at which breakthrough takes place is denoted as breakthrough time ( $t_b$ ). Similarly, the volume that has been fed to the bed is defined as breakthrough volume ( $V_b = t_b * Q_{feed}$ , being  $Q_{feed}$ : feed volumetric flow). The ratio of uptake sorbate (target analyte) mass up to breakthrough point ( $m_b$ ) to the sorbent mass is defined as dynamic sorption capacity ( $W_d$ ). Analogously, the point where the adsorbent is exhausted is denoted as saturation point; and in this work, we considered that it takes places when  $C_x/C_0 = 0.95$ , this point determines the equilibrium sorption capacity when working in dynamic conditions ( $W_e$ ). The maximum mass of sorbate can be calculated by integrated the area above of the breakthrough curve (up to  $C_x/C_0 = 0.95$ ). The ratio of dynamic sorption capacity to equilibrium sorption capacity is denoted as bed efficiency. It is an indicator of the practical usage of the adsorbent capacity. A bed efficiency of 100 % would indicate that there is no mass transfer limitations and all the available sorption capacity would be used before breakthrough. On the contrary, an efficiency close to 0 % would indicate that the sorption rate is controlled by external/internal diffusion and the target molecules are eluting from the sorption unit even at low sampling volumes. Low bed efficiencies could be attributed to low sorbent affinity towards the sorbate, low effective diffusivity values (due to very torturous pores or strong chemical

interactions between pore walls and target molecules) or steric hindrance (pore size less than the kinetic diameter of target molecule).

### 5. 2. 1. WHEELER MODEL

---

The Wheeler adsorption rate equation was firstly published in 1969 by Wheeler to describe the adsorption process of VOCs over granular activated carbon packed beds assuming isothermal conditions, homogenous carbon granular distribution, invariable bed capacity (working at the plateau region in the isotherm) and lack of any other parametric interrelationships [184]. It is derived from a mass balance between vapor entering, retained within and exiting the bed. Although it is commonly used for determining the service life-time of air-purifying respirator cartridges – mostly packed with activated charcoal – it has also been employed to characterize sampling cartridges and preconcentrators in similar scenarios as we proposed [133].

The time required for a certain fractional breakthrough (typically, 1 to 10%) to occur can be calculated as follows:

$$t_b = \frac{W_e \rho_b}{C_0} \left[ \tau - \frac{1}{k_v} \ln \left( \frac{C_0}{C_x} \right) \right] \quad (27)$$

where  $t_b$  is the gas breakthrough time (min),  $C_0$  is the inlet concentration ( $\text{g}/\text{cm}^3$ ),  $C_x$  is the outlet concentration ( $\text{g}/\text{cm}^3$ ),  $\tau = W_b/(\rho_b Q)$  is the bed residence time (min),  $Q$  is the volumetric flow rate ( $\text{cm}^3/\text{min}$ ),  $\rho_b$  is the bulk density of the material ( $\text{g}/\text{cm}^3$ ),  $k_v$  is the pseudo first adsorption rate constant ( $\text{min}^{-1}$ ),  $W_b$  is the adsorbent weight (g) and  $W_e$  is the saturation capacity ( $\text{g}/\text{g}$ ). (27) is sustained assuming negligible desorption of adsorbed molecules (high equilibrium adsorption constant and low concentration of analyte) and inlet concentration large enough to assure being on the plateau of the adsorption isotherm, i.e. invariant equilibrium sorption capacity [185].

In (27),  $\rho_b$  is determined as a property of the adsorbent material. Originally, it was conditioned by the granular size of the adsorbent – granular activated carbon – when filled by gravity settling in a container column.  $C_0$ ,  $C_x$  and  $Q$  are set by the test conditions. When plotting  $t_b$  as a function of  $W_b$ , experimental points lie on a straight line from whose slope and x-axis intercept, the properties of  $W_e$  and  $k_v$  can be calculated. The x-axis intercept ( $\rho_b Q/k_v$ ) in  $C_0/C_x$  is considered to be the critical bed weight or that weight of adsorbent just sufficient to reduce

the inlet concentration to the chosen exit concentration.  $W_e$  is a function of relative pressure or concentration and thus depends on  $C_0$ . Finally, to determine  $k_v$  we must first define the adsorption process as an equilibrium reaction between the chemical species in the gas phase ( $A_{gas}$ ) and the species adsorbed in the solid ( $A^*$ ) that takes place at certain temperature. Furthermore, the chemical species is adsorbed with a certain rate of adsorption and, at the same time, desorbs with a certain rate of desorption:



During adsorption we considered that  $k_1 \gg k_{-1}$ , thus the desorption process is negligible, so we can express the adsorption ratio as:

$$r_{ads} = k_1[*][A] = k_v[A] \quad (29)$$

where  $[*]$  is the concentration of active sites on the sorbent and  $[A]$  is the species concentration in the gas phase.

### 5. 2. 2. YOON-NELSON MODEL

Yoon and Nelson presented in 1984 a semi-empirical gas adsorption model that was able to predict the whole breakthrough curve of gases in activated charcoal [186]. It assumes that the rate of decrease in the probability of adsorption for each adsorbate molecule is probability of adsorbate breakthrough of the adsorbent. Outlet concentration can be expressed as (30).

$$C_x = C_0 \frac{1}{1 + e^{k_{YN}(\tau_{YN} - t)}} \quad (30)$$

where  $k_{YN}$  is a kinetic constant ( $\text{min}^{-1}$ ) and  $\tau_{YN}$  is the breakthrough time when  $C_x/C_0 = 0.5$ .

If we rewrite both Wheeler and Yoon-Nelson equations to an expression in the form  $\ln(C_x/(C_0 - C_x)) = a \cdot t - b$  we get (31) from the Wheeler model and (32) from the second.

$$\ln\left(\frac{C_x}{C_0 - C_x}\right) = \frac{k_v C_0}{\rho_b W_e} t - \frac{k_v W_b}{\rho_b Q} \quad (31)$$

$$\ln\left(\frac{C_x}{C_0 - C_x}\right) = k_{YN} t - \tau_{YN} k_{YN} \quad (32)$$

This reformulation allows easily to relate both models through (33) and (34).



$$k_{YN} = \frac{k_v C_0}{\rho_b W_e} \quad (33)$$

$$\tau_{YN} = \frac{k_v W_b}{k_{YN} \rho_b Q} \quad (34)$$

Since this model is easier to implement in the commercial software OriginPro 2018 (OriginLab), the Wheeler model parameters ( $k_v$ ,  $W_e$ ) have been estimated from the fitting of the experimental breakthrough curves using the Yoon-Nelson model.

## 5.3. COMPUTATIONAL SIMULATION OF SORPTION PROCESS ON $\mu$ -PRECONCENTRATORS

A computational model of the adsorption process has been implemented using FEM software COMSOL Multiphysics.

### 5.3.1. MATHEMATICAL MODEL

The 3-D finite element model considers three coupled phenomena: fluid dynamics, transport of diluted species and surface reaction. Fluid dynamics model pressure gradient and velocity distribution of the circulating gas inside the microfluidic cavity. Transport of diluted species models the concentration profile of the sorbate in the carrier gas along the  $\mu$ -preconcentrator. Finally, the surface reaction models the consumption of sorbate in the gas phase due to its adsorption on the active sorptive layer. Transport of diluted species coupled with surface reaction module allows to simulate the special distribution of concentration on both the gas and the adsorbent phase as a function of time on stream.

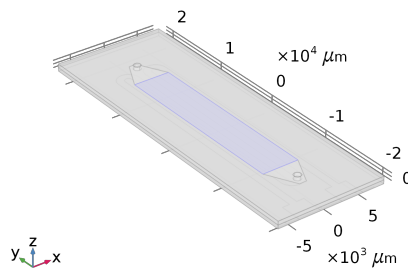


Figure 5.2. 3D model of the  $\mu$ -fluidic device. The blue section indicates the adsorbent coating.

The determination of adsorption parameters  $k_{ads}$  and  $W_e$  we have taken the inverse model approach. Thus, to get the desired simulation results, we are going to look for the optimal values of  $k_{ads}$  and  $W_e$  that provide the closest match between our experimental data and the simulation solutions. The optimization method is based on the minimization of the sum of the squares of the differences between the data sets, and the problem is going to be formulated as a least-squares optimization problem.

The simulated system parameters are compiled on Table 5.1. We are considering the case of a compressible fluid, so viscosity and density other carrier gas are pressure and temperature dependant.

TABLE 5.1. PARAMETERS EMPLOYED TO MODEL THE ADSORPTION PROCESS INSIDE THE  $\mu$ -DEVICE

Geometry parameters	Value
Adsorbent length, $l_1$	25 mm
$\mu$ -device length, $l_2$	33 mm
Adsorbent width, $w_1$	5 mm
$\mu$ -device width, $w_2$	1 mm
Si wafer thickness, $t_{Si}$	500 $\mu$ m
Borofloat wafer thickness, $t_{pyrex}$	500 $\mu$ m
$\mu$ -channel depth, $t_{\mu C}$	20 / 40 / 100 $\mu$ m
Adsorbent thickness, $t_{ads}$	From 0.8 to 9.16 $\mu$ m
Inlet/outlet diameter, $d_{inlet/outlet}$	1 mm
Gas parameters	Value
Dynamic viscosity, $\mu$	$17.6 \cdot 10^{-6}$ Pa·s
Density, $\rho$	1.16 kg/m <sup>3</sup>
Temperature, T	293 K
Hexane diffusion in N <sub>2</sub> , $D_{hexane}$	$20 \cdot 10^{-6}$ m <sup>2</sup> /s
Feeding flowrate	5 / 10 STP cm <sup>3</sup> /min
Hexane feeding concentration, $C_{0, hexane}$	$41 \cdot 10^{-4}$ mol/m <sup>3</sup>
DMMP feeding concentration, $C_{0, DMMP}$	$13 \cdot 10^{-4}$ mol/m <sup>3</sup>

5. 3. 1. 1. Fluid dynamics

Alike Chapter IV, the carrier gas inside the microcavity was modelled considered laminar regime and compressive fluid flow. Since transient state is not relevant for our study as the microdevice always work with a steady gas flow, we only considered stationary state study, i.e., non-time dependent. The equations that describes carrier gas flow inside the microcavity are the following:

$$\nabla \cdot (\rho \mathbf{u}) = 0 \quad (35)$$

$$0 = \nabla \cdot \left[ -p\mathbf{I} + \mu(\nabla \mathbf{u} + (\nabla \mathbf{u})^T) - \frac{2}{3}\mu(\nabla \cdot \mathbf{u})\mathbf{I} \right] + \mathbf{F} \quad (36)$$

where  $\rho$  is the density ( $\text{kg/m}^3$ ),  $\mathbf{u}$  is the velocity vector ( $\text{m/s}$ ),  $p$  is pressure (Pa),  $\mu$  is the dynamic viscosity ( $\text{Pa}\cdot\text{s}$ ) and  $\mathbf{F}$  is the volume force vector ( $\text{N/m}^3$ ).

(35) is the continuity equation and represents the conservation of mass, which is derived by considering a unit volume of the medium and states that the rate of increase of the mass of the carrier gas within an elementary unit equals to the net mass flux into the volume. The conservation of momentum is stated by (36). Since we are dealing with a stationary state study, acceleration forces that are represented on the left side are considered null; on the other hand, the right side represents pressure gradient and viscosity forces. Besides, in order to solve those equations, the following assumptions are made:

4. Carrier gas flow rate is fixed at the inlet of the microdevice and constant during the overall experiment.
5. No slip condition on the walls of the microcavity,  $\mathbf{u} = 0$ .
6. Outflow is at atmospheric pressure.

5. 3. 1. 2. Transport of diluted species

The analyte concentration distribution at the gas phase is modelled according the second Fick's law, considering both diffusion and convection transports mechanism (37). Unlike the carrier gas, the concentration of analyte in the gas phase is not constant through time, i.e., time-dependant study, since we have a consumption of diluted species as they are being adsorbed. The consumption rate  $R$  is equally time and spatial dependant, since depends on the degree of saturation of such layer. The following equations are solved to describe the distribution of the sorbate molecules through time on stream:

$$\mathbf{N} = -D\nabla c + \mathbf{u}c \quad (37)$$

$$\frac{\partial c}{\partial t} + \nabla \cdot (-D\nabla c) + \mathbf{u} \cdot \nabla c = R \quad (38)$$

where  $c$  is the concentration of the diluted specie in gas phase ( $\text{mol}/\text{m}^3$ ),  $D$  is the diffusion coefficient of analyte in the carrier gas ( $\text{m}^2/\text{s}$ ),  $\mathbf{u}$  is the flow velocity,  $R$  is the consumption rate of the sorbate due to adsorption on the sorptive layer ( $\text{mol}/(\text{m}^3 \cdot \text{s})$ ) and  $N$  is the concentration flux ( $\text{mol}/(\text{m}^2 \cdot \text{s})$ ).

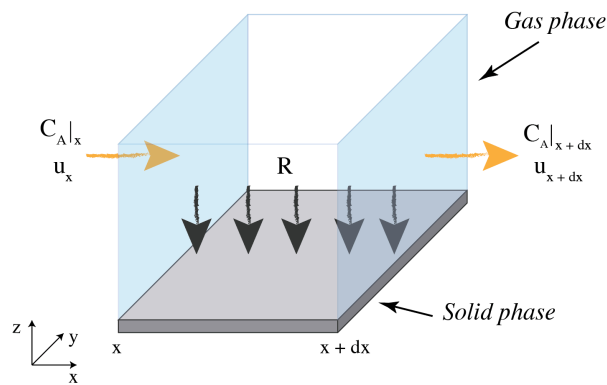


Figure 5.3. Gas phase mass balance on a differential volume.

In (38), the first term of the left side is the rate of accumulation of the diluted specie, whilst the second term indicates the mass transport due to diffusion of the specie in the carrier gas and the third the transport due to convection. The velocity field  $\mathbf{u}$  has been calculated previously by fluid dynamics. On the right side, the term  $R$  represents the increase of species inside the system due to an external inward flux (Figure 5.3). In this case, we must consider an outward flux due to the fact that the adsorbent acts as a sink point, and thus adsorbing flux is formulated as  $-R$ . Also, the following assumptions have been made:

1. Inlet concentration is constant and known through the whole sorption period simulation,  $c = C_0$ .
2. At the outlet it is assumed that convection is the dominating transport mechanism, and that the diffusive transport can be neglected, thus  $\mathbf{n} \cdot (-D\nabla c) = 0$ , considering  $\mathbf{n}$  the surface normal vector.

3. Only outward flux is located at the adsorbent boundary and it is due to adsorption, i.e.,  $\mathbf{n} \cdot \mathbf{N} = \mathbf{n} \cdot (c\mathbf{u} - D\nabla c) = R$ . At the rest of the boundaries,  $-\mathbf{n} \cdot \mathbf{N} = 0$ .

### 5.3.1.3. Surface reaction

The adsorption process has been modelled as a surface reaction between the gas species and the adsorbent boundary. To model the equilibrium reaction on the surface, we considered the Langmuir adsorption model. This model is based on the following assumptions:

1. There is a maximum surface concentration of adsorbate at which the surface becomes saturated.
2. Adsorption rate constants do not depend on the partial coverage of adsorbate, i.e., adsorption sites are identical and mutually independent.
3. Adsorption is a pseudo first order process whose rate is linear in the adsorbate concentration in the bulk phase adjacent to the surface, as well as the proportion vacant of sites:

$$r_{ads} = k_1[A][*] \quad (39)$$

4. Desorption is a first order process whose rate is linear in the partial coverage of adsorbate:

$$r_{des} = k_{-1}[A*] \quad (40)$$

Considering the aforementioned assumptions, at the adsorbent surface we have the following mass balance:

$$\frac{\partial c_s}{\partial t} + \nabla \cdot (-D_s \nabla c_s) = r_{ads} - r_{des} = R \quad (41)$$

where  $c_s$  is the concentration of the specie on the sorptive surface ( $\text{mol}/\text{m}^2$ ),  $D_s$  is the diffusion coefficient of the specie inside the sorbent material,  $r_{ads}$  is the adsorption rate ( $\text{mol}/(\text{m}^2 \cdot \text{s})$ ) and  $r_{des}$  is the desorption rate ( $\text{mol}/(\text{m}^2 \cdot \text{s})$ ). Following Langmuir adsorption model,  $r_{ads}$  and  $r_{des}$  are expressed as:

$$r_{\text{ads}} = k_1 \cdot p_A \cdot * \quad (42)$$

$$r_{\text{des}} = k_{-1} \cdot A^* \quad (43)$$

where  $k_1$  is the forward rate of adsorption, i.e., from gas phase to the surface;  $p_A$  is the partial pressure of the diluted specie (Pa);  $A^*$  is the fraction of active sites occupied by adsorbed molecules and  $k_{-1}$  is the reverse rate of adsorption, i.e., from surface to gas phase. To couple surface concentration of the specie to gas concentration of the specie, we rewrite (42) and (43) into (44) (45) considering  $A^* = c_s / \Gamma_s$  and  $p_A = c \cdot R \cdot T$ , where  $\Gamma_s$  is the total surface concentration of active sites ( $\text{mol}/\text{m}^2$ ),  $c$  is the concentration of the specie in the gas phase ( $\text{mol}/\text{m}^3$ ),  $R$  is the gas constant ( $\text{J}/(\text{mol}\cdot\text{K})$ ) and  $T$  is temperature (K).

$$r_{\text{ads}} = k_{\text{ads}} \cdot c \cdot \left(1 - \frac{c_s}{\Gamma_s}\right) \quad (44)$$

$$r_{\text{des}} = k_{\text{des}} \cdot \frac{c_s}{\Gamma_s} \quad (45)$$

where  $k_{\text{ads}} = k_1 \cdot R \cdot T$  is the rate constant for adsorption ( $\text{m}/\text{s}$ ) and  $k_{\text{des}} = k_{-1}$  is the desorption kinetic constant ( $\text{mol}/(\text{m}^2\cdot\text{s})$ ). Finally, considering (44) and (45), (41) yields to:

$$\frac{\partial c_s}{\partial t} + \nabla \cdot (-D_s \nabla c_s) = k_{\text{ads}} \cdot c \cdot \left(1 - \frac{c_s}{\Gamma_s}\right) - k_{\text{des}} \frac{c_s}{\Gamma_s} \quad (46)$$

Lastly, the following assumption have been made:

1. We considered the adsorbent as a 2D geometry and no diffusion of the specie inside the material, thus  $\nabla \cdot (-D_s \nabla c_s) = 0$ .
2. We considered at room temperature that the desorption rate is negligible in comparison with the adsorption rate, thus we can assume  $k_{\text{des}} = 0$ .
3. At initial time, we have a fresh adsorbent, with no specie adsorbed on it.
4. The boundary condition at the fluid/solid interphase results through the coupling of the mass balance in the fluid phase with the sorption rate on the active surface:

$$\mathbf{n} \cdot (-D \nabla c + \mathbf{c} \mathbf{u}) = -k_{\text{ads}} \cdot c \cdot \left(1 - \frac{c_s}{\Gamma_s}\right) \quad (47)$$

5.3.2. EVALUATION OF ADSORPTION PARAMETERS  $K_{ADS}$  AND  $\Gamma_s$ 

The estimation of the adsorption rate ( $k_{ads}$ ) and the surface concentration of active sites ( $\Gamma_s$ ) were calculated by fitting experimental data to computational results by the least square method. This approach is based on the minimization of the error between experimental to modelled data through a least square objective function (40), where  $c_{exp,t}$  is the experimental data at time  $t$  and  $c_{out,CFD,t}$  is the modelled result at the same time  $t$ .

$$obj = \sum_t (c_{exp,t} - c_{out,CFD,t})^2 \quad (48)$$

We used the sparse nonlinear optimizer (SNOPT) parameter estimation method [187], which is a general-purpose system for constrained optimization. In our case, we used an optimality tolerance of  $10^{-3}$  and initial parameter values were  $k_{ads} = 1$  m/s and  $\Gamma_s = 1$  mol/m<sup>2</sup>.

Experimental breakthrough data was obtained for a 100  $\mu$ m-depth  $\mu$ -preconcentrator loaded with 1184  $\mu$ g silicalite evaluated for 352 mg/m<sup>3</sup> n-hexane in dry N<sub>2</sub> at room temperature. The gas mixture was prepared in a 10 L Tedlar bag and drag at 5 STP cm<sup>3</sup>/min through the  $\mu$ -device using a vacuum pump (UN86KTDC, KNF Neuberger) downstream and a needle valve to control the flow rate. The eluted gas has been monitored using a gas chromatograph with a flame ionizator detector (Agilent/HP 6890) and injecting an aliquot of the outlet stream via an automatic six-port valve equipped with a 250  $\mu$ L sampling loop into a GC column (6 m long, 320  $\mu$ m inner diameter, 0.25  $\mu$ m thick Rtx-1 stationary phase, Restek).

Figure 5.4 shows the evolution of n-hexane through time both in the gas and in the solid phase that have been modelled using the experimental data as reference. Under those conditions, the objective function (40) is locally minimal when  $k_{ads} = 6.46 \cdot 10^{-3}$  m/s and  $\Gamma_s = 5.07 \cdot 10^{-3}$  mol/m<sup>2</sup>. As can be seen on Figure 5.4.a-d, the outlet n-hexane concentration modelled fits satisfactorily with the experimental data and we can see how the adsorption of the analyte is being performed uninformedly without exhibiting any preferential spots. Furthermore, the modelled results allow us to visualize the mass transfer wave front along the time on stream (Figure 5.4.e-h) which experimentally is not possible to be registered.

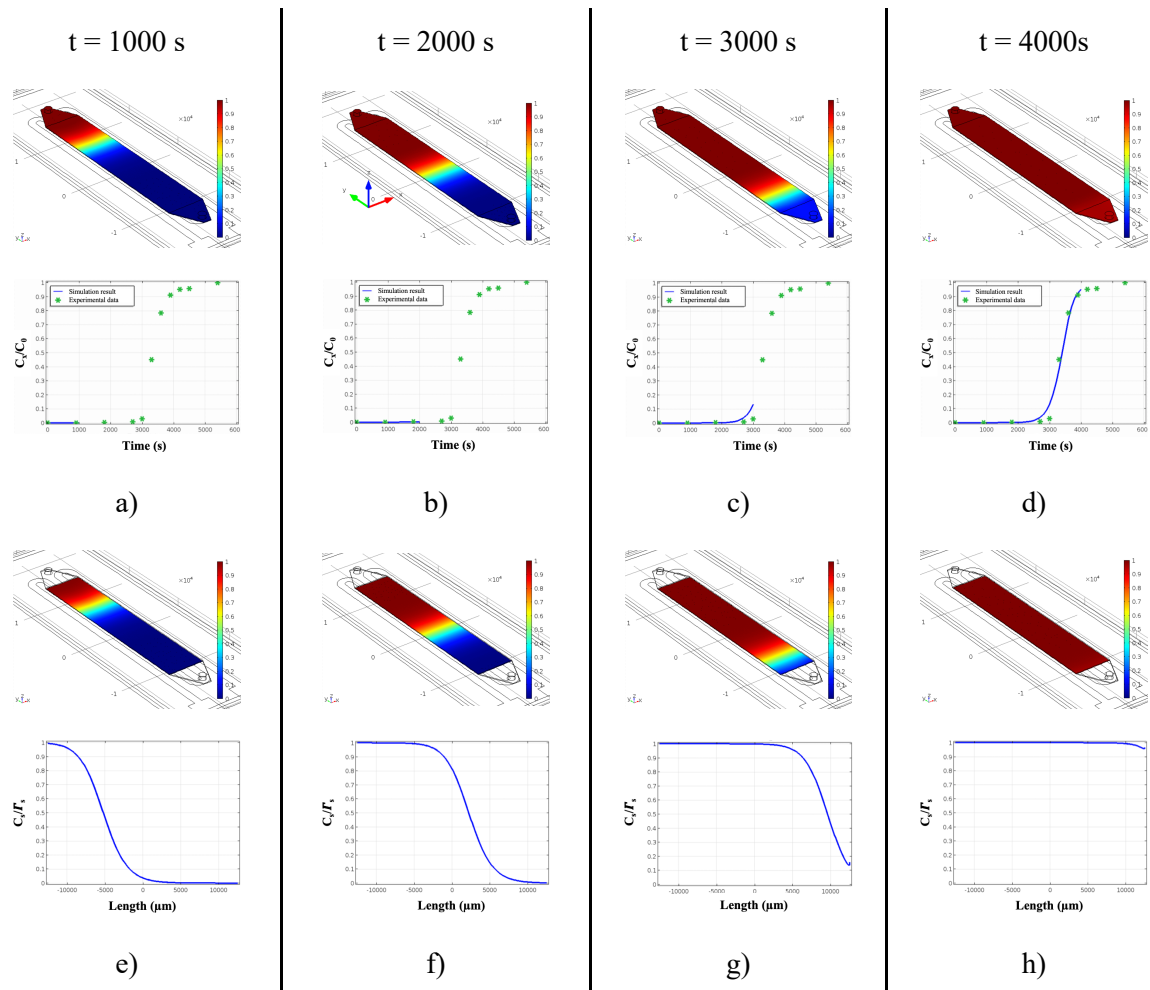


Figure 5.4. Evolution of gas phase concentration through time ( $C_g/C_0$  vs  $t$ ): upper is depicted the concentration profile along the fluidic path whereas down it is shown the experimental breakthrough data along the average normalized concentration at the outlet: a)  $t = 1000$  s, b)  $t = 2000$  s, c)  $t = 3000$  s and d)  $t = 4000$  s. Evolution of solid phase concentration through time ( $C_s/G_s$  vs  $t$ ): upper is depicted the concentration at the adsorbent surface whereas down it is shown the concentration across the  $y$ -axis: e)  $t = 1000$  s, f)  $t = 2000$  s, g)  $t = 3000$  s and h)  $t = 4000$  s.

Additionally, to further validate the results calculated from the 3D CFD model, it has been calculated experimentally the value of  $\Gamma_s$ . Using a silicalite-coated  $\mu$ -cantilever as a mass sensor (as described on Chapter III), n-hexane atmospheres in range of concentration from 352  $\text{mg}/\text{m}^3$  to 1756  $\text{mg}/\text{m}^3$  in dry  $\text{N}_2$  at room temperature have been measured to determine  $W_e$  of the silicalite sorbent (Figure 5.5.a). The different n-hexane mixtures have been prepared from a calibrated 3517  $\text{mg}/\text{m}^3$  pressured tank in dry  $\text{N}_2$  and further dilution with dry  $\text{N}_2$ . The mass gain of the adsorbent has been registered after reaching equilibrium with its surroundings. Pseudoequilibrium capacity values (ratio of sorbate to adsorbent mass) have been plotted and



fitted to a Langmuir isotherm with a coefficient of determination of  $R^2 = 0.9913$  (Figure 5.5.b). When comparing the modelled equilibrium sorption capacity of the silicalite  $W_e$  (which can be calculated from  $\Gamma_s$  considering and adsorbent interface surface of  $1.25 \text{ cm}^2 - w_1 \times l_1$  – adsorbent thickness of  $4 \text{ }\mu\text{m}$  and density of silicalite of  $2.2 \text{ g/cm}^3$ ) with the calculated from cantilever experiments, the error between both is below 10 % ( $W_{e,\text{Silicalite}} = 5.46 \text{ \%wt}$  vs  $W_{e,\text{experimental}} = 5.02 \text{ \%wt}$ ).

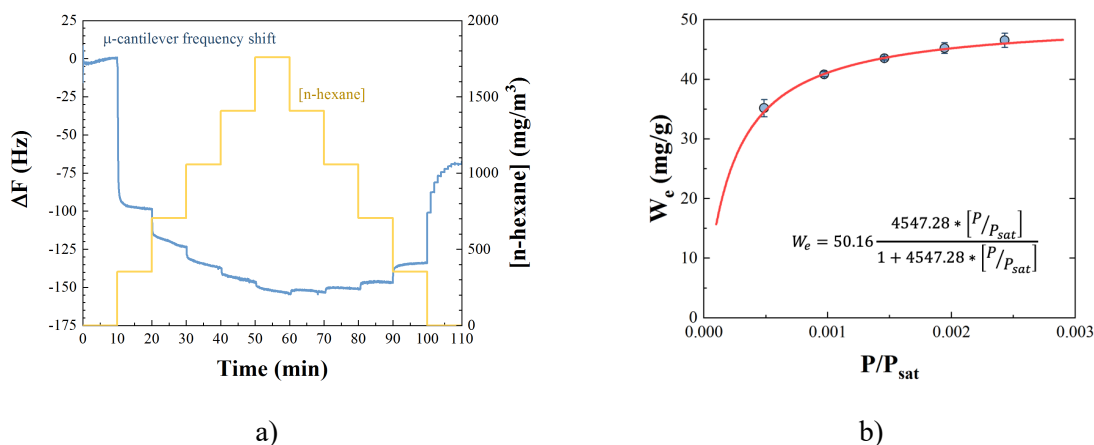


Figure 5.5. Evaluation of equilibrium sorption capacity using silicalite-coated  $\mu$ -cantilevers. a)  $\mu$ -cantilever frequency shift as result of adsorbent mass gain after being exposed to n-hexane in the range of concentration from  $352 \text{ mg/m}^2$  to  $1756 \text{ mg/m}^3$  at 293 K. b) n-hexane adsorption isotherm of silicalite fitted to the Langmuir equation with a coefficient of determination of 0.9913.

Although, the proposed mathematical model is considered satisfactory for the simulation of n-hexane sorption on silicalite-modified pre-concentrator. However, some consideration of the limitations of the model must be taken. We have considered that the adsorption process is not hindered by diffusional limitations in the sorptive layer. Depending on the sorbate properties (kinetic diameter, polarity, chemical structure) and the adsorbent material (textural properties, tortuosity of inner channels, surface chemistry of pore walls), the sorbate-sorbent interactions are notably affected and adsorption process may be heavily influenced by internal diffusion, and thus, invalidating the proposed model. In order to overcome this limitation, the model should have considered the nature of the sorptive coating (layer thickness; macro-, meso- and microporosity values; intra- and intercrystalline diffusion coefficient of analyte into the sorptive phase), which is beyond the scope of this work. Taking this limitation into account, the

computational model has been applied on those cases where  $\mu$ -preconcentrator bed efficiency show values higher than 80 %.

## **5. 4. EXPERIMENTAL SET-UP USED FOR THE EVALUATION OF PERFORMANCE OF MODIFIED $\mu$ -DEVICES**

### **5. 4. 1. TRACE-LEVEL ANALYTE ATMOSPHERES GENERATION**

---

Different strategies were approached to generate test atmospheres: calibrated gas bottles, *ad-hoc* gas bags, and permeation tubes.

#### 5. 4. 1. 1. Calibrated gas bottles

Calibrated gas bottles are the easiest approach to arrange a reliable, trace-level gas stream. They are high pressure, gas cylinders of certain volume filled with a small amount of analyte, which is certified by the provider, and a dilution gas (commonly air or nitrogen), thus the outlet concentration is known. Unfortunately, this solution is not available for any analyte, since the stability of the gas mixture inside the cylinder depends on the chemical properties of the analyte.

In our case, a calibrated 500 ppmV n-hexane bottle gas was used. The flow fed to the microdevice was controlled with a massflow controller. In order to provide smaller n-hexane concentrations, and additional stream of N<sub>2</sub> was used for dilution.

#### 5. 4. 1. 2. Tedlar sampling bags

Tedlar sampling bags (Supelco) are small volume (1 L to 10 L), inert PVF (polyvinyl fluoride) bags used to collect samples of gases. For this work, the bags were filled with dry N<sub>2</sub> and a small amount in liquids form of target compound was injected and let evaporated. Knowing the amount of gas in the bag as well as the injected analyte, a theoretical concentration can be calculated assuming full evaporation and no preferential adsorption on the walls of the bag or the inlet septum. This method was used to prepare gas mixtures of n-hexane, toluene and DMMP in dry N<sub>2</sub> as well as in the presence of interferent. For this work, bags containing 162 mg/m<sup>3</sup> and 267 mg/m<sup>3</sup> DMMP in dry N<sub>2</sub> at room temperature, 377 mg/m<sup>3</sup> toluene in dry N<sub>2</sub> and 352 mg/m<sup>3</sup> n-hexane as well as gas mixtures of DMMP-toluene (162 mg/m<sup>3</sup> DMMP and 120 mg/m<sup>3</sup> toluene and 267 mg/m<sup>3</sup> DMMP and 377 mg/m<sup>3</sup> toluene) and DMMP-n-decane (162

mg/m<sup>3</sup> DMMP and 120 mg/m<sup>3</sup> n-decane). Gas mixtures of DMMP and water (162 mg/m<sup>3</sup> DMMP and 30% RH at 293 K) were also prepared but eventually could not be used since DMMP was hydrolysed and decomposed in contact with water [188], thus the concentration was not stable.

#### 5.4.1.3. *Permeation tube*

Permeation tubes are small cylinders (about 15 cm in length, and 1 cm in diameter) filled with the analyte in liquid form. The two extremes of the tube are sealed, and the permeation is produced through the cylinder walls at a known rate at certain temperature of the analyte in gas phase, which is certified by the manufacturer. This equipment was mainly used in our set-up to generate DMMP trace-level atmospheres, due to its accuracy and stability over time (Figure 5.6).

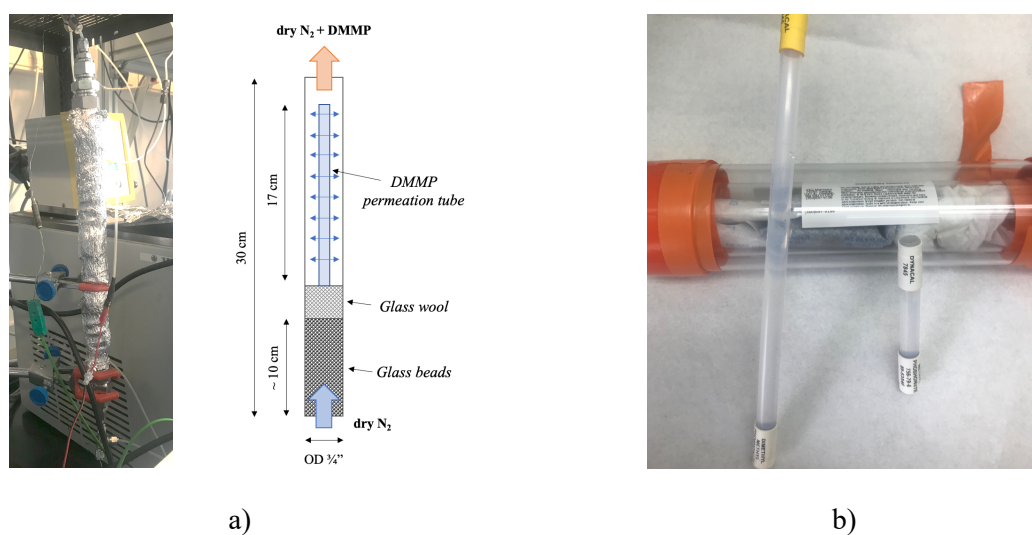


Figure 5.6. a) Left: DMMP vapor generation system, right: DMMP vapor generator schematic, the dry N<sub>2</sub> flows firstly through a bed of glass beads to thermalize after which flows around the permeation tube (depicted as a blue cylinder on the scheme). b) DMMP permeation tubes used to generate high concentration DMMP vapors (left) and low concentration vapors (right).

The DMMP trace-level, atmosphere generation set-up consisted on a 1” diameter, stainless steel cylinder where the permeation tube (VICI) was placed. A heating tape connected to PID controller with a type K thermocouple fixed inside the stainless-steel cylinder is used. A bed of glass beads was installed upstream to guarantee the temperature of the carrier gas, at the

entrance of the stainless-steel cylinder. The concentration at the outlet of the permeation tube system is given by:

$$C = \frac{P \cdot \frac{24.46}{m_w}}{Q} \quad (49)$$

where  $C$  is the concentration (ppmV),  $P$  is the permeation rate (ng/min),  $m_w$  is the molecular weight of the analyte and  $Q$  is the mass flow in mL/min. The constant 24.46 is the molar volume at the reference conditions ( $T = 25 \text{ }^\circ\text{C}$ ,  $p = 1 \text{ atm}$ ).

TABLE 5.2. OPERATIONAL CONDITIONS OF THE DMMP VAPOR GENERATION SYSTEM

	<i>Low concentration</i>	<i>High concentration</i>
Permeation rate	2.35 ng/min	1629.96 ng/min
Error	$\pm 3.07 \%$ ( $\pm 0.07 \text{ ng/min}$ )	$\pm 0.71 \%$ ( $\pm 11.57 \text{ ng/min}$ )
Temperature	30 $^\circ\text{C}$	100 $^\circ\text{C}$
Mass flow, $Q$	10 mL/min	10 mL/min
Concentration	0.24 mg/m <sup>3</sup> (0.046 ppmV)	162 mg/m <sup>3</sup> (32.150 ppmV)

As carrier gas, a stream of N<sub>2</sub> (99.9%) was firstly dried with a desiccator filter and then circulating through the permeation tube system at 10 mL/min. Outflow concentration at this flow rate and considering a permeation rate of 1629.96 ng/min  $\pm 0.71 \%$  at 100  $^\circ\text{C}$  (certified by the manufacturer) was 162 mg/m<sup>3</sup> (32 ppmV). This stream was further diluted with an additional dry N<sub>2</sub> stream. Resulting concentrations were: 17 mg/m<sup>3</sup> (3 ppmV), 32 mg/m<sup>3</sup> (6 ppmV) and 81 mg/m<sup>3</sup> (16 ppmV). The characteristics of the permeation tubes used in our set-up as well as operation conditions are shown on Table 5.2.

To assess the stability of the DMMP/N<sub>2</sub> gas mixture, it was monitored the concentration of the flow stream downstream the DMMP vapor generation system with a theoretical concentration of 162 mg/m<sup>3</sup> at 10 STP cm<sup>3</sup>/min and room temperature. Results were compared to those generated by a saturation train compose of two bubblers in series connected, kept in an ice bath and filled with liquid DMMP and using as carrier gas inert N<sub>2</sub> at 10 STP cm<sup>3</sup>/min resulting in the same theoretical concentration. In this case, the monitoring was effectuated along several

months. In both cases, the gas mixture was registered using a gas chromatograph coupled with a mass spectrometer.

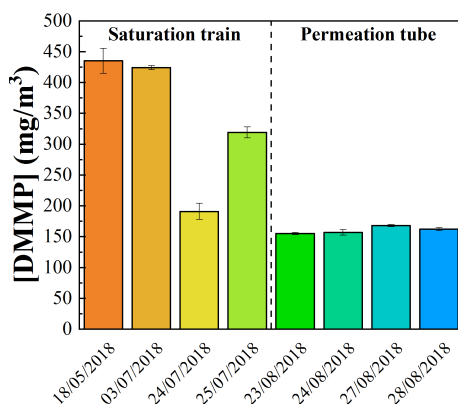


Figure 5.7. Comparison of DMMP concentration downstream de vapor generation systems using either a saturation train or a permeation tube.

As can be seen in Figure 5.7, the registered DMMP concentration generated by the saturation train is very variable, due to the lack of control of the saturators temperature as well as variable bubbling effectiveness. On the other hand, the concentration registered from the DMMP vapor generator using the permeation tube remained constant.

#### 5. 4. 2. EXPERIMENTAL SET-UP

Dynamic and adsorption properties of the coated microfluidic devices have been assessed by analysing breakthrough curves. These have been obtained by circulating known concentrations of analyte diluted in carrier gas at certain mass flow at room temperature and analysing the composition of the eluted gas. Analysis of the outlet current was performed using either a mass spectrometer or a gas chromatograph couple with mass spectrometer. The fluidic connections between the microdevice and the detector were performed using either stainless steel 1/8" or 320  $\mu$ m inner-diameter, deactivated fused silica capillaries. To avoid analyte condensation on the different valves and metallic connections, those areas were locally heated at 70 – 80 °C using thermal mats.

As mass spectrometer, it was used an Omnistar GSD 301 (Pfeiffer Vacuum) and it was used mainly for the hexane adsorption experiments. In that case, it was continually monitored the characteristic n-hexane mass  $m/z = 56$  as well as the characteristic nitrogen mass  $m/z = 28$ ,

as reference. This equipment was also used in preliminary DMMP adsorption experiments, but its use was abandoned due to lack of sensitivity at concentrations of interest.

An extremely sensitive gas chromatograph coupled with mass spectrometer Shimadzu GCMS QP2010 was mainly used to study DMMP adsorption. The eluted gas concentration was sampled every 60 s in a 500  $\mu\text{L}$  inert steel, sampling loop at 10  $\text{cm}^3/\text{min}$  STP and characteristic masses  $m/z = 79, 94, 109$  and 124 were measured. A nonpolar PLOT column (SH-RT-Q-BOND, 30 m long, 320  $\mu\text{m}$  inner diameter) was used to separate DMMP from the sporadic interferences and dilution  $\text{N}_2$  gas. In order to get a sharp DMMP peak in a reasonable analysis time, the column oven was kept at 240  $^\circ\text{C}$  throughout the experiment.

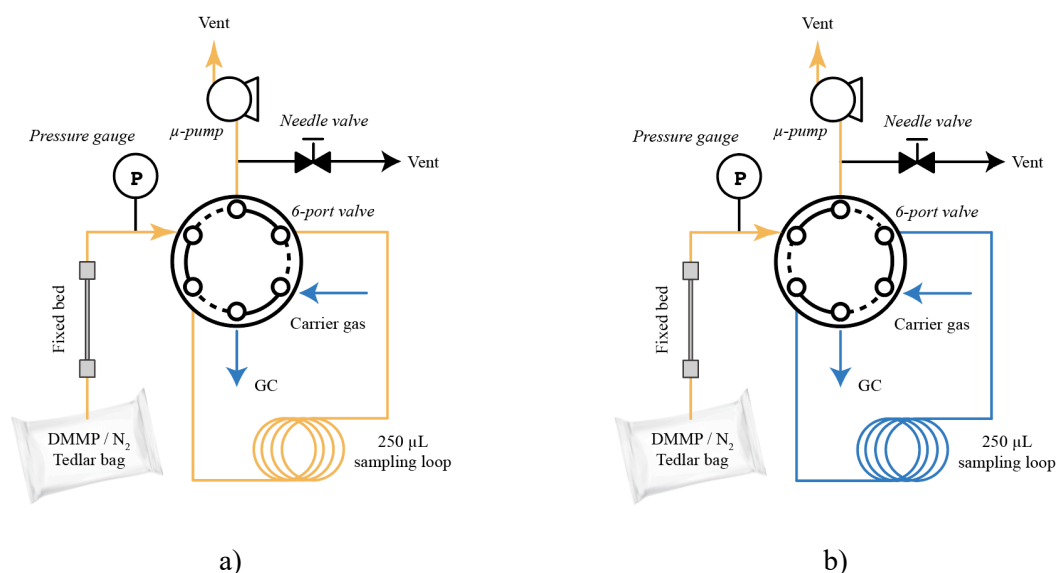


Figure 5.8. Schematic of the set up installed at the University of Michigan. a) Sampling loop filling. b) Aliquot injecting into the GC.

Experiments performed at the facilities of the group of Zellers at the University of Michigan (USA) were done with a gas chromatograph equipped flame-ionization detector Model 7890A (Agilent Technologies) and using sample-loop injections and gas mixtures taken from the Tedlar bag (Figure 5.8). Gas mixtures were drawn from the bag and through the fixed bed adsorbent packed in an Inconel tubing (5 cm long, 1.59 mm outer diameter, 1.35 mm inner diameter) at 10  $\text{cm}^3/\text{min}$  STP using a vacuum pump (UN86KTDC, KNF Neuberger) and periodically (every 3 min) directing an aliquot of the outlet stream into GC column (6 m long, 320  $\mu\text{m}$  inner diameter, 0.25  $\mu\text{m}$  thick Rtx-1 stationary phase, Restek) via a six-port valve equipped

with a 250  $\mu$ L gas sampling loop. A needle valve was placed upstream to from the pump and used to finely tune gas flow rate.

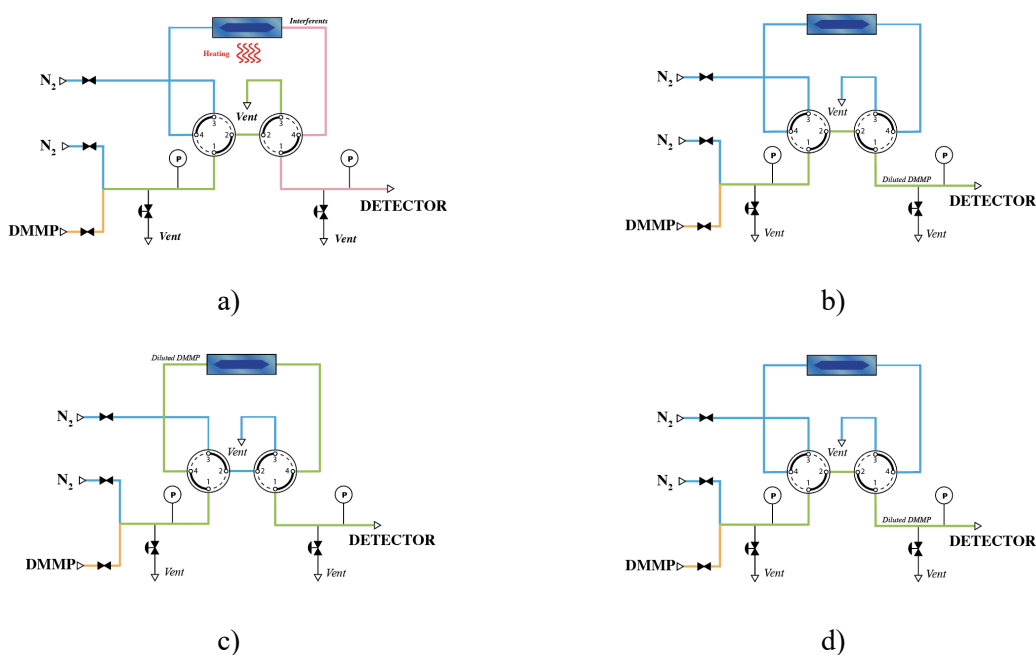


Figure 5.9. Scheme of flow arrangement in the experimental set-up installed at the University of Zaragoza: a) adsorbent pre-treatment, b) analyte baseline, c) analyte adsorption and d) analyte desorption.

A conventional breakthrough test comprises the following steps (Figure 5.9 depicts the schematics of the set up installed at the University of Zaragoza):

1. *Adsorbent pre-treatment*: before the adsorption experiment, the adsorbent is regenerated thermally by placing the microdevice on a hotplate at 200  $^{\circ}$ C while inert  $N_2$  sweeps the cavity and degas the sorptive layer. Ideally this step is performed until no undesirable specie was detected.
2. *Analyte baseline*: analyte was fed directly into the detector to obtain the baseline signal that is used for calibration. To avoid contamination on the adsorbent material, dry  $N_2$  is circulated through the microdevice while this step takes place.
3. *Analyte adsorption*: analyte is fed to the microdevice until sorbent saturation, which is assessed by previous calibration ( $C_{\text{exit}} = C_0$ ).

*Analyte desorption*: the analyte was desorbed under the same conditions as step 1).

## 5. 5. INITIAL ASSESSMENT ON $\mu$ -PRECONCENTRATOR PERFORMANCE WITH $C_6H_{14}$ VAPOURS

The first set of microdevices designs were initially explored to analyse the  $n$ - $C_6H_{14}$  sorption performance on cavity configurations based on the best configuration in terms of adsorbate/adsorbent contact and flow distribution, a second set of miniaturized designs was proposed for further testing with DMMP. The  $\mu$ -devices topologies used in the preliminary experiments are presented in Figure 5.10.

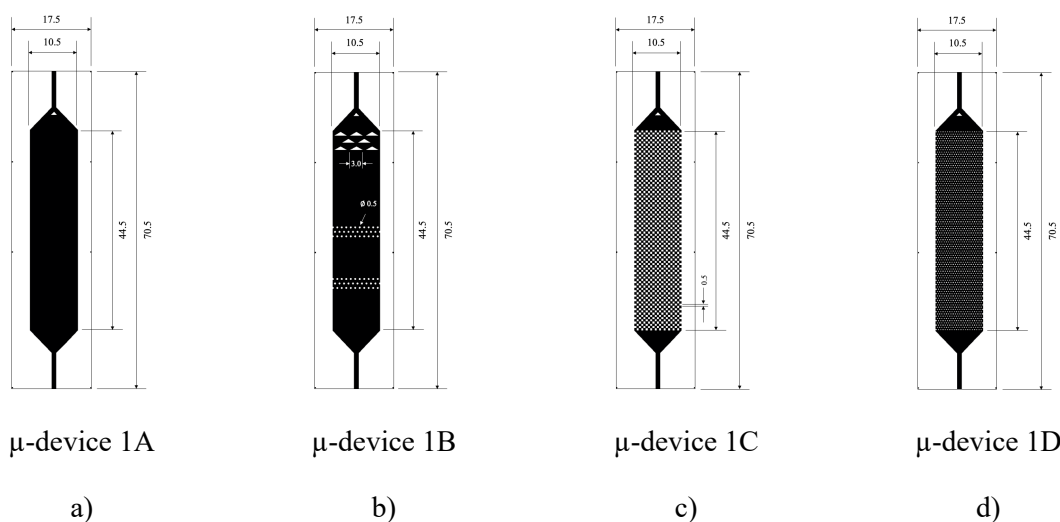


Figure 5.10. Top view of the  $\mu$ -devices used for preliminary testing with  $n$ - $C_6H_{14}$ .

Such preliminary experiments were performed with  $n$ -hexane since it is a stable, non-sticky and easy-to-detect volatile organic compound ( $P_v = 20.17$  kPa @ 298 K). Concentration in dry  $N_2$  was chosen sufficient high to provide confidence on the detection ( $C_0 = 1760$  mg/m<sup>3</sup> or 500 ppmV). The sorbate was fed at 5 STP cm<sup>3</sup>/min while maintaining the microdevice at room conditions. *In situ* synthesized silicalite films (4  $\mu$ m thick) were used as sorptive layers due to its high reproducibility and homogeneity resulting in adsorbent loadings on chip from 2.46 mg to 4.28 mg. Inlet and outlet connections were performed through 1/8" Swagelok connectors glued with epoxy resin and 1/8" stainless-steel pipelines were used in the experimental set-up. Similar experiment were performed in a fixed bed configuration (Swagelok) packed with 4.8 mg of silicalite in powder form ( $d_{particle} = 80$   $\mu$ m) and diluted with glass powder (1:10, silicalite : glass powder) for comparison purposes.



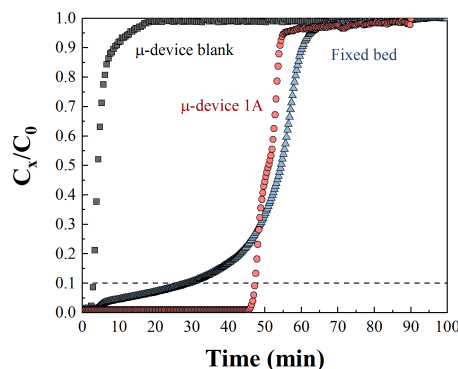


Figure 5.11. Breakthrough curves for a silicalite modified  $\mu$ -preconcentrator (red dots), a fixed bed packed with silicalite crystals diluted in glass powder (blue triangles) after being exposed to  $1760 \text{ mg/m}^3$   $n\text{-C}_6\text{H}_{14}$  at  $5 \text{ STP cm}^3/\text{min}$  and room temperature. An unmodified  $\mu$ -device has been used as a reference (black squares).

Breakthrough analysis of tested microdevices reveal better performance than fixed-bed counterparts as shown in Figure 5.11 for an empty  $\mu$ -preconcentrator ( $\mu$ -device blank), a silicalite coated  $\mu$ -preconcentrator ( $\mu$ -device 1A) and the fixed-bed packed with discrete silicalite crystals (fixed-bed). The uniform thickness of the sorptive layer along the whole microchannel (10.5 mm wide) notably improves solid-gas contact, avoiding bypass and preferential flow paths, as typical of fixed-bed concentrators packed with discrete particles. Dynamic capacities of the fabricated microdevices ranges from 63 to 95 mg/g, i.e. 2-fold the capacity shown by packed bed configuration. This clearly indicates better gas-solid contact and exploitation of sorption capacities of the zeolite, due to the higher exposed surface area per volume unit on zeolite films in comparison with a fixed bed of silicalite microparticles. In general, the four proposed designs exhibit high bed efficiency, circa 90 %, and there is not found any significant difference. The silicalite layer has been successfully integrated even in complex topologies. Table 5.3 compiles the breakthrough analysis of the proposed microdevices designs as well as the fixed bed concentrator: adsorbent mass ( $m_{\text{coating}}$ ), contact time calculated from sorbent volume ( $\tau$ ), breakthrough volume ( $V_b$ ), dynamic sorption capacity ( $W_d$ ), equilibrium sorption capacity ( $W_e$ ) and bed efficiency.

TABLE 5.3. SUMMARY OF THE  $N-C_6H_{14}$  BREAKTHROUGH ANALYSIS OF THE PROPOSED MICRODEVICES @ 1760 MG/M<sup>3</sup> IN DRY  $N_2$  AT ROOM TEMPERATURE

<i>Sorption unit</i>	$m_{coating}^*$ (mg)	$\tau$ (ms)	$V_b$ (STP cm <sup>3</sup> )	$W_d$ (mg/g)	$W_e$ (mg/g)	<i>Bed efficiency</i>
Fixed bed	4.8	19**	109	40	85	47
$\mu$ -device 1A	4.4	26	160	66	72	92
$\mu$ -device 1B	4.1	25	184	78	87	90
$\mu$ -device 1C	4.6	15	133	95	107	89
$\mu$ -device 1D	4.7	20	121	63	66	95

\*Calculated theoretically assuming a cavity depth of 100  $\mu$ m and  $\rho_{silicalite} = 2.2$  mg/mL. \*\*Calculated assuming a well-packed, homogeneous spherical particle in a triclinic distribution (maximum porosity = 0.26)

According to the experimental results shown in Table 5.3, cavity design does not seem to play a crucial role. For the sake of simplicity, the second set of miniaturized devices are based mainly on design 1A. Though those intended to be integrated with poly-ionic liquid films are also based on design 1D.

The potential for device miniaturization is explored by the Wheeler model, equation (27) [189], [190], using the n-hexane breakthrough results of Design 1A as reference. This model correlates design and operational parameters and involves both thermodynamics and kinetics. One of the practical limits of miniaturization is the critical bed residence time,  $\tau_{critical}$ . This can be calculated through the Wheeler model (27), by forcing  $V_b$  or  $t_b$  to be 0 and solving the equation for  $Q_{critical}$  or  $\tau_{critical}$ . That is, for a given value of  $Q$ , this defines the minimum volume of the microdevice; or for a given size, this determines the critical maximum flow rate,  $Q_{critical}$ ; at which we can operate without bypassing the  $\mu$ -device, i.e. that breakthrough is being measurable. Based on our experimentally evaluated equilibrium and kinetic parameters ( $k_v$  and  $W_e$ ), the critical values are 29 ms and 109 cm<sup>3</sup>/min STP for  $\tau_{critical}$  and  $Q_{critical}$ , respectively. The minimum concentrator total volume is 2.43  $\mu$ L for 5 cm<sup>3</sup>/min STP flow rate, i.e. 4.5% of the free volume  $\mu$ -device 1A (as seen on Chapter IV, Table 4.2). Similarly, the standard flow rate is 4.5% of the estimated critical value of 109 cm<sup>3</sup>/min STP; indicating that it could be enlarged further to reduce sampling time. With a goal of developing a general guideline for stipulating maximum operating flow rates of  $\mu$ -preconcentrators; a cut-off value at 60% bed efficiency, i.e.

$W_d = 0.6 \cdot W_e$  at breakthrough point, is generally adopted [189], [190]. The value of bed residence time associated with this efficiency cut-off is considered the minimum safe value,  $\tau_{\text{safe}}$ , and the corresponding safe (i.e. maximum recommended) flow rate is therefore designated  $Q_{\text{safe}}$ . The as calculated values are 72 ms and 44 cm<sup>3</sup>/min STP for  $\tau_{\text{safe}}$  and  $Q_{\text{safe}}$ , respectively. It could be concluded that the operational performance of the as prepared  $\mu$ -concentrators is amenable for further improvement by increasing the flow rate values and reducing overall dimensions. Based on these remarks, a miniaturization of the original devices took place and led to the second generation of  $\mu$ -preconcentrators (design 2.A and design 2.B.a – d, presented on Chapter IV), which features a total volume 3.5 times lower than the previous generation (14.8  $\mu\text{L}$  vs 53.0  $\mu\text{L}$ ) but still 6 times higher than estimated minimum volume (14.8  $\mu\text{L}$  vs 2.43  $\mu\text{L}$ ).

## **5. 6. EVALUATION OF DMMP SORPTION ON FUNCTIONAL $\mu$ -PRECONCENTRATOR**

This section comprises the preconcentration study with functional  $\mu$ -device presented on Chapter IV, Table 4.4. All of the experiments were performed using the GCMS for monitoring the breakthrough curve, feeding the  $\mu$ -devices with DMMP/N<sub>2</sub> mixtures prepared with the permeation tube.

The results have been organized according to the textural properties of the functional materials: microporous and mesoporous or dense moieties, but always deployed as thick films on Si based surface.

Additional experiments with packed graphitized active carbons in fixed bed configuration and modified graphitized active carbons were done in collaboration with the group of Prof. Zellers at his facilities at the University of Michigan.

### **5. 6. 1. $\mu$ -PRECONCENTRATORS MODIFIED WITH MICROPOROUS MATERIALS**

---

The evaluated microporous materials evaluated include hydrophobic MFI-type zeolite (silicalite-1) and MOF-type materials (Zn-MIM, Zn-DMCAPZ and Cu-BTC).

### 5. 6. 1. 1. *Silicate based $\mu$ -preconcentrators*

DMMP sorption on silica microporous materials was tested on MFI-zeolite-modified  $\mu$ -preconcentrators with in situ synthesized silicalite films of 4  $\mu\text{m}$ -thick. Theoretical adsorbent mass loading assuming  $\rho_{\text{SIL}} = 2.2 \text{ g/cm}^3$  was 1184  $\mu\text{g}$ . Experiments were conducted at DMMP concentrations ranging from 17 to 162  $\text{mg/m}^3$  in dry  $\text{N}_2$  at room temperature and at flowrates from 10 to 90  $\text{mL/min}$ . Before each assay, the material was pre-treated overnight at 473 K under dry  $\text{N}_2$ . Operational conditions of the silicalite modified  $\mu$ -devices are presented in Table 5.4.

TABLE 5.4. OPERATIONAL CONDITIONS OF THE SILICALITE MODIFIED  $\mu$ -PRECONCENTRATORS

<i>Sorption unit</i>	<i>[DMMP] (mg/m<sup>3</sup>)</i>	<i>DMMP/N<sub>2</sub> flow rate (STP cm/min)</i>	<i>u<sub>gas</sub> (cm/s)</i>	<i>t (ms)</i>
Sil_20um $d_{\mu\text{PC}} = 20 \mu\text{m}$ $t_{\text{sil}} = 4 \mu\text{m}$ $m_{\text{sil}} = 1184 \mu\text{g}$	17	10	208	3.55
	32	10	208	3.55
	81	10	208	3.55
	162	10	208	3.55
	17	10	208	3.55
	17	30	1.18	1.18
	17	50	0.71	0.71
	17	90	0.39	0.39

Figure 5.12 shows the breakthrough curves for the silicalite-modified  $\mu$ -preconcentrator when DMMP concentration in dry  $\text{N}_2$  at room temperature varies from 17  $\text{mg/m}^3$  to 162  $\text{mg/m}^3$  but the flow rate remains at 10  $\text{cm}^3/\text{min}$  STP (Figure 5.12.a) and DMMP adsorption pseudoequilibrium data calculated from breakthrough experiments Figure 5.12.b. Silicalite modified  $\mu$ -preconcentrator exhibits great breakthrough volume ( $V_b = 18.6 \text{ L}$ ) at low concentration and flow rates (10  $\text{cm}^3/\text{min}$  STP @ 17  $\text{mg/m}^3$  DMMP at room temperature), as well as DMMP mass uptake ( $m_b = 316 \mu\text{g}$ ). As expected, at higher DMMP concentrations, breakthrough volumes diminish (down to 2.5 L @ 162  $\text{mg/m}^3$  DMMP at room temperature), whereas dynamic sorption capacity remains constant ( $W_d = 325 \pm 40 \text{ mg/g}$ ). Equilibrium sorption capacity is slightly inferior at low concentration ( $W_e = 296 \text{ mg/g}$  @ 17  $\text{mg/m}^2$  DMMP at room temperature) than at

higher concentrations ( $W_e = 391 \text{ mg/g}$  @  $162 \text{ mg/m}^3$  DMMP at room temperature) indicating that as the DMMP concentration decreases, thus DMMP partial pressure decreases, we are drifted from the plateau stage of the DMMP isotherm and shifting to the linear range, as can be seen on Figure 5.12.b. It is also worthy to underline that sorption process is carried out with the chip equilibrated with the laboratory environment, where thermostatic conditions are not preserved. Therefore, the estimation of sorption isotherm related parameters is quite ambitious. Overall, bed efficiency maintains constant at all concentrations above  $90 \pm 1.3 \%$ , in agreement with the exceptional gas-solid contact provided by the homogeneous  $4 \mu\text{m}$  thick silicalite layer at conditions  $\tau = 3.6 \text{ ms}$  and  $u_{\text{gas}} = 208 \text{ m/s}$ .

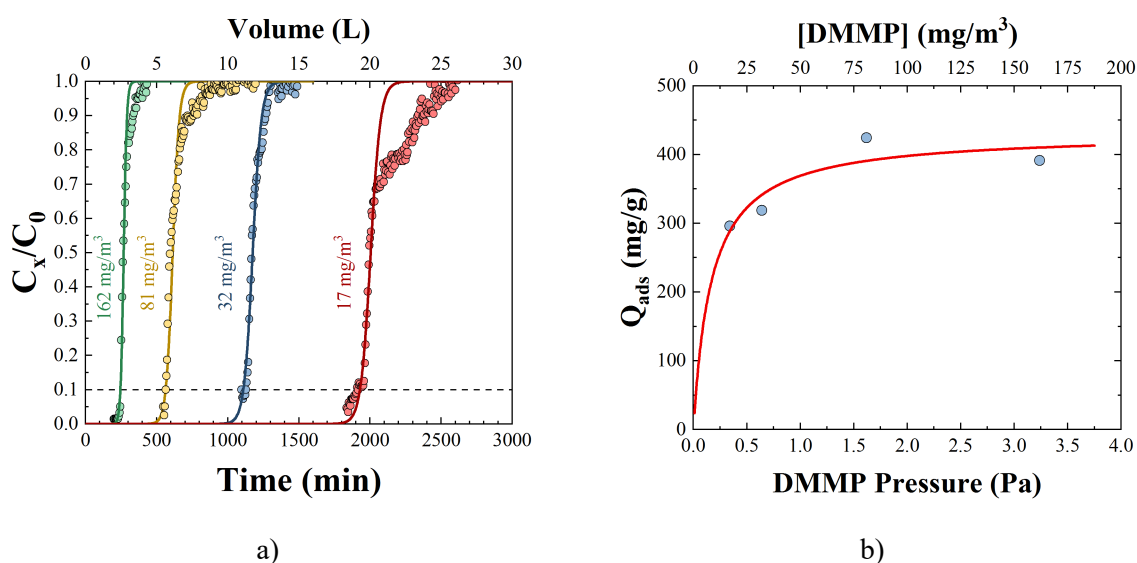


Figure 5.12. Breakthrough curves for silicalite-modified  $\mu$ -preconcentrators at  $10 \text{ cm}^3/\text{min}$  STP of  $17 \text{ mg/m}^3$  (red),  $32 \text{ mg/m}^3$  (blue),  $81 \text{ mg/m}^3$  (yellow) and  $162 \text{ mg/m}^3$  (green) DMMP in dry  $\text{N}_2$  at room temperature. Experimental data were fitted to the Yoon-Nelson model. b) DMMP adsorption isotherm at room temperature. Blue dots are experimental data acquired from breakthrough analysis.

Breakthrough experimental data were fitted to a Yoon-Nelson model, as well as the Wheeler model. Fitting parameters are compiled on Table 5.5:  $k_{\text{YN}}$  and  $\tau_{\text{YN}}$  are Yoon-Nelson fitting parameters, whereas  $k_v$  and  $W_{e,\text{Wheeler}}$  are Wheeler's. Coefficient of determination ( $R^2$ ) in all the cases are over 90 %, and for concentrations above  $32 \text{ mg/m}^3$  are over 98%. Analogously to  $n\text{-C}_6\text{H}_{14}$  on silicalite  $\mu$ -preconcentrators, the 3D computational model was applied to simulate DMMP sorption. However, satisfactory results were not obtained as the very thin geometry led extremely big meshes and high computational costs.

TABLE 5.5. ADSORPTION RESULTS AND FITTING YOON-NELSON AND WHEELER PARAMETERS FOR BREAK-THROUGH CURVES AT DMMP CONCENTRATIONS FROM 17 TO 162 MG/MG<sup>3</sup> AT 293 K AND 10 STP CM<sup>3</sup>/MIN FLOW RATE

[DMMP] (mg/m <sup>3</sup> )	t <sub>b</sub> (min)	W <sub>d</sub> (mg/g)	W <sub>e</sub> (mg/g)	k <sub>YN</sub> (1/min)	τ <sub>YN</sub> (min)	k <sub>v</sub> (1/min) ·10 <sup>5</sup>	W <sub>e,Wheeler</sub> (mg/g)	R <sup>2</sup>
17	1860	267	296	0.029	2005	9.8	288	0.9247
32	558	382	424	0.033	1176	6.6	318	0.9755
81	252	346	391	0.044	613	4.6	420	0.9853
162	245	335	380	0.101	275	4.7	376	0.9726

Likewise, as flow rate increases from 10 up to 90 cm<sup>3</sup>/min STP, breakthrough time reduces from 1860 min to 227 min, whereas breakthrough volumes accounts for 21.2 ± 2.2 L and dynamic sorption capacity remains at W<sub>d</sub> = 305 ± 32 mg/g (Figure 5.13.a). However, bed efficiency decreases from 90 to 78% as flow rate increases, which can be associated to the unusual dispersion of experimental points above 60 % cut-off.

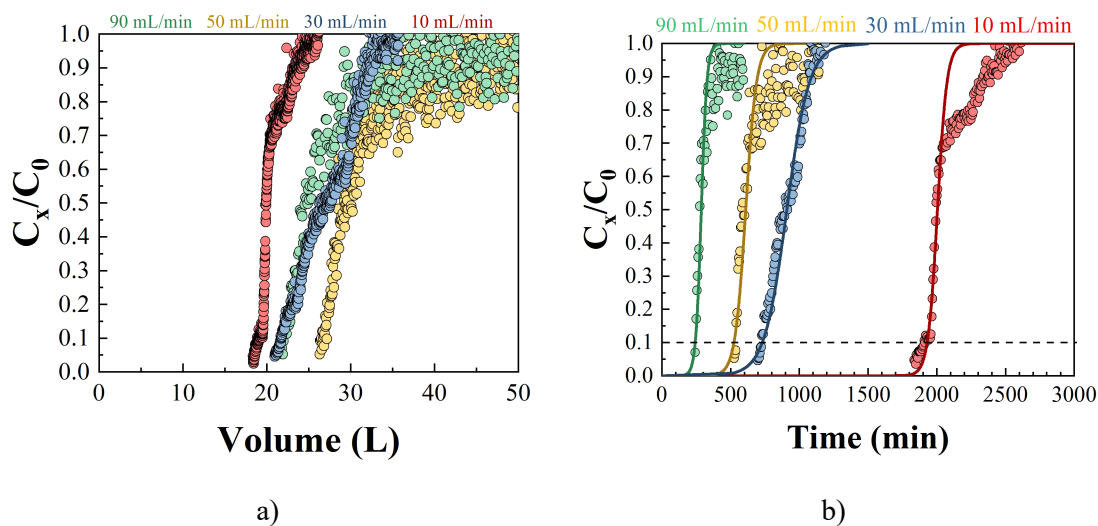


Figure 5.13. a) Breakthrough curves for silicalite-modified  $\mu$ -preconcentrators at 10 (red), 30 (blue), 50 (yellow) and 90 (green) mL/min of 17 mg/m<sup>3</sup> DMMP in dry N<sub>2</sub> at room temperature. b) Experimental breakthrough data (dots) fitted to the Yoon-Nelson adsorption model (solid line).

On Figure 5.13.b is depicted the Yoon-Nelson fitting to the experimental breakthrough data and in Table 5.6 are compiled the fitting Yoon-Nelson and Wheeler parameters. The coefficient of determination ( $R^2$ ) in all the studied cases is  $> 90\%$ , so the analytical model predicts satisfactorily the experimental data. Dynamic sorption is adequately described and equilibrium sorption capacities are closely related to experimental data ( $W_{e,\text{experimental}} = 372 \text{ mg/g}$  vs  $W_{e,\text{Wheeler}} = 370 \text{ mg/g}$  @  $90 \text{ STP cm}^3/\text{min}$  and  $17 \text{ mg/m}^3 \text{ DMMP}$ ). As expected, the equilibrium sorption capacity remains constant independently of feed flow rate.

TABLE 5.6. ADSORPTION RESULTS AND FITTING YOON-NELSON AND WHEELER PARAMETERS FOR BREAKTHROUGH CURVES AT FLOW RATES FROM 10 TO 90 STP  $\text{cm}^3/\text{min}$  AND  $17 \text{ mg/m}^3 \text{ DMMP}$  AT ROOM TEMPERATURE.

$Q$ ( $\text{cm}^3/\text{min}$ )	$t_b$ ( $\text{min}$ )	$W_d$ ( $\text{mg/g}$ )	$W_e$ ( $\text{mg/g}$ )	$k_{YN}$ ( $1/\text{min}$ )	$\tau_{YN}$ ( $\text{min}$ )	$k_v$ ( $1/\text{min}$ ) $\cdot 10^5$	$W_{e,\text{Wheeler}}$ ( $\text{g/g}$ )	$R^2$
10	1860	267	296	0.029	2005	9.8	288	0.9247
30	704	303	388	0.012	909	5.7	396	0.9923
50	495	355	439	0.026	610	13.1	438	0.9590
90	227	293	372	0.049	287	21.4	370	0.9677

#### 5. 6. 1. 2. MOF based $\mu$ -preconcentrators

The MOF-modified  $\mu$ -preconcentrators evaluated in this work are presented on Table 5.7. Experiments were conducted at standard conditions defined as:  $162 \text{ mg/m}^3 \text{ DMMP}$  in dry  $\text{N}_2$  at room temperature and total flow rate of  $10 \text{ cm}^3/\text{min}$  STP. Furthermore, Cu-BTC\_ES was evaluated also at DMMP concentration from  $17$  to  $81 \text{ mg/m}^3 \text{ DMMP}$  in dry  $\text{N}_2$ . The functional coatings were previously activated overnight at  $473 \text{ K}$  under dry  $\text{N}_2$ .

TABLE 5.7. MOF-MODIFIED  $\mu$ -PRECONCENTRATORS USED IN THIS WORK

Sorption unit	Design	Cavity depth ( $\mu\text{m}$ )	Coating method	$t_{\text{adsorbent}}$ ( $\mu\text{m}$ )	$m_{\text{adsorbent}}$ ( $\mu\text{g}$ )
Zn-DMCAPZ_SC	2.B.a	20	Spin coating	7.1	368
Zn-DMCAPZ_LbL	2.B.b	20	Layer by layer	0.8	17
Zn-MIM_SC	2.B.b	20	Spin coating	9.2	474
Zn-MIM_ALD	2.B.b	20	Atomic layer deposition (precursors) + Hydrothermal synthesis	1.0	51
Cu-BTC_ES	2.B.b	20	Electrosynthesis	4.7	113
uPC_Cu	2.B.b	20	Cu patterning on Borofloat substrate	0.5	309

### Zn based $\mu$ -preconcentrators

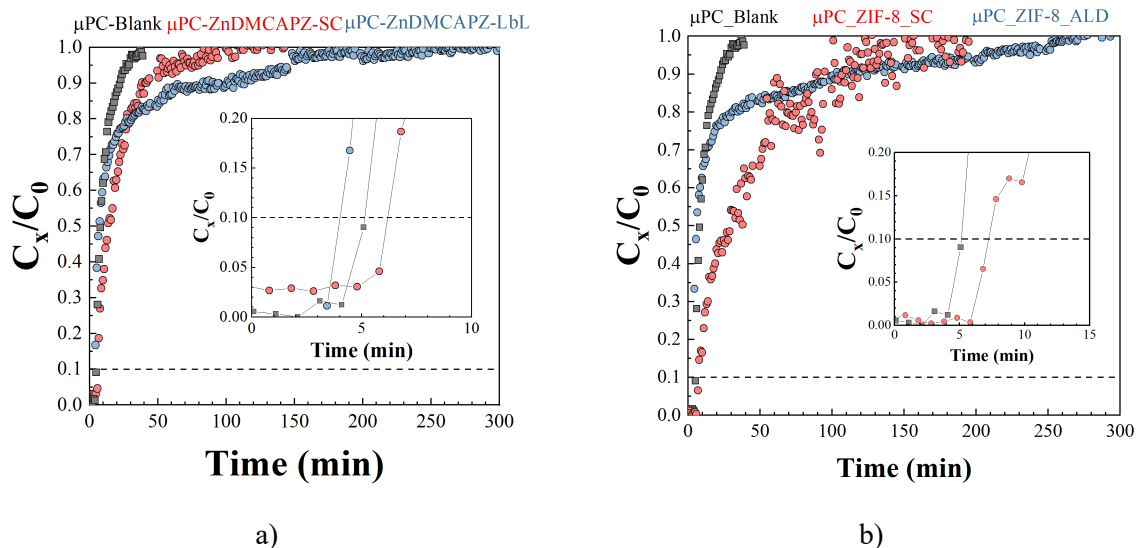


Figure 5.14. Breakthrough curves for MOF-modified  $\mu$ -preconcentrators at  $162 \text{ mg/m}^3$  DMMP in dry  $\text{N}_2$  at room temperature and  $10 \text{ cm}^3/\text{min}$  STP: a) Zn-DMCAPZ\_SC (red) vs Zn-DMCAPZ\_LbL (blue), b) Zn-MIM\_SC (red) vs Zn-MIM\_ALD (blue).

Figure 5.14 exhibit DMMP breakthrough curves for each MOF  $\mu$ -preconcentrator feed at standard conditions. As a reference an uncoated  $\mu$ -devices ( $\mu\text{PC\_Blank}$ ) has included as a



reference as well as the Cu based electrode used as substrate for Cu-BTC electrosynthesis procedure.

As can be observed, DMMP adsorption breakthrough volumes are exceptionally low for the  $\mu$ -devices modified with thin films (35 mL for Zn-DMCAPZ\_LbL and unquantifiable volume for Zn-MIM\_ALD, since DMMP already elutes at the first registered point when  $C_x/C_0 = 0.3$ ). On the contrary, for their counterparts with thicker films the breakthrough volumes account for 58 mL for Zn-DMCAPZ\_SC and 67 mL for Zn-MIM\_SC (Figure 5.14.b and c). These functional  $\mu$ -preconcentrators are characterized by low MOF loading, below 55  $\mu\text{g}$ ; hindering a reliable quantification of the equilibrium sorption capacity. For these two  $\mu$ -devices prepared by spin-coating, the sorbent loading exceeds 350  $\mu\text{g}$  (see Table 5.7) and the equilibrium sorption capacity is in the same range that the one calculated for the silicalite-modified  $\mu$ -preconcentrators (346 mg/g) although having 70-fold adsorbent mass. Overall, the results of MOF based  $\mu$ -preconcentrators prepared by LbL or ALD approach are subjected to a great uncertainty due to scarce amount of sorbent material, its heterogenous deposition and the deficient gas-solid contact. These circumstances lead to low bed efficiency values, i.e. below 15 %, and unnoticeable breakthrough point.

TABLE 5.8. BREAKTHROUGH RESULT FOR ZN-DMCAPZ AND ZN-MIM MODIFIED  $\mu$ -PRECONCENTRATORS FOR 162 MG/M<sup>3</sup> DMMP AT 10 STP CM<sup>3</sup>/MIN AND ROOM TEMPERATURE

<i>Sorption unit</i>	<i>u<sub>gas</sub></i> (cm/s)	<i>t</i> (ms)	<i>t<sub>b</sub></i> (min)	<i>W<sub>d</sub></i> (mg/g)	<i>W<sub>e</sub></i> (mg/g)	<i>Bed efficiency</i>
Zn-DMCAPZ_SC	101	6.30	6.8	30	82	37
Zn-DMCAPZ_LbL	174	0.33	3.6	331	2422	14
Zn-MIM_SC	308	8.13	7.8	27	145	18
Zn-MIM_ALD	85	0.89	0	0	844	0

On  $\mu$ -preconcentrators with higher MOF loading or thicker coatings, the bed efficiencies and breakthrough volumes still remains low. This behaviour clearly indicates that DMMP uptake by MOF materials is somewhat constrained by diffusional limitations inside the microporous network. For Zn-DMCAPZ, its microporous opening sites ( $d_{\text{pore,Zn-DMCAPZ}} = 0.6 \text{ nm}$ ), where the interactions between the analyte and the framework become stronger, are in close to

the range of the kinetic diameter of DMMP molecule ( $d_{kDMMP} \approx 0.57$  nm). This provokes a fast adsorption on the external surface of the MOF crystals due to the high affinity between the DMMP molecules and the metallic cluster, which is also the cause of slow surface diffusion inside the internal microporosity, further exacerbated by its tortuous channel configuration. The slow diffusion not only intra-crystalline but also inter-crystalline can be associated to the discrepancies between the different equilibrium sorption capacity values: 82 mg/g for the Zn-DMCAPZ\_SC vs 2422 mg/g for the Zn-DMCAPZ\_LbL. Its synthesis using the layer by layer approach results in a practical MOF monolayer, where thickness is given by the size of the individual crystal. The spin coating of already synthesized Zn-DMCAPZ crystals leads to a series of MOF particles stack one on top of another. In the case of the monolayer coating, inter-crystalline diffusion does not play a limiting role since all the crystals present at least one side exposed to the gas phase. On the other hand, for a multilayer of stacked crystals, the inter-crystalline diffusion is not negligible. Because of that, the equilibrium sorption capacity estimated from dynamic experiments can lead to severe discrepancies.

In the case of Zn-MIM, although sharing the same metallic cluster than Zn-DMCAPZ (ZnO) and features a bigger pore diameter ( $d_{pore,Zn-MIM} = 1.2$  nm), breakthrough volume for thin films is almost none, as a big fraction of DMMP elutes at the first registered point. The low dynamic sorption capacity is due to the difficult access to the big cages, since DMMP must pass through narrow 0.3 nm flexible windows that interconnect the pockets. Analogously as layer-by-layer synthesis, the hydrothermal synthesis of Zn-MIM using ZnO as metal precursor deposited by ALD leads to a monolayer of crystal-size thickness in opposition to the thick layers of stacked crystals that are as result of spin coating method. For the monolayer Zn-MIM, the external surface available for DMMP adsorption is low enough to not be able to completely remove the analyte from the gas stream when using Zn-MIM\_ALD preconcentrator. On the contrary, thick layers prepared by spin coating result in an increase number of active sites, so the effect of the intra-crystalline diffusion is not as prominent as before. The apparent equilibrium sorption discrepancies estimated from dynamic experiments over different Zn-MIM  $\mu$ -device follow a similar discussion to the one dedicated to the Zn-DMCAPZ devices. Overall, the breakthrough volume for Zn-MIM devices is still lower than with silicalite microporous due steric hindrance within the MOF micropores.

### Cu-BTC based $\mu$ -preconcentrators

Breakthrough testing was performed on Cu-BTC functionalized  $\mu$ -devices and also on analogues without MOF coating, denoted as uPC\_Cu, for reference purposes. In addition, a blank experiment with a sealed microdevice without micropatterned Cu electrode (uPC\_0) was carried out for baseline subtraction. Additionally, theoretical adsorption isotherms have been calculated by combination of Monte Carlo (MC) simulations, in particular, by using the Metropolis–Hastings algorithm and molecular dynamics calculations based on UFF [191] as a force field.

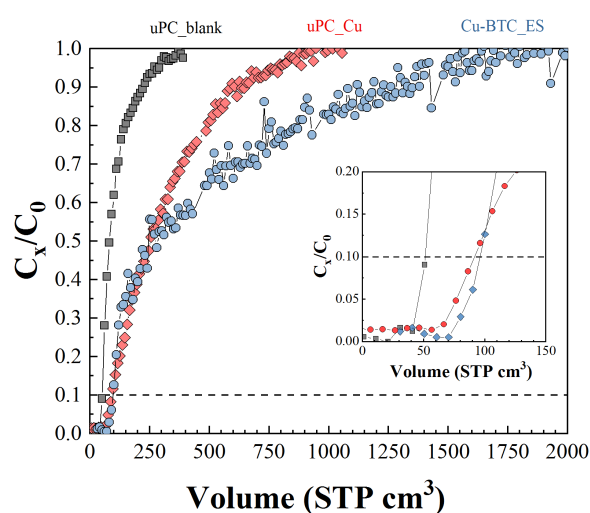


Figure 5.15. Breakthrough testing for microdevices exposed to 162 mg/m<sup>3</sup> (32 ppmV) of DMMP 10 STP cm<sup>3</sup> /min dry N<sub>2</sub>: without Cu electrode (black), without (red) and with Cu-BTC coating (blue). Insert: detail of the breakthrough curve.

The breakthrough curves shown in Figure 5.15, indicates that both uPC\_Cu and Cu-BTC\_ES material present close DMMP breakthrough time (9.1 min and 11.8 min respectively, thus 91 STP cm<sup>3</sup> and 118 STP cm<sup>3</sup> breakthrough volume at 162 mg/m<sup>3</sup>). However, dynamic adsorption capacity is higher in Cu-BTC\_ES than in uPC\_Cu: 179 mg/g vs 48 mg/g (Table 5.9). In fact, the adsorption rate – which can be inferred by the slope of the breakthrough curve – is similar in both microdevices up to values of 0.5  $C_x/C_0$ .

TABLE 5.9. BREAKTHROUGH RESULT FOR CU-BTC MODIFIED  $\mu$ -PRECONCENTRATORS FOR 162 MG/M<sup>3</sup> DMMP AT 10 STP CM<sup>3</sup>/MIN AND ROOM TEMPERATURE

Sorption unit	$u_{gas}$ (cm/s)	$t$ (ms)	$t_b$ (min)	$W_d$ (mg/g)	$W_e$ (mg/g)	Bed efficiency
Cu-BTC_ES	217	1.93	118	179	718	24
$\mu$ PC-Cu	171	0.21	9	48	162	29

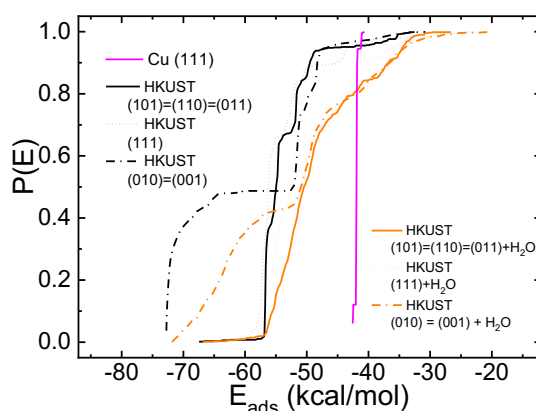


Figure 5.16. Montecarlo simulations of DMMP interactions over Cu-BTC and CuO<sub>2</sub> surface without and with co-adsorbed water).

Figure 5.16 shows the adsorption energies for DMMP in absence of co-adsorbed water. Crystal orientation of the simulated Cu-BTC slab plays an important role in DMMP surface adsorption. Morphologies of the structures are also investigated (see supplementary information). The (110), (101), (011) and (111) orientations for Cu-BTC slabs show similar appearance: oval-shape holes (13.2 Å x 18.6 Å). The (010) and (001) orientations present a cross-shape trench of 6.5 Å, and the intersection of these trenches provides holes of 16.2 Å in diameter. The (110), (101), (011) and preferential (111) crystallographic planes exhibit similar adsorption energies, ca. -55 kcal/mol. On the contrary, the (010) and (001) orientations possess two energy distribution probabilities centered at -51 kcal/mol and -73 kcal/mol, respectively. Additionally, the average of adsorption energy for DMMP adsorbed inside the Cu-BTC micropores is lower than -30 kcal/mol. The estimated adsorbate-adsorbent interaction energy on Cu<sub>2</sub>O surfaces is -37 kcal/mol, as depicted in Figure 5.16. This value is lower than the analogue for any Cu-BTC surface but high enough to explain this behaviour.

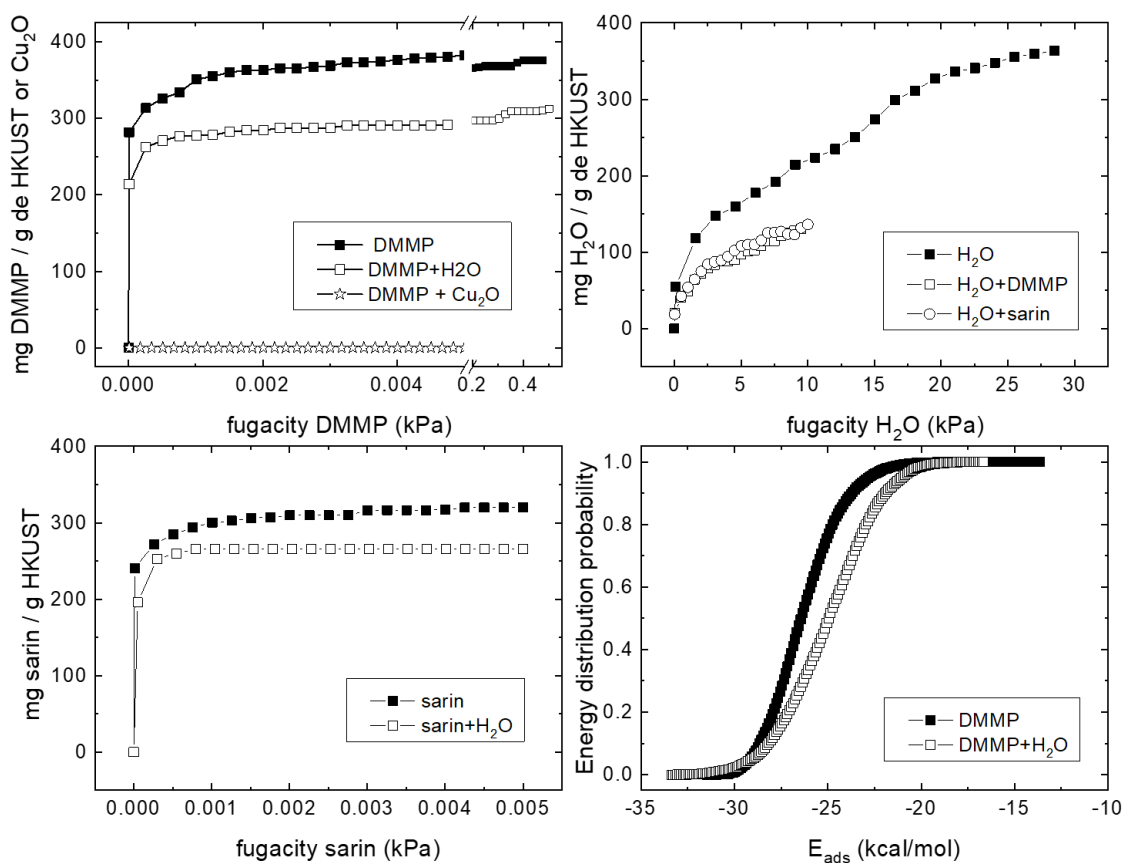


Figure 5.17. Simulated adsorption isotherms of DMMP, water and sarin gas at 298 K on Cu-BTC and Cu<sub>2</sub>O surfaces and energy distribution probability for DMMP adsorbed inside the micropores for single and binary mixtures.

Figure 5.17 presents the calculated adsorption isotherms of DMMP, water and sarin gas on Cu-BTC microporosity at 298 K and the energy distribution probability for DMMP adsorbed inside pores in presence and absence of water. For the calculations 30000 steps and 1000000 production steps have been set on MC parameters. This distribution correlates in same way than observed on case of surface adsorption. In general, the adsorbate uptake values for single components are higher than those calculated for binary mixtures. Thus, 73% of reduction for water uptake in DMMP presence is recorded, a similar value than obtained experimentally (70%). However, DMMP shows a 20% of theoretical decay while experimentally shows a 61%. Our explanation resides in the strong interactions of DMMP with the external surface which are underestimated in the calculated isotherms, where only the molecules inside the micropores contribute to the theoretical approximation. Furthermore, the predicted values for Sarin gas are rather similar to those of DMMP analogue, supporting the suitability of Cu-BTC for Sarin gas detection.

The adsorption isotherm of DMMP on Cu<sub>2</sub>O structure (Figure 5.17) shows an equilibrium value of almost zero indicating the adsorption of DMMP over this oxide is only due to external surface interactions. From  $C_x/C_0$  higher than 0.5, the adsorption rate notably decays on the Cu-BTC functionalized microdevices. Our explanation relies on the saturation of the DMMP adsorption sites distributed on the external surface. Thus, DMMP molecules, strongly adsorbed on the surface of the Cu<sub>2</sub>O/Cu crystalline impurities and those on the external surface of Cu-BTC crystals, start to diffuse inside the microporous structure. In this adsorption regime, intra-crystalline diffusional limitations become controlling although the adsorbate-adsorbent interactions within the micropores are less energetic. Whereas uPC\_Cu becomes saturated after sampling 772 STP cm<sup>3</sup> of DMMP/N<sub>2</sub>, the higher surface area of the Cu-BTC coating increases that volume up to 1541 STP cm<sup>3</sup>. Overall, the equilibrium adsorption capacity for DMMP is 691 mg/g for uPC\_Cu-BTC @ 162 mg/m<sup>3</sup>. This DMMP uptake clearly overpasses standard adsorption materials such as active carbons (30.4 mg/g @ 230 mg/m<sup>3</sup>) [192] or Tenax TA (39 mg/g @ 500 mg/m<sup>3</sup>) [193]; as well as certain theoretical values calculated for MOFs (e.g. MIP-177 @ 245 mg/g, UiO-66 @ 403 mg/g) [194].

### 5. 6. 2. $\mu$ -PRECONCENTRATORS MODIFIED WITH MESOPOROUS SILICA

---

DMMP adsorption on  $\mu$ -preconcentrators containing mesoporous silica nanoparticles was evaluated in 40  $\mu$ m-depth devices coated with MCM-48 nanoparticles by spin coating. After 10 spin coating cycles, coating thickness measured by profilometry resulted in  $2.90 \pm 3.23$   $\mu$ m which corresponded to 527  $\mu$ g of adsorbent. To investigate the influence of adsorbent thickness, MCM-48 was deposited on 8  $\mu$ m-depth  $\mu$ -preconcentrators to promote sorbent-sorbate contact. Adsorbent thickness was measured by profilometry resulting in layer of  $0.54 \pm 0.30$   $\mu$ m ( $m_{\text{MCM-48}} = 175$   $\mu$ g) and  $3.81 \pm 1.91$   $\mu$ m ( $m_{\text{MCM-48}} = 1241$   $\mu$ g) for 1 and 20 cycles respectively.

The functional  $\mu$ -preconcentrators were evaluated for DMMP preconcentration from atmospheres containing 32 mg/m<sup>3</sup> to 162 mg/m<sup>3</sup> in dry N<sub>2</sub> at room temperature and a mass flow of 10 cm<sup>3</sup>/min STP. Additional experiments were carried out at 20 cm<sup>3</sup>/min STP for 81 mg/m<sup>3</sup> DMMP and 50 cm<sup>3</sup>/min STP for 32 mg/m<sup>3</sup> DMMP in dry N<sub>2</sub> at room temperature to check the influence of external diffusional limitations. Table 5.10 compiles the operational conditions of the breakthrough test proposed for MCM-48 modified  $\mu$ -preconcentrators. Before each experiment, the material was degassed at 494 K under dry N<sub>2</sub> overnight.

TABLE 5.10. OPERATIONAL CONDITIONS OF THE MCM-48 FUNCTIONALIZED  $\mu$ -PRECONCENTRATORS

Sorption unit	Cavity depth ( $\mu\text{m}$ )	$t_{\text{MCM-48}}$ ( $\mu\text{m}$ )	MCM-48 mass ( $\mu\text{g}$ )	DMMP/N <sub>2</sub> flow rate (STP cm/min)	$u_{\text{gas}}$ (cm/s)	$t$ (ms)
MCM-8um-1L	8	0.54	176	10	447	0.49
MCM-8um-20L	8	3.81	1241	10	796	3.38
MCM-40um-10L	40	2.79	527	10	90	2.48
MCM-40um-10L	40	2.79	527	20	179	1.24
MCM-40um-10L	40	2.79	527	50	448	0.50

Although sharing the same chemical nature than silicate, the dynamic sorption capacities of MCM\_40um\_10L vary from 11.15  $\mu\text{g}$  (21 mg/g) @ 32 mg/m<sup>3</sup> to 23  $\mu\text{g}$  (43 mg/g) @ 162 mg/m<sup>3</sup> DMMP; thus, reduced in comparison with silicalite counterparts: from 348  $\mu\text{g}$  (294 mg/g) @ 32 mg/m<sup>3</sup> to 409  $\mu\text{g}$  (346 mg/g) @ 162 mg/m<sup>3</sup> DMMP (Figure 5.18). These differences between microporous and mesoporous silica materials are related to the weaker interactions due to the bigger pore size of the MCM-48 ( $d_{\text{pore}} = 3.5 \text{ nm}$ ) in comparison with the smaller pore of silicalite ( $d_{\text{pore}} = 0.6 \text{ nm}$ ), which is closer to the kinetic diameter of DMMP ( $dk_{\text{DMMP}} = 0.57 \text{ nm}$ ). In spite of the higher specific surface area of the mesoporous material ( $S_{\text{MCM-48}} = 1233 \text{ m}^2/\text{g}$  vs  $S_{\text{Silicalite}} = 334 \text{ m}^2/\text{g}$ ), equilibrium sorption capacity is lower than its microporous counterpart ( $W_{\text{e,MCM48}} = 88 \text{ mg/g}$  @ 162 mg/m<sup>3</sup> DMMP vs  $W_{\text{e,Silicalite}} = 391 \text{ mg/g}$  @ 162 mg/m<sup>3</sup> DMMP).

Table 5.11 compiles Yoon-Nelson and the Wheeler model fitting parameters of experimental MCM-48 breakthrough data shown in Figure 5.18. In this case, coefficient of determination in all the cases is > 99 %, and predicted data adjust satisfactorily to experimental both at dynamic sorption stage and at equilibrium. Thanks to the bigger pore dimension of MCM-48, the strength of interactions with guest molecules favours the diffusion of adsorbed species to the mesoporous channels, ensuring enough concentration of available sorption sites on the external surface.

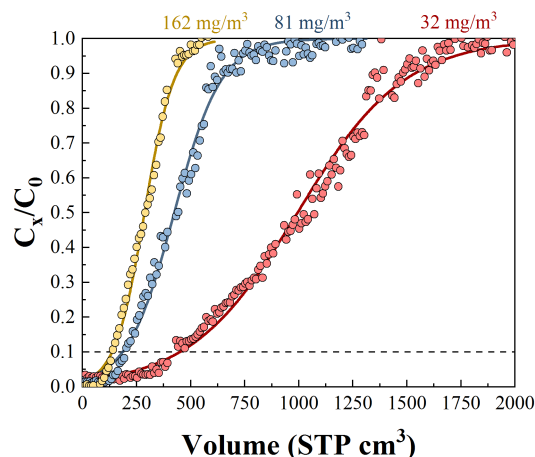


Figure 5.18. Breakthrough curves of MCM-48 modified  $\mu$ -preconcentration for exposures of DMMP/N<sub>2</sub> at 32 (red), 81 (blue) and 162 mg/m<sup>3</sup> (yellow) at room temperature and 10 STP cm<sup>3</sup>/min, experimental data have been fitted to the Yoon-Nelson model (solid line).

TABLE 5.11. ADSORPTION RESULTS AND FITTING YOON-NELSON AND WHEELER PARAMETERS FOR BREAKTHROUGH CURVES AT DMMP CONCENTRATIONS FROM 32 TO 162 MG/MG<sup>3</sup> AT 293 K AND 10 STP CM<sup>3</sup>/MIN FLOW RATE

[DMMP] (mg/m <sup>3</sup> )	$t_b$ (min)	$W_d$ (mg/g)	$W_e$ (mg/g)	$k_{YN}$ (1/min)	$\tau_{YN}$ (min)	$k_v$ (1/min) $\cdot 10^5$	$W_{e,Wheeler}$ (mg/g)	$R^2$
32	35	21	60	0.040	99	1.7	60	0.9901
81	16	25	65	0.084	43	1.5	66	0.9921
162	14	43	88	0.146	29	1.8	88	0.9952

Figure 5.19 shows the breakthrough results for MCM\_8um\_1L and MCM\_8um\_20L, with an adsorbent layer of  $0.54 \pm 0.30 \mu\text{m}$  ( $m_{\text{MCM-48}} = 176 \mu\text{g}$ ) and  $3.81 \pm 1.91 \mu\text{m}$  ( $m_{\text{MCM-48}} = 1241 \mu\text{g}$ ), when they are exposed to 10 STP cm<sup>3</sup>/min of 162 mg/m<sup>3</sup> DMMP at room temperature. Breakthrough volume for the 0.54  $\mu\text{m}$  coating is 148 mL, whereas dynamic sorption capacity accounts for 24  $\mu\text{g}$  DMMP adsorbed. For the 3.81  $\mu\text{m}$  coating, breakthrough volume increases up to 408 mL, resulting in 65  $\mu\text{g}$  for dynamic sorption capacity. These values are within the expected range due to the level of accuracy for thickness/loading of MCM-48 determination. In this scenario, we can observe that thick adsorbent layers, although having more adsorbent mass, performs worse at the same gas flow rate due to intercrystalline diffusion, than



thin layers, where this phenomenon is barely noticeable. As for equilibrium sorption capacity, we observed values up to 75  $\mu\text{g}$  for 0.54  $\mu\text{m}$  coating and 46  $\mu\text{g}$  for 3.81  $\mu\text{m}$  coating, which is up to 8.7-fold higher than observed in 40  $\mu\text{m}$ -depth  $\mu$ -devices. Since DMMP adsorption in MCM-48 mesoporous materials appears to be driven by external diffusion primarily, the decrease of gas free section increases the velocity of the gas inside at the same flow rates (from 90 cm/s to 445 cm/s for the 0.54  $\mu\text{m}$  coating and 795 cm/s for the 3.81  $\mu\text{m}$  coating) resulting in a more efficient mass transfer from the gas to the solid phase. When we compared two devices with the same free gas section ( $\sim 93\%$ ), in this case 0.54  $\mu\text{m}$  coatings present the same free section as the 40  $\mu\text{m}$ -depth microdevices ( $t_{\text{MCM-48}} = 2.79 \mu\text{m}$ ), we can see that breakthrough volumes present close values (148 mL vs 141 mL, respectively) but dynamic sorption capacity is increased in the 0.54  $\mu\text{m}$  coating device (from 43 mg/g to 136 mg/g) (Table 5.12).

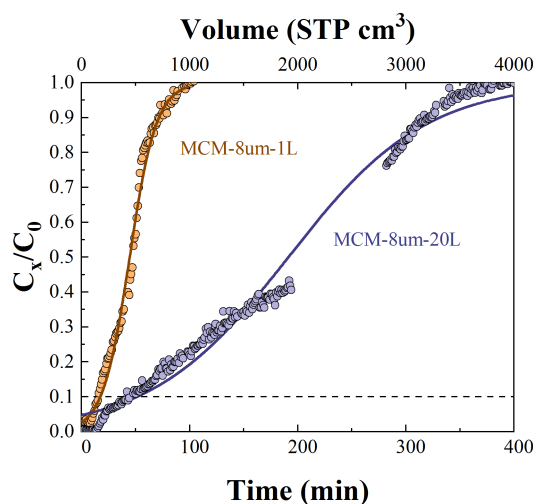


Figure 5.19. Influence of adsorbent thickness at 162  $\text{mg}/\text{m}^3$  DMMP at room temperature and 10 STP  $\text{cm}^3/\text{min}$  flow rate:  $0.54 \pm 0.30 \mu\text{m}$  (orange) vs  $3.81 \pm 1.91 \mu\text{m}$  (blue)

Figure 5.20.a shows that doubling the gas velocity (from  $u_{\text{gas}} = 90 \text{ cm/s}$  to  $u_{\text{gas}} = 179 \text{ cm/s}$ ) on MCM\_40um\_10L devices does not affect the shape of the breakthrough curve, and breakthrough volume and dynamic sorption capacity remains unaltered ( $V_b = 165 \text{ mL}$ ,  $m_b = 13 \mu\text{g}$ , 25  $\text{mg}/\text{g}$  @ 81  $\text{mg}/\text{m}^3$  DMMP at room temperature) indicating that the adsorption is govern by external diffusion at those experimental conditions (Table 5.12). However, at high gas velocities ( $u_{\text{gas}} = 448 \text{ cm/s}$ ) breakthrough volume drops to 229 mL @ 32  $\text{mg}/\text{m}^3$  DMMP (when  $u_{\text{gas}} = 90 \text{ cm/s}$ ,  $V_b = 348 \text{ mL}$ ) as well as dynamic sorption capacity (7  $\text{mg}/\text{g}$  @ 32  $\text{mg}/\text{m}^3$  DMMP vs 11  $\text{mg}/\text{g}$  @ 32  $\text{mg}/\text{m}^3$  DMMP) as a result of a lower contact time (Figure 5.20.b).

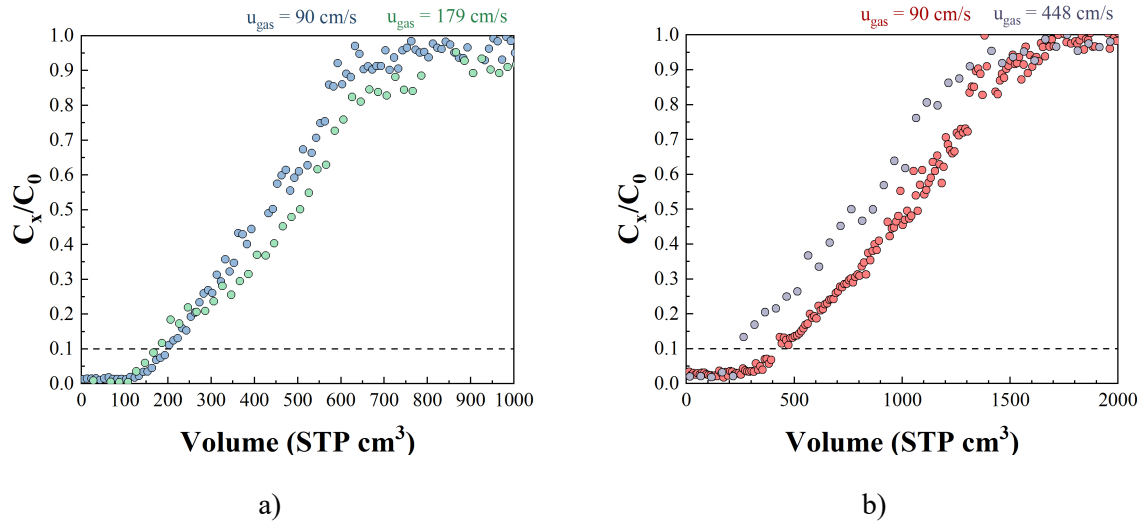


Figure 5.20. a) Influence of gas velocity at  $81 \text{ mg/m}^3$  DMMP at room temperature:  $90 \text{ cm/s}$  (blue) and  $179 \text{ cm/s}$  (green); b) Influence of gas velocity at  $32 \text{ mg/m}^3$  DMMP at room temperature:  $90 \text{ cm/s}$  (red) and  $448 \text{ cm/s}$  (purple).

TABLE 5.12. BREAKTHROUGH RESULTS FOR MCM-48 MODIFIED  $\mu$ -PRECONCENTRATORS AT THE OPERATIONAL CONDITIONS PRESENTED IN TABLE 5.10

Sorption unit	[DMMP] ( $\text{mg/m}^3$ )	$u_{\text{gas}}$ ( $\text{cm/s}$ )	$t$ (ms)	$t_b$ (min)	$W_d$ ( $\text{mg/g}$ )	$W_e$ ( $\text{mg/g}$ )	Bed efficiency
MCM-8 $\mu\text{m}$ -1L	162	447	0.49	15	136	413	33
MCM-8 $\mu\text{m}$ -20L	162	796	3.38	41	53	418	13
MCM-40 $\mu\text{m}$ -10L	32	90	2.48	35	21	60	35
MCM-40 $\mu\text{m}$ -10L	81	90	2.48	16	25	65	39
MCM-40 $\mu\text{m}$ -10L	162	90	2.48	14	43	88	49
MCM-40 $\mu\text{m}$ -10L	32	448	0.50	5	14	48	29
MCM-40 $\mu\text{m}$ -10L	81	179	1.24	9	27	74	37

### 5. 6. 3. $\mu$ -PRECONCENTRATORS MODIFIED WITH POLY-IONIC LIQUIDS

The evaluation of DMMP sorption properties of poly-(ionic liquid) films was performed in two complementary scenarios: over graphitized active carbons and as thick films in  $\mu$ -

preconcentrators. The experiments performed with the modified active carbons was performed at the University of Michigan. They involved the coating of commercial graphitized active carbons (Carbopack X, Supelco) with imidazolium-based ionic liquids (as described on Chapter II): 1-butyl-3-methylimidazolium bis(trifluoromethanesulfonyl)-imide (BIL) and in situ UV polymerized film of protic ionic liquid 1-H-3-vinylimidazolium bis(trifluoromethanesulfonyl)imide (PIL). These experiments aimed to validate the used of protic imidazolium based ionic liquid in comparison with their non-protic counterpart. The experiments performed with PIL-modified  $\mu$ -devices were performed at the University of Zaragoza following the same protocols described for the microporous and mesoporous coated  $\mu$ -preconcentrators.

#### 5. 6. 3. 1. DMMP sorption process on poly-(ionic liquids) supported on graphitized active carbons

Organophosphorus sorption capacities of Carbonpack-X (C-X), C-X coated with BIL (C-X/BIL) and C-X coated with PIL (C-X/PIL) were evaluated by breakthrough analysis, using as target molecule the sarin surrogate dimethyl methylphosphonate (DMMP, 97%, Sigma Aldrich) in dry  $N_2$ . It also has been assessed DMMP sorption in the presence of humidity (30 % RH) or interferents with similar kinetic diameter ( $dk_{\text{toluene}} = 0.58 \text{ nm}$  [195],  $dk_{\text{DMMP}} = 0.57 \text{ nm}$  [196],  $dk_{\text{decane}} = 0.99 \text{ nm}$ ) or vapor pressure ( $P_{v,\text{toluene}} = 3.79 \text{ kPa @ } T = 298 \text{ K}$ ,  $P_{v,\text{decane}} = 0.19 \text{ kPa @ } T = 298 \text{ K}$ ,  $P_{v,\text{DMMP}} = 0.13 \text{ kPa @ } T = 298 \text{ K}$  [197]). The IL-modified carbons were packed in Inconel tubing (5 cm long, 1.59 mm OD, 1.35 mm ID) wrapped with coiled nickel-chromium alloy resistance wire (NIC-60, Omega Engineering).

Figure 5.21 shows breakthrough curve results of C-X, C-X/BIL and C-X/PIL when they are exposed to  $162 \text{ mg/m}^3$  DMMP in dry  $N_2$  and with binary mixtures of DMMP – toluene ( $162 \text{ mg/m}^3$  and  $120 \text{ mg/m}^3$  respectively) and DMMP – decane ( $162 \text{ mg/m}^3$  and  $120 \text{ mg/m}^3$ ). C-X exhibits greater selectivity towards non-polar, low-volatile compounds such as decane (0.07 Debye), where no breakthrough volume has been registered after 2 h of continuous exposure, in comparison with polar compounds of same volatility ( $P_{v,\text{decane}} = 0.19 \text{ kPa @ } T = 298 \text{ K}$ ,  $P_{v,\text{DMMP}} = 0.13 \text{ kPa @ } T = 298 \text{ K}$ ) such as DMMP (3.62 Debye). Furthermore, higher volatile compounds such as toluene ( $P_{v,\text{toluene}} = 3.79 \text{ kPa @ } T = 298 \text{ K}$ , 0.36 Debye) present breakthrough volumes similar to DMMP ( $P_{v,\text{DMMP}} = 0.13 \text{ kPa @ } T = 298 \text{ K}$ , 3.62 Debye) in spite of their dipole moment differences:  $V_{b,\text{toluene}} = 46 \text{ mL @ } 377 \text{ mg/m}^3$  toluene vs  $V_{b,\text{DMMP}} = 52 \text{ mL @ } 267 \text{ mg/m}^3$  DMMP (Table 5.13).

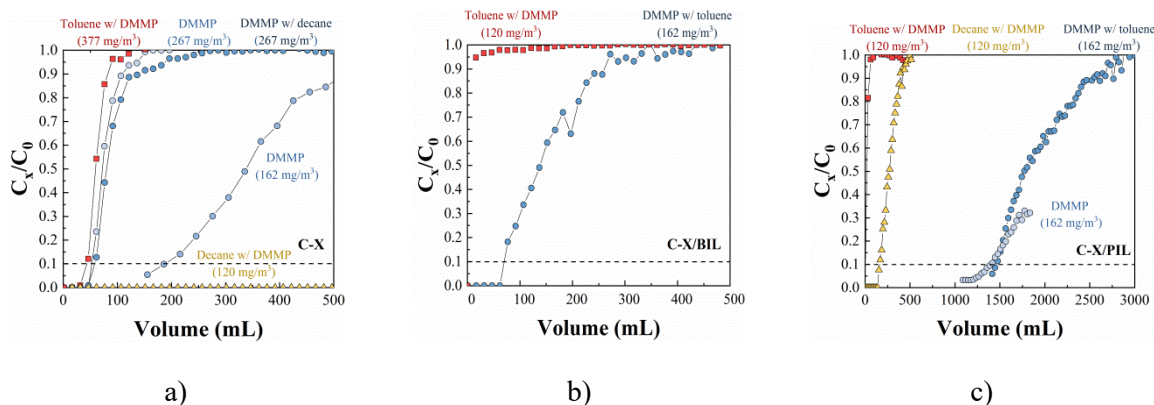


Figure 5.21. Breakthrough curves for: a) C-X, b) C-X/BIL and c) C-X/PIL. Red squares: toluene, blue circles: DMMP and yellow triangles: *n*-decane. Concentration of each analyte is indicated above each corresponding breakthrough curve. Dashed line at  $C_x/C_0 = 0.1$  indicates where breakthrough was considered.

Commonly, C-X (surface area = 240 m<sup>2</sup>/g) is considered to be a better sorbent for non-polar, lower volatility compounds ( $0.34 < P_v < 0.01$  kPa @ 298 K) [198] than for higher volatility targets, where higher surface area carbons exhibit better performance, such as Carboxen 1000 (surface area = 1200 m<sup>2</sup>/g) [133]. However, adsorption is on a carbon based material an heterogenous process that is not only driven by surface area, but many other factors come into play such as low energy London dispersive forces between adsorbent and sorbate [199], pore sized distribution (microporosity, mesoporosity) [200] as well as experimental conditions (analyte concentration, gas velocity or co-existing adsorbates) [63].

Regarding modified carbon, protic polymeric ionic liquid coating (C-X/PIL) greatly increases C-X affinity towards organophosphorus compounds. In fact, the DMMP breakthrough volume increases up to 8 times, from 187 mL to 1470 mL, and equilibrium sorption capacity increases up to 2 times, from 56 mg/g to 129 mg/g. In addition, the selectivity towards less polar compounds diminishes: the registered breakthrough volume and equilibrium sorption capacities values for both decane and toluene are lower than the exhibited by non-modified CX counterparts.

On the contrary, the coating with non-protic ionic liquid (BIL), does not improve DMMP sorption properties of C-X (breakthrough volume and equilibrium sorption capacities are reduce to 67 mL and 24 mg/g respectively), although its selectivity towards less polar compounds is severely modified (toluene is almost completely bypassed). These observations highlights the enormous potential of IL moieties to separate polar from non-polar analytes as well as

undergo multiple solvent-solute interactions, according to Abraham model such as non-bonding and  $\pi$ -electron, dipole, hydrogen bonding and cohesion and dispersion interactions [201].

TABLE 5.13. BREAKTHROUGH RESULTS FOR C-X AND IL MODIFIED C-X FIXED BED CONFIGURATIONS FOR DMMP, TOLUENE AND DECANE AT ROOM TEMPERATURE

Sorption unit	Analyte	[Analyte] (mg/m <sup>3</sup> )	t <sub>b</sub> (min)	W <sub>d</sub> (mg/g)	W <sub>e</sub> (mg/g)	Bed efficiency
C-X	DMMP	162	15	136	413	33
	DMMP w/toluene	267	10	3	5	67
	DMMP w/decane	267	10	3	5	63
	Toluene w/DMMP	377	41	53	418	13
	Decane w/DMMP	120	> 120	> 29	-	-
C-X/BIL	DMMP w/toluene	162	14	4	9	45
	Toluene w/DMMP	120	< 0	-	-	-
C-X/PIL	DMMP	162	145	98	*	*
	DMMP w/toluene	162	145	98	129	76
	Toluene w/DMMP	120	< 0	-	-	-
	Decane w/DMMP	120	17	8	13	62

\*Experiment was finished before saturating the adsorbent.

5. 6. 3. 2. DMMP sorption process on poly-(ionic liquids) films deposited on  $\mu$ -preconcentrators

Following previous results, non-protic imidazolium-based ionic liquids were discarded, and the  $\mu$ -preconcentrator were functionalized with in situ polymerized PIL films. On Table 5.14 presents the five poly-IL-modified  $\mu$ -preconcentrators used for testing DMMP preconcentration at room temperature. The breakthrough experiments were performed at 162 mg/m<sup>3</sup> DMMP in dry N<sub>2</sub> at room temperature. For SD\_40um and DD\_40um the experiments were performed with a mass flow of 10 cm<sup>3</sup>/min STP, i.e.  $u_{\text{gas}}$  of 167 cm/s and 100 cm/s respectively and contact times of 1.93 ms and xxx ms. DD\_20um was performed at 4 mL/min and 10 mL/min which result in gas velocities of 100 cm/s and 251 cm/s, and contact times of 8 and 15 ms. DD\_20x20 and DD\_50x50 were evaluated at 10 mL/min, which led to gas velocities of 211 cm/s and contact times of 238 ms.

TABLE 5.14. POLY-(IONIC LIQUIDS)-MODIFIED  $\mu$ -PRECONCENTRATORS USED IN THIS WORK

Designation	Design	$d_{\mu\text{PC}}$ ( $\mu\text{m}$ )	Coating	$t_{\text{PIL}}$ ( $\mu\text{m}$ )	$m_{\text{PIL}}$ (mg)
SD_40um	2.B.b	40	Static deposition	19.5	6.35
DD_40um	2.B.a	40	Dynamic deposition	34.6	2.70
DD_20um	2.B.a	20	Dynamic deposition	6.7*	2.20
DD_20x20	2.B.c	20	Dynamic deposition	4.2*	2.20
DD_50x50	2.B.d	20	Dynamic deposition	6.0*	2.20

\*PIL thickness has been calculated considering a homogenous coating.

On Figure 5.22 are shown the DMMP breakthrough curves at room temperature were we can analyse: the influence of the deposition procedure and the solute-solvent contact at different headspaces, feed gas velocities and cavity designs.

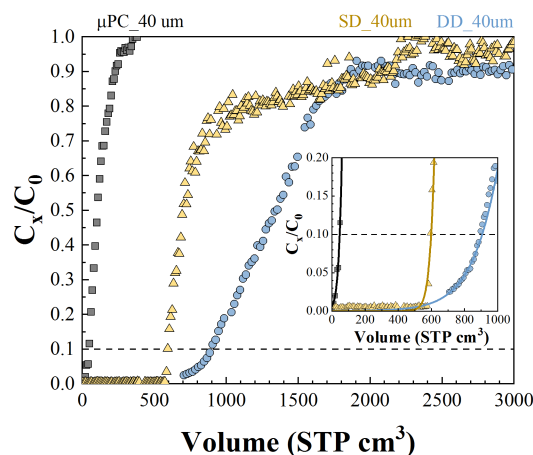


Figure 5.22.  $162 \text{ mg/m}^3$  DMMP adsorption breakthrough for IL-modified  $\mu$ -preconcentrators at room temperature on  $40 \text{ }\mu\text{m}$ -depth microdevices: static (yellow) vs dynamic (blue). Dashed line at  $C_x/C_0 = 0.1$  correspond to breakthrough volume. Insets: magnification at breakthrough point.

DMMP breakthrough testing of SD\_40um and DD\_40um reveal that both microdevices exhibit high breakthrough volume ( $586 \text{ STP cm}^3$  and  $838 \text{ STP cm}^3$  respectively) and thus dynamic sorption capacity ( $95 \text{ }\mu\text{g}$ ,  $49 \text{ mg/g}$  and  $136 \text{ }\mu\text{g}$ ,  $62 \text{ mg/g}$ ) towards DMMP at  $162 \text{ mg/m}^3$  at room temperature. The higher dynamic sorption capacity for the DD-40um device could be related to a more homogenous solvent deposition on the microcavity (check SEM cross-sections). On the contrary, bed efficiency is higher in the case of SD\_40um (62% vs 56%), due to the differences in film thickness and thus confirming DMMP sorption as diffusion dominated phenomena (Table 5.15).

As it is shown in Figure 5.23.a, by forcing solute-solvent contact by decreasing the microchannel depth from  $40 \text{ }\mu\text{m}$  to  $20 \text{ }\mu\text{m}$  (although solvent mass is also decreased) while gas velocity remains at  $u_{\text{gas}} = 100 \text{ cm/s}$  (by decreased feed mass flow from  $10 \text{ mL/min}$  to  $4 \text{ mL/min}$  on the DD\_20um), the effectiveness of the preconcentration increases from 56 % for DD-40um to 88 % for DD\_20 um, while the breakthrough volume does not severely be affected ( $735 \text{ mL}$  for DD\_20um vs  $838 \text{ mL}$  for DD\_40um) (Table 5.15). When the gas flow velocity is increased from  $100 \text{ cm/s}$  to  $251 \text{ cm/s}$  (increasing the flow rate from  $4 \text{ mL/min}$  to  $10 \text{ mL/min}$ ), breakthrough volume is decreased to  $604 \text{ mL}$  as well as dynamic sorption capacity (from  $119 \text{ }\mu\text{g}$ ,  $54 \text{ mg/g}$  @  $100 \text{ cm/s}$  to  $98 \text{ }\mu\text{g}$ ,  $46 \text{ mg/g}$  @  $251 \text{ cm/s}$ ) due to the lower contact time (Figure 5.23.b). On the other hand, the efficiency of the PIL film remains almost constant (Table 5.15).

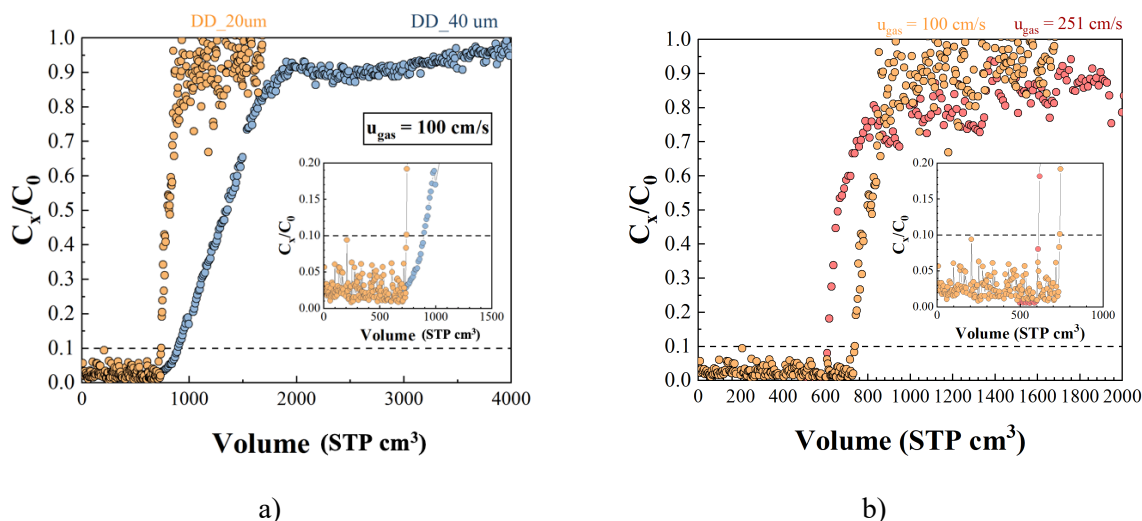


Figure 5.23. 162 mg/m<sup>3</sup> DMMP adsorption breakthrough for IL-modified  $\mu$ -preconcentrators at room temperature: a) influence of the solute-solvent contact at  $u_{gas} = 100$  cm/s: 20  $\mu$ m-depth (orange) vs 40  $\mu$ m-depth (blue); b) Influence of gas velocity:  $u_{gas} = 100$  cm/s (orange) vs  $u_{gas} = 251$  cm/s (red). Dashed line at  $C_x/C_0 = 0.1$  correspond to breakthrough volume. Insets: magnification at breakthrough point.

In order to improve solute-solvent contact, new designs of  $\mu$ -preconcentrators has been proposed with inner square-shaped pillars of 20  $\mu$ m (DD\_20x20um) and 50  $\mu$ m (DD\_50x50um) with a gap between each pillar of 20  $\mu$ m or 50  $\mu$ m respectively and coated following the same procedure as with DD\_20um and DD\_40um (Figure 5.24). This arrangement would increase bed residence and thus contact time between solute and solvent, as well as adsorbent mass loading since walls of the pillars increase surface area where the film could be deposited. Initial results (Figure 5.22.d) highlight the difficult to achieve a homogenous coating on intricate geometries. In fact, neither DD\_20x20um or DD\_50x50um achieves to overpass breakthrough volumes of the previous designs (Table 5.15). Considering that gas flow velocity has not drastically changed ( $u_{gas,max} = 211$  cm/s for DD\_20x20um and  $u_{gas,max} = 238$  cm/s for DD\_50x50u, vs  $u_{gas} = 251$  cm/s for DD\_20um) as well as contact time remains unaltered ( $\tau = 6$  ms), the worst performance of the new designs is derived from a worst adsorbent coating due to a more intricate geometry and the poor wettability of Si-etched interface with the VIL solvent (acetone).



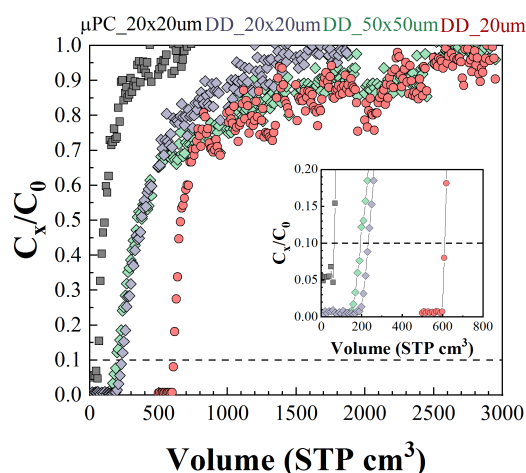


Figure 5.24. 162 mg/m<sup>3</sup> DMMP adsorption breakthrough for IL-modified  $\mu$ -preconcentrators at room temperature, design w/o pillars (red), design with inner 20x20  $\mu$ m pillars (purple), design with inner 40x40  $\mu$ m pillars (green). Dashed line at  $C_x/C_0 = 0.1$  correspond to breakthrough volume. Insets: magnification at breakthrough point.

TABLE 5.15. BREAKTHROUGH RESULT FOR PIL MODIFIED  $\mu$ -PRECONCENTRATORS FOR 162 MG/M<sup>3</sup> DMMP AT 10 STP CM<sup>3</sup>/MIN AND ROOM TEMPERATURE

Sorption unit	$u_{gas}$ (cm/s)	$t$ (ms)	$t_b$ (min)	$W_d$ (mg/g)	$W_e$ (mg/g)	Bed efficiency
SD_40um	163	17.32	59	15	24	62
DD_40um	617	7.37	84	50	89	56
DD_20um	251	5.95	61	45	72	62
DD_20x20	211	6.01	18	13	51	26
DD_50x50	238	6.30	22	16	38	42

## 5. 7. CONCLUSIONS

In this Chapter we have successfully evaluated the organophosphorus sorption capacities of modified  $\mu$ -preconcentrators with micro- and mesoporous materials as well as polymeric ionic liquid films. Breakthrough results at 162 mg/m<sup>3</sup> DMMP in dry N<sub>2</sub> at 293 K using a feeding mass flow of 10 STP cm<sup>3</sup>/min of the most prominent modified  $\mu$ -preconcentrators are shown

on Figure 5.25: in situ synthesized silicalite, MCM-48 coatings deposited on 40  $\mu\text{m}$ -depth  $\mu$ -devices, Cu-BTC growth by electrosynthesis, Zn-DMCAPZ deposited by spin coating, Zn-MIM deposited by spin coating and PIL films deposited by dynamic deposition and polymerized in 20  $\mu\text{m}$ -depth  $\mu$ -devices. It has been omitted the results of the graphitized active carbons and modified active carbons for not be feasible their integrations into our actual  $\mu$ -device. They are missing the results as well from the MOF thin films, i.e., Zn-DMCAPZ synthesized via layer-by-layer and Zn-MIM growth via hydrothermal synthesis from precursors deposited via atomic layer deposition, since their poor dynamic sorption performance.

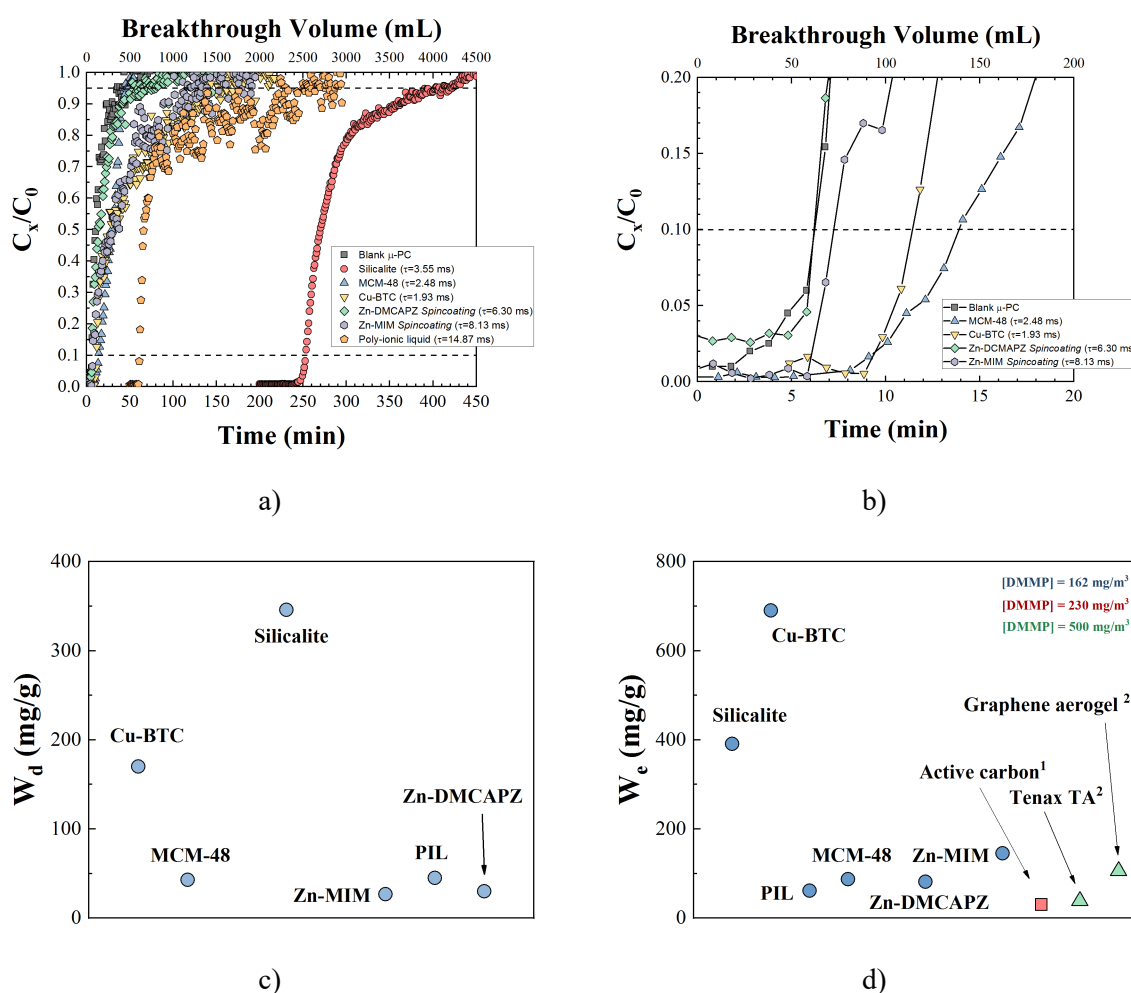


Figure 5.25. DMMP sorption performance of modified  $\mu$ -preconcentrators reported in this Chapter. a) Breakthrough comparison of the evaluated  $\mu$ -devices for 162  $\text{mg}/\text{m}^3$  DMMP in dry  $\text{N}_2$  at 293 K. b) Detail from previous breakthrough curve at low sampling volume. c) Dynamic sorption capacity for 162  $\text{mg}/\text{m}^3$  DMMP at 293 K of the proposed materials calculated from previous breakthrough curves.

*d) Equilibrium sorption capacity for 162 mg/m<sup>3</sup> DMMP at 293 K of the proposed materials calculated from breakthrough curves as well as reference data from bibliography (<sup>1</sup> [192], <sup>2</sup> [193]).*

Best dynamic sorption capacity is clearly exhibited by the silicate modified  $\mu$ -devices, with a total sampling volume over 2500 mL (409  $\mu$ g DMMP adsorbed), followed by PIL modified  $\mu$ -preconcentrators (608 mL, 98  $\mu$ g DMMP) (Figure 5.25.a). At low breakthrough volumes, MCM-48 modified  $\mu$ -devices performed slightly above that Cu-BTC devices (141 mL, 23  $\mu$ g DMMP vs 118 mL, 19  $\mu$ g DMMP), whereas Zn-DMCAPZ and Zn-MIM are not considered adequate for preconcentration purposes, due to their low breakthrough volume (Figure 5.25.d).

As for dynamic sorption capacity, silicalite present up to 10 times higher values than lower ones ( $W_{d,silicalite} = 346$  mg/g vs  $W_{d,Zn-MIM} = 27$  mg/g or  $W_{d,Zn-DMCAPZ} = 30$  mg/g) followed by Cu-BTC  $\mu$ -devices ( $W_{d,Cu-BTC} = 179$  mg/g). PIL modified devices, although having one of the highest breakthrough volumes (608 mL) does not shine at these parameter, and is close related to the value exhibit by MCM-48 ( $W_{d,PIL} = 45$  mg/g vs  $W_{d,MCM-48} = 43$  mg/g). On the other hand, equilibrium sorption capacity of Cu-BTC overpass the one exhibited by silicate ( $W_{e,Cu-BTC} = 698$  mg/g vs  $W_{e,Silicalite} = 391$  mg/g), which can be related to the higher specific surface of the MOF in comparison with the zeolite ( $S_{Cu-BTC} = 1855$  m<sup>2</sup>/g vs  $S_{Silicalite} = 334$  m<sup>2</sup>/g) and thus, presenting more active sites where DMMP can be adsorpted. Contrasting the calculated equilibrium capacities, all the evaluated materials present sorption capacities higher than the values reported even at higher DMMP concentrations ([192], [193]). In Table 5.16 are compiled the most relevant results of the modified  $\mu$ -devices for 162 mg/m<sup>2</sup> DMMP adsorption at room temperature and 10 STP cm<sup>3</sup>/min.

TABLE 5.16. BREAKTHROUGH CURVE RESULTS COMPARISON OF THE MODIFIED  $\mu$ -DEVICES FOR 162 MG/M<sup>3</sup> DMMP AT 10 STP CM<sup>3</sup>/MIN AND ROOM TEMPERATURE

	<i>Sorption unit</i>	<i>S<sub>surface</sub></i> (m <sup>2</sup> /g)	<i>u<sub>gas</sub></i> (cm/s)	<i>t</i> (ms)	<i>t<sub>b</sub></i> (min)	<i>W<sub>d</sub></i> (mg/g)	<i>W<sub>e</sub></i> (mg/g)	<i>Bed efficiency</i>
Zeolite	Sil_20um	334	208	3.55	245	335	380	88
MOFs	Zn-DMCAPZ_SC	1200	101	6.30	6.8	30	82	37
	Zn-DMCAPZ_LbL	1200	174	0.33	3.6	331	2422	14
	Zn-MIM_SC	1986	308	8.13	7.8	27	145	18
	Zn-MIM_ALD	1986	85	0.89	0	0	844	0
	Cu-BTC_ES	1855	217	1.93	118	179	718	24
Meso-porus	MCM-40um-10L	1233	90	2.48	14	43	88	49
PIL	SD_40um	-	98	5.33	59	49	78	62
	DD_40um	-	100	5.00	84	62	109	56
	DD_20um	-	251	5.95	61	45	72	62
	DD_20x20	-	211	6.01	18	13	51	26
	DD_50x50	-	238	6.30	22	16	38	42

**CHAPTER VI:**  
**PRECONCENTRATION OF ORGANOPHOSPHORUS**  
**COMPOUNDS**



## 6. PRECONCENTRATION OF ORGANOPHOSPHORUS COMPOUNDS

### 6. 1. INTRODUCTION

After presenting and characterizing the adsorbent materials, explore different approaches to integrate them into miniaturized fluidic devices and analysing their performance with organophosphorus compounds at trace level, we finally apply the most promising modified adsorbents to the preconcentration of ppb-traces of organophosphorus compounds. The selected microdevices have been chosen by their breakthrough volume and dynamic retention capacity and comprise a selection of one candidate of each family of materials presented in Chapter II: zeolitic materials (silicalite), MOF (Cu-BTC), mesoporous silica (MCM-48) and polymeric ionic liquid films (PIL).

Finally, the microsampling unit has been integrated into a gas sensor based on a functionalized microcantilever array (presented in Chapter III) (Figure 6.1). As a proof of concept, the whole  $\mu$ -preconcentrator –  $\mu$ -cantilever system has been used for detection of n-hexane at ppm level.

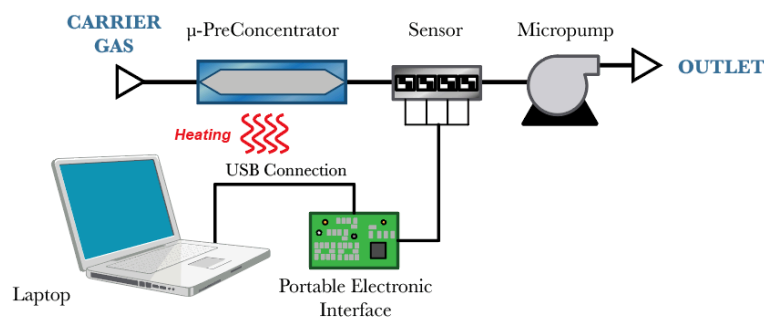


Figure 6.1. Microsampling unit connected to the gas sensor array based on functionalized microcantilever array.

## 6. 2. EVALUATION OF THE PRECONCENTRATION COEFFICIENT

Figure 6.2 shows a typical desorption peak registered downstream of preconcentration unit by a gas chromatograph coupled with a mass spectrometer. It can be seen, that the analyte bolus is transferred in a plug-flow fashion swept by the carrier gas.

Ideally, the desorption signal could be modelled as a Gaussian function, defined by its maximum amplitude and its width, which is commonly given by the full width at half maximum (FWHM). However commonly asymmetric peaks are observed: a sharp frontal edge with a shallow rear edge, which is known as tailing. This behaviour is due to the strength interactions of sorbent-sorbate and heat transfer constrains that causes a non-instantaneous release of the guest molecules from the stationary phase. Commonly, the asymmetric factor  $A_S$  is defined as ratio of the peak half-widths of the rear side and the front side of the desorption peak measured at 10 % of the peak height [202], however, to avoid uncertainties in the areas close to the base line, we have defined it at the half maximum (Figure 6.2).

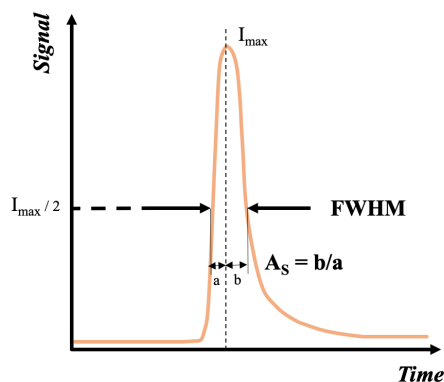


Figure 6.2. Graphical representation of a typical desorption peak. On the graph are shown the most important descriptive parameters: peak height  $I_{max}$ , full width at half maximum (FWHM) and the asymmetric factor  $A_S$ .

The preconcentration performance of the  $\mu$ -device as sampling unit is evaluated from its preconcentration coefficient, denoted as  $K$  [168]. According to IUPAC guidelines, this value is defined as the ratio of the air sample collected volume to the volume in which that same mass is released according to the quantification at the point of detection, assuming no transfer mass losses take place. Accordingly, the  $K$  estimation is carried out under experimental conditions



that guarantee the full adsorption of the target molecules in contact with the sorbent material, i.e. no breakthrough conditions and full desorption. As some authors have pointed out [190], the calculation of ‘preconcentration factors’ from the ratio of detection signals or peak areas registered with and without a preconcentration unit included in the system [203], [204] is not recommended since it does not afford any useful information about the critical performance parameters of a preconcentration unit. Thus, given a desorption peak, the preconcentration coefficient  $K$  is calculated according the IUPAC guidelines and no mass loss in transfer lines as follows:

$$K = \frac{V_{\text{sample collected}}}{V_{\text{sample desorbed}}} = \frac{Q_{\text{sampling}} * t_{\text{sampling}}}{Q_{\text{desorption}} * FWHM} \quad (50)$$

where  $Q_{\text{sampling}}$  is the feeding flow rate,  $t_{\text{sampling}}$  is the sampling time,  $Q_{\text{desorption}}$  is the flow rate at which the released sample is being flushing out and FWHM is the full width at half maximum of the desorption peak registered by the detector. From (40) we can conclude that high  $K$  values can be obtain by either sampling at high flow rates or for long times, while desorbing is preferred at small flow rates. The FWHM value at a certain  $Q$  is strongly dependent on the sorbate-sorbent interactions and can be decreased by increasing the operational temperature to promote the analyte desorption or just by improving the heater design.

## 6. 3. PROOF OF CONCEPT: PRECONCENTRATION OF VOCs

Preliminary preconcentration experiments were performed on 10.5 x 44.5 mm silicalite-coated  $\mu$ -preconcentrators (100  $\mu\text{m}$ -depth free microcavity coated with 4  $\mu\text{m}$  of silicalite growth *in situ*,  $m_{\text{silicalite}} = 4.4 \text{ mg}$ ) using as a target molecule n-hexane [189]. The aim of this set of experiment was to assess the functionality of the proposed  $\mu$ -device, such as, the integrated backside heater, the operating desorption parameters (temperature, mass flow) and the thermal suitability of  $\mu$ -fluidic connections. Furthermore, to verify the feasibility of the combined detection platform consisted on the preconcentration unit coupled with the gas detector, the silicate-modified  $\mu$ -preconcentration unit has been placed upstream the functionalized  $\mu$ -cantilever array presented on Chapter III and has been used to enhance the response signal of the gas sensor for the detection of 352  $\text{mg}/\text{m}^3$  of n-hexane in dry  $\text{N}_2$  at room temperature. Figure 6.3 depicts the experimental set-up used for the desorption characterization of the silicalite-coated  $\mu$ -device. 1759  $\text{mg}/\text{m}^2$  calibrated n-hexane in dry  $\text{N}_2$  was used as analyte and further diluted

with  $N_2$  until reaching desirable concentration when needed. Dry  $N_2$  was used to regenerate the adsorbent bed before each assay and as carrier gas while desorption. The detection of the n-hexane downstream the  $\mu$ -device was performed either with a mass spectrometer (Omnistar GSD 301, Pfeiffer Vacuum) for the desorption characterization experiments and a  $\mu$ -cantilever gas sensor coated with silicalite crystals ( $m_{\text{silicalite}} = 366 \text{ ng}$ ) presented on Chapter III.

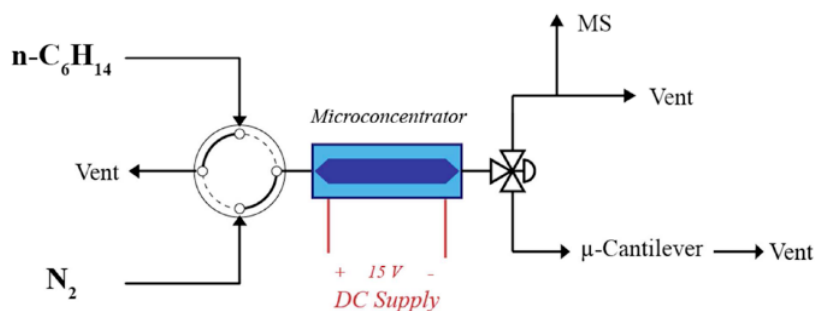


Figure 6.3. Experimental set-up for the characterization of desorption performance of the silicalite-modified  $\mu$ -preconcentrators.

### 6. 3. 1. DESORPTION TEMPERATURE ANALYSIS ON SILICALITE-MODIFIED $\mu$ -PRE-CONCENTRATORS

The desorption bandwidth plays a key role on the preconcentration performance. Desirable features include, among others, thermal heating with short time constants to reduce power consumption. Figure 6.4 shows the desorption peak at four desorption temperatures (378 K to 443 K) of n-hexane adsorbed in silicalite-modified  $\mu$ -devices after the exposure to  $1759 \text{ mg/m}^3$  n-hexane in dry  $N_2$  at room temperature for 90 min. Desorption temperature was achieved by applying DC voltage from 10 V to 20 V to the on-chip heaters during the whole desorption stage, i.e., above 5 min in duration.

As expected, whereas the area below the peak maintains constant (indicating a full material desorption), the peak bandwidth values decrease with temperature, ranging from 3.8811 min at 378 K to 1.7755 min at 443 K, due to the endothermic character of the desorption process, while the  $A_S$  does not change drastically ( $A_S = 1.5 \pm 0.07$ ). These values are clearly exceeding those commonly reported in the literature, within the order of few seconds [171], [205], [206] for VOCs on commercial carbons. This behaviour is related on the desorption temperature herein used, somewhat hindered by the  $\mu$ -fluidic connections capable to withstand maximum

temperature of 453 K. In fact, these values are clearly lower than those commonly reported in the literature for n-hexane desorption on MFI type zeolites around 573 K [207], or even those used on  $\mu$ -concentrators coated with activated carbons, around 498 K [171], [205], [206]. It could be concluded that the operational performance could be notably improved by using high-temperature  $\mu$ -fluidic connections.

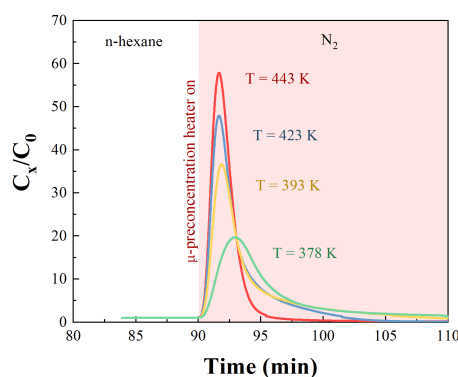


Figure 6.4. Influence of desorption temperature on bandwidth values for silicalite-coated  $\mu$ -preconcentrators.

### 6. 3. 2. PERFORMANCE OF THE COMBINED $\mu$ -PRECONCENTRATOR – $\mu$ -CANTILEVER SYSTEM FOR N-HEXANE DETECTION

The  $\mu$ -cantilever was coated with 366 ng of silicate crystals (as described previously) and the response of the sensor was calibrated upon exposure to different n-hexane concentration ranging from 352 mg/m<sup>3</sup> to 1759 mg/m<sup>3</sup> in dry N<sub>2</sub> at room temperature (298 K). The cantilever calibration was carried out with calibrated n-C<sub>6</sub>H<sub>14</sub>/N<sub>2</sub> mixture and followed the standard procedure already described in previous works within the group [150], [149], [68], as well as on Chapter III. In particular, concentration steps of 10 min were performed sequentially, i.e., 352 mg/m<sup>3</sup> then 704 mg/m<sup>3</sup> and so on until reaching the final concentration of 1759 mg/m<sup>3</sup>. Afterwards, a similar decreasing concentration pattern is applied.

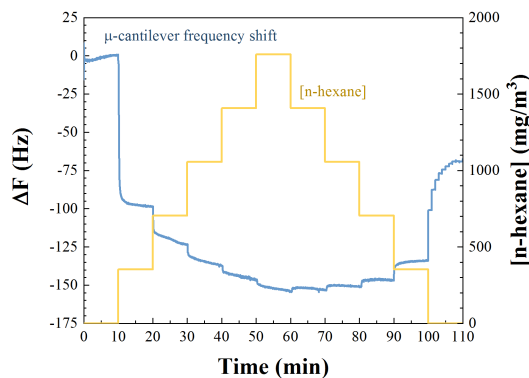


Figure 6.5. Evolution of the resonance frequency (blue line) upon the introduction of *n*-hexane vapours (yellow line) at room temperature for the Si  $\mu$ -cantilever coated with silicalite crystals.

Figure 6.5 shows the resulting frequency shift for each concentration step. From registered values, the calculated sensor sensitivity is 0.2981 Hz/ppmV. Accounting from the experimental signal noise ( $\sim 1$  Hz), the theoretical limit of detection (LOD) value below  $3.5 \text{ mg/m}^3$  is obtained. As it can be observed in Figure 6.5, the recovery of the baseline using dry  $\text{N}_2$  as sweep gas at room temperature is incomplete, indicating that hexane remains adsorbed due to the high affinity of the silicalite towards hexane. To this end, the *in-situ* zeolite degassing is performed by applying adequate DC voltage to the heating resistor embedded on the cantilever tip.

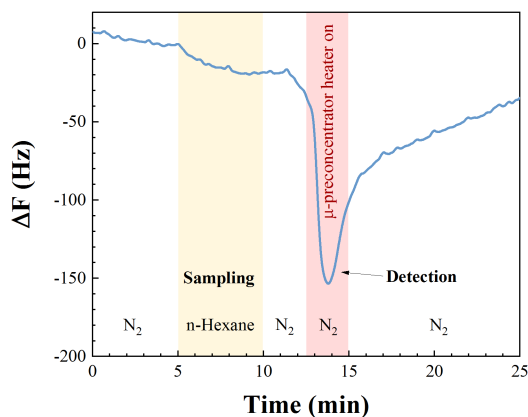


Figure 6.6. Adsorption-desorption experiment of  $352 \text{ mg/m}^3$  of *n*-hexane over a silicalite-modified  $\mu$ -preconcentrator followed by the Si  $\mu$ -cantilever coated with silicalite crystals.

Once the silicalite-functionalized  $\mu$ -cantilever calibration is accomplished and the sensing material is fully regenerated, the  $\mu$ -preconcentration unit is connected upstream of the of the  $\mu$ -cantilever sensor. Figure 6.6 shows a standard experiment with the combined system: preconcentrator unit and  $\mu$ -cantilever array sensor, both modified with silicalite-type zeolite.

Firstly, the resonant frequency baseline is established by sweeping dry N<sub>2</sub> at 10 STP cm<sup>3</sup>/min for 5 min. Afterwards, the sorption stage is performed for 352 mg/m<sup>3</sup> n-hexane in dry N<sub>2</sub> at 10 mL/min STP and room temperature for 5 min. During this period, the frequency shift registered, once stabilized, is ~ 20 Hz, i.e., lower than the sensor response depicted in Figure 6.5 for similar concentration (~ 100 Hz). This behaviour is indicating the hexane in the N<sub>2</sub> stream is being adsorbed on the  $\mu$ -preconcentrator. For the desorption stage, 10 STP cm<sup>3</sup>/min of dry N<sub>2</sub> was fed to the  $\mu$ -device. This injection, some delayed due to volume of transfer lines, modifies the sensor response; although the effect is clearly noticeable when the  $\mu$ -preconcentrator heater is activated for 2.5 min. A huge desorption peak is registered with a maximum frequency shift above 150 Hz. This instantaneous frequency shift correlates with the cantilever signal when directly exposed to ~ 1759 mg/m<sup>3</sup>. Thanks to the  $\mu$ -preconcentration stage, the whole system ‘ $\mu$ -preconcentrator plus  $\mu$ -cantilever’ improves 5-fold the n-hexane detection, i.e. a feeding concentration of 352 mg/m<sup>3</sup> produce a response of the sensor equal to the one observed at 1759 mg/m<sup>3</sup>. Once the DC power is off, n-hexane desorption of the  $\mu$ -preconcentrator by the sweep of the gas takes place at lower rate. Finally, silicalite from both the  $\mu$ -preconcentrator and the  $\mu$ -cantilever is fully regenerated by heating at 423 K.

## 6. 4. EXPERIMENTAL SET-UP FOR EVALUATING PRE-CONCENTRATION COEFFICIENT

Preconcentration experiments were performed with atmospheres of 2.65 mg/m<sup>3</sup> (520 ppbV) of DMMP in dry N<sub>2</sub>. Although this concentration is 8-fold higher than reported lethal value for sarin gas for exposure times up to 10 min (AEGL-3 = 0.38 mg/m<sup>3</sup>, 64 ppbV), it is fairly reasonable value to accurately characterize the  $\mu$ -device performance at a reproducible concentration without the need to use additionally dilution streams. As previously, atmospheres were generated by circulating 10 STP cm<sup>3</sup>/min of dry N<sub>2</sub> through a calibrated permeation tube of DMMP (VALCO, permeation rate of 148.41 ng/min  $\pm$  3.07 at 90 °C) and fed to the  $\mu$ -device. The monitoring of the desorption peak was performed with a gas chromatographer coupled with a mass spectrometer detector (GCMS, Shimadzu GCMS QP2010) downstream the  $\mu$ -device. The characteristic DMMP mass signals were followed ( $m/z$  = 79, 94, 109, 124) as well as the principal uma signals of the main decomposition products: methanol ( $m/z$  = 31), dimethyl ether ( $m/z$  = 45), CO<sub>2</sub> ( $m/z$  = 44) and formaldehyde ( $m/z$  = 29). In Table 6.1 are listed the four main characteristic masses of the decomposition products.

TABLE 6.1. CHARACTERISTIC MASSES OF THE MAIN DMMP DECOMPOSITION PRODUCTS

Product	Molecular formula	Characteristic masses*
		(m/z)
Carbon dioxide	CO <sub>2</sub>	44
Formaldehyde	CH <sub>2</sub> O	<u>29</u> , 30, 28
Dimethyl ether	C <sub>2</sub> H <sub>6</sub> O	<u>45</u> , 46, 29, 15
Methanol	CH <sub>4</sub> O	<u>31</u> , 32, 29, 15

\* Ordered from most to less intensity and underlined the main one.

Two preconcentration approaches were proposed: 1) desorption at static condition and 2) desorption at dynamic conditions. The first approach involves the desorption and focusing of the analyte in a confined environment, and then the bolus injection into the detector. The  $\mu$ -device in this set-up is placed inside a PEEK housing with the inlet and outlet hermetically sealed with tygon O-rings and screwing (Figure 6.7)

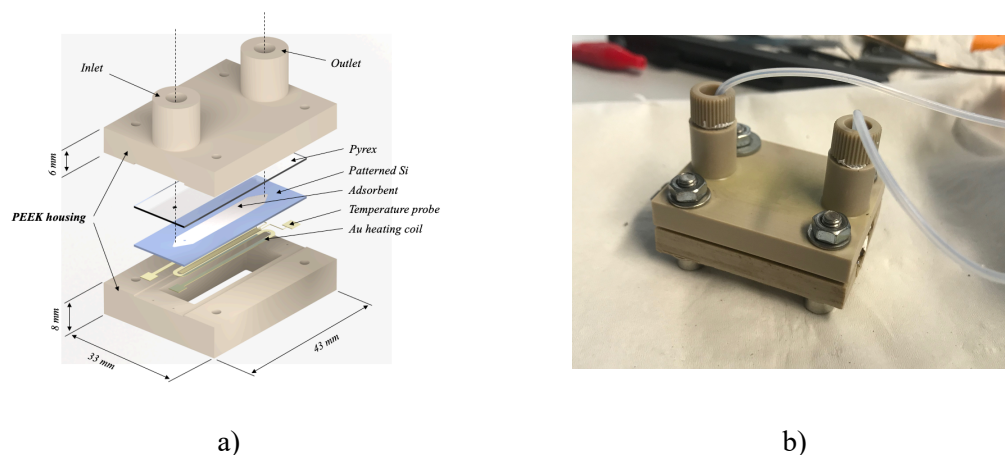


Figure 6.7. a) Schematic of the PEEK housing and the  $\mu$ -preconcentrator. b) PEEK housing with  $\mu$ -preconcentration within and Teflon fluidic connections.

3-way valves are connected upstream and downstream of the PEEK housing, allowing bypassing the gas flow from the  $\mu$ -device. The previous PEEK housing and 3-way valves are connected using 1/16" Teflon tubing. The experimental protocol involves the sampling of 2.65 mg/m<sup>3</sup> of DMMP in dry N<sub>2</sub> at room temperature and 10 STP cm<sup>3</sup>/min for certain time (Figure 6.8.a), after which the cavity is flushed with He from the GCMS carrier at flow rates from 1 to

5 STP  $\text{cm}^3/\text{min}$  for 5 min to evacuate the DMMP in the gas phase (Figure 6.8.b). The adsorbed analyte is thermally desorbed at 523 K for 5 min in a confined volume by closing the upstream and downstream valves (Figure 6.8.c); and then the analyte bolus is push out of the  $\mu$ -device by the GCMS carrier gas to the detector (Figure 6.8.d).

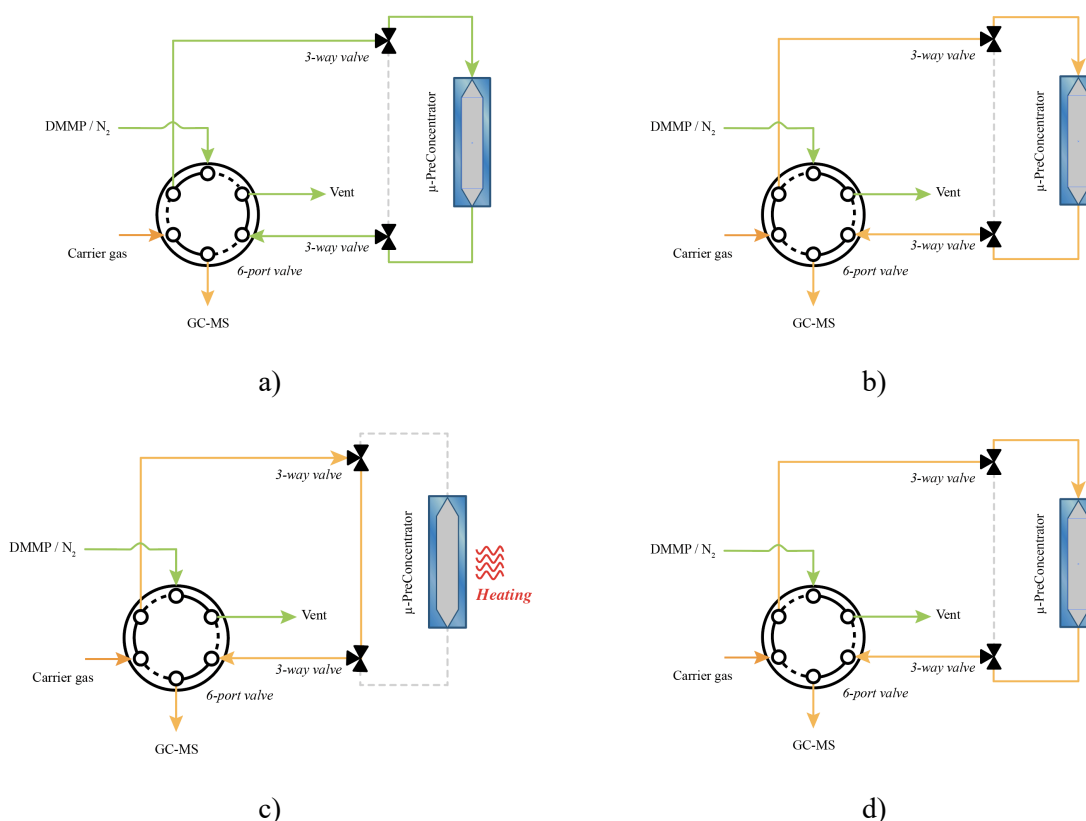


Figure 6.8. Static preconcentration set-up: a) DMMP sampling, b) He cavity flushing, c) DMMP desorption and focusing and d) DMMP desorption peak detection. Green line depicts DMMP/ $\text{N}_2$  flow path whereas orange line depicts He flow path.

The second approach simplifies the previous set-up and without the 3-way valves and without PEEK housing. The  $\mu$ -device is connected to the GCMS 6-port valve through capillary tubing ( $320 \mu\text{m}$  inner diameter) though high temperature septum glued to the Borofloat side of the device. In order to avoid adsorption of the DMMP in the faces of the septa, an intermediate layer of Kapton has been placed between the Borofloat side and the septum. This approach relies on the rapid thermal desorption of DMMP and the adequate carrier flow rate to push out the bolus in a plug-flow fashion, without the need of a focusing stage. Thus, the experimental protocol is reduced to the sampling of DMMP at room temperature and  $10 \text{ cm}^3/\text{min}$  for certain time (Figure 6.9.a), the flushing out of the unadsorbed DMMP with GCMS carrier gas for 5

min, after which, the adsorbent is rapidly heated at 523 K, releasing the DMMP and being pushed out to the detector by the GCMS carrier gas itself (Figure 6.9.b).

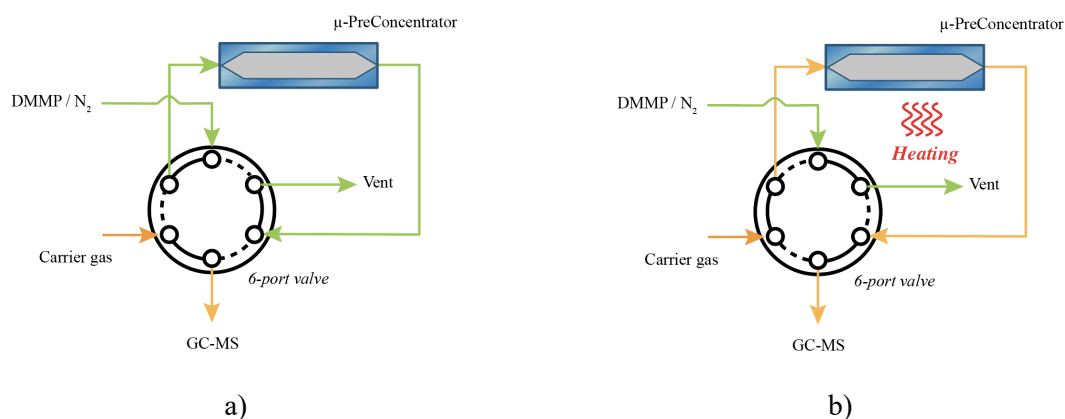


Figure 6.9. Dynamic preconcentration set-up. a) sampling of the DMMP/N<sub>2</sub> mixture. b) Thermal desorption and concentration of the DMMP adsorbed. Between a) and b) takes place a flushing stage (not depicted in the figure). Green line depicts DMMP/N<sub>2</sub> flow path whereas orange line depicts He flow path.

## 6. 5. EVALUATION OF THE $\mu$ -PRECONCENTRATOR COEFFICIENT

The evaluation of the preconcentration factor was performed for the microdevices that exhibited the better performance on the experiments proposed in Chapter V. In Table 6.2 are presented the microdevices chosen for the preconcentration of 2.65 mg/m<sup>3</sup> DMMP in N<sub>2</sub> at room temperature. The devices tested in this work comprise a selection of one candidate of each material families presented in Chapter II: zeolitic materials (silicalite), MOF (Cu-BTC), mesoporous silica (MCM-48) and polymeric ionic liquid films (PIL).



TABLE 6.2.  $\mu$ -PRECONCENTRATORS CHARACTERIZED FOR PRECONCENTRATION OF DMMP

Adsorbent	Coating method	$t_{\text{coating}}$ ( $\mu\text{m}$ )	$m_{\text{coating}}^3$ ( $\mu\text{g}$ )	$V_b^4$ ( $\text{cm}^3$ STP)	$W_d^4$ ( $\text{mg/g}$ )
Silicalite	<i>In situ</i> synthesis	4.0	1184	2525	346
MCM-48	Spin coating	2.7 <sup>1</sup>	527	141	43
Cu-BTC	Electro synthesis	4.7 <sup>1</sup>	113	38	122
PIL	Dynamic deposition (flat cavity)	6.7 <sup>2</sup>	2200	608	45
	Dynamic deposition (patterned cavity)	6.0 <sup>2</sup>	2200	218	16

<sup>1</sup> Measured by profilometry. <sup>2</sup> Theoretical deposition assuming homogeneous coating. <sup>3</sup> Calculated from adsorbent thickness and density of the material. <sup>4</sup> From experiments at 132  $\text{mg/m}^3$  DMMP in dry  $N_2$  at room temperature.

### 6. 5. 1. DETERMINATION OF EXPERIMENTAL CONDITIONS

First preconcentration experiments approach was focused on determining the best experimental approach, i.e., static desorption or dynamic desorption. Following the first approach (desorbing and focusing in static conditions), the MCM-48-modified  $\mu$ -preconcentrator was exposed to 0.25  $\text{mg/m}^3$  DMMP at room temperature for 5 min and the desorption was performed by heating for 5 min at 523 K the  $\mu$ -device with no desorption flow after which, the released DMMP was pushed out to the detector at 1  $\text{cm}^3/\text{min}$  STP with He.

Figure 6.10 shows the static desorption experiment performed on the MCM-48-modified  $\mu$ -device. It can be seen that after desorbing and focusing the release DMMP for 5 min, the sample injected present two distinctive peaks. Whereas the second peak can be related to the DMMP signal, the first peak presents an unusual mass spectra where the  $m/z = 79$  signal is more prominent than the  $m/z = 94$  (main mass signal spectra of DMMP is  $m/z = 94$ , followed by  $m/z = 79$ ). This peak may be attributed to the thermal decomposition of the O-ring at 523 K, although thermal characteristics indicate maximum temperatures close to 573 K. Furthermore, a second desorption stage has been performed, but this time, it has been performed dynamically

(without cutting the carrier flow rate), revealing newly two detected peaks with the same mass spectra configuration than before. Estimate  $K$  values of the two peaks attributed to DMMP were 17 and 18 for the O-ring (first desorption peak) and MCM-48 sorbent (second desorption peak) respectively.

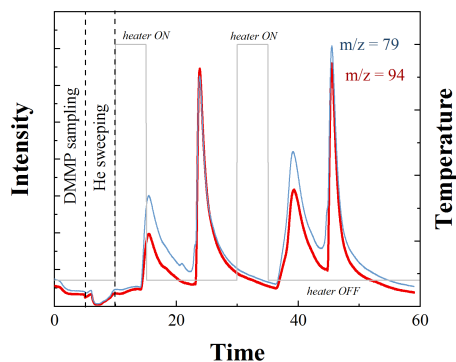


Figure 6.10. Static preconcentration experiment with an MCM-48 modified  $\mu$ -preconcentrator at  $0.26 \text{ mg/m}^3$  DMMP in dry  $\text{N}_2$ . Desorption and focusing of the sample were performed with no flow at 523 K for 5 min. Two consecutive desorption pulses with no sampling in-between were performed to assess the total release of the trapped DMMP. Characteristic DMMP mass:  $m/z=94$  (red),  $m/z=79$  (blue).

The same experiment was performed using the dynamic approach: DMMP desorption at 523 K while carrier gas swept the cavity at  $3 \text{ STP cm}^3/\text{min}$  using the Kapton as intermediate layer in the septum connections to avoid adsorption or decomposition. The device in this case was heated until fully desorption. Along with the MCM-48-modified  $\mu$ -device, a blank device was also analysed (without any adsorbent) as well as a bypassed assay with no  $\mu$ -device whatsoever. Figure 6.11 shows the main characteristic mass of DMMP ( $m/z = 94$ ) for the three experiments. It can be observed that no DMMP adsorption occurs is taking place at the walls of the fluidic piping, and the DMMP is swept easily out by He carrier gas. The blank  $\mu$ -preconcentrator exhibits a small desorption peak as product of DMMP adsorption on the inner walls of the cavity, although it can be negligible in comparison with the peak detected from the MCM-48 modified  $\mu$ -device. In this case, the  $K$  value is slightly inferior than with the previous approach (13 vs 18, for dynamic and static respectively) but we can assure with certainty that the all the DMMP adsorbed has been effectively released.

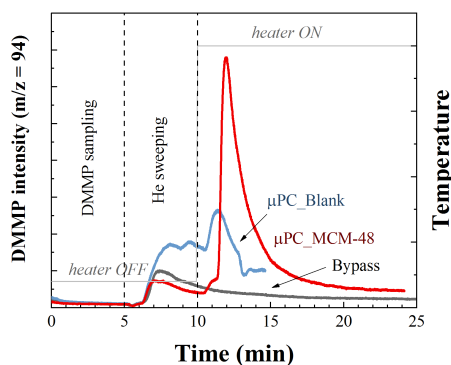


Figure 6.11. Dynamic preconcentration experiment with an MCM-48 modified  $\mu$ -preconcentrator at  $0.26 \text{ mg/m}^3$  DMMP in dry  $N_2$ . Desorption was performed at 523 K while He swept the cavity at 3 STP  $\text{cm}^3/\text{min}$ .

Furthermore, it has been optimized carrier flow rate in order to increase  $K$  value. Figure 6.12 shows a dynamic preconcentration experiment performed on the MCM-48 modified  $\mu$ -device for  $2.65 \text{ mg/m}^3$  DMMP at room temperature and different desorption flow rates (1, 3 and 5 STP  $\text{cm}^3/\text{min}$ ). In this case, the DMMP gas mixture has been sampled for 5 min, after which, the microcavity has been flush with carrier gas in order to evacuate the residual DMMP in the gas phase in the transfer lines. Then, the adsorbed DMMP is release rapidly by heating the  $\mu$ -device using the heater at the backside at 523 K and flushing out the device by the carrier gas from the GCMS (from 1 STP  $\text{cm}^3/\text{min}$  to 5 STP  $\text{cm}^3/\text{min}$ ). As can be observed in Figure 6.12, the increase of the carrier gas sharpens the desorption peak and thus bandwidth (FWHM) is diminished from 7.347 min at 1 STP  $\text{cm}^3/\text{min}$  to 1.071 STP min at 5  $\text{cm}^3/\text{min}$  (Table 6.3). However, maximum  $K$  is not found at 5 STP  $\text{cm}^3/\text{min}$  but at 3 STP  $\text{cm}^3/\text{min}$ , in despite of a wider desorption peak (FWHM = 1.311), as well as smaller  $A_S$  ( $A_S = 1.990$  for 3  $\text{cm}^3/\text{min}$  STP vs  $A_S = 3.724, 2.143$  for 1 and 5  $\text{cm}^3/\text{min}$  STP respectively), indicating that carrier gas flow rate is suitable to sweep the DMMP released in a plug-flow fashion.

To sum up, the experimental conditions to evaluate the preconcentration coefficient are based on the dynamic approach, using modified  $\mu$ -devices with capillary fluidic connections mounted through a high temperature septum with intermediate Kapton layer. The exposition to  $2.54 \text{ mg/m}^3$  DMMP vapour is performed at 10 STP  $\text{cm}^3/\text{min}$  and room temperature, whereas the desorption is performed at 3 STP  $\text{cm}^3/\text{min}$  and heating the  $\mu$ -device up to 523 K until complete release of DMMP from the sorbent coating.

TABLE 6.3. VARIATION OF PRECONCENTRATION COEFFICIENT WITH THE CARRIER FLOW RATE

$Q_{\text{carrier}}$ (STP cm <sup>3</sup> /min)	FWHM (min)	As	K
1	7.347	3.724	7
3	1.331	1.990	13
5	1.071	2.143	9

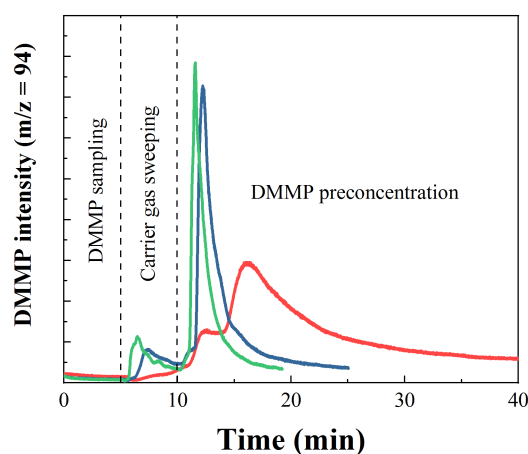


Figure 6.12. Dynamic preconcentration experiment performed on an MCM-48 modified  $\mu$ -preconcentrator for 2.65 mg/m<sup>3</sup> DMMP at room temperature at 10 mL/min. Desorption mass flow has been varied from 1 to 5 cm<sup>3</sup>/min STP.

### 6. 5. 2. DMMP PRECONCENTRATION COEFFICIENT ON $\mu$ -DEVICES MODIFIED WITH SILICEOUS BASED SORBENTS

Two siliceous sorbents have been studied in this work: silicalite and MCM-48. Both of them are based on SiO<sub>4</sub> but arrange in a different structure configuration: silicalite is a microporous material with straight and sinusoidal channels of circa 0.5 nm in diameter, whereas MCM-48 is a mesoporous material with pores of 3.5 nm and intertwined channel configuration.

As previously shown in Chapter V, silicalite-coated  $\mu$ -devices exhibited the highest breakthrough volumes (up to 18 599 STP cm<sup>3</sup> at 132 mg/m<sup>3</sup> DMMP and 10 STP cm<sup>3</sup>/min) as

well as high dynamic sorption capacity (267 mg/g). Thus, for an adsorbent layer above 1 mg, the maximum DMMP that can be trapped before breakthrough is circa 300  $\mu\text{g}$ , which, for an ambient DMMP concentration of 2.65  $\text{mg}/\text{m}^3$  of DMMP in dry  $\text{N}_2$  at room temperature, could be ideally sampled to 100 STP L of gas.

Preconcentration experiments for 2.65  $\text{mg}/\text{m}^3$  of DMMP at room temperature performed with silicate modified  $\mu$ -devices were unsuccessful. Unexpectedly, no DMMP peak signal was found upon the desorption step at 523 K and flushing of the chamber with 3  $\text{cm}^3/\text{min}$  STP He. In order to assess the temperature range where the DMMP is release, 20 mg of degassed (for 72 h at 423 K) silicalite, as well as hydrated, were exposed to vapours of DMMP in a close vessel and left equilibrated for 72 h. Differential thermogravimetric analysis of both samples reveal that DMMP desorption temperature is in the range from 298 K to 523 K (Figure 6.13). For a dehydrated sample, the DMMP uptake was found to be 116  $\text{mg}/\text{g}_{\text{drySilicalite}}$ , whereas for the hydrated sample, it was 93  $\text{mg}/\text{g}$  (expressed per gram of dehydrated zeolite).

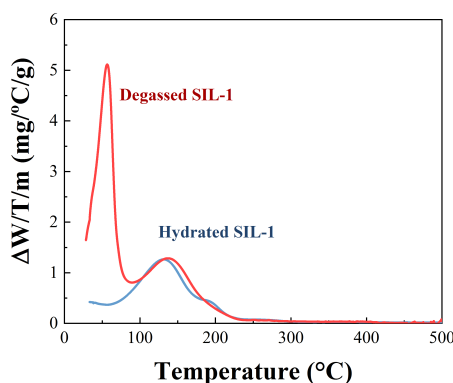


Figure 6.13. DTA analysis of a degassed (red line) and hydrated (blue line) silicalite sample that has been exposed to DMMP vapours in a closed vessel for 72 h.

Assuming that working temperature is adequate for complete DMMP desorption, the explanation could rely on the DMMP decomposition on the silicalite surface. It has been reported that surface  $-\text{OH}$  groups of zeolitic materials may act as active sites for decomposition reaction of DMMP in presence of  $\text{O}_2$  and  $\text{H}_2\text{O}$  [188]. Figure 6.14 shows the proposed reaction pathway on Y type zeolite at 473 K, resulting in the following decomposition products: methyl phosphonic acid (MPA), dimethyl ether ( $\text{CH}_3\text{OCH}_3$ ), methanol ( $\text{CH}_3\text{OH}$ ) formaldehyde ( $\text{CH}_2\text{O}$ ), carbon monoxide ( $\text{CO}$ ) and dioxide ( $\text{CO}_2$ ).

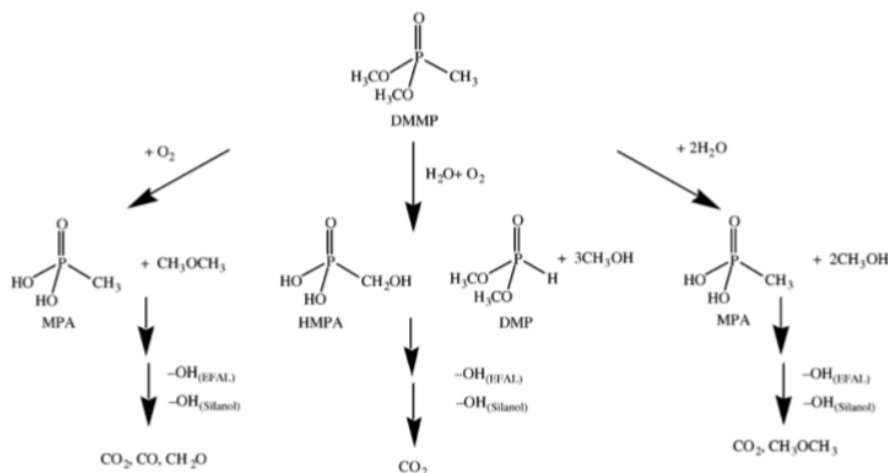


Figure 6.14. Proposed reaction scheme for the thermal reaction of DMMP,  $H_2O$  and  $O_2$  on nanocrystalline NaY at 473 K [188].

Accordingly, Figure 6.15 shows the evolution of GM-MS intensities for the characteristic mass signal for DMMP ( $m/z = 94$ ) as well as the decomposition products (methanol,  $m/z = 31$ ; dimethyl ether,  $m/z = 45$ ;  $CO_2$ ,  $m/z = 44$ ; and formaldehyde,  $m/z = 29$ ) registered at the outlet of the silicalite-modified  $\mu$ -device after sampling  $2.65 \text{ mg/m}^3$  DMMP at room temperature and  $10 \text{ STP cm}^3/\text{min}$ . As it can be observed, after 30 min of sampling, if not heating is applied, registered signals correspond to formaldehyde and  $CO_2$  are attributed to the DMMP hydrolysis even with almost inert  $N_2$  ( $N_2$  may contain a trace-level water content after being dried with a desiccant filter) (Figure 6.15.a). On the other hand, after heating the  $\mu$ -device at 523 K while flushing the silicalite coating with  $3 \text{ STP cm}^3/\text{min}$  He, DMMP as well as methanol and dimethyl ether and additional  $CO_2$  and formaldehyde (Figure 6.15.b) are detected at the outlet. These experiments confirm that DMMP is partially decomposed at 523 K, hindering their application for collection and sampling or organophosphorous compounds

The same experiments have been performed on the MCM-48 modified  $\mu$ -device. Figure 6.16.a shows the evolution of  $K$  for a DMMP concentration of  $2.64 \text{ mg/m}^3$  as a function of the sampling volume, ranging from  $50 \text{ STP cm}^3$  to  $1200 \text{ STP cm}^3$ . Assuming the entire release of the collected DMMP mass by thermal flushing at 473 K, the desorption volume is given by the carrier gas flow rate that sweeps the microdevice, i.e.  $3 \text{ STP cm}^3/\text{min}$ , and the full width is evaluated from the half maximum (FWHM) of the registered desorption peak. As can be seen, there is direct correlation between  $K$  and sample volume, i.e., higher values of  $K$  are observed at higher sample volume in agreement with published literature [190], with a maximum  $K$  of 381 after collecting 3168 ng of DMMP ( $V_{\text{sample}} = 1200 \text{ STP cm}^3$ ) (Table 6.4).

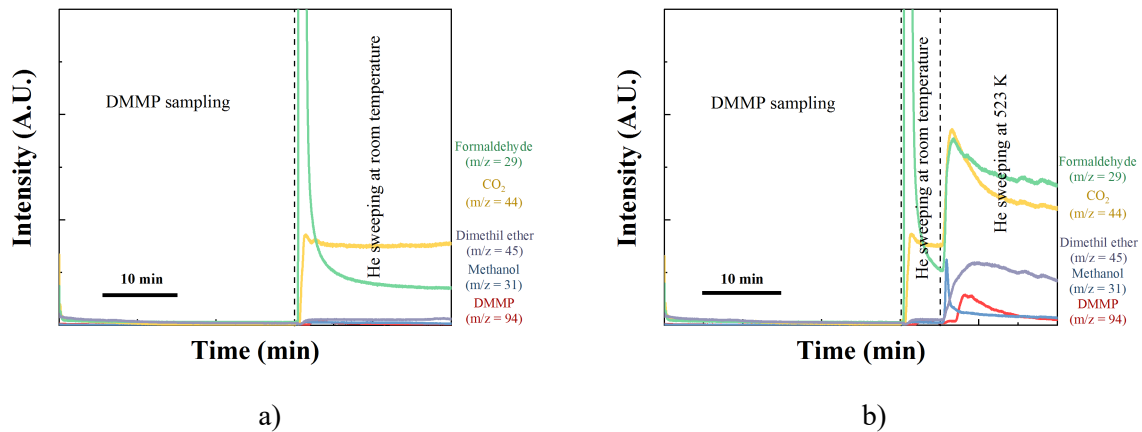


Figure 6.15. Monitoring of the composition for the outlet of silicalite modified  $\mu$ -device exposed to  $2.65 \text{ mg/m}^3$  DMMP at room temperature for 30 min at  $10 \text{ STP cm}^3/\text{min}$ : a)  $\mu$ -device flushed with He at room temperature. b)  $\mu$ -device flushed with He at 523 K.

TABLE 6.4. EVALUATION OF PRECONCENTRATION COEFFICIENT FOR MCM-48 MODIFIED  $\mu$ -DEVICES EXPOSED TO  $2.54 \text{ MG/M}^3$  DMMP AT ROOM TEMPERATURE

$V_{\text{sampling}}$ (STP $\text{cm}^3$ )	FWHM (min)	As	K
50	1.311	1.990	13
100	1.384	2.149	24
300	1.185	3.352	84
600	1.094	1.559	183
1200	1.051	1.595	381

Plotting  $K$  values as a function of the DMMP mass adsorbed by the  $\mu$ -device we can observe that data can be fitted linearly ( $K = 0.1184 * m_{\text{DMMP}}$ ,  $R^2 = 0.9989$ ). Through the linear equation and the dynamic adsorption capacity calculated in Chapter V for  $32 \text{ mg/m}^3$  of DMMP in dry  $\text{N}_2$  at room temperature assuming no deviation from the plateau of the DMMP adsorption isotherm ( $21.2 \text{ mg/g}$ ), we could predict a theoretical maximum preconcentration factor. Consequently, the maximum DMMP adsorbed for an MCM-modified  $\mu$ -device with 0.5 mg of

adsorbent would be circa 11  $\mu\text{g}$ , which at 2.68  $\text{mg}/\text{m}^3$  DMMP at room temperature would be needed to sample up to 4160  $\text{cm}^3$  of gas mixture and theoretically would present a predicted  $K$  of 1320.

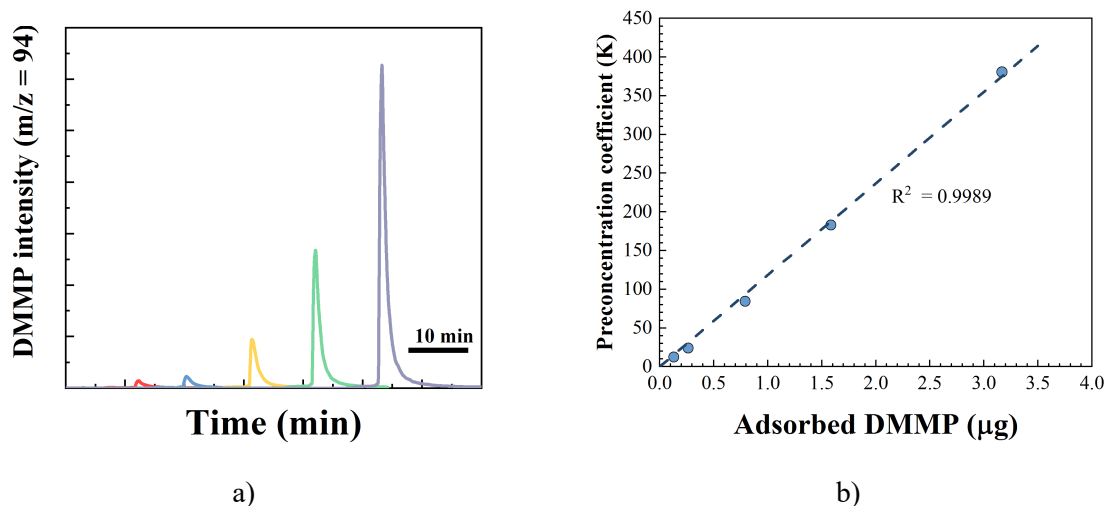


Figure 6.16. a) Preconcentration experiments with MCM-48-modified  $\mu$ -device for 2.65  $\text{mg}/\text{m}^3$  of DMMP in dry  $\text{N}_2$  at room temperature. b) Linear dependency of preconcentration factor as a function of DMMP mass uptake.

### 6. 5. 3. DMMP PRECONCENTRATION COEFFICIENT ON CU-BTC MODIFIED $\mu$ -DEVICES

Previous dynamic experiments with the functional Cu-BTC microdevices provide insight to determine the operating window for a consistent  $K$  determination. As seen on Chapter V, the characterization of CWA adsorption process on  $\mu$ -preconcentrators coated with electro synthesized Cu-BTC ( $m_{\text{Cu-BTC}} = 113 \mu\text{g}$ ) presented a dynamic retention capacity of 122  $\text{mg}/\text{g}$  for 132  $\text{mg}/\text{m}^3$  of DMMP at room temperature. Thus, Cu-BTC modified  $\mu$ -devices would theoretically present a breakthrough volume at the proposed DMMP concentration (2.64  $\text{mg}/\text{m}^3$  DMMP in dry  $\text{N}_2$  at 298 K) up to 5230 STP  $\text{cm}^3$ , assuming that equilibrium conditions correspond to the plateau of DMMP adsorption isotherm.

The evolution of  $K$  for surrogate concentration of 2.65  $\text{mg}/\text{m}^3$  (520 ppbV) as a function of the sample volume, varying from 100 STP  $\text{cm}^3$  to 600 STP  $\text{cm}^3$  is shown in Figure 6.17. As before, it has been assumed the entire release of the collected DMMP mass by thermal flushing at 473 K, so  $K$  is given by the carrier gas flow rate (3 STP  $\text{cm}^3/\text{min}$ ) and the full width at half



maximum (FWHM) of the registered desorption peak. As previously shown on MCM-48 modified  $\mu$ -devices, higher values of  $K$  are observed at higher sample volume with a maximum  $K$  of 171 after collecting 1584 ng of DMMP ( $V_{\text{sample}} = 600 \text{ STP cm}^3$ ) (Table 6.5). Such preconcentration coefficient would require 60 min of sampling at  $10 \text{ STP cm}^3/\text{min}$ . It must be emphasized; however, that similar breakthrough volumes and  $K$  values are attained at higher sampling rates i.e.  $100 \text{ STP cm}^3/\text{min}$ , for microfluidic cavities  $40 \mu\text{m}$  depth at the expense of higher hydraulic losses. Thus, the sampling period could be likely tuned according to the analytical duty cycles imposed by the final application.

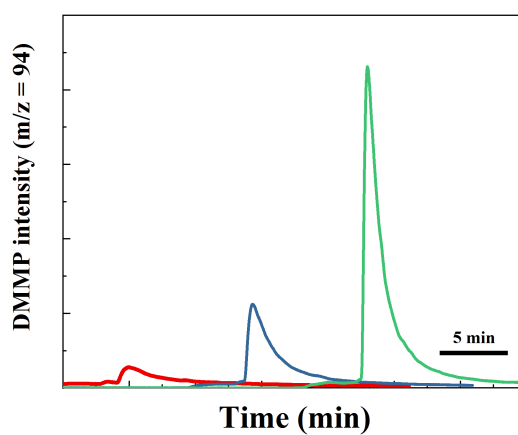


Figure 6.17. a) Preconcentration experiments with Cu-BTC-modified  $\mu$ -preconcentrator for  $2.64 \text{ mg/m}^3$  of DMMP in dry  $\text{N}_2$  at room temperature.

TABLE 6.5. EVALUATION OF PRECONCENTRATION COEFFICIENT FOR CU-BTC MODIFIED  $\mu$ -DEVICES EXPOSED TO  $2.54 \text{ MG/M}^3$  DMMP AT ROOM TEMPERATURE

$V_{\text{sampling}}$ (STP $\text{cm}^3$ )	FWHM (min)	As	K
100	3.059	3.460	11
300	1.828	3.899	55
600	1.171	2.994	171

#### 6. 5. 4. DMMP PRECONCENTRATION COEFFICIENT ON PILS MODIFIED $\mu$ -DEVICES

Preconcentration performance of PIL films has been characterized in two different  $20 \mu\text{m}$ -depth  $\mu$ -device configurations: 1) a flat microcavity (PIL\_DD) and 2) a microcavity

patterned with 50 x 50  $\mu\text{m}$  columns with the inner walls coated with a thin-film of  $\text{Al}_2\text{O}_3$  (PIL\_DD\_50x50 $\text{Al}_2\text{O}_3$ ). Deposition method has been identical in both cases resulting in a theoretical layer thickness of 6.7  $\mu\text{m}$  for PIL\_DD and 6.0 for PIL\_DD\_50x50 $\text{Al}_2\text{O}_3$  assuming a homogeneous coating and a theoretical PIL mass of 2.20 mg in both cases.

After being degassed at 523 K for 15 min, the PIL-modified  $\mu$ -devices have been exposed to a stream of 10 STP  $\text{cm}^3/\text{min}$  of 2.65  $\text{mg}/\text{m}^3$  DMMP in dry  $\text{N}_2$  at room temperature from 10 to 120 min. After which, a stream of He at 3  $\text{cm}^3/\text{min}$  STP has been circulated through the fluidic system to evacuate the DMMP in the gas phase. Then, the materials have been heating up to 523 K and DMMP desorption peak has been registered.

TABLE 6.6. EVALUATION OF PRECONCENTRATION COEFFICIENT FOR PILS MODIFIED  $\mu$ -DEVICES EXPOSED TO 2.54  $\text{MG}/\text{M}^3$  DMMP AT ROOM TEMPERATURE

Sorption unit	$V_{\text{sampling}}$ (STP $\text{cm}^3$ )	FWHM (min)	As	K
PIL_DD	100	2.611	2.954	13
	300	2.077	2.146	48
	600	1.750	2.510	114
PIL_DD_50x50/ $\text{Al}_2\text{O}_3$	100	2.806	3.899	12
	300	3.035	1.789	33
	600	2.475	2.403	81
	1200	1.326	0.867	302

Figure 6.18 shows the DMMP desorption peaks of PIL\_DD and PIL\_DD\_50x50 $\text{Al}_2\text{O}_3$  after sampling from 100  $\text{cm}^3$  STP to 600  $\text{cm}^3$  STP in the case of PIL\_DD and 1200  $\text{cm}^3$  STP for PIL\_DD\_50x50 $\text{Al}_2\text{O}_3$ . The  $\mu$ -devices present at the conditions tested,  $K$  values up to 114 for PIL\_DD and 81 for PIL\_DD\_50x50 $\text{Al}_2\text{O}_3$  when volumes up to 600  $\text{cm}^3$  STP are sampled. Furthermore, for PIL\_DD\_50x50 $\text{Al}_2\text{O}_3$ ,  $K$  value up to 302 has been achieved after sampling 1200  $\text{cm}^3$  STP (Table 6.6).

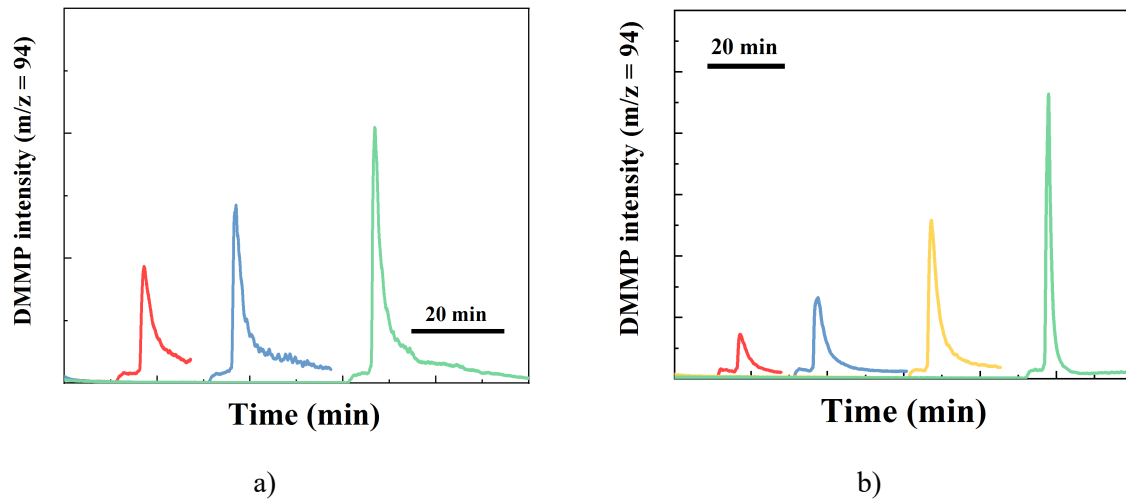


Figure 6.18. Preconcentration experiments for  $2.64 \text{ mg/m}^3$  of DMMP in dry  $\text{N}_2$  at room temperature for a) PIL\_DD and b) PIL\_DD\_50x50Al<sub>2</sub>O<sub>3</sub>.

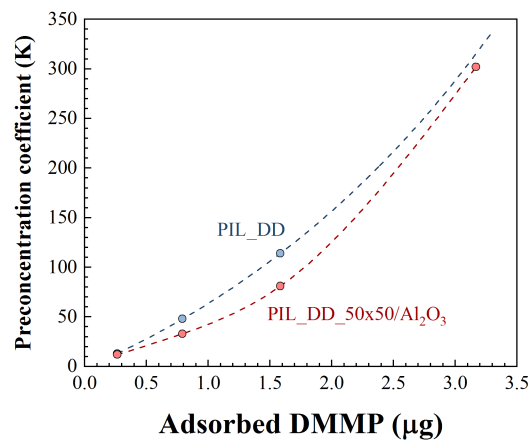


Figure 6.19. Preconcentration factor as a function of DMMP mass uptake of PIL\_DD (blue) and PIL\_DD\_50x50Al<sub>2</sub>O<sub>3</sub> (red). Dotted lines are the predicted trend assuming exponential regression.

$K$  values as a function of the DMMP mass adsorbed are represented in Figure 6.19. It can be observed that data does not follow a linear trend, but a slightly exponential regression.  $K$  values for PIL\_DD are slightly higher than for PIL\_DD\_50x50Al<sub>2</sub>O<sub>3</sub>, probably due to the quicker heating of the Si surface in comparison with the patterned surface, where the Si mass is higher.

## 6. 6. CONCLUSIONS

TABLE 6.7. SUMMARY OF THE RESULTS OF THE PRECONCENTRATION COEFFICIENT FOR THE MODIFIED  $\mu$ -DEVICES TESTED IN THIS CHAPTER

$V_{\text{sampling}}$ (STP $\text{cm}^3$ )	MCM-48		Cu-BTC		PIL			
					PIL_DD		PIL_DD_50x50/ $\text{Al}_2\text{O}_3$	
	K	FWHM (min)	K	FWHM (min)	K	FWHM (min)	K	FWHM (min)
100	24	1.384	11	3.059	13	2.611	12	2.806
300	84	1.185	55	1.828	48	2.077	33	3.035
600	183	1.094	171	1.171	114	1.750	81	2.475
1200	381	1.051	-	-	-	-	302	1.326

We have assessed the feasibility of our functionalized  $\mu$ -devices for the preconcentration of an organophosphorus surrogate, DMMP, at trace level ( $2.65 \text{ mg/m}^3$  at room temperature). By operating at the optimal conditions (sampling volume, flow rate, sampling time),  $K$  values up to 381 for MCM-48, 171 for Cu-BTC and 302 for PIL films have been achieved, with sampling volumes ranging from 600 STP  $\text{cm}^3$  to 1200 STP  $\text{cm}^3$ , desorption flow rates of  $3 \text{ cm}^3/\text{min}$  STP and desorption temperatures up to 523 K. Particularly outstanding are the results obtained for the MCM-48 modified  $\mu$ -device, exhibiting high linearity of  $K$  values in regarding of the DMMP mass adsorbed, and with a predicted maximum  $K$  value of 1320 after sampling 4160  $\text{cm}^3$  (Table 6.7).

On the other hand, it has been observed the unexpected thermal catalytic decomposition of DMMP on silicalite adsorbents and it paves the way to integrate in CWA decontamination applications or reusable gas filters. Although a proper catalytic analysis is still needed to be done; high adsorption capacity, thermal and chemical stability, hydrophobicity and catalytic properties of silicalite proves to be a good candidate for such applications.

Finally, it has been demonstrated the feasibility of a combined ' $\mu$ -preconcentrator –  $\mu$ -cantilever' based gas detector for the sensing of VOC at trace level that can be easily applied

also to CWA sensing. Although the true potential of the solution herein presented relies on its applicability to any kind of commercial detector. For example, quantitative “on field” determination of NAs can be realized by integrating this functional  $\mu$ -preconcentrator with downstream Surface Enhanced Raman Spectroscopy (SERS) based sensor with a DMMP detection limit as low as 130 ppbV and 100 s of response time, already developed in our group [208] (Figure 6.20). Sarin acute exposure guideline level (AEGL-3) is 64 ppbV for an exposure of 10 min [16], i.e. the persons expose above this concentration for this period could experience life-threatening health effects or death. Thus, the combined MCM-48  $\mu$ -preconcentrator coupled with a SERS unit would enable the rapid identification of Sarin when present at concentrations below the threshold AEGL3 value.

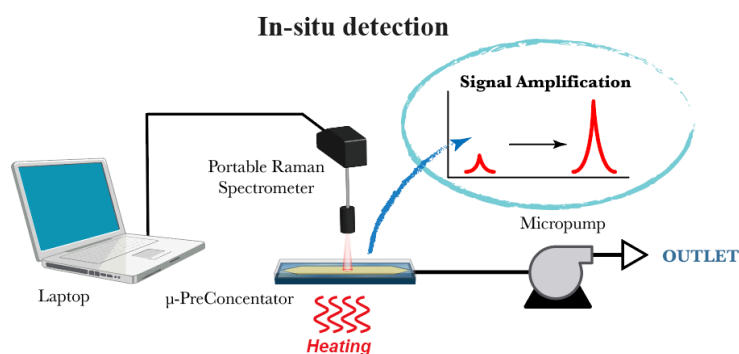


Figure 6.20. Integration of the  $\mu$ -preconcentration unit in a functional electronic nose for CWA monitoring based on Raman spectroscopy.



# **CHAPTER VII:**

## **MAIN CONCLUSIONS AND FUTURE WORK**





## 7. MAIN CONCLUSIONS AND FUTURE WORK

The results obtained throughout the Thesis led to a series of conclusions that have been pointed out in detail at the end of each respective Chapter. Herein, it is summarized the most relevant results and conclusions of this dissertation.

- Based on scientific literature revision, it has been identified sorbents whose textural properties and surface chemistry promote a preferential interaction with nitro- and phosphoryl-groups, and thus are of interest for adsorption of explosive-related and organophosphorus compounds. Sorbents whose framework include electro-donor cations such as  $\text{Cu}^{2+}$  or  $\text{Fe}^{3+}$  are of interest to promote sorbent-sorbate interactions. Acidic materials are also of interest due to the formation of charge-transfer complexes with target molecules. Steric limitations present in sorbents with pore size similar to the kinetic diameter of the target molecule enhance the strength of sorbate-sorbent interactions.
- Different approaches for the incorporation of the nanoporous sorbent in the  $\mu$ -devices have been developed in order to preserve their physico-chemical properties. These procedures mainly include the ex-situ synthesis of the sorbent in powder form and further deposition by spin-coating as well as the in-situ synthesis of polycrystalline films on Si based substrates.
- Ex-situ procedures have been applied to the deposition of the mesoporous silica material MCM-48 as well as Zn-DMCAPZ and Zn-MIM type MOFs. The sorbent is firstly synthesized in powder form (particles submicrometric in size) and the deposited by spin coating on the substrate. The homogeneity of the resulting coatings is highly dependent on the number of depositions cycles and the resulting layers present low reproducibility due to the non-homogenous distribution of the particles after spin coating (as result of the process, the particles aggregates into bigger clusters) and texturized surface of Si substrate as result of wet etching procedure. On the other hand, it stands as a straightforward protocol to scale up at wafer level that can be easily applied to other sorbents in powder form.
- In-situ synthesis of polycrystalline films have been performed with silicalite, Cu-BTC, Zn-DMCAPZ and Zn-MIM materials. Hydrothermal growth of silicalite by

ex-situ synthesis on Si substrates previously seeded with silicalite nanoparticles yields to homogenous and reproducible coatings 4  $\mu\text{m}$  thick. Zn-DMCAPZ coatings have been prepared over an Au (50 nm) modified Borofloat substrates following a layer-by-layer approach rendering in maximum thickness around 1  $\mu\text{m}$  after 20 cycles. Polycrystalline Cu-BTC films have been obtained by electrochemical synthesis on Cu-Ti electrodes (500 nm Cu, 40 nm Ti) micropatterned on a Borofloat substrate, achieving coatings up to 4.7  $\mu\text{m}$ . Zn-MIM coatings less than 1  $\mu\text{m}$  thick have been attempted by solvothermal synthesis on ZnO (100 nm) modified Si substrates. In both cases, the Cu and Zn surfaces are used as the heterogeneous metal source for the Cu-BTC and Zn-MIM synthesis, respectively.

- In situ UV polymerization of commercial imidazole-based protic ionic liquid (PIL) has been achieved in continuous mode over already sealed microdevices, with flat or patterned cavity configurations. Final PIL coatings on flat cavities result in non-continuous films with thickness above 30  $\mu\text{m}$ . On patterned configurations, the experimental conditions for deposition leads to preferential deposition at the inlet of the microdevices and scarce on the inner patterned pillars, thus an optimization of the deposition process is still required.
- The functionalization of commercial graphitized carbon sorbents, 200 microns in size, has been satisfactorily performed with PIL films in situ polymerized on the external surface, i.e. PIL loadings of 0.53 g/g measured by TGA. The protic PIL coatings greatly increase graphitized carbons affinity towards organophosphorus compounds, with DMMP sorption capacities enhance from 56 mg/g to 129 mg/g. Additionally, the selectivity towards less polar compounds such as toluene or n-decane, diminishes in comparison with unfunctionalized carbons. The easy modification of sorbent properties with protic PIL coatings emerges as a promising line of investigation for promoting specific sorption properties on commercial graphitized carbons.
- The detection of nitroaromatic compounds in dry and humid conditions has been carried out with  $\mu$ -cantilevers functionalized with titanosilicates, mesoporous silica material or metalorganic frameworks.  $\mu$ -cantilevers coated with amino functionalized titanosilicate ETS-10 as well as Cu-BTC modified  $\mu$ -cantilever exhibited remarkable response towards o-MNT as result of the interaction between the

electron deficient character of the nitroaromatic compound and the electron donor properties of the amine groups or the Cu node from the metal cluster, respectively. On the contrary, the amino functionalization of mesoporous silica MCM-48 does not improve the sorption properties over pristine MCM-48. This observation is attributed to: a) a decrease of the specific surface area of the modified material (from over 1200 m<sup>2</sup>/g to less than 500 m<sup>2</sup>/g); and, b) clogging of the mesopores opening (pore volume decreases from over 1.1 cm<sup>3</sup>/g to circa 0.2 cm<sup>3</sup>/g).

- The evaluation of a gas sensing unit based on an array of 8 μ-cantilevers functionalized with micro- and mesoporous materials has been performed for a common explosive taggant (DMDNB) and commercial explosives (detonant cord and C-4) in gas phase at ambient conditions. In order to discard the effect from interferents present at ambient conditions (such as ambient humidity) in the sensor responses, the differential response (ratio of explosive response signal to baseline) has been measured. Additionally, to increase the vapours emanating from the solid explosives, and thus the analyte concentration, the target compounds were heated up to 343 K. However, the detection was still challenging due to the number of concomitant interferents that commercial explosive present (such as plasticisers, binder and oils) and low vapor pressure of explosive related molecules even at 343 K.
- Two generation of micropreconcentrators designs have been fabricated on Si substrates following a process layout compatible with the thermal stability of the proposed sorbents. The design of the microfluidic devices has been assisted by a 3-D finite element model that accounts for fluid dynamics inside the microfluidic path as well as heat distribution from the integrated heating coil. The numerical model has been satisfactorily validated by comparison with experimental data (microdevice drop pressure and temperature of the heating coil).
- The organophosphorus sorption process has been evaluated with micropreconcentrators modified with micro- and mesoporous materials and polymeric ionic liquid films using as target molecules the surrogate DMMP. Silicalite based micropreconcentrators exhibit breakthrough volumes over 18 STP L and dynamic sorption capacity up to 270 mg/g for 162 mg/m<sup>3</sup> DMMP at 10 STP cm<sup>3</sup>/min and room temperature as well as high bed efficiencies (over 90 %). MCM-48 modified

microdevices exhibit poorer sorption performance than its microporous counterpart in spite of the higher surface area and pore size. In general, MOFs modified micropreconcentrators although exhibit high equilibrium capacities at static conditions, present low breakthrough volumes and dynamic sorption capacities as result of a fast adsorption on the external surface of the MOF crystals due to the high affinity between DMMP and the metallic cluster and the slow diffusion inside the internal microporosity, exacerbated by the tortuous channel configuration. Micropreconcentrators modified with PIL coatings prepared by in-situ polymerization by dynamic deposition outperform breakthrough volumes and dynamic sorption capacities of the devices prepared by static deposition (breakthrough volumes above 800 STP cm<sup>3</sup> and dynamic sorption capacities up 50 mg/g of devices prepared by dynamic deposition in comparison with breakthrough values of 500 STP cm<sup>3</sup> and capacities of 15 mg/g of devices prepared by static deposition). Although the homogeneity of the layer is higher in the devices prepared by static deposition, the high surface-area ratio of the first ones improves the solvation of DMMP molecules. Patterned microfluidic devices modified with PIL films does not improve un-patterned counterparts due to a deficient deposition of the sorbent film.

- A numerical 3-D mathematical finite element model has been developed to simulate the fluid and adsorbent phase evolution during the sorption process. The model has been satisfactorily assess to model the sorption process of n-hexane on 100 μm-depth microfluidic devices although its application with 20 and 40 μm depth microdevices has been discarded due to high computational cost as result of the high number elements needed to model the thin cavity without compromising the goodness of the meshing.
- The preconcentration coefficient of the modified micropreconcentrators has been evaluated with gas mixtures of DMMP in N<sub>2</sub> at ppb level (500 ppb). Best preconcentration performance has been achieved with MCM-48 modified micropreconcentrators in comparison with Cu-BTC and PIL counterparts. The high pore size of the MCM-48 and channel distribution allow a faster desorption and easier evacuation of adsorbed DMMP molecules than microporous configurations (Cu-BTC) or releasing from the solvent (PIL). The linear correlation of preconcentration

coefficient with adsorbed DMMP allows to predict a theoretical maximum pre-concentration coefficient, assuming no deviation from the plateau of the DMMP isotherm, resulting in a value of 1320.

- Silicalite modified micropreconcentrators lead to catalytic decomposition of DMMP at 523 K. The presence of DMMP hydrolysis products, mainly methanol and dimethyl ether, is recorded at the outlet of the microdevice when thermal flushing after being exposed to DMMP gas mixtures. It is suggested that the surface –OH groups of the silicalite may act as active sites for the decomposition reaction of DMMP in presence of O<sub>2</sub> and H<sub>2</sub>O. This paves the way to the integration of silicalite in CWA decontamination applications or reusable gas filters. Although a proper catalytic analysis is still needed to be done; the high adsorption capacity, thermal and chemical stability and hydrophobic character of silicalite prove to be a good candidate for such applications.
- The feasibility of a combined ‘μ-preconcentrator – μ-cantilever’ miniaturized sensing platform for detection of VOC at trace level has been demonstrated. In addition, the experimentation carried out with DMMP surrogate supports that a similar approach is applicable to NAs detection; and further progress is being done in this field. Although the true potential of the preconcentration approach herein presented relies on its applicability to any kind of commercial detector; a quantitative ‘on field’ determination of NAs can be realized by integrating this functional μ-preconcentrator with downstream Surface Enhanced Raman Spectroscopy (SERS) based sensor. Based on this concept, our preliminary results with core-shell MCM-48/Au plasmonic sorbents reveal DMMP detection limit as low as 130 ppbV and 100 s of response time. Currently, the research efforts are focused on this approach due to such core-shell nanostructures allow the label free, reliable and reproducible identification of DMMP (by its spectral molecular fingerprint) on portable microfluidic chips where preconcentration and detection take place on the same chip.



## 7. CONCLUSIONES Y TRABAJO FUTURO

Los resultados obtenidos a lo largo de esta Tesis han dado lugar a una serie de conclusiones expuestas al final de cada respectivo Capítulo. Aquí se resumen los resultados más relevantes and las conclusiones de este trabajo.

- A partir de la revisión bibliográfica de los últimos avances científicos realizados se han identificado los sorbentes cuyas propiedades texturales y química superficial fomentan la interacción preferencial con grupos nitro y fosforil, y por tanto son interesantes para la adsorción de compuestos explosivos y organofosforados. Sorbentes cuya estructura incluya cationes donantes de electrones como  $\text{Cu}^{2+}$  o  $\text{Fe}^{2+}$  son interesantes para promover la interacción sorbente-sorbato. Al igual que los materiales ácidos son igualmente interesantes debido a la formación de complejos de transferencia de carga con las moléculas diana. Las limitaciones estéricas presentes en sorbentes con tamaño de poro similar al diámetro cinético de las moléculas diana mejoran la fortaleza de las interacciones sorbente-sorbato.
- Se han realizado diferentes aproximaciones a la integración de sorbentes nanoporosos en los  $\mu$ -dispositivos con el objetivo de preservar sus propiedades fisicoquímicas. Estos procesos incluyen principalmente la síntesis ex situ de los sorbentes en forma de polvo y su posterior deposición por centrifugación, así como de la síntesis in situ de películas policristalinas en sustratos silíceos.
- Los procesos ex situ han sido aplicados en la deposición de sílice mesoporosa MCM-48 así como de los polímeros de coordinación porosa Zn-DMCAPZ y Zn-MIM. Los sorbentes han sido sintetizados en forma de polvo (con tamaños de partícula submicrométricos) y depositados por centrifugación en el sustrato. La homogeneidad del recubrimiento resultante es muy dependiente del número de ciclos de deposición. Las capas realizadas presentan una baja reproducibilidad dada por la distribución no homogénea de las partículas después del depósito (dada su tendencia a la agregación fruto del proceso de depósito) y de la textura superficial del sustrato como resultado del proceso de grabado húmedo. Por otra parte, esta estrategia brilla por su capacidad de ser escalable a nivel oblea y fácilmente aplicable a otros sorbentes en forma de polvo.

- La síntesis in situ de películas policristalinas ha sido realizada con los siguientes materiales: silicalita, Cu-BTC, Zn-DMCAPZ y Zn-MIM. El crecimiento hidrotérmico de las capas de silicalita a partir de semillas sintetizadas ex situ previamente da como resultado películas de 4  $\mu\text{m}$  de espesor altamente reproducibles. Los recubrimientos con Zn-DMCAPZ han sido realizados sobre capas de oro (50 nm) depositadas en sustratos de Borofloat siguiendo un proceso de capa por capa, consiguiendo un espesor máximo de 1  $\mu\text{m}$  después de 20 ciclos. Las películas policristalinas de Cu-BTC han sido obtenidas mediante síntesis electroquímica sobre electrodos de Cu-Ti (500 nm de Cu, 40 nm de Ti) dibujados en sustratos de Borofloat, consiguiendo recubrimientos de hasta 4.7  $\mu\text{m}$ . Los recubrimientos de Zn-MIM, de menos de 1  $\mu\text{m}$  de espesor, han sido realizados por síntesis solvotérmica en sustratos silíceos con capas de ZnO (100 nm). En ambos casos, la superficie de Cu y Zn son usadas como fuentes heterogéneas de metal en la síntesis de Cu-BTC y Zn-MIM, respectivamente.
- La polimerización UV in situ de líquidos iónicos próticos, comerciales y basados en imidazol (PIL) ha sido conseguida por deposición continuada en microdispositivos sellados, tanto en configuraciones de cavidad sin y con geometrías interiores. Los recubrimientos de PIL en las cavidades planas (sin pilares) han dado como resultado películas de espesores por encima de 30  $\mu\text{m}$ . En configuraciones con geometrías interiores, las condiciones experimentales para la deposición de las películas resultan en el recubrimiento preferencial en la entrada del microdispositivo y escasa en el interior del área de pilares, es por ello por lo que una optimización del proceso es todavía requerida.
- La funcionalización de sorbentes basados en carbón grafitizado, de 200  $\mu\text{m}$  de tamaño, ha sido realizada satisfactoriamente con recubrimiento de PIL polimerizados in situ sobre la superficie externa, con cargas de PIL de hasta 0.53 g/g medidas por TGA. Los recubrimientos de PIL incrementa enormemente la afinidad de los carbones grafitizados hacia compuestos organofosforados, con capacidades de sorción hacia el DMMP mejoradas hasta 2 veces (desde 56 mg/g hasta 129 mg/g). Así mismo, la selectividad hacia compuestos polares (tales como tolueno o n-decano) decrece en comparación con los carbones sin funcionalizar. El sencillo proceso de funcionalización con recubrimientos de PIL emerge como



una prometedora línea de investigación en la promoción de propiedades específicas de adsorción en carbones comerciales grafitizados.

- La detección de compuestos nitroaromáticos en condiciones secas y húmedas ha sido llevada a cabo con micropalanca funcionalizadas con titanosilicatos, materiales mesoporosos silíceos y polímeros de coordinación porosa. Las micropalanca funcionalizadas con titanosilicatos aminados, así como con Cu-BTC presentan respuestas destacables hacia el o-MNT como resultado de la interacción entre el carácter electrónicamente deficiente del nitroaromático y las propiedades electrónicas donantes del grupo amino o del nodo de Cu, respectivamente. Por el contrario, la funcionalización con grupos amino de la sílice mesoporosa MCM-48 no mejora las capacidades de sorción en comparación con la MCM-48 pura. Esta observación se puede atribuir a: 1) una disminución en el área superficial del material modificado (disminución del área superficial de 1200 m<sup>2</sup>/g a menos de 500 m<sup>2</sup>/g) y b) a la obstrucción de la apertura de los mesoporos (disminución del volumen de poro de 1.1 cm<sup>3</sup>/g a 0.2 cm<sup>3</sup>/g).
- La evaluación de la unidad de sensado de gas basada en un chip de 8 micropalanca funcionalizadas con materiales micro- y mesoporosos ha sido realizada para un marcador de explosivos común (DMDNB) y dos explosivos comerciales (cordón detonante y C-4) en fase gas a condiciones ambientales. Para descartar el efecto de las interacciones ambientales (como la humedad) en la respuesta del sensor, se ha medido la respuesta diferencial de cada palanca (ratio de respuesta ante el explosivo con respecto a la línea base). A su vez, para incrementar la emanación de vapores del explosivo sólido, y así su concentración en fase gas, este ha sido calentado hasta 343 K. Sin embargo, aún así la detección de los compuestos explosivos sigue constituyendo un reto dado el número de interferentes concomitantes presentes en las muestras (plastificantes, aglutinantes, aceites) y de la baja presión de vapor de las moléculas diana incluso a temperaturas de 343 K que dificultan enormemente su detección.
- Dos generaciones de diseño de micropreconcentradores han sido fabricados en sustratos silíceos siguiendo procesos de fabricación compatibles con la estabilidad térmica de los sorbentes propuestos. El diseño de los dispositivos microfluídicos ha sido asistido por un modelo tridimensional por elementos finitos basado

en la dinámica de fluidos en el interior del dispositivo, así como de la distribución térmica desde la espira de calefacción integrada. El modelo numérico ha sido validado satisfactoriamente a partir de resultados experimentales (pérdida de carga en el dispositivo, temperatura en la espira de calefacción).

- El proceso de sorción de compuestos organofosforados ha sido evaluado en micropreconcentradores modificados con materiales micro- y mesoporosos y películas de líquidos iónicos, usando como molécula diana el simulante DMMP. Los micropreconcentradores modificados con capas de silicalita presentan valores de ruptura de hasta 18 STP L y capacidades de sorción dinámica de hasta 270 mg/g para 162 mg/m<sup>3</sup> de DMMP a 10 STP cm<sup>3</sup>/min y temperatura ambiente, así como de altas eficiencias de lecho (por encima de 90 %). Los micropreconcentradores modificados con MCM-48 presentan peores rendimientos de sorción que su análogo microporoso a pesar de su elevada área superficial y tamaño de poro. En general, los micropreconcentradores modificados con polímeros de coordinación porosa, aunque se caracterizan por elevadas capacidades de sorción en condiciones estáticas, presentan bajos volúmenes de ruptura y de capacidades de sorción dinámicas como resultado de la rápida adsorción en la superficie del cristal del material debido a la elevada afinidad entre el DMMP y el nodo metálico y a la baja difusión hacia la microporosidad interior, exacerbada por su tortuosa configuración de canales. Los micropreconcentradores modificados con recubrimientos de PIL preparados por polimerización in situ y deposición continuada presentan elevados volúmenes de ruptura y capacidades de sorción dinámica en comparación con los dispositivos preparados por deposición estática (volúmenes de ruptura por encima de 800 STP cm<sup>3</sup> y capacidades de sorción dinámica de 50 mg/g en el caso de los preparados por deposición continuada en comparación con volúmenes de ruptura de 500 STP cm<sup>3</sup> y capacidades de 15 mg/g de aquellos preparados por deposición estática). Aunque la homogeneidad de las capas preparadas por deposición estática es más elevada que aquellas preparadas por deposición dinámica, el hecho de que las capas de estos últimos sean más irregulares ocasiona que la ratio superficie-área resultado en mejores capacidades de solvatación de las moléculas de DMMP. Los dispositivos con geometrías en el interior de la cavidad no presentan mejoras con respecto a las cavidades sencillas dada la deficiente deposición del recubrimiento.

- Se ha desarrollado un modelo tridimensional matemático para la simulación de la evolución de la fase fluida y el adsorbente durante el proceso de sorción. El modelo ha sido validado satisfactoriamente para el proceso de sorción de n-hexano en microdispositivos de 100  $\mu\text{m}$  de profundidad, sin embargo, su aplicación en dispositivos de menor profundidad (20  $\mu\text{m}$  y 40  $\mu\text{m}$ ) ha tenido que ser descartada dado el alto coste computacional, como resultado del alto número de elementos de necesarios para modelar geometrías finas sin comprometer la calidad de la malla.
- El coeficiente de preconcentración ha sido evaluado para mezclas de gases de DMMP en nitrógeno a nivel de parte por billón (ppb). La mejor respuesta de preconcentración ha sido llevada a cabo por los microdispositivos modificados con MCM-48 en comparación con aquellas con Cu-BTC y PIL. El elevado tamaño de poro de la MCM-48 y su distribución de canales permiten la rápida desorción y fácil evacuación de las moléculas de DMMP adsorbidas que configuraciones microporosas (Cu-BTC) o liberaciones desde el solvente (PIL). La correlación lineal entre el coeficiente de preconcentración y el DMMP adsorbido permite predecir un valor teórico máximo de preconcentración de 1320, asumiendo la no desviación de la meseta de la isoterma de adsorción del DMMP.
- Los micropreconcentradores modificados con capas de silicalita producen la descomposición catalítica de DMMP a 523 K. La presencia de los productos de hidrólisis de DMMP, principalmente metanol y dimetil éter, ha sido registrada a la salida del microdispositivo cuando se han arrastrado térmicamente los compuestos liberados después de su exposición a mezclas gaseosas de DMMP. Se sugiere que los grupos hidroxilo superficiales de la silicalita actúan como centros activos para la reacción de descomposición del DMMP en presencia de  $\text{O}_2$  y  $\text{H}_2\text{O}$ . Este resultado se presenta como una alternativa en la integración de la silicalita en aplicaciones de descontaminación de agentes de guerra química o filtros reusables. Aunque un análisis minucioso es aún necesario, dada la alta capacidad de adsorción y la estabilidad térmica y química, así como del carácter hidrófobo de la silicalita, esta se presenta como una buena candidata para estas aplicaciones.
- La capacidad de detección de compuestos orgánicos volátiles a nivel traza de una plataforma minaturizada como puesta por el micropreconcentrador y las

micropalancas ha sido demostrada. Es más, la experimentación llevada a cabo con simulantes de DMMP fundamenta que una aproximación similar es posible para la detección de agentes nerviosos, de hecho, progresos posteriores están siendo desollados en este campo. Aunque el verdadero potencial del uso de los preconcentradores aquí presentados reside en su aplicabilidad a cualquier detector comercial, una determinación cuantitativa “en campo” de agentes nerviosos puede ser realizada integrando el micropreconcentrador funcional con un detector SERS (Surface Enhance Rahman Spectroscopy) aguas abajo. A partir de este concepto, resultados preliminares dentro del grupo con partículas plasmónicas sorbentes de MCM-48/Au revelan límites de detección de hasta 130 ppbV y tiempos de respuesta de 100 s. Actualmente, los esfuerzos de investigación están centrados en esta aproximación debido a que estas nanoestructuras permiten la identificación libre de marcación, fiable y reproducible de DMMP (a partir de su huella espectral) en chips portables microfluídicos donde la etapa de preconcentración y detección se encuentran en el mismo chip.

# **BIBLIOGRAPHY**



## 8. BIBLIOGRAPHY

- [1] E. Survey, “HEEDING THE CALL BEYOND THE VOTE A STRONGER PARLIAMENT TO LISTEN TO CITIZENS VOICES.”
- [2] “BBC NEWS | In Depth.” [Online]. Available: <http://news.bbc.co.uk/2/shared/spl/hi/guides/457000/457031/html/>. [Accessed: 05-Feb-2020].
- [3] “BBC - London - London Bombings - Bombing: Reaction Timeline.” [Online]. Available: [http://www.bbc.co.uk/london/content/articles/2005/07/12/bomb\\_timeline\\_feature.shtml](http://www.bbc.co.uk/london/content/articles/2005/07/12/bomb_timeline_feature.shtml). [Accessed: 05-Feb-2020].
- [4] R. T. Delfino, T. S. Ribeiro, and J. D. Figueroa-Villar, “Organophosphorus compounds as chemical warfare agents: a review,” *J. Braz. Chem. Soc.*, vol. 20, no. 3, pp. 407–428, 2009.
- [5] H. John *et al.*, “Fatal sarin poisoning in Syria 2013: forensic verification within an international laboratory network,” *Forensic Toxicol.*, vol. 36, no. 1, pp. 61–71, Jan. 2018.
- [6] R. Liu, Z. Li, Z. Huang, K. Li, and Y. Lv, “Biosensors for explosives: State of art and future trends,” *TrAC Trends Anal. Chem.*, vol. 118, pp. 123–137, 2019.
- [7] S. Singh, “Sensors—An effective approach for the detection of explosives,” *J. Hazard. Mater.*, vol. 144, no. 1, pp. 15–28, 2007.
- [8] R. G. Ewing, M. J. Waltman, D. A. Atkinson, J. W. Grate, and P. J. Hotchkiss, “The vapor pressures of explosives,” *TrAC Trends Anal. Chem.*, vol. 42, pp. 35–48, 2013.
- [9] “Organización para la Prohibición de las Armas Químicas.” [Online]. Available: <https://www.opcw.org/es>. [Accessed: 03-Feb-2020].
- [10] N. Bouvet, G. T. Linteris, V. I. Babushok, F. Takahashi, V. R. Katta, and R. Krämer, “A comparison of the gas-phase fire retardant action of DMMP and Br<sub>2</sub> in co-flow diffusion flame extinguishment,” *Combust. Flame*, vol. 169, pp. 340–348, 2016.
- [11] I. J. Zvonkina, P. Gkountara, M. Hilt, and M. Franz, “New printing inks with barrier performance for packaging applications: Design and investigation,” *Prog. Org. Coatings*, vol. 77, no. 3, pp. 646–656, 2014.

- [12] A. S. More, T. Lebarbé, L. Maisonneuve, B. Gadenne, C. Alfos, and H. Cramail, "Novel fatty acid based di-isocyanates towards the synthesis of thermoplastic polyurethanes," *Eur. Polym. J.*, vol. 49, no. 4, pp. 823–833, 2013.
- [13] K. Pobiega, K. Kraśniewska, and M. Gniewosz, "Application of propolis in antimicrobial and antioxidative protection of food quality – A review," *Trends Food Sci. Technol.*, vol. 83, pp. 53–62, 2019.
- [14] K. Ganesan, S. Raza, and R. Vijayaraghavan, "Chemical warfare agents," *J. Pharm. Bioallied Sci.*, vol. 2, no. 3, p. 166, Jul. 2010.
- [15] O. US EPA, "About Acute Exposure Guideline Levels (AEGs)." <https://www.epa.gov/acute-exposure-guideline-levels>
- [16] O. US EPA, "Agent GB (Sarin) Results - AEGL Program." <https://www.epa.gov/agent-gb-sarin>
- [17] G. J. Francis, D. B. Milligan, and M. J. McEwan, "Detection and quantification of chemical warfare agent precursors and surrogates by selected ion flow tube mass spectrometry," *Anal. Chem.*, vol. 81, no. 21, pp. 8892–8899, 2009.
- [18] R. J. Harper, J. R. Almirall, and K. G. Furton, "Identification of dominant odor chemicals emanating from explosives for use in developing optimal training aid combinations and mimics for canine detection," *Talanta*, vol. 67, no. 2, pp. 313–327, 2005.
- [19] M. K. Habib, "Controlled biological and biomimetic systems for landmine detection," *Biosens. Bioelectron.*, vol. 23, no. 1, pp. 1–18, 2007.
- [20] P. Rabinowitz *et al.*, "Animals as sentinels of bioterrorism agents," *Emerg. Infect. Dis.*, vol. 12, no. 4, pp. 647–652, Apr. 2006.
- [21] X. Li *et al.*, "Rapid, on-site identification of explosives in nanoliter droplets using a UV reflected fiber optic sensor," *Anal. Chim. Acta*, 2012.
- [22] S. Delile, A. Aussage, T. Maillou, P. Palmas, V. Lair, and M. Cassir, "Electrochemical detection of nitromethane vapors combined with a solubilization device," *Talanta*, 2015.
- [23] Y. Cui, S. N. Kim, R. R. Naik, and M. C. McAlpine, "Biomimetic peptide nanosensors," *Acc. Chem. Res.*, 2012.



- [24] C. Miao, D. Li, Y. Zhang, J. Yu, and R. Xu, "AIE luminogen functionalized mesoporous silica nanoparticles as efficient fluorescent sensor for explosives detection in water," *Microporous Mesoporous Mater.*, 2014.
- [25] S. J. Patil, N. Duragkar, and V. R. Rao, "An ultra-sensitive piezoresistive polymer nano-composite microcantilever sensor electronic nose platform for explosive vapor detection," *Sensors Actuators, B Chem.*, 2014.
- [26] T. Ponrathnam, J. Cho, P. U. Kurup, J. Kumar, and R. Nagarajan, "Enhancing detection of nitroaromatic vapors by utilizing polymer coatings on quartz crystal microbalances having strong dipoles," *Sensors Actuators, B Chem.*, 2015.
- [27] A. Hakonen *et al.*, "Detection of nerve gases using surface-enhanced Raman scattering substrates with high droplet adhesion," *Nanoscale*, 2016.
- [28] V. Kumar and H. Rana, "Chromogenic and fluorogenic detection and discrimination of nerve agents Tabun and Vx," *Chemical Communications*. 2015.
- [29] X. X. Hu, Y. T. Su, Y. W. Ma, X. Q. Zhan, H. Zheng, and Y. B. Jiang, "A near infrared colorimetric and fluorometric probe for organophosphorus nerve agent mimics by intramolecular amidation," *Chem. Commun.*, 2015.
- [30] J. Zang, C. X. Guo, F. Hu, L. Yu, and C. M. Li, "Electrochemical detection of ultratrace nitroaromatic explosives using ordered mesoporous carbon," *Anal. Chim. Acta*, 2011.
- [31] P. Montmeat, F. Veignal, C. Methivier, C. M. Pradier, and L. Hairault, "Study of calixarenes thin films as chemical sensors for the detection of explosives," *Appl. Surf. Sci.*, 2014.
- [32] D. Spitzer *et al.*, "Bio-inspired explosive sensors and specific signatures," in *Procedia Engineering*, 2014.
- [33] R. S. Dudhe, J. Sinha, D. S. Sutar, A. Kumar, and V. R. Rao, "Poly(3-hexylthiophene) and hexafluoro-2-propanol-substituted polysiloxane based OFETs as a sensor for explosive vapor detection," in *Sensors and Actuators, A: Physical*, 2011.

- [34] R. Bharadwaj and S. Mukherji, "Gold nanoparticle coated U-bend fibre optic probe for localized surface plasmon resonance based detection of explosive vapours," *Sensors Actuators, B Chem.*, 2014.
- [35] M. Boehme, F. Voelklein, and W. Ensinger, "Low cost chemical sensor device for supersensitive pentaerythritol tetranitrate (PETN) explosives detection based on titanium dioxide nanotubes," *Sensors Actuators, B Chem.*, 2011.
- [36] A. Gingras *et al.*, "Fluorescent proteins as biosensors by quenching resonance energy transfer from endogenous tryptophan: Detection of nitroaromatic explosives," *Biosens. Bioelectron.*, 2013.
- [37] C. Barthet, P. Montméat, N. Eloy, and P. Prené, "Detection of explosives vapours using a multi-quartz crystal microbalance system," in *Procedia Engineering*, 2010.
- [38] Y. Gui, C. Xie, J. Xu, and G. Wang, "Detection and discrimination of low concentration explosives using MOS nanoparticle sensors," *J. Hazard. Mater.*, 2009.
- [39] Y. M. Taha, C. A. Odame-Ankrah, and H. D. Osthoff, "Real-time vapor detection of nitroaromatic explosives by catalytic thermal dissociation blue diode laser cavity ring-down spectroscopy," *Chem. Phys. Lett.*, 2013.
- [40] D. Matatagui *et al.*, "Characterization of an array of Love-wave gas sensors developed using electrospinning technique to deposit nanofibers as sensitive layers," *Talanta*, 2014.
- [41] P. A. Baker, M. N. Goltz, A. M. Schrand, D. Y. Yoon, and D. S. Kim, "Organophosphate vapor detection on gold electrodes using peptide nanotubes," *Biosens. Bioelectron.*, 2014.
- [42] L. Pascual *et al.*, "A 'humid electronic nose' for the detection of nerve agent mimics; A case of selective sensing of DCNP (a Tabun mimic)," *Sensors Actuators, B Chem.*, 2014.
- [43] D. C. Tiwari, R. Sharma, K. D. Vyas, M. Boopathi, V. V. Singh, and P. Pandey, "Electrochemical incorporation of copper phthalocyanine in conducting polypyrrole for the sensing of DMMP," *Sensors Actuators, B Chem.*, 2010.
- [44] Y. Liu, C. L. Chen, Y. Zhang, S. R. Sonkusale, M. L. Wang, and M. R. Dokmeci, "SWNT based nanosensors for wireless detection of explosives and chemical warfare agents," *IEEE Sens. J.*, 2013.

- [45] L. Kong *et al.*, “Novel pyrenehexafluoroisopropanol derivative-decorated single-walled carbon nanotubes for detection of nerve agents by strong hydrogen-bonding interaction,” *Analyst*, 2010.
- [46] R. Yoo, J. Kim, M. J. Song, W. Lee, and J. S. Noh, “Nano-composite sensors composed of single-walled carbon nanotubes and polyaniline for the detection of a nerve agent simulant gas,” *Sensors Actuators, B Chem.*, 2015.
- [47] Y. Wang *et al.*, “Flexible gas sensors with assembled carbon nanotube thin films for DMMP vapor detection,” *Sensors Actuators, B Chem.*, 2010.
- [48] S. C. Lee *et al.*, “Effects of textural properties on the response of a SnO<sub>2</sub>-based gas sensor for the detection of chemical warfare agents,” *Sensors*, 2011.
- [49] O. S. Kwon *et al.*, “Multidimensional conducting polymer nanotubes for ultrasensitive chemical nerve agent sensing,” *Nano Lett.*, 2012.
- [50] M. L. Bungabong, P. Bin Ong, and K. L. Yang, “Using copper perchlorate doped liquid crystals for the detection of organophosphonate vapor,” *Sensors Actuators, B Chem.*, 2010.
- [51] S. Sarkar and R. Shunmugam, “Polynorbornene derived 8-hydroxyquinoline paper strips for ultrasensitive chemical nerve agent surrogate sensing,” *Chem. Commun.*, 2014.
- [52] J. Yao *et al.*, “Concise and Efficient Fluorescent Probe via an Intramolecular Charge Transfer for the Chemical Warfare Agent Mimic Diethylchlorophosphate Vapor Detection,” *Anal. Chem.*, 2016.
- [53] I. Sayago *et al.*, “Graphene oxide as sensitive layer in Love-wave surface acoustic wave sensors for the detection of chemical warfare agent simulants,” *Talanta*, 2016.
- [54] Y. Pan *et al.*, “Selective surface acoustic wave-based organophosphorus sensor employing a host-guest self-assembly monolayer of  $\beta$ -Cyclodextrin derivative,” *Sensors (Switzerland)*, 2015.
- [55] V. V. Singh *et al.*, “Micromotor-based on-off fluorescence detection of sarin and soman simulants,” *Chem. Commun.*, 2015.

[56] S. Goswami, S. Das, and K. Aich, “Fluorescent chemodosimeter based on spirobenzopyran for organophosphorus nerve agent mimics (DCP),” *RSC Adv.*, 2015.

[57] “Using Unmanned Aerial Vehicles (UAVs) for CBRN Reconnaissance | CBRNe Portal.” [Online]. Available: <http://www.cbrneportal.com/using-unmanned-aerial-vehicles-uavs-for-chemical-biological-radiological-nuclear-cbrn-reconnaissance/>. [Accessed: 05-Feb-2020].

[58] “ESG Elektroniksystem- und Logistik-GmbH.” [Online]. Available: <https://esg.de/>. [Accessed: 05-Feb-2020].

[59] “UAV-Based Collectors/Detectors | Research International.” [Online]. Available: [https://www.resrchintl.com/UAV\\_Index.html](https://www.resrchintl.com/UAV_Index.html). [Accessed: 05-Feb-2020].

[60] “Flying UAV Laboratory (COTS system) | Research International.” [Online]. Available: [https://www.resrchintl.com/Flying\\_UAV\\_Lab.html](https://www.resrchintl.com/Flying_UAV_Lab.html). [Accessed: 05-Feb-2020].

[61] “News-detailview - EMT Penzberg.” [Online]. Available: [https://www.emt-penzberg.de/en/aktuelles/news-page-details/browse/1/article/7000th-flight-tactical-unmanned-aircraft-system-tuas-luna.html?tx\\_ttnews%5BbackPid%5D=53&cHash=92e2fab6174210dcfbd40846496723b8](https://www.emt-penzberg.de/en/aktuelles/news-page-details/browse/1/article/7000th-flight-tactical-unmanned-aircraft-system-tuas-luna.html?tx_ttnews%5BbackPid%5D=53&cHash=92e2fab6174210dcfbd40846496723b8). [Accessed: 05-Feb-2020].

[62] “LUNA Technical Data - EMT Penzberg.” [Online]. Available: <https://www.emt-penzberg.de/en/produkte/drohnsystem/spezifikationen.html>. [Accessed: 05-Feb-2020].

[63] X. Zhang, B. Gao, A. E. Creamer, C. Cao, and Y. Li, “Adsorption of VOCs onto engineered carbon materials: A review,” *J. Hazard. Mater.*, vol. 338, pp. 102–123, 2017.

[64] C.-Y. Huang, M. Song, Z.-Y. Gu, H.-F. Wang, and X.-P. Yan, “Probing the Adsorption Characteristic of Metal–Organic Framework MIL-101 for Volatile Organic Compounds by Quartz Crystal Microbalance,” *Environ. Sci. & Technol.*, vol. 45, no. 10, pp. 4490–4496, Apr. 2011.

[65] R. R. Bansode, J. N. Losso, W. E. Marshall, R. M. Rao, and R. J. Portier, “Adsorption of volatile organic compounds by pecan shell- and almond shell-based granular activated carbons,” *Bioresour. Technol.*, vol. 90, no. 2, pp. 175–184, 2003.

- [66] Y. Guo, Y. Li, T. Zhu, and M. Ye, "Effects of Concentration and Adsorption Product on the Adsorption of SO<sub>2</sub> and NO on Activated Carbon," *Energy & Fuels*, vol. 27, no. 1, pp. 360–366, Dec. 2012.
- [67] A. Lichtenstein *et al.*, "Supersensitive fingerprinting of explosives by chemically modified nanosensors arrays," *Nat. Commun.*, vol. 5, p. 4195, Jun. 2014.
- [68] M. P. Pina, I. Pellejero, M. Urbiztondo, J. Sesé, and J. Santamaría, "Explosives detection using nanoporous coatings," *Micro-Nanotechnol. Sensors, Syst. Appl. III*, vol. 8031, p. 803124, 2011.
- [69] D. Vassena, A. Kogelbauer, and R. Prins, "Potential routes for the nitration of toluene and nitrotoluene with solid acids," *Catal. Today*, 2000.
- [70] B. Modén, P. Da Costa, B. Fonfè, D. K. Lee, E. Iglesia, and D. K. Lee, "Kinetics and mechanism of steady-state catalytic NO decomposition reactions on Cu-ZSM5," *J. Catal.*, 2002.
- [71] A. Guzmán-Vargas, G. Delahay, and B. Coq, "Catalytic decomposition of N<sub>2</sub>O and catalytic reduction of N<sub>2</sub>O and N<sub>2</sub>O + NO by NH<sub>3</sub> in the presence of O<sub>2</sub> over Fe-zeolite," *Appl. Catal. B Environ.*, 2003.
- [72] P. G. Datskos, N. V. Lavrik, and M. J. Sepaniak, "Detection of Explosive Compounds with the Use of Microcantilevers with Nanoporous Coatings," *Sens. Lett.*, 2004.
- [73] D. Troya, A. C. Edwards, and J. R. Morris, "Theoretical Study of the Adsorption of Organophosphorous Compounds to Models of a Silica Surface," *J. Phys. Chem. C*, vol. 117, no. 28, pp. 14625–14634, Jul. 2013.
- [74] A. R. Wilmsmeyer *et al.*, "Infrared Spectra and Binding Energies of Chemical Warfare Nerve Agent Simulants on the Surface of Amorphous Silica," *J. Phys. Chem. C*, vol. 117, no. 30, pp. 15685–15697, Aug. 2013.
- [75] Z. Ni, J. P. Jerrell, K. R. Cadwallader, and R. I. Masel, "Metal-organic frameworks as adsorbents for trapping and preconcentration of organic phosphonates," *Anal. Chem.*, vol. 79, no. 4, pp. 1290–1293, 2007.

- [76] C. Montoro *et al.*, “Capture of nerve agents and mustard gas analogues by hydrophobic robust MOF-5 type metal-organic frameworks,” *J. Am. Chem. Soc.*, vol. 133, no. 31, pp. 11888–11891, 2011.
- [77] C. Carrillo, G. Martínez, I. Julián, M. P. Pina, and R. Mallada, “Adsorción e hidrólisis de compuestos organofosforados con MOFs basados en Zr,” in *VII Congreso Nacional de I+D en Defensa y Seguridad*, 2019.
- [78] K. Ma *et al.*, “Scalable and Template-Free Aqueous Synthesis of Zirconium-Based Metal–Organic Framework Coating on Textile Fiber,” *J. Am. Chem. Soc.*, vol. 141, no. 39, pp. 15626–15633, Sep. 2019.
- [79] J. E. Mondloch *et al.*, “Destruction of chemical warfare agents using metal–organic frameworks,” *Nat. Mater.*, vol. 14, no. 5, pp. 512–516, 2015.
- [80] R. M. Crooks, “Interactions between self-assembled monolayers and an organophosphonate,” *Situ*, 1997.
- [81] C. Montoro *et al.*, “Capture of Nerve Agents and Mustard Gas Analogues by Hydrophobic Robust MOF-5 Type Metal-Organic Frameworks.,” *J. Am. Chem. Soc.*, vol. 133, no. 31, pp. 11888–11891, 2011.
- [82] M. Agrawal, D. F. Sava Gallis, J. A. Greathouse, and D. S. Sholl, “How Useful Are Common Simulants of Chemical Warfare Agents at Predicting Adsorption Behavior?,” *J. Phys. Chem. C*, vol. 122, no. 45, pp. 26061–26069, 2018.
- [83] J. L. Anderson, J. Ding, T. Welton, and D. W. Armstrong, “Characterizing Ionic Liquids On the Basis of Multiple Solvation Interactions,” *J. Am. Chem. Soc.*, vol. 124, no. 47, pp. 14247–14254, Nov. 2002.
- [84] M. H. Abraham, A. Ibrahim, and W. E. Acree, “Partition of compounds from gas to water and from gas to physiological saline at 310 K: Linear free energy relationships,” *Fluid Phase Equilib.*, vol. 251, no. 2, pp. 93–109, Feb. 2007.
- [85] M. H. Abraham and W. E. Acree Jr, “Descriptors for the Prediction of Partition Coefficients and Solubilities of Organophosphorus Compounds,” *Sep. Sci. Technol.*, vol. 48, no. 6, pp. 884–897, Feb. 2013.

- [86] J. Roquerol *et al.*, “Recommendations for the characterization of porous solids,” *Pure Appl. Chem.*, vol. 66, no. 8, pp. 1739–1758, 1994.
- [87] A. Tավարո and E. Drioli, “Zeolite Membranes,” *Adv. Mater.*, vol. 11, no. 12, pp. 975–996, Aug. 1999.
- [88] E. M. Flanigen *et al.*, “Silicalite, a new hydrophobic crystalline silica molecular sieve,” *Nature*, vol. 271, no. 5645, pp. 512–516, 1978.
- [89] J. Rocha and M. W. Anderson, “Microporous Titanosilicates and other Novel Mixed Octahedral-Tetrahedral Framework Oxides,” *Eur. J. Inorg. Chem.*, 2000.
- [90] M. Taramasso, S. Milanese, G. Perego, Milan, and B. Notari, “Preparation of Porous Crystalline Synthetic Material Comprised of Silicon and Titanium Oxides,” *United States Pat.*, no. 19, pp. 1–8, 1983.
- [91] F. Mani, J. A. Sawada, and S. M. Kuznicki, “Comparative adsorption study of EVS-10 and ETS-10,” *Microporous Mesoporous Mater.*, vol. 204, pp. 43–49, 2015.
- [92] L. Lv, M. P. Hor, F. Su, and X. S. Zhao, “Competitive adsorption of Pb<sup>2+</sup>, Cu<sup>2+</sup>, and Cd<sup>2+</sup> ions on microporous titanosilicate ETS-10,” *J. Colloid Interface Sci.*, vol. 287, no. 1, pp. 178–184, 2005.
- [93] P. Shariaty, M. Jahandar Lashaki, Z. Hashisho, J. Sawada, S. Kuznicki, and R. Hutcheon, “Effect of ETS-10 ion exchange on its dielectric properties and adsorption/microwave regeneration,” *Sep. Purif. Technol.*, vol. 179, pp. 420–427, 2017.
- [94] Y. Krisnandi, E. Lachowski, and R. Howe, “Effects of Ion Exchange on the Structure of ETS10,” *Cheminform*, vol. 37, Feb. 2006.
- [95] K. Vellingiri, L. Philip, and K.-H. Kim, “Metal–organic frameworks as media for the catalytic degradation of chemical warfare agents,” *Coord. Chem. Rev.*, vol. 353, pp. 159–179, Dec. 2017.
- [96] S. S.-Y. Chui, S. M.-F. Lo, J. P. H. Charmant, A. G. Orpen, and I. D. Williams, “A Chemically Functionalizable Nanoporous Material [Cu<sub>3</sub>(TMA)<sub>2</sub>(H<sub>2</sub>O

)&lt;sub&gt;3&lt;/sub&gt;]&lt;sub&gt;&lt;em&gt;n&lt;/em&gt;&lt;/sub&gt;,” *Science* (80-.), vol. 283, no. 5405, pp. 1148 LP – 1150, Feb. 1999.

[97] K. S. Park *et al.*, “Exceptional chemical and thermal stability of zeolitic imidazolate frameworks,” *Proc. Natl. Acad. Sci. U. S. A.*, vol. 103, no. 27, pp. 10186–10191, Jul. 2006.

[98] S. Tanaka *et al.*, “Adsorption and Diffusion Phenomena in Crystal Size Engineered ZIF-8 MOF,” *J. Phys. Chem. C*, vol. 119, no. 51, pp. 28430–28439, 2015.

[99] L. T. Gibson, “Mesosilica materials and organic pollutant adsorption: Part A removal from air,” *Chem. Soc. Rev.*, vol. 43, no. 15, pp. 5163–5172, 2014.

[100] C.T.Kresge, M.E.Lenowicz, W.J.Roth, J.C.Vartuli, and J.S.Bech, “Ordered mesoporous molecular sieves synthesized by a liquid-crystal template mechanism,” *Nature*, vol. 359, no. October, pp. 710–712, 1992.

[101] Z. Allothman, “A Review: Fundamental Aspects of Silicate Mesoporous Materials,” *Materials (Basel)*, vol. 5, pp. 2874–2902, Dec. 2012.

[102] T.-W. Kim, P.-W. Chung, and V. S.-Y. Lin, “Facile Synthesis of Monodisperse Spherical MCM-48 Mesoporous Silica Nanoparticles with Controlled Particle Size,” *Chem. Mater.*, vol. 22, no. 17, pp. 5093–5104, 2010.

[103] H. Nulwala, A. Mirjafari, and X. Zhou, “Ionic liquids and poly(ionic liquid)s for 3D printing – A focused mini-review,” *Eur. Polym. J.*, vol. 108, pp. 390–398, Nov. 2018.

[104] B. P. Regmi, R. Chan, and M. Agah, “Ionic liquid functionalization of semi-packed columns for high-performance gas chromatographic separations,” *J. Chromatogr. A*, vol. 1510, pp. 66–72, Aug. 2017.

[105] W. R. Collin, N. Nuñovero, D. Paul, K. Kurabayashi, and E. T. Zellers, “Comprehensive two-dimensional gas chromatographic separations with a temperature programmed microfabricated thermal modulator,” *J. Chromatogr. A*, vol. 1444, pp. 114–122, Apr. 2016.

[106] “Solvionic | Cleaner solvents for sustainable chemistry.” [Online]. Available: <https://en.solvionic.com/>. [Accessed: 10-Dec-2019].



- [107] F. Almazan, L. Val, M. A. Urbiztondo, M. P. Pina, and J. Santamaria, “ $\mu$ -Preconcentrators Using Protic Imidazolium Polyionic Liquids for Chemical Warfare Agents Sampling at Trace Level,” in *2019 20th International Conference on Solid-State Sensors, Actuators and Microsystems & Eurosensors XXXIII (TRANSDUCERS & EUROSENSORS XXXIII)*, 2019, pp. 1415–1418.
- [108] J. Sterte, S. Mintova, G. Zhang, and B. J. Schoeman, “Thin molecular sieve films on noble metal substrates,” *Zeolites*, vol. 18, no. 5–6, pp. 387–390, May 1997.
- [109] S. Mintova, V. Valtchev, V. Engström, B. J. Schoeman, and J. Sterte, “Growth of silicalite-1 films on gold substrates,” *Microporous Mater.*, vol. 11, no. 3, pp. 149–160, 1997.
- [110] V. Valtchev, J. Hedlund, B. J. Schoeman, J. Sterte, and S. Mintova, “Deposition of continuous silicalite-1 films on inorganic fibers,” *Microporous Mater.*, vol. 8, no. 1, pp. 93–101, 1997.
- [111] J. L. H. Chau, Y. S. S. Wan, A. Gavriilidis, and K. L. Yeung, “Incorporating zeolites in microchemical systems,” *Chem. Eng. J.*, vol. 88, no. 1–3, pp. 187–200, Sep. 2002.
- [112] J. A. . Pieterse, S. Booneveld, and R. . van den Brink, “Evaluation of Fe-zeolite catalysts prepared by different methods for the decomposition of N<sub>2</sub>O,” *Appl. Catal. B Environ.*, vol. 51, no. 4, pp. 215–228, Aug. 2004.
- [113] R. Kefirov, A. Penkova, K. Hadjiivanov, S. Dzwigaj, and M. Che, “Stabilization of Cu<sup>+</sup> ions in BEA zeolite: Study by FTIR spectroscopy of adsorbed CO and TPR,” *Microporous Mesoporous Mater.*, vol. 116, no. 1–3, pp. 180–187, Dec. 2008.
- [114] A. Eguizábal *et al.*, “Novel hybrid membranes based on polybenzimidazole and ETS-10 titanosilicate type material for high temperature proton exchange membrane fuel cells: A comprehensive study on dense and porous systems,” *J. Power Sources*, vol. 196, no. 21, pp. 8994–9007, Nov. 2011.
- [115] K. Shanjiào, D. Tao, L. Qiang, D. Aijun, Z. Yanying, and P. Huifang, “Preparation and application of zeolite beta with super-low SiO<sub>2</sub>/Al<sub>2</sub>O<sub>3</sub> ratio,” *J. Porous Mater.*, vol. 15, no. 2, pp. 159–162, Apr. 2008.

- [116] S. Sachdeva, A. Pustovarenko, E. J. R. Sudhölter, F. Kapteijn, L. C. P. M. de Smet, and J. Gascon, “Control of interpenetration of copper-based MOFs on supported surfaces by electrochemical synthesis,” *CrystEngComm*, vol. 18, no. 22, pp. 4018–4022, 2016.
- [117] A. Martinez Joaristi, J. Juan-Alcañiz, P. Serra-Crespo, F. Kapteijn, and J. Gascon, “Electrochemical synthesis of some archetypical Zn<sup>2+</sup>, Cu<sup>2+</sup>, and Al<sup>3+</sup>-metal organic frameworks,” *Cryst. Growth Des.*, vol. 12, no. 7, pp. 3489–3498, 2012.
- [118] S. Sachdeva *et al.*, “Sensitive and Reversible Detection of Methanol and Water Vapor by In Situ Electrochemically Grown CuBTC MOFs on Interdigitated Electrodes,” *Small*, vol. 13, no. 29, p. 1604150, Aug. 2017.
- [119] K. Kanaya and S. Okayama, “Penetration and energy-loss theory of electrons in solid targets,” *J. Phys. D. Appl. Phys.*, vol. 5, no. 1, pp. 43–58, 1972.
- [120] V. M. Koleshko and I. V. Kiryushin, “Electromigration threshold of thin-film conductors,” *Thin Solid Films*, vol. 192, no. 1, pp. 181–191, 1990.
- [121] M. Todeschini, A. Bastos da Silva Fanta, F. Jensen, J. B. Wagner, and A. Han, “Influence of Ti and Cr Adhesion Layers on Ultrathin Au Films,” *ACS Appl. Mater. Interfaces*, vol. 9, no. 42, pp. 37374–37385, Oct. 2017.
- [122] S. Hsu, H. Chen, and K. Chen, “Cosputtered Cu/Ti Bonded Interconnects With a Self-Formed Adhesion Layer for Three-Dimensional Integration Applications,” *IEEE Electron Device Lett.*, vol. 33, no. 7, pp. 1048–1050, 2012.
- [123] S.-L. Cheng and M.-F. Chen, “Fabrication, characterization, and kinetic study of vertical single-crystalline CuO nanowires on Si substrates,” *Nanoscale Res. Lett.*, vol. 7, no. 1, p. 119, Feb. 2012.
- [124] S. D. Worrall *et al.*, “Metal-organic framework templated electrodeposition of functional gold nanostructures,” *Electrochim. Acta*, vol. 222, pp. 361–369, 2016.
- [125] M. Alfè, V. Gargiulo, L. Lisi, and R. Di Capua, “Synthesis and characterization of conductive copper-based metal-organic framework/graphene-like composites,” *Mater. Chem. Phys.*, vol. 147, no. 3, pp. 744–750, 2014.

- [126] A. Bétard, S. Wannapaiboon, and R. A. Fischer, “Assessing the adsorption selectivity of linker functionalized, moisture-stable metal-organic framework thin films by means of an environment-controlled quartz crystal microbalance,” *Chem. Commun.*, vol. 48, no. 85, pp. 10493–10495, 2012.
- [127] A. Bétard, R. A. Fischer, A. Bétard, and R. A. Fischer, “Metal–Organic Framework Thin Films: From Fundamentals to Applications.,” *Chem. Rev.*, vol. 112, no. 2, pp. 1055–1083, Feb. 2012.
- [128] Y. Pan, Y. Liu, G. Zeng, L. Zhao, and Z. Lai, “Rapid synthesis of zeolitic imidazolate framework-8 (ZIF-8) nanocrystals in an aqueous system,” *Chem. Commun.*, vol. 47, no. 7, pp. 2071–2073, 2011.
- [129] M. Drobek *et al.*, “An innovative approach for the preparation of confined ZIF-8 membranes by conversion of ZnO ALD layers,” *J. Memb. Sci.*, vol. 475, pp. 39–46, Feb. 2015.
- [130] H. Nigar, B. Garcia-Baños, F. L. Peñaranda-Foix, J. M. Catalá-Civera, R. Mallada, and J. Santamaría, “Amine-functionalized mesoporous silica: A material capable of CO<sub>2</sub> adsorption and fast regeneration by microwave heating,” *AIChE J.*, vol. 62, no. 2, pp. 547–555, 2016.
- [131] K. Sarkar *et al.*, “Organic-inorganic hybrid mesoporous materials as regenerable sensing systems for the recognition of nitroaromatic explosives,” *Chempluschem*, 2013.
- [132] D. Carmona, F. Balas, and J. Santamaria, “Pore ordering and surface properties of FDU-12 and SBA-15 mesoporous materials and their relation to drug loading and release in aqueous environments,” *Mater. Res. Bull.*, vol. 59, pp. 311–322, 2014.
- [133] C. J. Lu and E. T. Zellers, “A dual-adsorbent preconcentrator for a portable indoor-VOC microsensor system,” *Anal. Chem.*, vol. 73, no. 14, pp. 3449–3457, 2001.
- [134] J. Wang, J. Ma, and E. T. Zellers, “Room-temperature-ionic-liquid coated graphitized carbons for selective preconcentration of polar vapors,” *J. Chromatogr. A*, p. 460486, Aug. 2019.

- [135] “Product Im0408a / 1-Butyl-3-methylimidazolium bis(trifluoromethanesulfonyl)imide 99.9%.” [Online]. Available: <https://en.solvionic.com/products/1-butyl-3-methylimidazolium-bistrifluoromethanesulfonylimide-99.9>. [Accessed: 04-Dec-2019].
- [136] “Zeolyst | Zeolyst International Zeolyst International.” [Online]. Available: <https://www.zeolyst.com/>. [Accessed: 22-Feb-2020].
- [137] M. P. P. Iritia *et al.*, “Explosives Detection by Array of Si  $\mu$  -Cantilevers Coated with Titanosilicate-Type Nanoporous Materials,” *IEEE Sens. J.*, vol. 16, no. 10, pp. 3435–3443, 2016.
- [138] H. Nigar, B. Garcia-Baños, F. L. Peñaranda-Foix, J. M. Catalá-Civera, R. Mallada, and J. Santamaría, “Amine-functionalized mesoporous silica: A material capable of CO<sub>2</sub> adsorption and fast regeneration by microwave heating,” *AIChE J.*, vol. 62, no. 2, pp. 547–555, Feb. 2016.
- [139] J. A. S. Costa, R. A. de Jesus, D. O. Santos, J. F. Mano, L. P. C. Romão, and C. M. Paranhos, “Recent progresses in the adsorption of organic, inorganic, and gas compounds by MCM-41-based mesoporous materials,” *Microporous Mesoporous Mater.*, vol. 291, p. 109698, 2020.
- [140] S. Deshmukh, R. Bandyopadhyay, N. Bhattacharyya, R. A. Pandey, and A. Jana, “Application of electronic nose for industrial odors and gaseous emissions measurement and monitoring – An overview,” *Talanta*, vol. 144, pp. 329–340, 2015.
- [141] X. Bai, B. Lu, X. Chen, B. Zhang, and J. Tang, “Reversible detection of vancomycin using peptide-functionalized cantilever array sensor,” *Biosens. Bioelectron.*, vol. 62, pp. 145–150, 2014.
- [142] N. Khemthongcharoen, W. Wonglumsom, A. Suppat, K. Jaruwongrungrsee, A. Tuantranont, and C. Promptmas, “Piezoresistive microcantilever-based DNA sensor for sensitive detection of pathogenic *Vibrio cholerae* O1 in food sample,” *Biosens. Bioelectron.*, vol. 63, pp. 347–353, 2015.
- [143] C. Li, X. Chen, Z. Zhang, J. Tang, and B. Zhang, “Gold Nanoparticle-DNA conjugates enhanced determination of dopamine by aptamer-based microcantilever array sensor,” *Sensors Actuators B Chem.*, vol. 275, pp. 25–30, 2018.

- [144] D. D. Shin, D.-G. Lee, K. P. Mohanchandra, and G. P. Carman, “Thin film NiTi microthermostat array,” *Sensors Actuators A Phys.*, vol. 130–131, pp. 37–41, 2006.
- [145] R. Berger, C. Gerber, J. K. Gimzewski, E. Meyer, and H. J. Güntherodt, “Thermal analysis using a micromechanical calorimeter,” *Appl. Phys. Lett.*, 1996.
- [146] X. L. Feng, R. He, P. Yang, and M. L. Roukes, “Very high frequency silicon nanowire electromechanical resonators,” *Nano Lett.*, 2007.
- [147] S. Cai *et al.*, “In situ construction of metal–organic framework (MOF) UiO-66 film on Parylene-patterned resonant microcantilever for trace organophosphorus molecules detection,” *Analyst*, vol. 144, no. 12, pp. 3729–3735, 2019.
- [148] Y. Bao, P. Xu, S. Cai, H. Yu, and X. Li, “Detection of volatile-organic-compounds (VOCs) in solution using cantilever-based gas sensors,” *Talanta*, vol. 182, pp. 148–155, 2018.
- [149] M. A. Urbiztondo *et al.*, “Zeolite-modified cantilevers for the sensing of nitrotoluene vapors,” *Sensors Actuators B Chem.*, vol. 137, no. 2, pp. 608–616, Apr. 2009.
- [150] M. A. Urbiztondo *et al.*, “Detection of organic vapours with Si cantilevers coated with inorganic (zeolites) or organic (polymer) layers,” *Sensors Actuators B Chem.*, vol. 171–172, pp. 822–831, Aug. 2012.
- [151] M. Villarroya *et al.*, “System on chip mass sensor based on polysilicon cantilevers arrays for multiple detection,” *Sensors Actuators, A Phys.*, 2006.
- [152] B. Mitra and A. Gaitas, “Thermally actuated tapping mode atomic force microscopy with polymer microcantilevers,” *Rev. Sci. Instrum.*, 2009.
- [153] B. Ilic, S. Krylov, and H. G. Craighead, “Theoretical and experimental investigation of optically driven nanoelectromechanical oscillators,” *J. Appl. Phys.*, 2010.
- [154] B. Ilic *et al.*, “Single cell detection with micromechanical oscillators,” *J. Vac. Sci. Technol. B Microelectron. Nanom. Struct.*, 2001.
- [155] G. Stemme, “Resonant silicon sensors,” *J. Micromechanics Microengineering*, 1991.
- [156] A. Boisen, S. Dohn, S. S. Keller, S. Schmid, and M. Tenje, “Cantilever-like micromechanical sensors,” *Reports Prog. Phys.*, 2011.

- [157] M. Hoummady, E. Farnault, T. Yahiro, and H. Kawakatsu, “Simultaneous optical detection techniques, interferometry, and optical beam deflection for dynamic mode control of scanning force microscopy,” *J. Vac. Sci. Technol. B Microelectron. Nanom. Struct.*, 1997.
- [158] J. D. Adams *et al.*, “Piezoelectric self-sensing of adsorption-induced microcantilever bending,” *Sensors Actuators, A Phys.*, 2005.
- [159] P. Clément *et al.*, “Gas discrimination using screen-printed piezoelectric cantilevers coated with carbon nanotubes,” *Sensors Actuators, B Chem.*, 2016.
- [160] A. N. Cleland, M. Pophristic, and I. Ferguson, “Single-crystal aluminum nitride nanomechanical resonators,” *Appl. Phys. Lett.*, 2001.
- [161] R. D. Blevins, “Formulas for natural frequency and mode shape,” 1979.
- [162] K. Y. Yasumura *et al.*, “Quality factors in micron- and submicron-thick cantilevers,” *J. Microelectromechanical Syst.*, 2000.
- [163] P. Mohanty, D. A. Harrington, K. L. Ekinici, Y. T. Yang, M. J. Murphy, and M. L. Roukes, “Intrinsic dissipation in high-frequency micromechanical resonators,” *Phys. Rev. B - Condens. Matter Mater. Phys.*, 2002.
- [164] D. M. Photiadis and J. A. Judge, “Attachment losses of high Q oscillators,” *Appl. Phys. Lett.*, 2004.
- [165] D. Garcia-Romeo *et al.*, “Portable lock-in amplifier for microcantilever based sensor array. Application to explosives detection using Co-BEA type zeolites as sensing materials,” in *IEEE SENSORS 2014 Proceedings*, 2014, vol. 2014-Decem, no. December, pp. 1419–1422.
- [166] F. Patolsky *et al.*, “Supersensitive fingerprinting of explosives by chemically modified nanosensors arrays,” *Nat. Commun.*, vol. 5, no. 1, pp. 1–12, 2014.
- [167] F. Patolsky, Y. Engel, A. Pevzner, E. Flaxer, G. Davidi, and R. Elnathan, “Supersensitive Detection of Explosives by Silicon Nanowire Arrays,” *Angew. Chemie Int. Ed.*, vol. 49, no. 38, pp. 6830–6835, 2010.

- [168] G. Serrano, T. Sukaew, and E. T. Zellers, "Hybrid preconcentrator/focuser module for determinations of explosive marker compounds with a micro-scale gas chromatograph," *J. Chromatogr. A*, vol. 1279, pp. 76–85, 2013.
- [169] R. M. Healy *et al.*, "Assessment of a passive sampling method and two on-line gas chromatographs for the measurement of benzene, toluene, ethylbenzene and xylenes in ambient air at a highway site," *Atmos. Pollut. Res.*, vol. 10, no. 4, pp. 1123–1127, Jul. 2019.
- [170] G. Gregis *et al.*, "Characterization of materials toward toluene traces detection for air quality monitoring and lung cancer diagnosis," *Mater. Chem. Phys.*, vol. 192, pp. 374–382, 2017.
- [171] T. Sukaew and E. T. Zellers, "Evaluating the dynamic retention capacities of microfabricated vapor preconcentrators as a function of flow rate," *Sensors Actuators, B Chem.*, vol. 183, pp. 163–171, 2013.
- [172] E. H. M. Camara, P. Breuil, D. Briand, N. F. de Rooij, and C. Pijolat, "A micro gas preconcentrator with improved performance for pollution monitoring and explosives detection," *Anal. Chim. Acta*, vol. 688, no. 2, pp. 175–182, 2011.
- [173] A. B. A. Dow and W. Lang, "Design and Fabrication of a Micropreconcentrator Focuser for Sensitivity Enhancement of Chemical Sensing Systems," vol. 12, no. 7, pp. 2528–2534, 2012.
- [174] M. J. Madou, *Fundamentals of microfabrication*. 1997.
- [175] K. R. Williams, K. Gupta, and M. Wasilik, "Etch rates for micromachining processing - Part I," *J. Microelectromechanical Syst.*, vol. 5, no. 4, pp. 256–269, 1996.
- [176] T. Songsheng, R. Boudreau, and M. L. Reed, "Anisotropic etching of silicon on {111} and near {111} planes," *Sensors Mater.*, vol. 13, no. 5, pp. 303–313, 2001.
- [177] K. R. Williams, K. Gupta, and M. Wasilik, "Etch rates for micromachining processing - Part II," *J. Microelectromechanical Syst.*, vol. 12, no. 6, pp. 761–778, 2003.
- [178] S. J. Bleiker, V. Dubois, S. Schröder, G. Stemme, and F. Niklaus, "Adhesive wafer bonding with ultra-thin intermediate polymer layers," *Sensors Actuators, A Phys.*, vol. 260, pp. 16–23, Jun. 2017.

- [179] A. C. Lapadatu and H. Jakobsen, “Anodic Bonding,” in *Handbook of Silicon Based MEMS Materials and Technologies: Second Edition*, Elsevier Inc., 2015, pp. 599–610.
- [180] D. E. CARLSON, “Ion Depletion of Glass at a Blocking Anode: I, Theory and Experimental Results for Alkali Silicate Glasses,” *J. Am. Ceram. Soc.*, 1974.
- [181] T. R. Anthony, “Anodic bonding of imperfect surfaces,” *J. Appl. Phys.*, 1983.
- [182] A. Cozma and B. Puers, “Characterization of the electrostatic bonding of silicon and Pyrex glass,” *J. Micromechanics Microengineering*, 1995.
- [183] B. Moulkoç, H. V. Jansen, J. W. Berenschot, H. J. M. Ter Brake, K. M. Knowles, and M. C. Elwenspoek, “Characterization of MEMS-on-tube assembly: Reflow bonding of borosilicate glass (Duran®) tubes to silicon substrates,” *J. Micromechanics Microengineering*, 2009.
- [184] L. A. Jonas and J. A. Rehrmann, “IN GAS ADSORP-,” 1972.
- [185] J. A. Rehrmann and L. A. Jonas, “Dependence of gas adsorption rates on carbon granule size and linear flow velocity,” *Carbon N. Y.*, vol. 16, no. 1, pp. 47–51, 1978.
- [186] Y. H. E. E. YOON and J. H. NELSON, “Application of Gas Adsorption Kinetics I. A Theoretical Model for Respirator Cartridge Service Life,” *Am. Ind. Hyg. Assoc. J.*, vol. 45, no. 8, pp. 509–516, Aug. 1984.
- [187] N. Andrei, “A SQP algorithm for large-scale constrained optimization: SNOPT,” *Springer Optim. Its Appl.*, vol. 121, no. 1, pp. 317–330, 2017.
- [188] K. Knagge, M. Johnson, V. H. Grassian, and S. C. Larsen, “Adsorption and thermal reaction of DMMP in nanocrystalline NaY,” *Langmuir*, 2006.
- [189] F. Almazán *et al.*, “Zeolite based microconcentrators for volatile organic compounds sensing at trace-level: Fabrication and performance,” *J. Micromechanics Microengineering*, vol. 26, no. 8, 2016.
- [190] J. Bryant-Genevier and E. T. Zellers, “Toward a microfabricated preconcentrator-focuser for a wearable micro-scale gas chromatograph,” *J. Chromatogr. A*, vol. 1422, pp. 299–309, Nov. 2015.



- [191] A. K. Rappe, C. J. Casewit, K. S. Colwell, W. A. Goddard, and W. M. Skiff, "UFF, a full periodic table force field for molecular mechanics and molecular dynamics simulations," *J. Am. Chem. Soc.*, vol. 114, no. 25, pp. 10024–10035, Dec. 1992.
- [192] A. T. Vu, K. Ho, and C. H. Lee, "Removal of gaseous sulfur and phosphorus compounds by carbon-coated porous magnesium oxide composites," *Chem. Eng. J.*, vol. 283, pp. 1234–1243, 2016.
- [193] Q. Han, L. Yang, Q. Liang, and M. Ding, "Three-dimensional hierarchical porous graphene aerogel for efficient adsorption and preconcentration of chemical warfare agents," *Carbon N. Y.*, vol. 122, pp. 556–563, 2017.
- [194] C. V. Soares, A. A. Leitão, and G. Maurin, "Computational evaluation of the chemical warfare agents capture performances of robust MOFs," *Microporous Mesoporous Mater.*, vol. 280, pp. 97–104, May 2019.
- [195] C. D. Baertsch, H. H. Funke, J. L. Falconer, and R. D. Noble, "Permeation of Aromatic Hydrocarbon Vapors through Silicalite–Zeolite Membranes," *J. Phys. Chem.*, vol. 100, no. 18, pp. 7676–7679, Jan. 1996.
- [196] X. Lu, V. Nguyen, X. Zeng, B. J. Elliott, and D. L. Gin, "Selective rejection of a water-soluble nerve agent stimulant using a nanoporous lyotropic liquid crystal–butyl rubber vapor barrier material: Evidence for a molecular size-discrimination mechanism," *J. Memb. Sci.*, vol. 318, no. 1, pp. 397–404, 2008.
- [197] "Hazardous Substances Data Bank (HSDB)." [Online]. Available: <https://toxnet.nlm.nih.gov/cgi-bin/sis/htmlgen?HSDB>. [Accessed: 11-Dec-2019].
- [198] M. R. Ras, F. Borrull, and R. M. Marcé, "Sampling and preconcentration techniques for determination of volatile organic compounds in air samples," *TrAC Trends Anal. Chem.*, vol. 28, no. 3, pp. 347–361, Mar. 2009.
- [199] F. J. Lopez-Garzon, M. Domingo-Garcia, and M. Pyda, "Studies of the surface properties of active carbons by inverse gas chromatography at infinite dilution," *Langmuir*, vol. 9, no. 2, pp. 531–536, May 2002.

- [200] C. Herry, M. Baudu, and D. Raveau, "Estimation of the influence of structural elements of activated carbons on the energetic components of adsorption," *Carbon N. Y.*, vol. 39, no. 12, pp. 1879–1889, 2001.
- [201] J. L. Anderson, J. Ding, T. Welton, and D. W. Armstrong, "Characterizing Ionic Liquids On the Basis of Multiple Solvation Interactions," *J. Am. Chem. Soc.*, vol. 124, no. 47, pp. 14247–14254, Nov. 2002.
- [202] K. Dettmer-Wilde and W. Engewald, *Practical Gas Chromatography: A Comprehensive Reference*. 2014.
- [203] B. Alfeeli and M. Agah, "MEMS-Based selective preconcentration of trace level breath analytes," *IEEE Sens. J.*, 2009.
- [204] M. Y. Wong, W. R. Cheng, M. H. Liu, W. C. Tian, and C. J. Lu, "A preconcentrator chip employing  $\mu$ -SPME array coated with in-situ-synthesized carbon adsorbent film for VOCs analysis," *Talanta*, 2012.
- [205] S. J. Kim, G. Serrano, K. D. Wise, K. Kurabayashi, and E. T. Zellers, "Evaluation of a microfabricated thermal modulator for comprehensive two-dimensional microscale gas chromatography," *Anal. Chem.*, 2011.
- [206] S. K. Kim, H. Chang, and E. T. Zellers, "Microfabricated gas chromatograph for the selective determination of trichloroethylene vapor at sub-parts-per-billion concentrations in complex mixtures," *Anal. Chem.*, 2011.
- [207] A. F. P. Ferreira *et al.*, "Adsorption of hexane isomers on MFI type zeolites at ambient temperature: Understanding the aluminium content effect," *Microporous Mesoporous Mater.*, 2013.
- [208] M. Lafuente *et al.*, "Highly sensitive SERS quantification of organophosphorous chemical warfare agents: A major step towards the real time sensing in the gas phase," *Sensors Actuators B Chem.*, vol. 267, pp. 457–466, 2018.